AFRL-ML-WP-TR-1998-4202

RESEARCH ON ADVANCED NONDESTRUCTIVE EVALUATION (NDE) METHODS FOR AEROSPACE STRUCTURES

Prepared by:
Alan Berens, Jeffrey Fox, Brian Frock, Prasanna Karpur, Edward Klosterman, Richard Martin, Theodoros Matikas, Mark Ruddell, Shamachary Sathish
UNIVERSITY OF DAYTON RESEARCH INSTITUTE
Structural Integrity Division
300 College Park Drive
Dayton, Ohio 45469-0120

Courtney Daniels, Trent Neel
ADVANCED RESEARCH AND APPLICATIONS CORPORATION
425 Lakeside Drive
Sunnyvale, CA

George Frantziskonis, Jung Woo
THE UNIVERSITY OF ARIZONA
College of Engineering and Mines
Department of Civil Engineering and Engineering Mechanics
Tucson, AZ 85721

REPORT DATE: October 1998

FINAL REPORT FOR 9 SEP 94 THROUGH 30 SEP 98

MATERIALS AND MANUFACTURING DIRECTORATE
Air Force Research Laboratory
Air Force Materiel Command
Wright-Patterson AFB, OH 45433-7817

NOTICE

THIS TECHNICAL REPORT HAS BEEN REVIEWED AND IS APPROVED FOR PUBLICATION.

THOMAS J. MORAN, Project Engineer
Nondestructive Evaluations Branch
Metals, Ceramics & NDE Division

JAMES C. MALAS, Acting Chief
Nondestructive Evaluations Branch
Metals, Ceramics & NDE Division

GERALD J. PETRAK, Assistant Chief
Metals, Ceramics & NDE Division
Materials & Manufacturing Directorate

REPORT DOCUMENTATION PAGE

Form Approved OMB No. 074-0188

1. AGENCY USE ONLY (Leave blank)	2. REPORT DATE	3. REPORT TYPE AND DATES COVERED
	October 1998	9 Sep 94 to 30 Sep 98

4. TITLE AND SUBTITLE
Research on Advanced Nondestructive Evaluation (NDE) Methods for Aerospace Structures

5. FUNDING NUMBERS
C-F33615-94-C-5213
PE-62102F
PR-2418
TA-40
WU-05

6. AUTHOR(S) Alan Berens, Brian Frock, Jeffrey Fox, Prasanna Karpur, Edward Klosterman, Richard Martin, Theodoros Matikas, Mark Ruddell and Shamachary Sathish, UDRI. Courtney Daniels and Trent Neel, ARACOR. George Frantziskonis and Jung Woo, Univ. of Arizona

7. PERFORMING ORGANIZATION NAME(S) AND ADDRESS(ES)
University of Dayton Research Institute
300 College Park
Dayton, OH 45469-0120

8. PERFORMING ORGANIZATION REPORT NUMBER
UDR-TR-1998-00130

9. SPONSORING / MONITORING AGENCY NAME(S) AND ADDRESS(ES)
Materials and Manufacturing Directorate
Air Force Research Laboratory
Air Force Materiel Command
Wright-Patterson AFB, OH 45433-6544
POC: THOMAS J. MORAN, AFRL/MLLP, 937-255-9800

10. SPONSORING / MONITORING AGENCY REPORT NUMBER
AFRL-ML-WP-TR-1998-4202

11. SUPPLEMENTARY NOTES

12a. DISTRIBUTION / AVAILABILITY STATEMENT	12b. DISTRIBUTION CODE
Approved for public release; distribution is unlimited	

13. ABSTRACT *(Maximum 200 Words)*
Studies were conducted to determine the capabilities and limitations of ultrasonic, eddy-current, x-ray CT and wavelet analysis techniques for characterizing aerospace-material properties and for detecting and quantifying defects in aerospace materials. Digital signal-processing techniques were applied to conventional ultrasonic signals to improve mapping of corrosion. Acoustic microscopy methods were studied for fiber-matrix interface characterization, evaluating multi-fiber-reinforced materials and for rapid mapping of Rayleigh-wave velocities. The circumferential creeping wave technique was optimized for detection of cracks emanating from fuel weep-holes in wet-wing aircraft. Capabilities of the MAUS III were demonstrated at trade shows, professional society meetings and conferences. The High Precision Scanning Acoustic Microscope was used to characterize corrosion pits and exfoliation corrosion, and to image voids in ceramic capacitors and laser-shock-peened engine blades. Dozens of X-ray CT application scans were made for governmental agencies and industrial companies. Digital imaging techniques were developed to improve the detection of corrosion in eddy-current images and a study was conducted to determine the reliability of an eddy-current inspection system. Software and hardware for the experimental equipment were developed and upgraded to maintain the state-of-the-art status of the AFRL/MLLP-branch systems.

14. SUBJECT TERMS NDE
Ultrasonics, Acoustic Microscopy, MAUS III, Digital Signal Processing, Corrosion Mapping, Lamb Waves, Circumferential Creeping Waves, Eddy-Current Reliability, X-Ray CT, Wavelet Analysis

15. NUMBER OF PAGES 248

16. PRICE CODE

17. SECURITY CLASSIFICATION OF REPORT	18. SECURITY CLASSIFICATION OF THIS PAGE	19. SECURITY CLASSIFICATION OF ABSTRACT	20. LIMITATION OF ABSTRACT
Unclassified	Unclassified	Unclassified	SAR

Table of Contents

Table of Contents *(Continued)*

List of Figures

List of Tables

Foreword

This final technical report describes the work accomplished during the period from 9 September 1994 through 30 September 1998 by the University of Dayton Research Institute (UDRI) and the Advanced Research and Applications Corporation (ARACOR) for the AFRL/ Materials and Manufacturing Directorate under Contract Number F33615-94-C-5213. Dr. Thomas Moran of the Nondestructive Evaluation Branch (MLLP), Metals, Ceramics and NDE Division, was the Contract Monitor at the beginning and ending of the contract; Dr. Robert Crane, also of the MLLP Branch, was the Contract Monitor during the middle of the contractual period.

Mr. Brian G. Frock of the UDRI Structural Integrity Division was the Principal Investigator for the contract. Mr. Robert Andrews, Division Head of the Structural Integrity Division, was the Program Manager. The following UDRI employees contributed to the work: Dr. Alan Berens, Mr. Jeffrey Fox, Dr. Prasanna Karpur, Mr. Edward Klosterman, Mr. Richard Martin, Dr. Theodoros Matikas, Mr. Mark Ruddell and Dr. Shamachary Sathish. Mr. Courtney Daniels, Mr. Trent Neel, Dr. Nicola Dusaussoy and Dr. James J. LePage of ARACOR contributed to the x-ray CT work effort. Dr. George Frantziskonis, an Associate Professor at the University of Arizona, and Mr. Jung Woo, a PhD candidate at the University of Arizona, conducted the Wavelet Analyses efforts. Ms. Marla McCleskey was responsible for typing and assembling the monthly progress reports. Ms. Jacquelyn Hawkins and Ms. Andrea Snell were responsible for typing this final report.

Section 1
Executive Summary

This contractual effort was initiated to shorten the length of time required to "reduce to use" the results of basic NDE research programs. It was, therefore, designed as a bridge to: (1) establish two-way communications between the basic R&D community and the applications community, and (2) refine and optimize basic NDE research results so that they could be put into practice by the applications community. The design objectives were accomplished by organizing the program into four tasks as shown in Table 1.1.

Table 1.1 – Four-Task Technical Program Organization

TASK I – Applications Area Selection and Technique Capability Assessment
• Identify specific NDE applications • Conduct R&D studies to define NDE requirements which may be met using techniques/ systems developed under the Air Force research program • Prioritize and list the NDE requirements
TASK II – Technique Development
• Develop NDE techniques to meet the requirements which were identified in Task I
TASK III – NDE Technique Optimization
• Optimize the most promising techniques/systems from Task II • Acquire and scan a number of material/component specimens to develop statistically significant database which will demonstrate the applicability of the technique to the requirements identified in Task I
TASK IV – Technology Transition
• Identify potential users of the techniques/systems from Task III in the Air Force and civilian communities • Perform initial technology transition through communication, collaborative efforts, and/or publication of results • Maintain awareness of the state-of-the-art in NDE and identify improvements which may be made to the NDE systems in the Materials Directorate • Upgrade hardware and/or software for the NDE instruments of the MLLP Branch of the Materials Directorate to improve the capabilities for meeting the NDE requirements identified in Task I

Task I Efforts

Three application areas were selected for Task I efforts. These were: (1) material-damage-accumulation monitoring, (2) fiber-matrix-interface characterization, and (3) enhancement of the detection and characterization of microstructure in Titanium materials.

Measurement of the acoustic nonlinear parameter was the technique selected for monitoring accumulation of damage in materials. This study is still in its infancy, but shows promise for monitoring damage accumulation.

Scanning acoustic microscopy was studied for detecting and characterizing fiber-matrix-interface properties in already processed materials. The acoustic microscopy methods have shown enough capabilities to advance to the Task II stage (technique development).

Measurement of the velocity of an acoustic wave in a single fiber of a composite material was examined for inferring the degree of matrix consolidation during curing of the material. This effort did not advance beyond the initial stages of measurement.

Wavelet analysis techniques were studied for enhancing the detection and characterization of microstructure in Titanium materials. More work is needed before the capabilities of using wavelet analysis for enhancing the detection and characterization of microstructure in Titanium materials can be assessed.

Task II Efforts

Within this Task area, existing techniques were modified and/or further developed to address four major areas of concern to the Air Force. These areas were: (1) corrosion detection, (2) detection of flaws in electron-beam welds and diffusion bonds, (3) characterization of adhesive joints, and (4) imaging defects in multi-layered metal-matrix composites.

Image histogram techniques were modified and further developed to help detect corrosion in eddy-current images of multi-layered aluminum wing-skin structures. After developmental studies, these techniques were demonstrated to the requesting agency, SM-ALC, for further evaluation and possible application.

Signal processing techniques were modified and applied to three-dimensional ultrasonic A-scans of corroded aluminum sheets to determine their capabilities and limitations for imaging hidden corrosion. The results of this study were provided to Air Force civilian personnel in the MLSA branch of AFRL Materials and Manufacturing Directorate for possible additional studies.

Time-of-flight (TOF) resolution studies were conducted with the High Precision Scanning Acoustic Microscope (HIPSAM) system to estimate the best obtainable depth-wise accuracy and resolution of that system.

TOF measurements of corrosion pits and exfoliation corrosion were accomplished with HIPSAM to develop an ultrasonic NDT technique for quantifying the depth of corrosion pits, as well as the thickness and lateral extent of exfoliation corrosion in thin aluminum plates.

TOF C-scans of high-voltage ceramic capacitors were carried out with HIPSAM to provide both lateral and depth information of any voids and/or cracks detected in the devices.

TOF C-scans of laser-shock-peened engine blade specimens were accomplished with HIPSAM to detect and image voids within the blade specimens.

Conventional ultrasonic scanning techniques were applied to successfully image disbonds in parts of diffusion-bonded engine rotor disks. These parts were from a shattered engine rotor.

Ultrasonic Lamb-wave techniques were further developed for characterizing adhesive joints in bonded structures. While the technique shows some promise, considerable effort would need to be expended before this technique could be transitioned to use.

Ultrasonic Lamb-wave techniques were also further developed for rapid imaging of defects in multi-layered metal-matrix composites. This technique did not show enough promise to advance beyond the Task II stage.

Task III Efforts

The circumferential creeping-wave technique was optimized for detection of cracks emanating from fuel weep-holes in aircraft wing-skin risers. The optimized technique was demonstrated on C-141 wing-skin risers to Air Force civilian and contractor personnel at WR-ALC. The technique is still under consideration for application by personnel at WR-ALC.

Task IV Efforts

Within this task newly developed technology was communicated and demonstrated to potential users, experimental systems within the MLLP branch were modified and upgraded to maintain state-of-the-art capabilities, and meetings were held with appropriate personnel to determine Air Force NDT needs.

The Mobile AUtomated Scanner (MAUS III) was demonstrated at numerous trade shows, competitive events, and equipment shows and exhibitions to publicize its NDT capabilities. It

was also used to inspect parts and structures, and some of its operating capabilities and limitations were characterized.

X-ray CT systems upgrades (both hardware and software) were made throughout the course of the contract. In particular, spike removal, knife-edge correction, and ring-correction algorithms were developed and implemented on the Tomoscope. A cross-talk-reduction algorithm was developed and installed on the LAM/DE system. These upgrades significantly improved the imaging capabilities of both systems. In addition, a new FeinFocus x-ray source was installed on the Tomoscope system.

X-ray CT application scans were made for other governmental agencies, universities and industrial companies. Some of the scans were made under a CRDA established during this contract.

Hardware and software upgrades were made to the computer systems in the branch. In addition, a new submersible load frame was constructed and integrated into the HIPSAM system.

Five Air Force ALC visits were made during the course of the contract. These were made to obtain information about Air Force NDT needs and to discuss potential solutions to existing Air Force NDT problems.

Papers and presentations were written and made during the contractual effort to help communicate and transition the results of the R&D efforts to potential users.

Section 2

TASK I – Application Area Selection and Technique Capability Assessment

2.1 Design and Development of Acoustic Lenses for Nonlinear Acoustic Imaging

In conventional acoustic imaging of materials, an acoustical signal of a specific frequency is focused on (or within) the material and the amplitude of the returned signal is captured to generate acoustic images. The contrast in the image is related to linear elastic properties (such as attenuation, velocity, second order elastic constants). In many situations, e.g., materials under stress or fatigued materials, the changes in second order elastic constants are too small to provide high enough contrast for meaningful material characterization. On the other hand, it is well documented in the literature that, in many situations – including stress and/or fatigue – materials show significantly large changes in nonlinear acoustic behavior. Detection of second harmonic generation is the most often used experimental approach for investigating nonlinear acoustic behavior. In this method, an acoustic signal of frequency (f) is propagated through the material and the material-generated second harmonic acoustic signal of frequency (2f) is detected. The ratio of the second harmonic signal's amplitude (A_2) to the input fundamental frequency signal's amplitude (A_1) is a measure of the nonlinear behavior of the material.

Most of the studies of nonlinear elastic behavior of materials have been global in nature and have been performed on large samples. Studies related to the possibility of performing local acoustic-nonlinearity measurements have been very limited. The majority of these attempts have used either acoustic transmission or acoustic lenses of complex geometric design. UDRI developed a simple acoustic lens capable of focusing an acoustic signal in a sample placed in water and receiving the second harmonic signal after reflection from the sample. The lens was tested by transmitting a 6 MHz signal and receiving a 12 MHz signal. Since the transmitted beam was focused (spot size = 0.25 mm), the amplitude of the signal was quite high; that helped generate a second harmonic signal. Although observation of a second harmonic in the received signal is an indication of second harmonic generation, the most conclusive test is to observe a quadratic dependence of the amplitude of the second harmonic signal as a function of fundamental amplitude. To confirm this behavior, the amplitude of the second harmonic signal has been measured by varying the funda-

mental signal amplitude in several materials. Plots of A_2 vs. A_1^2 are shown in Figures 2.1-1, 2.1-2 and 2.1-3, respectively, for metallic, ceramic and polymeric materials. As expected, a quadratic behavior was observed and the slope for each material was found to be different.

In these experiments, acoustic waves were propagated through the lens material, water and the sample and back again to the transducer. Hence, the received signal was a mixture of the nonlinear elastic behavior of the lens material, water and the sample. It is well known that the nonlinear properties of water are much larger than those of the solids. In order to extract the local nonlinear behavior of the sample from the mixed signal, UDRI is developing both experimental methodology and theoretical models. In spite of the many complexities, the nonlinearity of the lens material and water remains constant while scanning a material to generate an image. Thus, any changes in the contrast can be attributed to the variations in the local nonlinear behavior of the material under investigation.

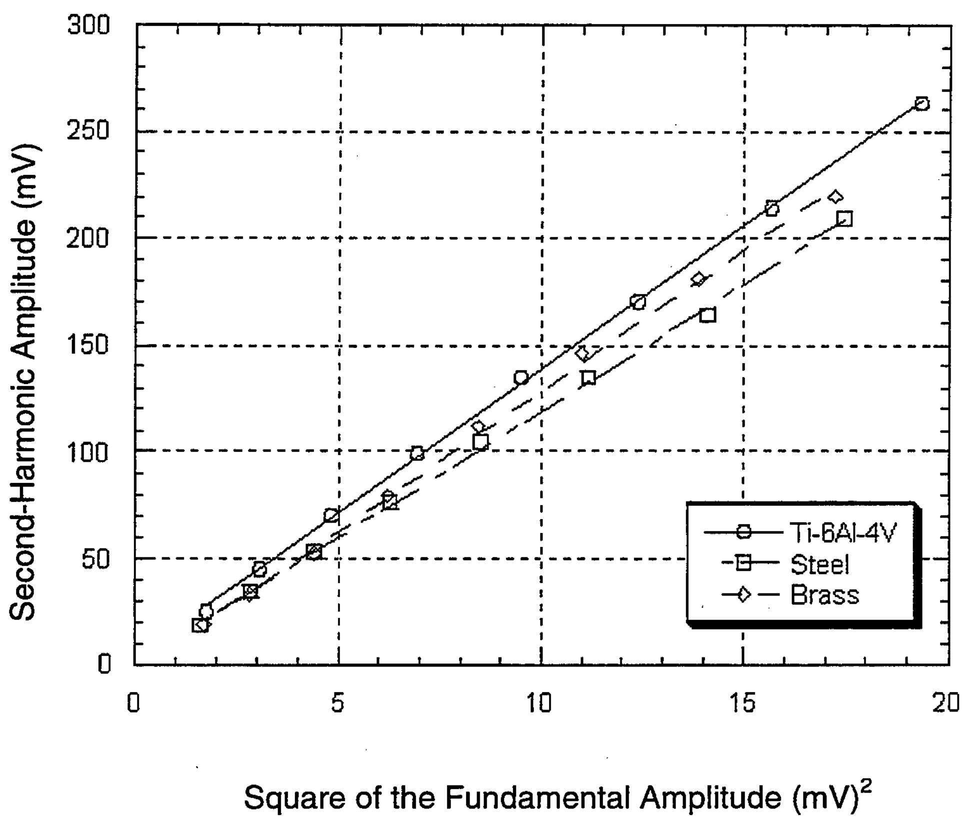

FIGURE 2.1-1
Acoustic Nonlinearity Plot for Metallic Materials

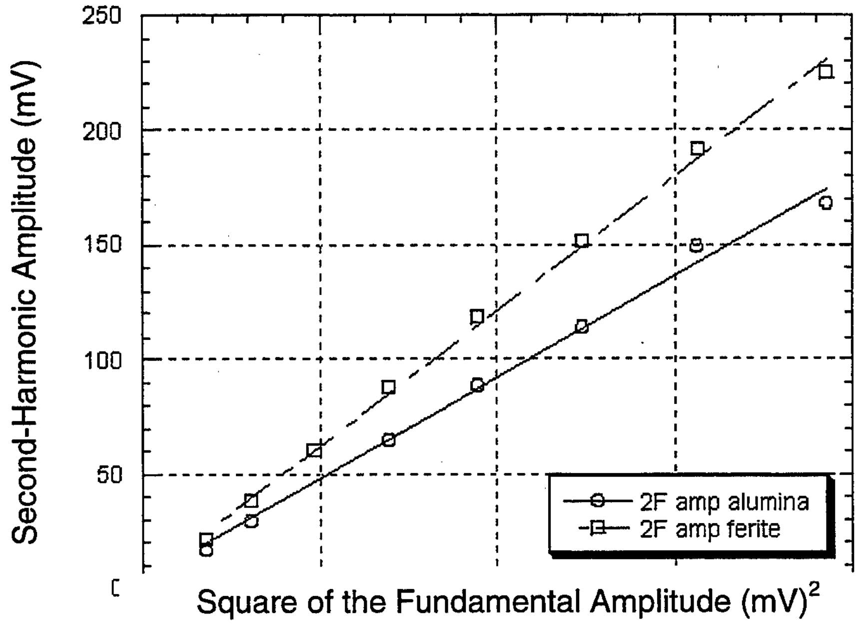

FIGURE 2.1-2
Acousitc Nonlinearity Plot for Ceramic Materials

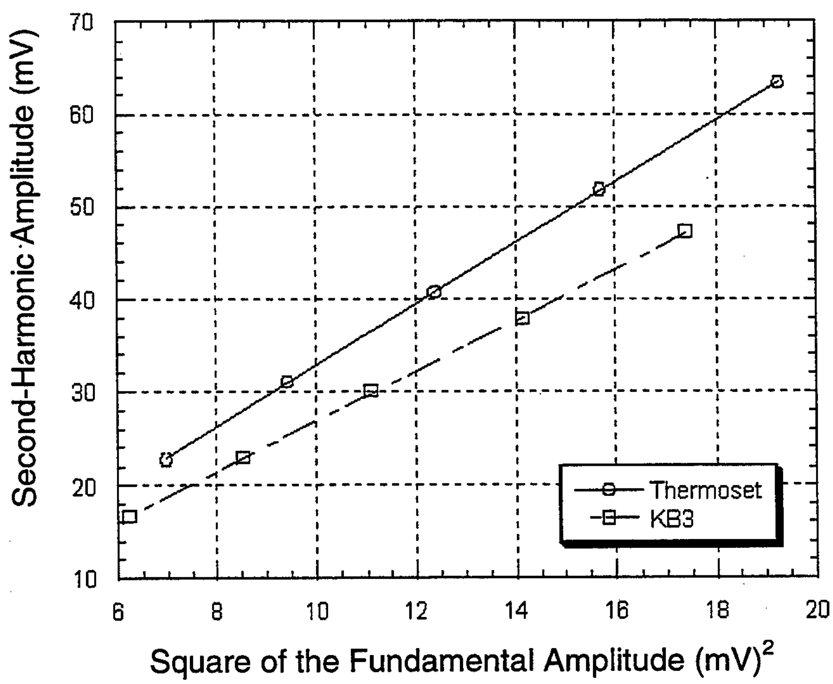

FIGURE 2.1-3
Acoustic Nonlinearity Plot for Polymeric Materials

2.2 Assessment of Scanning Acoustic Microscopy Capabilities

2.2.1 Capability for Determining Fiber-Matrix Interface Properties of Single-Fiber Samples

A Scanning Acoustic Microscope (SAM) technique has been used to determine important interface/interphase properties of a single fiber embedded in a matrix material. This technique allows the fiber to be imaged directly; subsequent analysis of the image (taken after mechanical load testing) allows an assessment of the fiber fragmentation to be made, and also allows the critical fragmentation length to be determined accurately. Determination of the critical fragmentation length, in turn, allows the interfacial shear strength (IFSS) of the fiber matrix interface – an important parameter for determination of a fiber-reinforced material's load-carrying capability – to be calculated.

Most single fiber fragmentation tests have been limited to optically transparent materials in which a photo-elastic technique can be used. In an attempt to extend the technique to non-transparent materials, acoustic-emission [Netravali, et. al.] and shear-wave back reflection of low frequency ultrasonic waves [Drzal] have been proposed. A major difficulty with the acoustic emission technique is the development of a suitable signal amplitude threshold criterion to isolate acoustic emission signals due to fiber breakage from signals due to other sources. Another difficulty is that the thicknesses of composite specimens are often comparable to the wavelength of sound in the material at acoustic emission frequencies. This can result in the generation of plate mode vibrations that travel with velocities that are complex combinations of longitudinal and shear waves in the matrix. Such a situation complicates the determination of the fiber-fragment critical length from the wave arrival times. In the shear-wave back reflection technique, an unequivocal determination of the fragmentation length (of the order of microns) is often obscured by the low resolution of the acoustic images (on the order of hundreds of microns). Moreover, as the fragments become smaller, the image interpretation and the clear identification of the breaks become more difficult due to the presence of several fragments within the diameter of the acoustic beam. The SAM technique discussed here overcomes many of the limitations associated with both acoustic-emission-based techniques and low-resolution ultrasonic scanning methods (shear-wave back reflection).

To test the SAM technique, two composite samples having a single 7 μm diameter carbon fiber centered along the axis of a dog-bone-shaped, optically-transparent matrix were prepared

for study by the Department of Mechanical Engineering at the University of Tennessee. These two samples (labeled A and B) had a gauge length of 30 mm, a width of 4 mm, and a thickness of 2 mm. Optically-transparent epoxy was used for the matrix material so that photo-elastic measurements of fiber fragmentation lengths could be directly compared to those obtained from application of the SAM technique.

Photo-elastic studies of the fiber fragmentation were performed on Sample A while it was loaded in tension and the appropriate critical length was measured. After these measurements, the sample was polished to reduce both the thickness and the surface topography for SAM observations. SAM measurements using a 200 MHz acoustic lens were performed at NESB, NASA Langley Research Center using the ELSAM acoustic microscope. The SAM images had high contrast, making observation of the fiber breaks possible. The SAM images also showed other features similar to the breaks at unexpected places; this made a clear determination of the fragmentation length difficult. To investigate these features, Sample B was loaded under the SAM. This sample was polished on both sides to reduce the thickness and to keep the fiber symmetrical about the middle line during the axial loading. The acoustic images obtained before any application of load showed a good interface between the fiber and the matrix. As the load was increased to about one fifth of the load required to break the fiber, bright spots resembling breaks appeared at various places along the length of the fiber. Multiple breaks were not possible since the load was too low to cause even a single break. Therefore, it was concluded that the bright spots were debonds at the fiber-matrix interface. Further increases in load gave rise to the fiber breaks, but no changes were observed in the bright spots which had appeared prior to fiber breakage.

At this point, the results from Sample A were re-examined. A trapped air bubble in the sample was chosen as a reference for both SAM and photo-elastic images. Given the results from the tests on Sample B, the bright spots observed between the fiber breaks were not considered to be additional fiber breaks. The lengths of the fragments were measured from the middle of the one break to the middle of the next break. This measurement of fiber lengths from the SAM images agreed to within 3% of the measurements from the photo-elastic images. Further analysis of the acoustic images showed a possibility of measurement of the debond lengths from the broken edges.

It has been shown that the SAM technique can: (1) image fiber fragments in single-fiber test specimens, (2) provide information about the debonded regions that appear prior to fiber breaks, (3) be used to measure critical fragmentation lengths, and (4) be used to measure debond lengths from the broken edges of the fiber. A paper describing this study in detail has been submitted for publication in the *Journal of Materials Research.* A copy of that paper, titled "Assessment of Single Fiber Fragmentation Using Scanning Acoustic Microscopy," is included in Appendix A.

2.2.2 Capabilities for Evaluating Multi-Fiber Reinforced Materials

Additional capabilities of the SAM technique were determined for:

1. studying the degradation of the fiber-matrix interfaces due to elevated temperatures and fatigue loading,
2. nondestructively monitoring the accumulation and growth of damage at the fiber-matrix interface, as well as the initiation and propagation of matrix cracks, and
3. understanding interfacial failure mechanisms in MMCs due to fatigue.

The samples used during this assessment study were subjected to various mechanical tests, including room temperature mechanical fatigue, isothermal mechanical fatigue, and elevated temperature fatigue cycling in addition to thermo-mechanical fatigue (in-phase and out-of-phase) conditions. Subsequent destructive evaluations were used to verify the indications revealed by SAM images of interfacial regions of all the samples. The publication, "Ultrasonic Evaluation of Fiber-Matrix Interfacial Degradation of Titanium Matrix Composites Due to Temperature and Mechanical Loading," describes this study in detail and is included in Appendix A.

2.2.3 Rapid Mapping of Rayleigh-Wave Velocities

Measurement of local Rayleigh-wave velocities (V_R) in materials are most often performed using a scanning acoustic microscope. One of the earliest methods developed recorded the variation in the amplitude, V(z), of the tone burst signal reflected from the sample as the distance, "z," between the lens and the sample was varied. Periodic dips observed in the so-called V(z) curve have been shown to be caused by the interference between the specularly-reflected and Rayleigh-wave signals on the face of the transducer (see Figure 2.2.3-1). The periodicity (Δz) in the curve has been related to the Rayleigh-wave velocity in the material through

$$V_R = V_w\{1 - [1- (V_w /2F\Delta z)]^2\}^{-1/2} \qquad (1)$$

where F is the frequency of the acoustic signal and V_w is the velocity of sound in water. This methodology has been extended [Quate, et. al.] to perform highly accurate measurements (1 part in

10^4 m/s) [Kushibiki and Chubachi] of Rayleigh-wave velocities. These high accuracy measurements demand extreme precautions in the experimental set up, and minimal variations in the water temperature. Applying extensions of this method for imaging an area becomes quite time consuming and tedious.

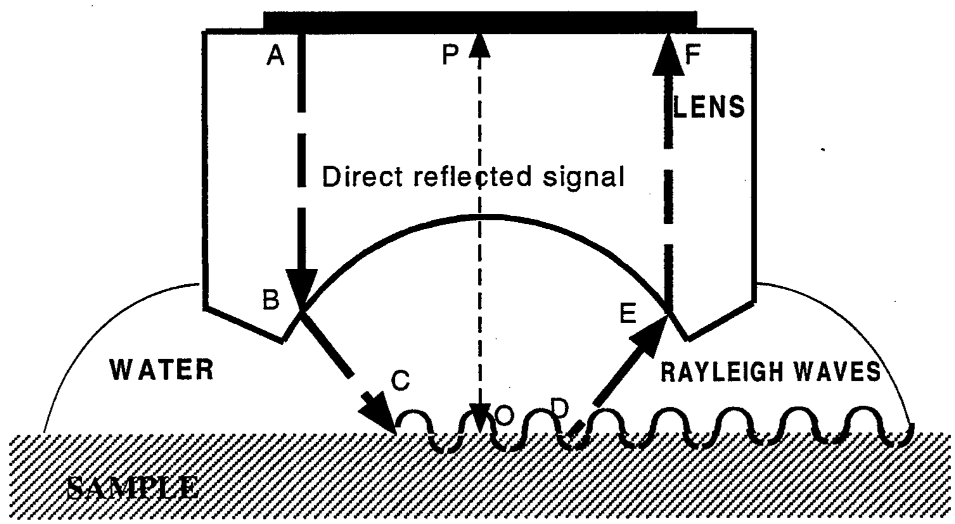

FIGURE 2.2.3-1
Rays Involved in Generating V(z) Curve
(Rayleigh Ray – AB-BC-DE-EF and Direct Ray – PO)

An alternate method uses impulse excitation of the lens and separation of the Rayleigh-wave signal from the speculary-reflected signal in the time domain [Kulik, et. al.]. This allows measurement of the time difference between the two signals and determination of the Rayleigh-wave velocity from the time difference. Measuring the time differences at two defocuses (see Equation 2 and Figure 2.2.3-2) simplifies the measurement and reduces the calculation time. The symbols in Equation 2 are explained in Figure 2.2.3-2

$$V_R = \frac{2(z_1 - z_2)}{[(tw_1 - tw_2)^2 - (tR_1 - tR_2)^2]^{1/2}} \qquad (2)$$

This methodology has been implemented on the UDRI-developed HIgh Precision Scanning Acoustic Microscope (HIPSAM) system in the AFRL/MLLP Branch. The capabilities of the technique have been determined by making measurements on an elastically isotropic E6 glass sample for which the Rayleigh-wave velocity is well documented. The system has been found to have an overall accuracy and precision of better than 0.5%.

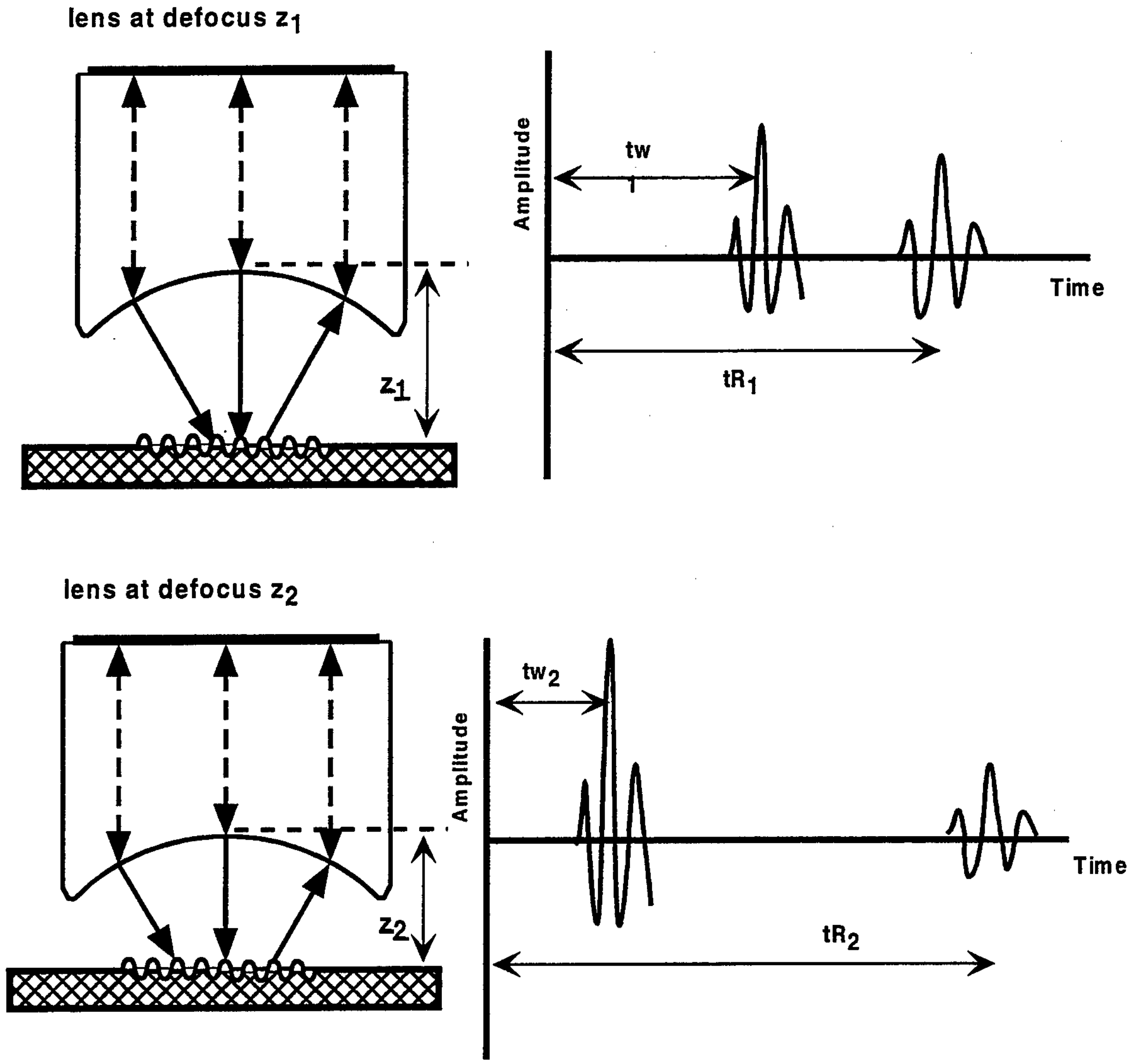

FIGURE 2.2.3-2
Temporal Separation of Specularly Reflected Wave and Rayleigh-Wave

The Rayleigh-wave velocity imaging method has been applied to Ti-6Al-4V samples with large-grain structure for studying velocity variations among grains, and to samples with grain colonies for studying velocity variations among colonies. It has also been utilized to measure the variation of the Rayleigh-wave velocity in a plastically-deformed zone in a sample of Ti-6Al-4V. The measurement methodology has also been extended – by using a cylindrical acoustic lens – to the study of anisotropic elastic properties of materials. More details and results regarding this topic can be found in a paper titled, "Rayleigh-Wave Velocity Mapping Using Scanning Acoustic Microscope." That paper is included in Appendix A.

2.3 Inferring Matrix Consolidation at a Fiber-Matrix Interface

The feasibility of using changes in single fiber acoustic velocity to infer the degree of matrix consolidation at the fiber-matrix interface was investigated. The testing was performed in situ on a silicon-carbide-fiber-reinforced glass-matrix composite during the curing process.

A long (approximately 2 m) piece of silicon carbide fiber was placed in a tube furnace. The center 100 mm of the fiber were encased in glass tape (powdered glass in a polymer binder) and the ends protruded through the furnace gas purge plumbing. Contact ultrasonic transducers were attached to the fiber ends, and the arrival time of the acoustic pulse through the fiber was monitored during the processing cycle.

The furnace was ramped up to 450 degrees C with an oxygen purge to remove the polymer binder from the glass tape. At 160 minutes, the furnace was purged with argon and the temperature was ramped up to 710 degrees C for a 90 minute hold prior to cool-down. These results are illustrated in Figure 2.3-1. Note that the acoustic transit time dramatically decreases between 185 and 230 minutes then remains stable for the duration of the experiment. Initial investigations indicate that the acoustic velocity may be used as feedback to modify the processing cycle.

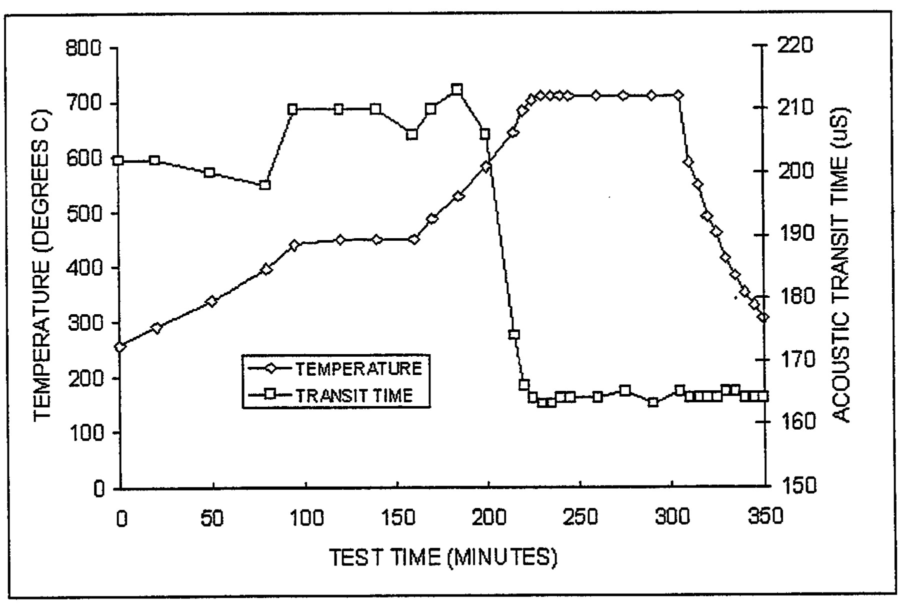

FIGURE 2.3-1
Plot of Acoustic Transit Time and Temperature Versus Time

A journal article titled, "The In Situ Sensor Guided Process Characterization of Advanced Composite Materials," describing this study in detail, was published in the September 1996 issue of the *Journal Of Materials*. A copy of that article is included in Appendix A of this report.

2.4 Wavelet Analysis of Titanium Microstructures

This program investigated the capabilities and limitations of wavelet analyses for determining the following microstructural characteristics of Titanium: type of microstructure, spatial uniformity of the microstructure, and the presence or absence of defects in the microstructure. Software for performing wavelet analyses on digitized optical images was developed and then tested on Titanium specimens with a variety of microstructure. The results are provided in a report included in Appendix A.

Section 3

TASK II – Technique Development

3.1 Histogram Techniques for Imaging Hidden Corrosion in Eddy-Current Images

A histogram technique was developed to help discriminate between "normal" and "anomalous (possibly corroded)" regions in eddy-current images of aircraft panel structures. The steps involved in applying the technique are outlined in Table 3.1-1.

Table 3.1-1. Histogram Technique for Corrosion Imaging

1. **Select several "assumed-normal" regions**
   a. Display several "normal-region" histograms
   b. Determine upper and lower bounds of "normal-region" histograms
2. **Display histogram of entire image**
   a. If corroded regions appear darker than "normal" regions, set the low-point, mid-point and high-point cutoffs at the lower bound of the "normal-region" histogram.
   b. If corroded regions appear lighter than "normal" regions, set the low-point, mid-point and high-point cutoffs at the upper bound of the "normal-region" histogram.

The technique can improve the consistency of the decision-making process for discriminating between "normal" and "anomalous" regions; it does not, however, provide an absolute method for discriminating between such regions. This work was undertaken in collaboration with civilian personnel from SM-ALC, McClellan AFB, CA as part of a broader supportive effort for the hidden-corrosion-detection program at OC-ALC, Tinker AFB, CA.

3.1.1 Some Preliminary Results from Applying the Technique

The results of applying the technique to an eddy-current image of an aluminum test-panel standard are shown in images "a" and "b" of Figure 3.1.1-1. The darker, rectangular areas are slots milled into the standard to simulate loss-of-thickness due to corrosion. The darker circular areas are rivets. The data for these images were acquired at 5 kHz from only one component of the eddy-current signal; thus, no impedance-plane information is included. Drawings, including panel dimensions as well as slot dimensions, are shown in Figure 3.1.1-2.

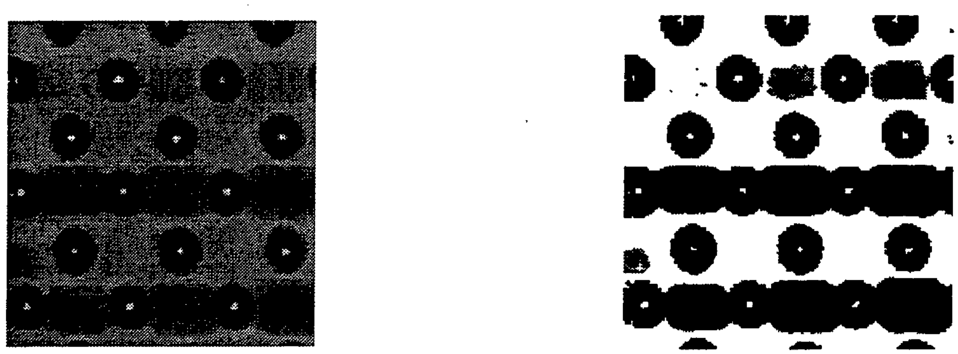

(a) (b)

FIGURE 3.1.1-1
Eddy-Current Images of Test-Panel Standard. The original is shown in "a", and the image resulting from application of the histogram technique in "b".

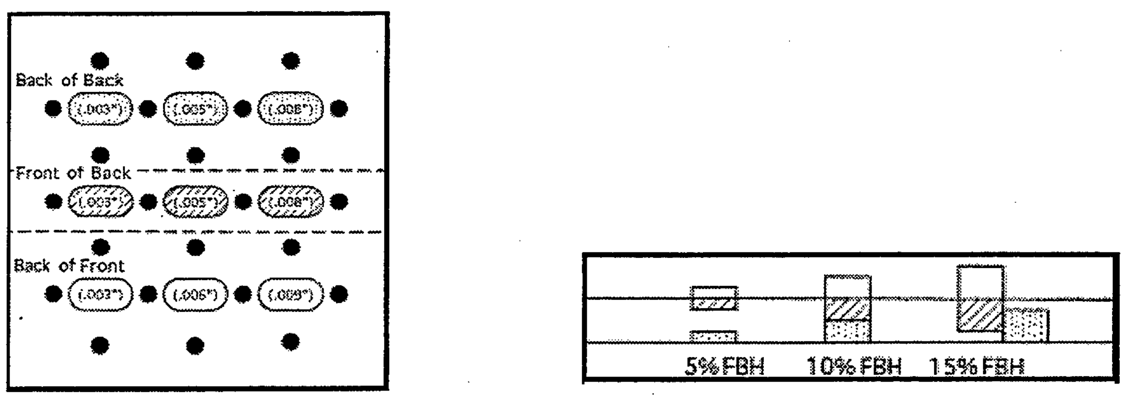

(a) (b)

FIGURE 3.1.1-2
Drawings of Test-Panel Standard. A top view is provided in "a"; a cross section in "b".

Application of the histogram technique to an aluminum aircraft-panel with suspected hidden corrosion is shown in images 'a" and "b" of Figure 3.1.1-3. The aluminum skin thicknesses, and gaps between the skins, are the same as those of the test panel (Figures 3.1.1-1 and 3.1.1-2). The data for these images were also acquired at 5 kHz from only one component of the eddy-current signal.

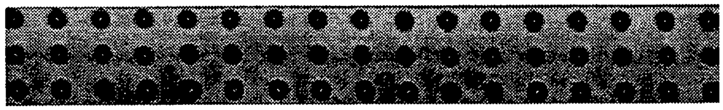

(a)

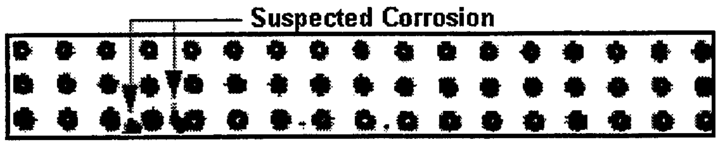

(b)

FIGURE 3.1.1-3
Eddy-Current Images of Aluminum Aircraft Panel with Suspected Hidden Corrosion. The original is shown in "a"; results of applying the histogram technique are shown in "b".

3.2 Signal Processing for Improved Imaging of Corrosion

C-scan image resolution improvements accruing from application of signal-processing techniques to three-dimensional RF B-scans were demonstrated to Mr. John Brausch of MSLA. Software gating and one-dimensional Fourier-deconvolution techniques were used to generate the improved images. The data were acquired from a 1mm (0.04 inch) thick aluminum sample with corrosion on one side only; the sample was interrogated from the smooth (non-corroded) side. A report, "Ultrasonic Imaging of Corroded Aluminum Sheet," which describes in detail the results of the study, is provided in Appendix A.

3.3 High Precision Scanning Acoustic Microscope (HIPSAM)

HIPSAM was used for several application scans during this contractual period. New software was developed and implemented, and older software was modified and upgraded. Hardware was also upgraded and/or added to maintain HIPSAM's state-of-the-art capabilities. The application scans, as well as the software and hardware modifications and upgrades, are described in this subsection.

3.3.1 HIPSAM Time-of-Flight (TOF) Resolution Study

This study was conducted to estimate the best obtainable resolution and accuracy of the HIPSAM system for quantifying pitting corrosion in thin aluminum plates. Flat-bottom holes were used to simulate the corrosion pits. A calibration standard was fabricated by milling flat-bottom holes into an 0.813 mm (0.016 in.) thick aluminum plate. Holes were milled into the sample to five different depths [0.064 mm through 0.318 mm (0.0025 in. through 0.0125 in.)]

with five different diameter holes [from 0.813 mm through 3.251 mm (0.032 in. through 0.128 in.)] milled into the sample at each of the five depths.

Data-Collection Parameters. The flat bottom hole panel was scanned with a 50 MHz, 12.7 mm (0.5 in.) diameter, 12.7 mm (0.5 in.) focal-length transducer aligned at normal incidence to the plate. The sample was oriented with the holes on the back surface so that TOF measurements could be made from the entry-surface echo to the back-surface or defect (hole) echo. The digitizer was operated at a rate of 2 billion samples per second with an A-scan length of 2048 data points. A 20 micron step size was used on both the X and Y axes. Two types of TOF data were collected. One measured TOF to the highest peak in a wide software gate positioned near the back surface, while the other measured TOF to a defined-amplitude threshold crossing in a narrower software gate near the back surface.

Measurements. Images of all 25 flat bottom holes were used to estimate both the depth and lateral dimensions of the holes. Figure 3.3.1-1 is an image of one of the flat bottom holes. A graph of "actual hole depths" as a function of "TOF scan determined depths" is shown in Figure 3.3.1-2 for one hole diameter.

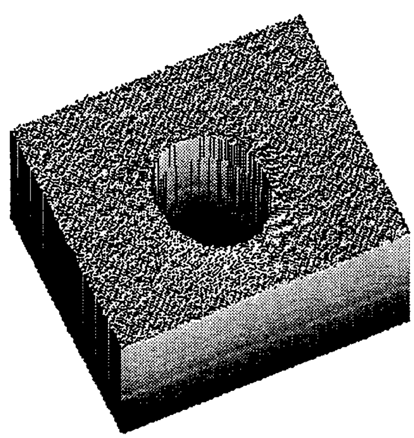

FIGURE 3.3.1-1
3-D TOF C-Scan Image of a 0.813 mm Diameter Flat-Bottom Hole with a Depth of 0.127 mm

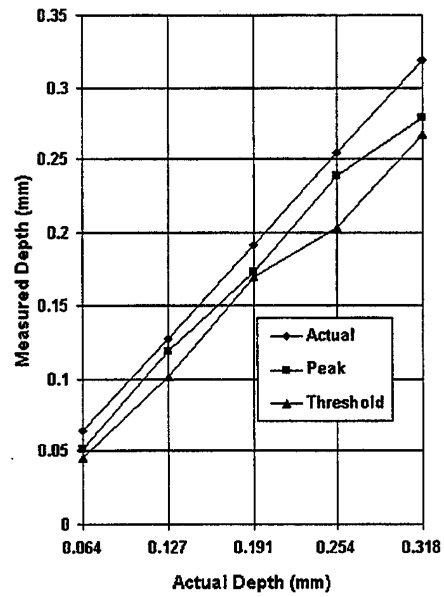

FIGURE 3.3.1-2
Actual vs. TOF Measured Depths for 5 Flat-Bottom Holes with a 0.813 mm Diameter.

Results. In general, TOF measurements were accurate to within 0.025 mm to 0.051 mm (0.001 in. to 0.002 in.) depending upon the depth and width of the hole. The peak TOF-measurement technique was accurate for larger diameter holes, while the threshold TOF-measurement technique was accurate for shallow, smaller diameter holes. Only the threshold TOF-measurement technique provided meaningful depth information for the smallest diameter holes. The "worst-case" hole [0.813 mm (0.032 in.) diameter and 0.064 mm (0.003 in.) depth] is near the limit of meaningful measurements for these tests.

Anomalous Results. TOF measurements on some of the small-diameter, shallow holes seemed to indicate that the bottoms of the holes extended outward (into the water) from the back surface of the base metal. It is believed that this "impossibility" was caused by such factors as: interference due to overlapping echoes (from the flat bottom hole and the back surface of the sample), mode conversions, and multi-path echoes. These types of errors are especially severe for the shallowest holes. Another source of error in the TOF measurements of holes is lack-of-flatness of the bottom of the holes.

3.3.2 TOF Measurements of Corrosion Pits and Exfoliation Corrosion

This study was conducted to develop an ultrasonic NDT technique for quantifying the depth of corrosion pits, as well as the thickness and lateral extent of exfoliation corrosion in thin

aluminum plates. It was accomplished by collecting TOF data from samples corroded by exposure in a salt-fog test chamber.

Sample Preparation. The corrosion samples were prepared and provided by Cortest Inc. of Columbus, Ohio, and included both pitting and exfoliation corrosion. These 3.251 mm (0.128 in.) thick (base metal) samples were prepared from both 2024-T3 and 7075-T6 Aluminum alloys using ASTM B-368 (for pitting) and ASTM G-34 (for exfoliation) specifications. The samples were corroded for exposure times of 1, 3, and 7 days. Cortest Inc. measured the dimensions of pits and exfoliation in these samples by metallographic cross sectioning after the ultrasonic testing. Pit depths in the 2024-T3 alloy ranged from 0.001 mm to 0.01 mm (0.00004 in. to 0.0004 in.), while for 7075-T6, the depths were 0.01 mm to 0.1 mm (0.0004 in. to 0.004 in.). Exfoliation depths ranged from 0.305 mm to 0.914 mm (.012 in. to 0.036 in.) for the 2024-T3 alloy and 0.152 mm to 0.914 mm (0.006 in. to 0.036 in.) for the 7075-T6 alloy.

Data-Collection Parameters. The transducer setup and implementation of software gates was identical to the setup previously described for the flat-bottom hole data-collection effort, except that the transducer frequency was lowered to 25 MHz and the number of points digitized per A-scan was increased to 4096. Signal attenuation due to sample thickness necessitated these changes.

Results. Figure 3.3.2-1 shows a C-scan of a small portion of the 7075-T6 sample with 3-day pitting corrosion. Data for this image were collected using the threshold TOF-measurement technique. This image consists of 512 X 512 pixels with 20-microns (7.87 X 10^{-07} in.) between pixels. Therefore, the total area covered is 10.24 X 10.24 mm (0.40 X 0.40 in.). Two large diameter pits and several small diameter pits are shown. The deepest pit (black) was 0.043 mm (0.0017 in.) deep. Other results (not shown here) have demonstrated that pits as small as 0.025 mm (0.001 in.) deep may be measured with this technique. Based on these results, the pits on the 2024-T3 alloy are too shallow to be measured with this technique, while the deeper pits on the 7075-T6 alloy can be measured with this technique.

Exfoliation corrosion on both alloy types was successfully imaged with the peak TOF-measurement technique and the threshold TOF-measurement technique. The maximum exfoliation corrosion depth measured was 0.279 mm (0.011 in.). The minimum exfoliation depth which can be measured with either of these techniques has not been determined.

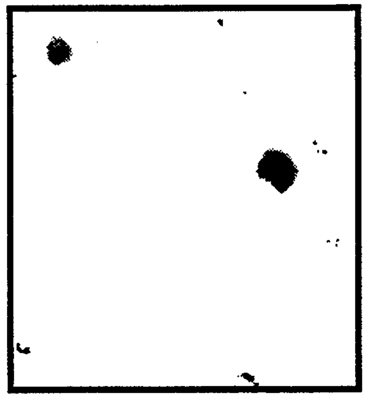

FIGURE 3.3.2-1
Threshold TOF C-Scan of 3-Day Pitting Corrosion.
The deepest pit (darkest) is .043 mm in depth.

3.3.3 TOF C-Scans of High-Voltage Ceramic Capacitors

Ultrasonic TOF C-scans of high-voltage ceramic capacitors were collected to provide both lateral and depth information of any voids and cracks. These are miniature ceramic capacitors [5.7 mm X 6.4 mm X 2.25 mm (0.224 in. X 0.252 in. X 0.089 in.)] and intended for high-density printed circuit board mounting. They have a relatively high capacitance value for their size and can be operated at 6000 volts. Internally, these capacitors consist of 4 stacks of capacitor plates. The 4 stacks are connected in series so that only 1500 volts are imposed upon each stack. These capacitors have exhibited shorter lifetimes than predicted, but the manufacturer has been unable to inspect the packages to insure a higher degree of reliability utilizing a SLAM system. The manufacturer sections the capacitors only on the centerline and has found no delaminations (voids).

The time-of-flight (TOF) C-scan images were collected at 20 MHz from each side (top and bottom) of each capacitor using the HIPSAM system. The TOF from the entry-surface to either the back-wall echo or a defect was stored. Ultrasonic attenuation within the package was very high and reflections from the stacks of plates caused multiple reflections. The C-scans indicated possible defects in most of the capacitors scanned. Significant cracks and voids were detected in 4 of the 5 capacitors initially inspected. Figure 3.3.3-1 is a typical image of one of these capacitors containing defects. Most defects are believed to be one of the following: (a) cracks or delaminations near edges, (b) voids very near the surfaces, or (c) a few small voids or delaminations (between plates) deep within the package. The AFRL/MLSA branch has performed destructive tests and has verified the existence of defects (delaminations and cracks) at the locations indicated in the ultrasonic time-of-flight C-scans. These defects were verified by sectioning,

polishing and photographing many slices through each capacitor. A report titled, "Analysis of Multilayer Chip Capacitors (Lot Code 9721 Failure Analysis)", was written describing the non-destructive and destructive testing effort.

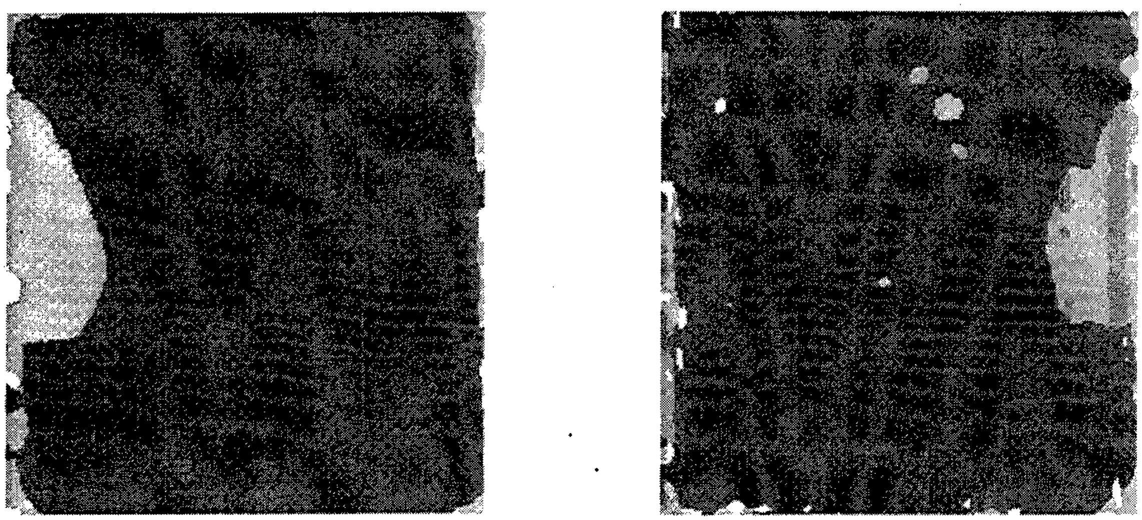

FIGURE 3.3.3-1
Time-of-Flight C-Scans of the Top and Bottom Sides of a Ceramic Capacitor at 20 MHz

The capacitor manufacturer used this information to improve their manufacturing process and submitted another batch of capacitors for testing. These capacitors had significantly fewer defects than the first batch, but still had some defects. The manufacturer is currently determining whether the remaining defects pose any threat to the lifetime of the capacitors. A report titled, "Analysis of Multilayer Chip Capacitors (Failure Analysis)", describes this effort in more detail.

3.3.4 TOF C-Scans of Laser Shock-Peened Engine Blade Specimens

Ultrasonic TOF C-scans were collected on three Ti-6Al-4V gas turbine engine blade specimens at a frequency of 50 MHz with a highly-focused transducer. No voids were imaged in the single-blade specimen which had not been laser shock-peened; voids were imaged in the two-blade specimens which had been laser shock-peened. All of the imaged voids were within areas on the specimens that had been laser shock-peened. All voids were near the middle of the total thickness of the specimen at the edge of the blade.

The specimen manufacturer submitted 2 additional specimens a year later. Scans indicated that the two new specimens had no voids. The manufacturer had increased the energy applied during the laser shock-peening process; this has apparently solved the manufacturing problem.

3.4 Ultrasonic Imaging of a Metal Matrix Composite Rotor Disc

Three broken pieces (designated as R1C, R2C and R3C) from a shattered engine rotor disc were ultrasonically scanned in an attempt to help determine the cause of failure. The rotor disc, the parts from which were provided by the Wright Laboratory ManTech Directorate, had an internal diameter of 25.4 cm (10 in.), an outer diameter of 50.8 cm (20 in.), and was 3.81 cm (1.5 in.) thick. It was designed and manufactured to have a Ti 6-4/SCS-6 ring of 13.97 cm (5.5 in.) inner radius, 17.8 cm (7 in.) outer radius, and a 2.54 cm (1 in.) thickness embedded in the Ti 6-4 metal. This ring and the titanium were diffusion bonded. The Ti 6-4 containing the composite ring formed the interior portion of the rotor disc. This interior portion was diffusion bonded to the rest of the disc. Because of the method used for manufacture, the disc had at least five diffusion-bonded regions, three radially-symmetric diffusion-bonded interfaces, and two axially-symmetric interfaces. These diffusion-bonded interfaces were the main failure-suspect regions.

The ultrasonic imaging was performed on all five of the interfaces using a 10 MHz immersion transducer. The ultrasonic images in both the axial and the radial direction revealed large areas of debonding at the diffusion-bonded interfaces (Figures 3.4-1 through 3.4-3). In order to compare our data with previous ultrasonic data (acquired before shattering), the images were sent to the engine manufacturer. It was later learned that the manufacturer had scanned only the two axially-symmetric diffusion-bonded interfaces, but had not scanned the radially-symmetric diffusion-bonded interfaces. The engine manufacturer's images of the axially-symmetric diffusion-bonded interfaces had revealed some debonded regions.

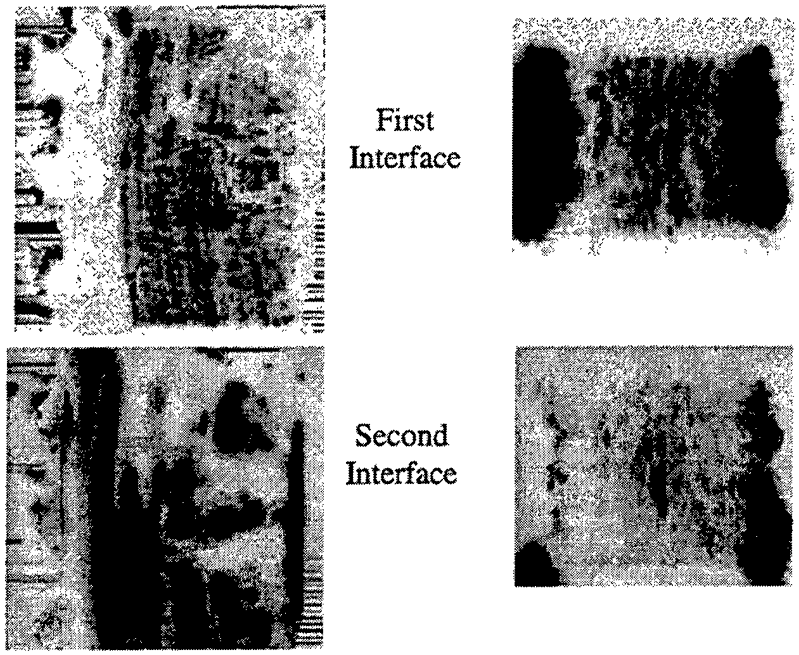

FIGURE 3.4-1
Ultrasonic C-Scan of Failed Rotor Disc, Sample R1C

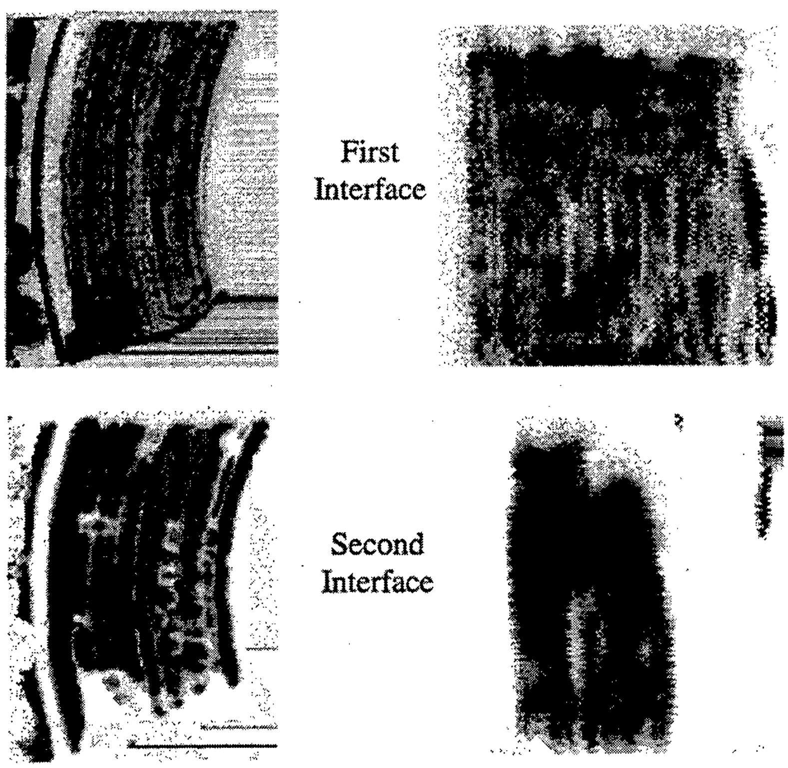

FIGURE 3.4-2
Ultrasonic C-Scan of Failed Rotor Disc, Sample R2C

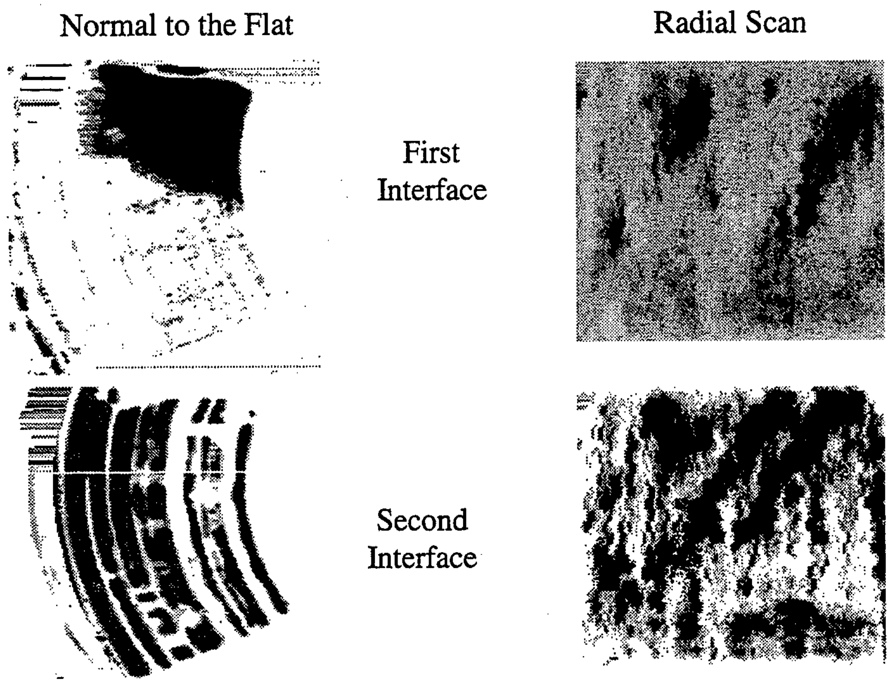

FIGURE 3.4-3
Ultrasonic C-Scan of Failed Rotor Disc, Sample R3C

3.5 Detection of Flaws in Electron-Beam Welds

Electron-beam welding is being utilized in aircraft systems, including the F-22 main fuselage sections and TF-39 turbine engine compressor blades. In an effort to assess the ultrasonic inspectability of certain components which were welded by this technique, several experiments were conducted on electron-beam welded titanium alloy plates.

The primary flaw type of interest involves work pieces that are in intimate contact but not properly fused, either due to lack of beam penetration or lateral deviation of the beam from the joint. Two types of test specimens were supplied (by a company experienced in electron-beam welding) to simulate the lack-of-fusion condition. One specimen consists of plates fully fused from one side with flat-bottom holes drilled into the weld zone. The other specimen consists of plates partially fused from both sides, leaving an unfused region in the center.

Four standard ultrasonic inspection techniques were evaluated in this investigation:

1. normal incidence pulse-echo
2. angle beam pulse-echo
3. fixed insonification, scanned detection
4. angle beam insonification, normal incidence detection (delta)

The normal-incidence pulse-echo technique was unsuccessful in directly detecting the unfused interface between the two work pieces, probably due to the flaw orientation (a plane parallel to the propagation direction). However, depth of fusion was observable with this technique in both the B- and C-scan modes. The welding process re-orients the titanium grain structure in the weld zone, significantly reducing grain scatter. As a result, a good weld produces an ultrasonic echo with low grain scattering through the entire thickness of the plate, while an incomplete weld causes increased grain scatter below (or between) the fused region(s).

Angle beam pulse-echo, fixed insonification, and the delta technique were all capable of detecting the flat bottom holes (more representative of a void). None of the techniques were able to directly detect the unfused interface.

3.6 Ultrasonic Lamb Wave Characterization of Adhesive Joints

Results of this effort have demonstrated the feasibility of using a Lamb-wave-based methodology for assessing adhesively bonded structures. The methodology is based on a novel displacement-distribution-profile approach for Lamb-wave mode selection in which the in-plane displacement distribution across the thickness of the sample is used as a measure of mode sensitivity to interfacial conditions.

The steps necessary for the theoretical modeling of Lamb-wave propagation in the structure and for the calculation of the displacement, stress, and energy distributions have been developed. In addition, two adhesively-bonded samples have been used to demonstrate the feasibility of the methodology. One of the samples was an Al-epoxy-Al structure, while the other was a Cu-epoxy-Al structure. The physical dimensions of the samples were measured and the values were used in the theoretical model to generate the dispersion curves as well as the displacement profiles (in-plane displacement).

The results obtained in this study demonstrate the robustness, sensitivity and, therefore, the feasibility of the approach. It has been shown that interfacial features from individual interfaces can be imaged when the distribution-profile method is used to select the proper Lamb-wave modes. Any image-to-image deviations obtained by using different Lamb-wave modes can be described easily by changes in the corresponding displacement distributions at the interfaces.

While this work has shown the feasibility of Lamb-wave mode selection based on displacement distributions, further studies are necessary to understand the effect of the distribution patterns of normal displacement, stresses and energy. Also, experimental Lamb-wave imaging of a statistically significant number of samples, followed by destructive corroborative analyses, is necessary for optimization of the technique. This work is described in detail in a UDRI technical report titled, "Ultrasonic Lamb Wave Characterization of Adhesive Joints", and is included in Appendix A.

3.7 A New Lamb-Wave Technique for Imaging Defects in Multi-Layered Metal-Matrix Composites

A new leaky Lamb-wave technique was used to detect internal defects in a multi-layered, continuous-fiber-reinforced, composite-plate specimen. This new technique consisted of: (1) geometrically positioning the transducers to avoid null zones and specular reflections, (2) using tone-bursts at precise frequencies to excite Lamb-wave modes which were sensitive to defects at specific depths within the composite plate. Conventional Lamb-wave techniques capture data from within the null zone. Unfortunately, these "null-zone" techniques are sensitive to very slight variations in the distance between the transducers and the surface of the sample. The new technique is relatively insensitive to such variations. C-scan images generated by applying this new Lamb-wave scanning technique to multi-layered composite specimens demonstrated that it is sensitive to internal defects such as fiber breakage and matrix-burned-out zones in such specimens.

Conclusions from the Study. It was found in this study that the Lamb-wave scanning technique is able to image defects in internal layers of a multi-layered composite plate. It was also shown that different layers of the plate can be excited differently by various Lamb wave modes which are sensitive to various types of defects in these layers. A copy of a journal article, "An Approach to Determine the Experimental Transmitter-Receiver Geometry for the Reception of Leaky Lamb Waves," published on this topic is included in Appendix A.

3.8 Additional Technique-Development Studies

Additional studies conducted to develop techniques for specific application areas include the following:

1. Low-cost, single-chip accelerometers for use as inexpensive, rapid-assessment tools for acoustic-velocity measurements.
2. Chemiluminescent materials for locating the source of fuel leaks inside the wings of wet-wing aircraft.
3. Dripless ultrasonic-transducer couplers for use in inspection situations where large amounts of liquid couplant cannot be used.

Section 4

TASK III – NDE Technique Optimization

4.1 Detection of Cracks Emanating from Fuel Weep Holes

In August 1993, C-141 wings were found to have cracks originating from the fuel weep holes. As a result, all C-141Bs were inspected by eddy current to determine the severity of this cracking. The present inspection methodology requires that the wing tanks be emptied and purged of fuel to allow an operator to crawl inside the wing to perform the eddy current inspection. An alternative method, which uses split aperture, circumferential, ultrasonic creeping waves, was developed (Nagy et al., 1994) to detect the presence of an upward-growing crack by inspecting from the outside of the wing. In May 1995, a specialized transducer utilizing this technique was constructed by UDRI and tested at WR-ALC on wing panels that had been removed from service (as a result of eddy current tests).

The split-aperture-creeping-wave technique tested at WR-ALC utilizes two ultrasonic transducers with center-to-center spacing equal to the hole diameter (hence split aperture) to generate and receive a leaky creeping wave around the hole. A standard ultrasonic flaw detector may be used to drive the transducer and to observe the signals from the hole. By electrically switching the transducer between a single element (pulse-echo) mode and a dual element (pitch-catch) mode, the operator can quickly determine the presence or absence of a weep-hole crack.

In either mode, a portion of the incident acoustic pulse is specularly reflected from the near side of the hole; this signal is used as a time reference to judge the arrival time of the two possible situations for the creep wave. For an uncracked hole, the creep wave travels circumferentially around the hole and leaks back to the receiver (pitch-catch mode) at a time determined by the diameter of the hole. If the creeping wave encounters a crack emanating radially from the weep hole, a portion is reflected back toward the transmitting transducer and is detected in the pulse-echo mode. These conditions are illustrated in Figures 4.1-1 through 4.1-6, obtained from actual condemned C-141 wing panels. An optical photograph of a typical weep hole is shown in Figure 4.1-7, and the transducer is shown in use in Figure 4.1-8.

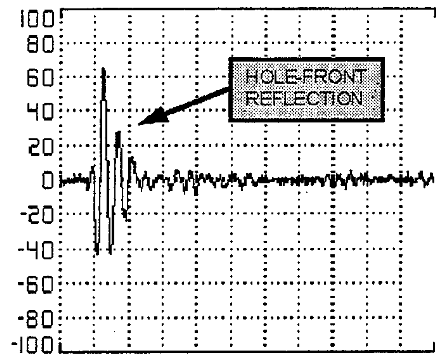

FIGURE 4.1-1
Uncracked Weep Hole, Pulse-Echo Mode.
The reflected creeping wave signal is not present.

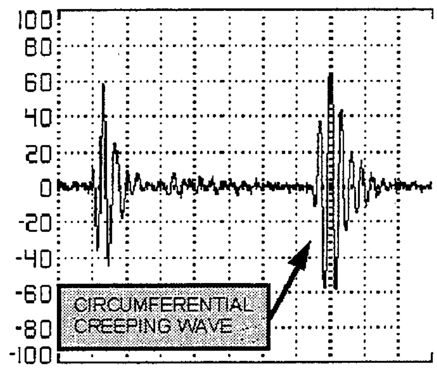

FIGURE 4.1-2
Uncracked Weep Hole, Pitch-Catch Mode.
The circumferential creeping wave signal is very strong.

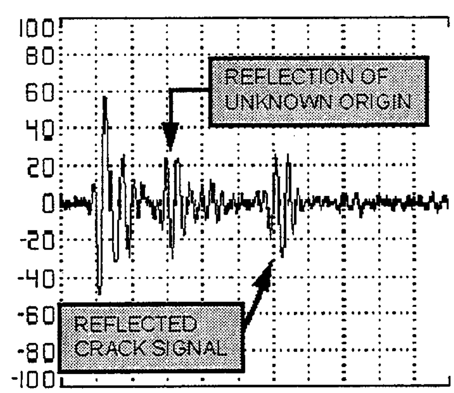

FIGURE 4.1-3
Moderately-Cracked Weep Hole, Pulse-Echo Mode.
The reflected creeping wave signal is present.

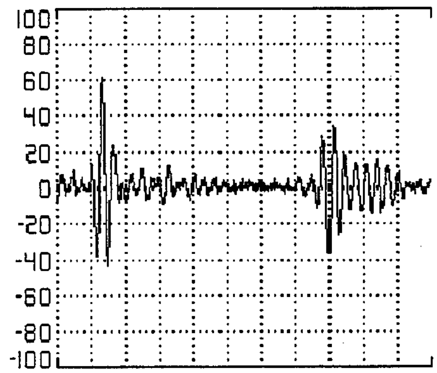

FIGURE 4.1-4
Moderately-Cracked Weep Hole, Pitch-Catch Mode.
The circumferential creeping wave signal is somewhat attenuated.

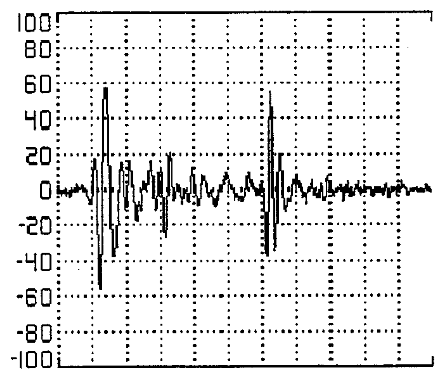

FIGURE 4.1-5
Severely-Cracked Weep Hole, Pulse-Echo Mode.
The reflected creeping wave signal is very strong.

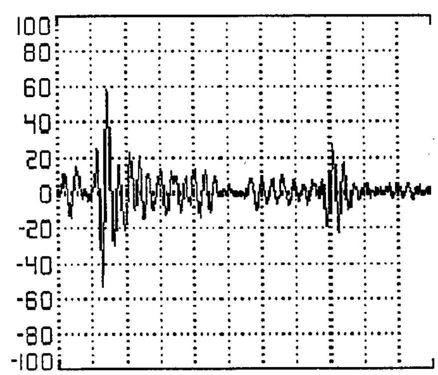

FIGURE 4.1-6
Severely-Cracked Weep Hole, Pitch-Catch Mode.
The circumferential creeping wave signal is highly attenuated.

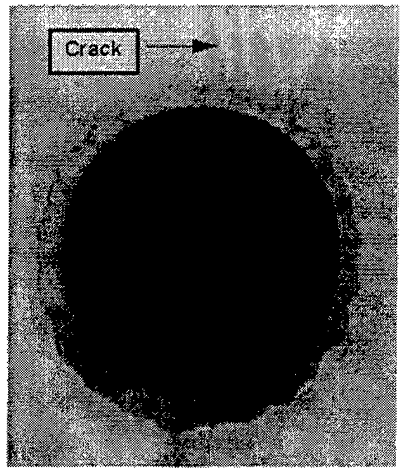

FIGURE 4.1-7
Fuel Weep Hole with Crack.

FIGURE 4.1-8
Laboratory Application of Transducer (hand-held sensor).

An adjustable creeping-wave-transducer was developed; the new transducers can be adjusted to allow optimization over a range of hole diameters. This represents an improvement over the original creeping-wave transducer, because it was optimized for 6.35 mm (0.25 in.) diameter holes and could not be adjusted for other hole-diameters. Two such "adjustable" transducers were constructed and tested on holes of various diameters; the results demonstrated the feasibility of the new device. These transducers have been sent to the AFRL/MLSA Branch for additional evaluation.

Section 5
TASK IV – Technology Transition

5.1 MAUS III Transition Efforts

Technology transition efforts with the MAUS III included demonstrations at trade shows, conferences and meetings; inspections of structures and samples; and Air Force ALC visits. Data collection, data analyses and modeling efforts were also conducted to improve our knowledge and understanding of the MAUS III capabilities and limitations. A CRDA, which included the use of the MAUS III, was signed with Air Force in 1997.

5.1.1 Resonance Mode Characterization and Modeling

Operating Characteristics. Survey ultrasonic-resonance data were acquired and analyzed to estimate some of the operating characteristics of the MAUS III system. Some of the important observations are:

1. Systematic errors remain in the output values – amplitude and phase – after the null voltages are removed from the peak-detected signal values;
2. Measured amplitude and phase output-versus-gain settings for constant inputs are nonlinear;
3. Under certain operating conditions, the measured outputs – amplitude and phase – decrease as the gain settings are increased; and
4. Considerable scatter exists in the phase output values at higher gain settings, i.e., the standard deviation of the scatter appears to increase with increasing gain settings. It appears to be possible to minimize the scatter by careful selection of the operating frequency.

An unpublished report, "Ultrasonic Resonance, Operating Characteristics," which describes the data acquisition and results in detail, is included in Appendix A.

Resonance Model. An EXCEL spreadsheet model of the change-in-shape of the "resonance amplitude vs. frequency" curve as a function of the amplitude gain value was developed. This model should prove to be a significant aid for training new personnel to use the ultrasonic resonance portion of the MAUS III.

5.1.2 Demonstrations at Trade Shows, Conferences and Meetings

Trade shows, conferences and meetings at which UDRI demonstrated the capabilities of the MAUS III are listed in Table 5.1-1

Table 5.1-1. Demonstrations at Trade Shows, Conferences and Meetings

EVENT	LOCATION	DATE
PRI Trade Show	Columbus, Ohio	December 1995
Air Force Wide NDI Conference	San Antonio, Texas	March 1996
Capabilities Demonstration	Airborne Express Maintenance Facility, Wilmington, Ohio	June 1996
ASM Conference	Cincinnati, Ohio	October 1996
SEMA Exhibition	Las Vegas, Nevada	November 1996
APBA Meeting	Detroit, Michigan	November 1996
PRI Trade Show	Columbus, Ohio	December 1996
Air Force 50^{th} Anniversary	Las Vegas, Nevada	April 1997
U.S. Air and Trade Show	Dayton, Ohio	July 1997
ASM Conference	Indianapolis, IN	September 1997
Miami Valley ASNT Meeting	Middletown, Ohio	March 1998

5.1.3 Inspection Applications

Inspection application of samples and structures performed by UDRI personnel are listed in Table 5.1-2. These inspection applications were performed as part of research efforts and technology transition efforts to determine the capabilities and limitations of the MAUS III, and to demonstrate the capabilities of the MAUS III to various governmental agencies and private industry. Reports describing some of these efforts in detail are provided in Appendix A. Capsule summaries of some of the efforts are provided in the following paragraphs.

Concrete Slab Inspections. Concrete slabs reinforced with thin (between two and six plies) sheets of graphite-epoxy composite material were scanned with the MAUS III using pulse-echo and resonance techniques. The objective of the scans was to image anomalies in the adhesive between the fiber-reinforced composite and the concrete slab. This effort was not successful.

Impact-Damaged Radomes. Impact-damaged radomes from an F-16 were scanned with the MAUS III using the resonance technique. The locations and lateral extents of the impact damage in each radome were successfully imaged.

Impact-Damaged Samples. Two impact-damaged, woven graphite-fiber-reinforced composite samples were scanned with the MAUS III using both resonance and pulse-echo techniques. The locations and lateral extents of the impact-damage sites were imaged.

Battle-Damage Repair. The MAUS III was used to inspect two composite test panels that were part of a Battle Damage Repair Program. The panels were curved in one direction, and had an approximately 12.7 cm (5 inch) diameter hole cut in the center. The hole had been patched with a thin aluminum plate on the inner (concave) curvature, filled with a polyester resin through the thickness, and covered on the outer (convex) curvature with a woven graphite-epoxy mat cured in place. The pulse-echo ultrasonic signal was able to penetrate the panel and image most of the mat-to-panel bond. However, the signal could not penetrate the polyester resin which filled the hole.

Table 5.1-2. Inspection Applications

APPLICATION	OBJECTIVES	RESULTS	WHERE PERFORMED
Fiber-reinforced composite sheet bonded to concrete slab – April 1996.	Image bond between slab and fiber-reinforce composite	Fiber-reinforced sheet too thin to allow imaging of adhesive bond	WPAFB, OH
F-16 radome – April 1996	Image damage in radome	Damage successfully imaged	WPAFB, OH
Honeycomb-core composite with simulated defects – July 1996	Image simulated defects	Simulated defects successfully imaged with resonance technique	WPAFB, OH
Impact-damaged woven graphite-fiber composite – July 1996	Image impact damage	Impact damage successfully imaged with resonance technique	WPAFB, OH
Impact-damaged multi-directional Gr-Ep composite – July 1996	Image impact damage	Impact damage successfully imaged with UT and resonance techniques	WPAFB, OH
Composite wing-box – February, 1997	Image ribs & spar joints	Image parts of the rib and spar joints	WPAFB, OH
Battle-Damage Repair	Inspect battle-damage repair sample	Pulse-echo signal could not penetrate the polyester resin filling the damage site	WPAFB, OH
Aluminum wing-skin lap joint – January 1998	Inspect lap joint for hidden corrosion	Lap-joint area imaged, no corrosion found	WPAFB, OH
Retired Boeing 707 – February 1998	Screen portions of aircraft to select parts for further scans	Performed screening scans on several areas of the 707	Rye Canyon, CA

5.2 NDE Reliability of the ECII Series E Eddy Current Inspection System

Under the ENSIP approach to ensuring the structural integrity of turbine engines, emphasis is centered on the size of flaws that might be present at the start of each period of operational usage. Accordingly, the capability of the inspection systems that are used in production and maintenance must be quantified in terms of the maximum flaw sizes that might be missed at an inspection. Because the inspection process is stochastic in nature for the small flaws of primary interest, capability must be characterized in terms of the probability of detecting cracks of a given size, POD(a). The POD(a) function is estimated from capability demonstration experiments using specimens and materials judged to be representative of the actual application. For the automated eddy current systems, NDE capability is defined as the best estimate of the crack length, which corresponds to a probability of detection of 0.90.

To evaluate the capability of the ECII Series E eddy current inspection system, General Electric Aircraft Engines conducted a large number of demonstration experiments using different

materials, specimen configurations, and signal processing methods. The original analyses of the resulting data did not account for violations of the statistical assumptions in the analysis approach specified by the Air Force. The study of this report was undertaken to evaluate the validity of these assumptions and, when necessary, to re-analyze data. The results of this study are presented in UDRI Technical Report #UDR-TR-95-45 titled, "NDE Reliability of the ECII Series E Eddy Current Inspection System". That report is included in Appendix A.

5.3 ALC Visits

Five fact-finding and/or technique demonstration trips were made to Air Force ALCs during the course of this contract. These visits are briefly described in Table 5.3-1.

Table 5.3-1. ALC Visits by UDRI Personnel

DATE	ALC	NUMBER OF PEOPLE	PURPOSE
February 1995	WR-ALC	One	Discuss C-141 fuel weep-hole inspection needs
August 1995	OC-ALC	One	MAUS III training & discuss NDE needs with ALC personnel
May 1996	OC-ALC	Two	Discuss NDE corrosion detection techniques with on-line inspectors
March 1997	OO-ALC	One	Attend Quarterly NDI Managers Meeting
September 1998	OO-ALC	One	Discuss corrosion-inspection techniques and needs

5.4 HIPSAM System Upgrades

5.4.1 <u>Software Upgrades</u>

Major software upgrades made to HIPSAM during the course of this contract are listed in Table 5.4.1-1.

5.4.2 <u>Hardware Upgrades</u>

Submersible Load Frame. A UDRI-constructed submersible load frame was installed on HIPSAM during the course of this contract. This device was designed to apply a calibrated static load to a specimen and to apply cyclic loading for fatigue testing. Since it is submersible, HIPSAM can scan the sample at user-specified times after a specific number of loading cycles without removing the sample from the load frame. Thus, the device can be used to study the progression of damage as it accumulates under specific loading conditions.

Table 5.4.1-1. HIPSAM Software Additions and Modifications

1. B-Scan Data Collection Capabilities • Single-line scans • Multi-line (3-D) scans • Gated scans (for single-line or 3-D scan) – store all and/or selected portion of each A-scan • Average up to 512 A-scans at each data collection location • Rectify and/or frequency filter each A-scan
2. Rayleigh Wave Capabilities and Features • 3-D V(z) curve data collection • 3-D Fourier magnitude data (single frequency) collection from directly reflected wave and Rayleigh wave • Rayleigh-wave-velocity images in C-scan format generated from stored single-frequency amplitude • Rayleigh-wave velocity maps in a C-scan format computed using Time-of-Flight (TOF) techniques with better than 1% velocity accuracy • Improved time-of-flight algorithm for Rayleigh-wave TOF velocity map • Improved entry-surface-echo tracking algorithm for Rayleigh-wave TOF velocity map
3. C-scan Data Collection Capabilities • Peak-to-peak amplitude data collection and display for each software gate • 16-bit resolution TOF data collection and data storage • Frequency domain C-scan collection of Fourier magnitudes at any frequency • Simultaneous display of up to 4 C-scan images from software gates during data collection • Precise post-data-collection transducer positioning in X, Y, and Z to collect smaller-area higher-resolution scan
4. Display Features • Option to display images with up to 10 different color maps during data collection to aid in analysis • Slide show option with new images, preset colors and text to describe images
5. Error Handling • "Disable Error Messages" option in order to increase scanning speed • Additional error and instruction messages to assist operator
6. Miscellaneous • C-scan and B-scan data-collection algorithms integrated into a single HIPSAM program • Software to measure elapsed time in various software functions in order to optimize data-collection speed • Simultaneous data processing and DMA data transfer from the digitizer • Optimum motor-speed computation algorithm • New control-file options to make HIPSAM-generated control files compatible with UDRI-developed analyses, and signal/image-processing algorithms on both VAX and PC based systems • GPIB control of delay generator where feasible • National Instruments Digital Data Acquisition (NI-DAQ) library • Univision Software Development Support Library (SDSL) • Network operation with user friendly login and file transfers • Windows 95 OS software and LAN interface

Additional Hardware Upgrades. Other significant hardware upgrades, modifications and additions are listed in Table 5.4.2-1.

Table 5.4.2-1. HIPSAM Hardware Additions and Modifications

- Minimized cable length in equipment rack to reduce electrical noise
- Additional 110 volt outlets, circuits, switches and power/surge conditioners
- Integrated Pentium-based processor system into the HIPSAM system to replace older 80486-based system
- Bernoulli removable disk drive
- CD-ROM disk drive
- 1 Gbyte hard disk drive
- New RTD720A 2Gsps digitizer to replace older digitizer
- Additional 64Mbyte of RAM to system memory
- Underwater load frame and interface operation with HIPSAM system
- Printer capability for documentation of scan-setup information

5.5 Large-Tank Ultrasonic Scanning System Upgrades

5.5.1 New Data-Collection Application

This application collects A-scans in a raster-scan format, averages them "on-the-fly," and stores the single averaged A-scan in the B-scan file at the conclusion of the scan. This averaged A-scan represents a global transducer-specimen response over the scanned area. The averaged A-scan can then be subtracted from each individual A-scan in a B-scan file to enhance any variations among A-scans. This subtraction is performed by a different, previously-developed application.

5.5.2 Significant Software Modifications

Two software "bugs" were fixed. One caused scanning to halt when averaging a large number of A-scans. The other caused the A-scan RECTIFY and LOW-PASS FILTER algorithms to malfunction. In addition, the maximum number of A-scans that can be averaged was increased from 256 to 512.

5.6 X-Ray CT Systems – Software Modifications

The software modifications made to the x-ray CT systems improved the quality of images generated by the systems, decreased image reconstruction times, and expanded the capabilities of the systems. The major modifications are described in the following subsections.

5.6.1 Tomoscope System

Software modifications were made to the Tomoscope system to remove random spikes in the data, improve knife-edge corrections, and reduce visually-disturbing ring artifacts in images. Such modifications significantly improved the quality of images generated on the Tomoscope system when compared with those generated at the beginning of the effort.

Random Spike Removal. Random spikes are false readings of extraordinarily high x-ray photon counts which can result in a loss of spatial resolution, contrast sensitivity, and can also produce significant image artifacts. There are three data sets in which spikes may be present and from which they must be removed to improve the image quality. These data sets are: offset data, air scan data, and object attenuation data. Random-spike removal from the first two data sets was accomplished in April 1996, but the spike correction algorithm for the object-attenuation data set was not fully functional until March 1997. The completed algorithm allows great flexibility in the classification and removal of spikes.

Knife-Edge Correction. Micro-focus imaging is very susceptible to minute changes in source spot position. A slight change in the source spot location can have a dramatic effect on the system geometry calibration. To correct for movement in the source spot, the shadow of a tungsten pin (knife edge) located within the fan-beam collimator is monitored. Movement in the shadow of the knife-edge corresponds to source spot movement. The correction routine that tracked spot location worked very effectively in the past. However, with the new configuration, the routine performed less reliably than desired. Work began in April 1996 to address and correct this problem and concluded in July 1996 with significantly improved routines for tracking and identifying the knife-edge shadow.

Ring-Artifact Reduction. A new technique for cleaning up raw Tomoscope data was implemented in March 1988, resulting in images with significantly fewer visually-disturbing ring artifacts. In addition, detector calibration software has been developed which will further reduce ring artifacts when implemented.

Miscellaneous Modifications. The code book for the Tomoscope system was updated to document code changes made during the technical period of performance for this contract. Software was developed to append two temporally-separated Tomoscope data files. This allows a partial data set – acquired prior to a source-induced termination – to be appended to a data set

acquired after a restart of the system. This eliminates the need to completely rescan a part when problems with the source cause a scan termination.

A software debugger for development of software for the Tomoscope system was installed on the SGI workstation and reconstruction software routines were ported to the SGI system. This installed and ported software executes much faster on the SGI workstation than on other computers. Reconstruction of images from the raw data takes much less time now than at the beginning of the contractual effort.

A bad-pixel-mapping routine was ported to the IBM system in Building 71 at WPAFB, Ohio. Maps of bad pixels in the Tomoscope system can now be made at WPAFB rather than at Sunnyvale, California. Thus, considerable time and money can be saved when new bad-pixel maps need to be generated.

5.6.2 LAM/DE System

Cross-Talk Reduction. A new cross-talk-reduction algorithm was developed and installed on the LAM/DE system. The improvement in image quality was dramatic; however, some of the effects could not be corrected with software. Those remaining cross-talk effects must be corrected by modifying hardware to provide additional shielding of the detectors. A proposal was submitted to make this modification, but funding was not available during the contract period.

Reverse Engineering and 3-D Rendering. An image analysis package, ARCHIMEDES, capable of a host of reverse-engineering tasks and of 3-D image rendering was installed on the SGI workstation. This permitted research efforts in reverse engineering to accelerate. A simple preprocessor for ARCHIMEDES was developed to allow 3-D manipulation of CATS formatted CT data (e.g., LAM/DE data). Three-dimensional image analysis enables superior detection and characterization of part defects and anomalies. With this preprocessor LAM/DE can perform reverse engineering functions.

5.7 X-Ray CT Systems – Hardware Modifications

The hardware modifications made to the x-ray CT systems concentrated on obtaining a reliable x-ray source for the Tomoscope, replacing antiquated computer hardware with faster, more powerful equipment, and improving the alignment and calibration of existing hardware. The major modifications are described in the following subsections.

5.7.1 Tomoscope System

During the contract period, two new microfocus x-ray sources were delivered and integrated into the Tomoscope System. The L&W x-ray source was delivered in December 1994 and the FeinFocus x-ray source was delivered in January 1998. Neither source has proved to be as reliable as the LAM/DE x-ray source. New CCD detectors have been delivered and integrated into the detector package. Besides the detector package, the gantry, shutter, and knife-edge have all been modified.

L&W Source Vacuum System. Extensive modifications to the L&W source vacuum system and seals achieved "resting" vacuum improvements of two orders of magnitude and achieved an operational vacuum that would allow uninterrupted operation at voltage levels up to 250 kV. The as-delivered system would typically operate for only about 10 minutes before the vacuum interlock would disable the source to prevent catastrophic failure. One modification was the addition of a nitrogen back-fill system to reduce contamination due to ambient air when the system was brought up to atmospheric pressure. Another was the modification of the control cabinet to add a second ion-pump controller for separate control of the two ion pumps. A major vacuum problem was the reliable operation of the ion pumps. One of the two ion pumps was rebuilt, only to fail again the following month due to a controller failure.

L&W Source High Voltage Sockets. The high-voltage sockets on the L&W source were a problem from the beginning. First, a new cathode socket assembly had to be manufactured and installed. Then, a crack developed in the anode socket, which allowed silicone cooling fluid to enter the vacuum chamber and contaminate the system. When the new anode socket which was manufactured from brittle Macor ceramic was installed, it cracked again. A review of possible reasons for the third failure led to two conclusions. First, the L&W drawings for the Macor sockets did not match the original sockets. Subtle differences in such details as minimum curvature radii allowed undue stress concentrations. Second, a different ceramic material should be investigated for use in this application. Following modification of the socket drawings, another anode socket was manufactured and installed. For continued operation of the L&W x-ray source, a new socket design is recommended. The new socket should be made of an alumina-based ceramic, thus providing a significant increase in strength. The new socket could also incorporate brazed ceramic-to-steel interfaces, thus reducing vacuum problems and stress related to the

current crushed o-ring design. A technical interchange meeting was held with a potential supplier of alumina-based ceramic sockets. Modification to the cooling fluid flow of the anode socket were recommended. Some preliminary design work for a new socket was completed and three potential sources for improved high voltage sockets were identified, but the effort was placed on hold due to insufficient funding.

Arcing at the L&W Source Cathode. Soon after the L&W source became operational, it failed due to the breakdown of a relatively new emitter. The emitter was returned to the manufacturer for failure analysis. The manufacturer noted that a segment of the emitter had been violently broken away. This would be consistent with a high-voltage discharge (a common problem with the source). The emitter was replaced and the system was aligned and focused for the new emitter. An analysis of the high-voltage system identified a potential source of discharges in the socket assemblies. The connector within the ceramic sockets is not well designed for the containment of field stress and electron emissions. A commercial connector or a newly-designed connector should be incorporated into the design of any new ceramic sockets.

CCD Detectors. The problems associated with the L&W source mitigated the impact of a substantial slip in the delivery schedule of the CCD detectors. CCD delivery from EG&G Reticon, first anticipated in late February or early March 1995, slipped to October 1995 because of continuing CCD failures. Saar Associates concluded an in-depth analysis of failed CCDs in April 1995. Upon delivery, four CCD detectors were installed in the detector package and checked out at room temperature. Finally, in December 1995, the four detectors in the detector package were cooled and illuminated with x-rays from the L&W source and were shown to be functioning normally. Since delivery, three of the eight CCDs and two of the eight pre-amp boards have developed failures or partial failures either due to infant mortality or handling. Consequently the detector package is considered the most fragile component of the Tomoscope system and is only opened as a last resort when troubleshooting problems.

L&W Source Alignment. One of the first modifications made to improve the capability to align the electron beam with respect to the target was a change that enabled displaying positive or negative voltages on the steering coils rather than absolute values. The L&W source mounting design has been a problem from the start for proper alignment of the cathode chamber with respect to the anode chamber. A preliminary design for the Tomoscope source mounting hard-

ware was developed for more precise positioning of each chamber and the focus coil. Only the focus coil positioning hardware was purchased and installed. In addition, a drift-tube sensor was designed and installed to help in the positioning of the electron beam. After the entire source was carefully aligned using an alignment telescope, no further modifications to the source mounting hardware were found to be necessary. Lateral and vertical positioning of the focus coil with respect to the electron beam, enabled large displacements of the beam. Fine adjustments could be handled by the beam steering coil voltage control. The resulting improvements in the focusing process considerably improved the spatial resolution.

Safety Modifications. A series of modifications were made to ensure safe and reliable operation in the Building 71 environment. These included a total redesign of the interlock and safety circuits for the operation of the L&W source. When the FeinFocus source was delivered, the safety control features of this new system were integrated into the existing safety system by means of an interface unit designed and built by UDRI.

FeinFocus Source. Although the Tomoscope images were the best they had ever been, the L&W source continued to have operational problems. It was not stable and would frequently kick off during a scan, which resulted in many repeat scans. Finally, in September 1997, an order for a new FeinFocus source was placed, anticipating the solution of all source-related problems. The new FeinFocus x-ray source was delivered and appeared to be working well when it was first installed, but within a few weeks a problem had surfaced which causes it to shut down during long-duration scans, thus ruining the scan in progress. Early on, the FeinFocus field service engineers made unsuccessful attempts at solving the problem and finally referred it to the experts in Germany. No permanent solution has yet been developed by FeinFocus. Nevertheless, excellent scans have been made using the Tomoscope at lower operating voltages. Therefore a temporary solution is to avoid long duration scans and high power settings. The problem appears to be that the vacuum system currently on the x-ray tube cannot keep up at long duration, high power operation.

Miscellaneous Hardware Modifications. In order to better control the temperature of the CCDs, temperature monitors were placed within the detector package. Also, a new temperature control board for detector package cooling was manufactured and installed. The CCD preamp boards were modified by Saar Associates and installed in the detector package using new

mounting system components and a new connector geometry. Micrometer adjustment stops were installed on the detector aperture to permit repeatable positioning. A new B-axis mounting assembly and new gantry mounting hardware which allows precise positioning of the gantry assembly on the optical table was designed, manufactured, and installed. A new source shutter assembly was also manufactured and installed in the Tomoscope system. With the addition of the FeinFocus source, a new knife-edge positioning system, a shutter mounting platform, and a mount which allows precise vertical positioning of the source were developed and installed.

5.7.2 LAM/DE System

Signal-to-Noise Ratio Improvement. Early in the contract period, the signal-to-noise ratio was significantly increased by reducing the amount of scattered radiation which reaches the detectors. This reduction was achieved by adding more lead shielding at the outer ends of the detector package.

Alignment. In June 1995, performance measurements on the LAM/DE CT system revealed some minor alignment errors. The thickness collimator was shown to be off parallel by 0.6 mm (as measured from opposite ends of the detector package). Using the x-rays, the collimator was adjusted to within 0.02 mm. A minor adjustment in the source-to-detector distance was also required. Again in March 1997, it was discovered that there was a minor misalignment between the x-ray source and the slice thickness aperture resulting in a smaller thickness aperture setting than expected by the system. It was also determined that the part inspection plane was slightly skewed relative to the axis of rotation. These problems were corrected by additional alignment. Recalibration of the apertures resulted in close agreement between the aperture settings specified by the operator and the system hardware.

New Computers. A new SiliconGraphics workstation was installed to supplement the image analyses capabilities of the now-antiquated MicroVAX computer systems. These computer systems were not compatible with modern-day reverse-engineering software. A DEC Alpha computer was later purchased to take over the image reconstruction tasks and data archiving for the LAM/DE system. Data collection is still performed by the MicroVAX. In a similar manner, the SiliconGraphics workstation has taken over the image reconstruction tasks and data archiving for the Tomoscope system, as well as its reverse engineering role for LAM/DE. The IBM is still used for Tomoscope system data collection.

5.8 X-Ray CT – Facility Issues

In October 1996, it was determined that the supports for the exhaust stacks on Building 71 had degraded to the point that the stacks posed a potential hazard. The building had to be closed until the stacks could be removed. On-site research efforts continued, as is possible, from the ARACOR-Dayton office. Building modifications at the CT facility were concluded near the end of January 1997. A radiation safety survey, which qualified the modifications to the exterior walls of the building, was conducted on January 29, 1997. The computer equipment that had been disconnected and moved to minimize the potential of damage during building repairs was then restored to its former configuration. During February 1997, in the effort to restore the CT facility to full functionality, the scan control computer (SCC) for the LAM/DE CT system failed while calibrating the system. Initial discussions with the manufacturer indicated that the hard disk controller board was responsible for the SCC failure. A replacement board was procured. The problem remained; additional diagnostics determined that the power supply was at fault. A replacement power supply was procured which solved the SCC problem, and on-site research efforts resumed.

5.9 X-Ray CT– LAM/DE Dimensional Accuracy Studies

A research effort on the dimensional accuracy of LAM/DE CT images was conducted. The effort focused on the effects of CT system spatial resolution and contrast sensitivity on the dimensional accuracy in CT imagery. A cylindrical, aluminum test specimen with simple geometric shapes and patterns of known geometry was designed and manufactured. Images were acquired using a variety of scan parameter combinations. This allowed variability in system performance (in terms of spatial resolution and contrast sensitivity). A set of measurements was acquired from key features in the CT images. These measurements were compared with measurements from the same features using standard metrology practices. The study showed that LAM/DE images show 0.051 mm (0.002 in.) to 0.076 mm (0.003 in.) accuracy without calibration. Accuracy improved only slightly as system resolution improved (over the range encompassed by the study). However, as noise levels in the images rose above 5%, accuracy degraded. The results of the study were presented at the annual Review of Progress in Quantitative Nondestructive

Evaluation (QNDE). A paper was also submitted for inclusion in the conference proceedings under the title, “Dimensional Accuracy In X-Ray Computed Tomography Imaging”.

5.10 X-Ray CT – Scanning Applications

Tables 5.10-1 and 5.10-2 provide lists of the significant application scans conducted during the contract period grouped by fiscal year. Scan objectives and results of the scans conducted are briefly summarized in the table.

TABLE 5.10-1: LAM/DE CT Application Scans

FISCAL YEAR 95		
Application	**Objectives**	**Results**
AA Batteries	Provide map of internal structure.	Map of internal structure was provided.
Aluminum Casting	Demonstrate detectability of porosity, voids and other discontinuities in castings.	Detectability of porosity, voids and other discontinuities was demonstrated.
Aluminum Casting	Provide evaluation of passageway integrity.	The passageway suspected of causing a leak condition was found to be acceptable. The manufacturer will continue their analysis and probably require additional CT investigations.
B1 Bungee Link	Examine material integrity in region showing surface anomalies through die penetrant tests.	No sub-surface anomalies were identified. The material integrity appeared to be satisfactory.
Brake Drum Segment	Demonstrate utility of CT in characterizing cracks and voids at the wear surface.	Cracks and voids were clearly identified.
C-C Rotor	Provide density characterization.	Density characterization was provided.
C-C Spin Disk	Provide density characterization.	Density characterization was provided.
C/C Plates	Measure density variations.	Insufficient source energy prevented measurements.
C/SiC Turbine Rotor	Provide density information.	Data were provided according to manufacturer requirements.
Catalytic Converters	Provide nondestructive information on internal assembly.	Critical internal features of interest were characterized.
Ceramic Compacts	Examine for density distribution.	Density distributions were shown.
Ceramic Ring	Inspect for density variations and anomalies.	Results were poor; higher energy is required. The ring may be scanned at HAFB.
Composite Cylinder	Provide defect characterization.	Defect characterization was provided.
Damage Repair Composite Panels	Characterize the quality of several differing repair procedures.	Detailed information on the quality of the various repair procedures was provided.
Electric Motors	Compare CT capabilities with RTR results.	CT capabilities were demonstrated.

TABLE 5.10-1: LAM/DE CT Application Scans *(Continued)*

FISCAL YEAR 95 *(Continued)*		
Application	**Objectives**	**Results**
Electrical Automotive Parts	Demonstrate utility of Digital Radiography.	Digital Radiography was used to identify features of interest.
Exhaust Nozzle with Top-coat	Measure the top-coat thickness.	Top-coat measurements were not acquired due to blurring from the high-density base material.
F16 Flight Control Stick	Evalute utility of CT for in-situ detection of small cracks in the stick assembly.	Insufficient resolution prevented detection.
Fluid Control Components	Demonstrate diagnostic utility of CT.	The utility of CT applied to several parts and imaging objectives was demonstrated.
Gas Turbine Vane	Demonstrate geometry acquisition capabilities.	LAM/DE's geometry acquisition capabilities were demonstrated.
Head Slab Core	Evaluate densification of sand.	Variations in the sand core were quantified.
Hydromechanical Units	Provide wall measurements.	Wall measurements were provided.
Ignition Coils	Detect improper assembly.	Improper assembly was detectable.
Impact Damage Specimen	Demonstrate capability of CT to map impact damage.	Impact damage was identified.
MMC HIP Tooling	Evaluate equipment capability for examining MMC insert within a large titanium sample.	Insufficient source energy precluded successful characterization.
MMC Specimens	Describe geometric relationship between cladding and fiber-reinforced regions.	Geometric relationship between cladding and fiber-reinforced regions were characterized.
NASA LeRC TiMC Ring	Provide density characterization.	Density characterization was provided.
OSU Ceramic Specimens	Part of an ongoing study by the OSU to investigate density gradients during forming.	Data continue to be analyzed by OSU personnel.
Processed C/C Components	Provide density data for evaluation of new densification process.	Density data were provided for further evaluation of new densification process.
Processed C/C Disk	Provide density data for evaluation of new densification process.	Density data were provided for further evaluation of new densification process.

TABLE 5.10-1: LAM/DE CT Application Scans *(Continued)*

FISCAL YEAR 95 *(Continued)*		
Application	**Objectives**	**Results**
Processed C/C Panels and Rings	Provide density data for evaluation of new densification process.	Density data were provided for further evaluation of new densification process.
Processed C/C Plates	Provide density data for evaluation of new densification process.	Density data were provided for further evaluation of new densification process.
Radome Panel	Evaluate impact damage zones.	Impact damage was characterized.
Sculpted Rotor	Provide density characterization.	Density characterization was provided.
Spark Plug Insulators	Demonstrate utility of CT in characterizing cracks, voids and density gradients.	Characterization of cracks, voids and density gradients was achieved.
Test Specimen with Magnets	Determine effects of x-ray exposure on magnetic properties.	X-ray exposure had no effect on the magnetic properties. Additional scans with the HAFB 9-MeV system also had no effect. CT examination of an actual part will follow.
Textron C/C Specimens	Provide density data for evaluation of new densification process.	The CT data provided have assisted in the development of the new densification process.
Ti/SiC MMC Ring	Evaluate fiber distribution.	Fiber distribution evaluated.
Timber Sample	Demonstrate CT capability for differentiating clear wood areas from rot, knots and cracks.	Differentiation of clear wood areas from rot, knots and cracks was demonstrated.
Titanium Block with Weld	Provide density information in weld area yielding anomalous UT data.	Insufficient source energy precluded successful characterization.
Turbine Drive Shaft	Provide 3-dimensional contour data of internal feature.	Contour data of the internal feature was provided.
ZnO Pellets	Part of an on-going ceramic study by the OSU.	Data continue to be evaluated by OSU personnel.
Aluminum Boat Propeller	Compare cast geometry with CD-generated CAD design geometry.	Comparison is underway.

TABLE 5.10-1: LAM/DE CT Application Scans *(Continued)*

FISCAL YEAR 96		
Application	**Objectives**	**Results**
Aluminum End Cap	Inspect for corrosion.	No corrosion was detected.
Aluminum Nose Cone	Identify porosity, voids and shrink.	Minor anomalies were noted in the regions of interest. Destructive analysis showed uniform sponge porosity. A uniform, small-void porosity would not be apparent through CT without a comparative standard.
C/C Disk	Identify density variations.	Density variations were identified.
C/SiC Rotor	Identify density variations.	Density variations were identified.
Ceramic Powders	Characterize powder densification.	CT imagery provide powder densification data that cannot be obtained by other means. The OSU study of ceramic powders will soon be published.
Composite Panel	Demonstrate utility of CT in panel inspections.	Imagery of resin in panel score lines clearly demonstrate the utility of CT in panel inspections.
Disk Phantoms	Demonstrate application of ASTM standards.	Part of an ongoing study. Data was compared with additional data gathered over several months.
Grinding Wheels	Provide characterization data as input to failure analysis study.	Characterization data was provided. The data will be analyzed and correlated with failure modes.
Magnesium Steering Wheels	Identify porosity, voids and shrink.	A map of anomalies was provided.
MMC Ring	Characterize ring prior to spin tests.	Density characterizations were acquired. The rings will be spin tested (not to failure) and CT scanning will be repeated.

TABLE 5.10-1: LAM/DE CT Application Scans *(Continued)*

FISCAL YEAR 96 *(Continued)*		
Application	**Objectives**	**Results**
Sand Cores	Characterize sand compaction.	Compaction of sand was characterized.
Sculpted Rotor	Provide density data for evaluation of new densification process.	Density data were provided for evaluation of new densification process.
Slotted Rotor	Identify density variations.	Density variations were identified.
Sputtering Target	Inspect region showing poor solder bond indications in film radiography and UT.	The region suspect region from radiographic and UT testing was verified. However, CT imagery indicates the anomaly may be in the copper background material and not in the solder material. Additional UT and radiographic testing will be conducted.
Thermal Energy Storage Device	Show distribution of salts resulting from zero-gravity Space Shuttle testing.	Salt distributions were clearly imaged. The results will be used to modify NASA models of salt performance.
Turbine Blades	Identify density variations.	Density variations and other anomalies (e.g., cracks) were identified.
ZnO Pellets	Characterize density gradient formation during compaction of spray-dried ceramic granules.	Density gradients were identified. These data are part of an on-going study by the OSU. Articles for publication are being prepared.
FISCAL YEAR 97		
Active Control Material	Determine feasibility of using CT to show defects.	Resolution and penetration was insufficient to show defects.
Aluminum Foam Samples	Measure mean density and gradients in the samples.	Measurement of the mean density and density gradients in the samples was successful.
Automotive Sand Cores and Molds	Characterize compaction of sand in complex core and mold geometries.	CT inspections successfully identified density gradients in the sand. The data will be used for finite element models.

TABLE 5.10-1: LAM/DE CT Application Scans *(Continued)*

FISCAL YEAR 97 *(Continued)*		
Application	**Objectives**	**Results**
Carbon Composite Material from China	Determine feasibility of using CT to show internal structure of the material.	The feasibility scans clearly showed arrangement of very dense fibers within the carbon material.
Carbon Foam Samples	Measure mean density and gradients in the samples.	Measurement of the mean density and density gradients in the samples was successful.
Cast Iron Engine Block	Determine feasibility of reverse engineering cast iron components with LAM/DE.	Imagery of the engine block was noisy, but usable. Dimensional accuracy has yet to be determined.
Composite Flywheel	Determine feasibility of using CT to show internal flaws.	The feasibility scans clearly showed internal separation of the composite material of the flywheel.
Cylinder Block	Demonstrate CT capabilities for reverse engineering.	Imagery through the cast iron was quite noisy. However, reverse engineering was successfully demonstrated.
Engine Block	Examine engine block for porosity and voids.	Porosity and voids were located and quantified.
F-22 Castings	Perform digital radiographic inspection for inclusions.	Digital radiographic inspections of the titanium castings were not successful due to insufficient signal strength for the particular material and geometry in question.
Glass Cane Samples	Provide density map showing gradient structure and sample centroids.	The samples were well characterized in terms of density and the centroids of each sample.
Glass Compounds	Characterize density gradients.	Density gradients were characterized.
Hafnium-Carbide Wafers	Characterization of structure and density gradients through the thickness of the wafers.	Structure and density information was acquired.

TABLE 5.10-1: LAM/DE CT Application Scans *(Continued)*

FISCAL YEAR 97 *(Continued)*		
Application	**Objectives**	**Results**
Hinge Castings	Compare porosity in hipped and unhipped samples.	Significant differences were noted in the porosity level between the hipped and unhipped samples.
Inconel Rotor Blade	Determine the feasibility of using LAM/DE for reverse engineering scans of this part	LAM/DE has insufficient penetration energy to provide data sufficiently clean for reverse engineering of this part.
Metal Flange	Determine feasibility of using CT to show very small irregularities.	The feasibility scans showed that the very small holes and cuts machined into the part could not be detected by LAM/DE.
MMC Ring	Compare CT imagery from before and after spin testing.	Comparative data from before and after spin testing of the ring were provided to NASA.
Potted Metallurgy Parts	Determine feasibility of using CT to show density variation in the parts resulting from the manufacturing process.	The feasibility scans did show variations in density but the results were somewhat inconclusive due to noise and artifacts resulting from insufficient penetration energy.
Reverse Engineering Phantom	Assess relationship between measurement accuracy and critical performance parameters.	CT-based metrology and comparative analyses were performed and reported.
Reusable Solid Rocket Motor (RSRM) Nozzle Material	Characterize the "char zone" in the nozzle material following exposure to the 150 kW CO_2 laser in the LHMEL facility (LHMELII).	Characterization of the "char zone" in the nozzle material continues to be successful and extremely useful in the ongoing material study.
Rupture Disks	Inspect for hair-line fracture.	The hairline fracture was not resolved. Ultrasonic inspection is being considered.
Sand Molds for Ohio State University	Compare compaction characteristics of sand molds.	A variety of sand molds were characterized. The data are being analyzed by OSU personnel to properly model compaction characteristics for various processes and additives.

TABLE 5.10-1: LAM/DE CT Application Scans *(Continued)*

FISCAL YEAR 97 *(Continued)*		
Application	**Objectives**	**Results**
Scroll Castings	Characterize and compare porosity before and after hot isostatic pressing.	Significant porosity was noted in each of the sample castings. After HIPing, little change was noted.
Titan Flow Valve	Demonstrate CT examination of flow valve for proper assembly.	CT imagery successfully identified both proper and improper assemblies.
Titanium Rotor Blank	Demonstrate CT examination capabilities for nondestructive evaluation of prototype rotor.	The LAM/DE system's capability to properly inspect the prototype rotor was demonstrated.
Turbine Blades	Provide contour map of blades.	Contour map of turbine blades were generated using Archimedes. The contours were delivered to the manufacturer by way of the world wide web.
Wax Cylindrical Part	Determine feasibility of using CT for reverse engineering of low density parts.	The feasibility scans clearly showed the lower density wax part provided excellent CT images that could be used for reverse engineering applications.
FISCAL YEAR 98		
5-Axis-CNC Aluminum Part	Feasibility scans to determine if LAM/DE could provide adequate scans for reverse engineering efforts.	The feasibility scans showed adequate x-ray penetration and a series of scans of the part were completed to demonstrate reverse engineering capability to Robins AFB.
Aircraft Brake Pad Material	Feasibility scans to determine if CT can show suspected density gradients in the brake pad material.	The CT images were inconclusive in showing the expected density gradients due to noise and artifacts. Future plans indicate a desire to scan more samples with the pad material removed from the metal brackets and cut to provide a relatively square cross section.

TABLE 5.10-1: LAM/DE CT Application Scans *(Continued)*

FISCAL YEAR 98 *(Continued)*		
Application	**Objectives**	**Results**
Aluminum Pistons	To demonstrate the capability of CT to show internal manufacturing defects in piston castings.	The CT scans did show some manufacturing defects and the results will be evaluated by the manufacturer.
Aluminum Sample with Fly Ash	Conduct feasibility scans to determine capability of LAM/DE to show presence and distribution of fly ash material imbedded in the sample.	The scans showed multiple lower density pockets within the aluminum that are attributable to the inclusion of fly ash.
Aluminum Transmission Cover	Determine feasibility of establishing porosity and density variation in a sample transmission cover before HIP processing for comparison to the same cover after HIP processing.	The CT scans showed some regions of density variation. It will be interesting to compare these same regions in the sample after it has been HIP processed.
ARACOR Aluminum Pawn	Obtain a complete set of CT scans of the ARACOR pawn for a reverse engineering study.	The scan series consisted of 208 scans taken at 0.5 mm increments in the vertical direction. The total time to complete all scans was 80 hours. Images for the last couple of scans could not be reconstructed using the LAM/DE reconstruction software due to lower signal-to-noise ratios; however, the scan data was reconstructed using the convolution back-projection routines now in place on the Tomoscope system.

TABLE 5.10-1: LAM/DE CT Application Scans *(Continued)*

FISCAL YEAR 98 *(Continued)*		
Application	**Objectives**	**Results**
Automotive Cylinder Section Sand Molds	Obtain representative density data throughout the entire volume of the sand molds for use in computer modeling.	The first and last sand molds from a production run were scanned side-by-side under a CRADA arrangement with a major automobile manufacturer. Density variations were evident throughout the volumes of the two parts.
Automotive Windshield Wiper Blade	Demonstrate the capability of CT to provide images suitable for reverse engineering for comparison to laser scanning techniques.	130 scans of the part were completed with a vertical interval of 0.5mm. A point cloud was produced from the scan data and provided to the manufacturer. The initial impression of the data provided was that it was far superior to the data they have been able to obtain from their newly procured laser scanner.
Blisk Blank B-1	Determine feasibility of using CT to confirm anomalous indications found through ultrasonic testing on the test article.	LAM/DE did not have sufficient energy to confirm the anomalous indications. The noise artifacts overpowered any subtle indications.
Brass Rings for Navy Winches	Feasibility scans to show any abnormal density variation in the ring material that would account for anomalous wear in the wench mechanism.	The images showed density pockets and density variation throughout the rings. The results have been provided to the Navy and there is a potential for additional work.
Ceramic Light Bulbs	CRDA effort to show anomalies or problems in the ceramic bulbs resulting from different manufacturing or processing techniques.	LAM/DE did not have sufficient resolution to provide meaningful data. Tomoscope studies were very successful.

TABLE 5.10-1: LAM/DE CT Application Scans *(Continued)*

FISCAL YEAR 98 *(Continued)*		
Application	**Objectives**	**Results**
Ceramic Tools	Feasibility scans to determine if CT can show fractures and density gradients seen in SEM observations of green ceramic tool inserts.	Beam hardening effects dominated the images and masked any useful density gradient data.
Diamond Grinding Wheels	To characterize density variations in the ring of abrasive material cemented to the grinding wheel. This is a CRDA effort.	All wheels examined had some density variation in the grinding material. Some wheels, however, were more uniform. The manufacturer will attempt to correlate performance to uniformity.
Hafnium carbide infiltrated inserts	Determine feasibility of using CT to characterize density variations in the inserts.	The feasibility scans clearly showed dramatic density variations throughout the inserts. These samples are potential candidates for further analysis using acoustic tomography.
Large Composite Panel with Imbedded Shapes for UTEP Students	To provide CT data for data fusion studies being conducted during the summer.	Because of the size of the composite panel, only preview scans could be done. The LAM/DE preview scan did, however, show location of the imbedded metal shapes.
Lube Pump Casting	Feasibility scans to demonstrate dimensional measurement capability of LAM/DE on a pump casting.	The x-rays penetrated the casting, and the scans were sufficiently free of noise and artifacts to provide good dimensional measurements.
Magnesium Casting	CRDA effort to provide volume data for reverse engineering.	Feasibility scans showed that LAM/DE could provide the adequate scan data on the castings, and a CRDA effort was completed to provide the needed volume data.

TABLE 5.10-1: LAM/DE CT Application Scans *(Continued)*

FISCAL YEAR 98 *(Continued)*		
Application	**Objectives**	**Results**
Metal Missile Component	Feasibility scans to determine if LAM/DE can show any density variations in problem areas indicated by other inspection techniques.	Due to artifacts and noise present in the data, no conclusive evidence could be shown linking the CT data to problem areas previously identified.
Niobium Ingot with Shrinkage Porosity	Show feasibility to characterize internal flaws or defects in an expensive ingot.	The scans showed that the ingot was mostly free of internal defects except for a large defect near one of the ends. Sole reliance on visual inspection would have indicated the wrong end of the ingot as the best end.
Ohio State University Materials and Parts Samples (including alumina samples, green ceramic tile, sand molds, brick material, and samples containing cerium)	To conduct CT scans on different samples to demonstrate capability for new applications of CT and to provide density gradient data for ongoing studies.	Some of the CT scans provided very useful results for ongoing studies and potential applications. Other scans which were more exploratory didn't show much of interest.
Organic Matrix Composite Panels	Determine feasibility of using CT to measure density variations within the panel.	The panels were too large in lateral extent and too thin to allow clean CT density data.
Piston Heads	To determine if LAM/DE had sufficient penetration to enable an affordable series of CT scans for reverse engineering.	It was found that the only way to get clean images with LAM/DE on these heads was to scan them individually. The cost to perform a volume scan for reverse engineering of the two heads then became prohibitive.
Reusable Solid Rocket Motor (RSRM) Nozzle Material Samples	Characterize the "char zone" in the nozzle material following exposure to the 150 kW CO_2 laser in the LHMEL facility (LHMELII).	The results from these scans continue to provide the data needed to characterize the material response to the thermal and flow conditions being simulated in the LHMEL facility.

TABLE 5.10-1: LAM/DE CT Application Scans *(Continued)*

FISCAL YEAR 98 *(Continued)*		
Application	**Objectives**	**Results**
Sand Molds	Determine feasibility of using CT for measuring density variations in the sand.	Scans of the sand showed interesting density variations that could result in further study.
Subscale Titanium Rotor	Feasibility scans to determine if LAM/DE could show low density pockets seen in x-ray radiography.	Any low density pockets in the scans were indistinguishable from noise.
TiMC Ring	Repeat the same series of CT scans performed in previous sessions now after 9525 fatigue cycles to enable a search for evidence of material degradation.	The CT scans showed little change from the last series of scans.
Titanium Pressure Vessel	Feasibility scans to determine if CT could be used to inspect electron-beam weld lines on pressure vessels.	No useful data on the weld lines resulted from the LAM/DE scans.
Titanium Rotor	Perform CT scans to determine the capability of LAM/DE to detect very small notches, flat-bottomed holes, and high density inclusions.	The only clearly distinguishable artifact was one of the high density inclusions. The other inclusion was barely visible. The 0.030-inch-diameter flat-bottomed hole was discernible knowing exactly where to look. Neither the EDM notches nor the 0.010-inch-diameter flat-bottomed hole were detectable.
Titanium Stress Analysis Sample	To determine if CT could show any density variations in a titanium sample due to induced stress.	No density variation was observed that could be correlated to the induced stress in the sample.

TABLE 5.10-2: Tomoscope CT Application Scans

Application	Objectives	Results
FISCAL YEAR 97		
Aluminum Cylinder (0.5-inch diameter)	Determine the resolution of the Tomoscope in the current configuration.	Resolution of the Tomoscope in the current configuration was determined to be about 70 microns.
Aluminum Cylinder (1.5-inch diameter)	Verify the expanded field of view of the Tomoscope in the new configuration.	The Tomoscope was able to provide CT scans in the wider field of view using four CCDs.
Ultra-High Molecular Weight Polyethylene	Determine feasibility of using the Tomoscope to evaluate this material for small defects and degree of fusion.	The feasibility scans showed some internal structure and density variation in the material.
FISCAL YEAR 98		
Active Control Stack	Determine feasibility of using the Tomoscope for showing defects in the layers of the control stack.	The Tomoscope has insufficient energy to penetrate the sample and show the defects of interest.
Alumina Sample for Ohio State University	Feasibility scan to determine if CT can show density gradients in thin alumina parts.	CT data was provided to Ohio State University to support their ongoing studies. The thin, flat sample appeared to be very uniform in density, even around the holes near the edge of the samples.
Aluminum Cylinder	Obtain x-ray absorption data to test the detector calibration algorithms developed for reducing ring artifacts.	Because of problems with the new FeinFocus source in long duration scans, numerous attempts were made before a suitable scan was completed. The scan data will now be used to complete the checkout of the detector calibration software for ring artifact correction.

TABLE 5.10-2: Tomoscope CT Application Scans *(Continued)*

FISCAL YEAR 98 *(Continued)*		
Application	**Objectives**	**Results**
Ceramic Light Bulbs	CRDA effort to show anomalies or problems in the ceramic bulbs resulting from different manufacturing or processing techniques.	The Tomoscope images were excellent in showing cracks and voids in the ceramic material. The manufacturer was pleased with the images.
Ceramic Tools	Feasibility scans to determine if CT can show fractures and density gradients seen in SEM observations of green ceramic tool inserts.	Again just as in LAM/DE, the beam hardening effects dominated the images and masked any useful density gradient data.
Composite Spindle Section	Determine feasibility of using CT to find regions where marcelling occurs.	Very clear and distinct layers were observed in the Tomoscope CT scans as compared to the LAM/DE CT scans. However, no marcelling has yet been discovered, but the LAM/DE scans have provided several potential areas for further feasibility scans.
Concrete Sample for University of Utah	Feasibility scan to demonstrate the capability of the Tomoscope to resolve very small voids and very small internal structural elements of the concrete sample.	The CT data did resolve structural details such as very small voids and a mixture of different materials. Another scan with a thinner slice will be performed to improve the CT image.
Eddy Current Probes	Study the composition and internal structure of several probes in an effort to discover the cause of differing performance.	The Tomoscope preview scans and CT scans did show differences between the probes. Further investigation is required to determine which of these differences is a cause of poor performance.

TABLE 5.10-2: Tomoscope CT Application Scans *(Continued)*

FISCAL YEAR 98 *(Continued)*		
Application	**Objectives**	**Results**
Extruded Aluminum Blade Section	Determine feasibility of showing the bond line resulting from the extrusion process and any material inclusions.	The CT scans did show a definite bond line and possibly some inclusions of material in the aluminum.
Human Tooth with Fillings	Determine the feasibility of using CT to investigate such things as filling bond failure in human teeth.	The Tomoscope preview scans and CT scans did show much of the internal structure of the tooth. The initial scans were not successful in showing any problems in the bond line between the tooth and the filling. Additional scans parallel to the longitudinal axis were much more interesting to the researchers at Ohio State University and have potential application to their work.
Metal Blade with Internal Cooling Passages	Demonstrate Tomoscope image quality.	The CT images of this part clearly showed the geometry and location of the internal cooling passages.
Metal Matrix Composite Material	To show the improvement in image quality of the Tomoscope using the FeinFocus x-ray source.	The scans using the new FeinFocus x-ray source and the new processing software show improvements over scans of the same material in previous configurations.

TABLE 5.10-2: Tomoscope CT Application Scans *(Continued)*

FISCAL YEAR 98 *(Continued)*		
Application	**Objectives**	**Results**
NASA Tether from Failed Shuttle Experiment	To show the current capability of the Tomoscope on a high interest part scanned before recent improvements were made.	These recent Tomoscope images are much improved over previous images. Each part of the tether is clearly evident.
Pharmaceutical Pill and Rolled Material Samples	Feasibility scans to show capability of the Tomoscope in determining density gradients.	The CT images clearly showed slight density differences and gradients in the samples. The pharmaceutical engineers are eager to pursue a CRDA effort in the near future.
RSRM Nozzle Material Samples	Feasibility scans to demonstrate the potential utility of increased resolution in providing density data for the nozzle material samples being tested in the LHMEL facility. Search for further evidence of the density banding observed in LAM/DE scans.	The Tomoscope CT images showed much better resolution than the LAM/DE images. The samples just fit within the Tomoscope field of view. These scans opened up the real possibility of using the Tomoscope for some samples in the ongoing study where higher resolution is needed. The interesting density bands noted in the LAM/DE scans were much better resolved and more apparent in the Tomoscope images.
Section from the composite spindle	Determine feasibility of using the Tomoscope for showing evidence of marcelling in the layers of the composite material in regions identified by LAM/DE as potential sites for the occurrence of marcelling.	The Tomoscope CT scan did not show any marcelling at the site identified in LAM/DE CT scans as a good potential site.

TABLE 5.10-2: Tomoscope CT Application Scans *(Continued)*

FISCAL YEAR 98 *(Continued)*		
Application	**Objectives**	**Results**
Subscale Titanium Rotor	To determine if high resolution preview scans using the Tomoscope could show the small low density pockets seen in x-ray radiography.	A low density pocket was seen in a preview scan using the Tomoscope. CT scans of the same portion of the rotor using LAM/DE still failed to show anything.
Titanium Stress Analysis Sample.	To determine if the increased resolution of the Tomoscope would show any density variations due to stress in the titanium sample already scanned on LAM/DE.	Even with the higher resolution of the Tomoscope, no density variation was observed that could be correlated to the induced stress in the sample.

5.11 MLLP Branch Computing Resources

UDRI and ARACOR significantly upgraded the MLLP Branch computing resources during the period of performance of this contract. The computing resources at the end of the period of performance are illustrated in Figure 5.11-1 and outlined in Tables 5.11-1 through 5.11-5.

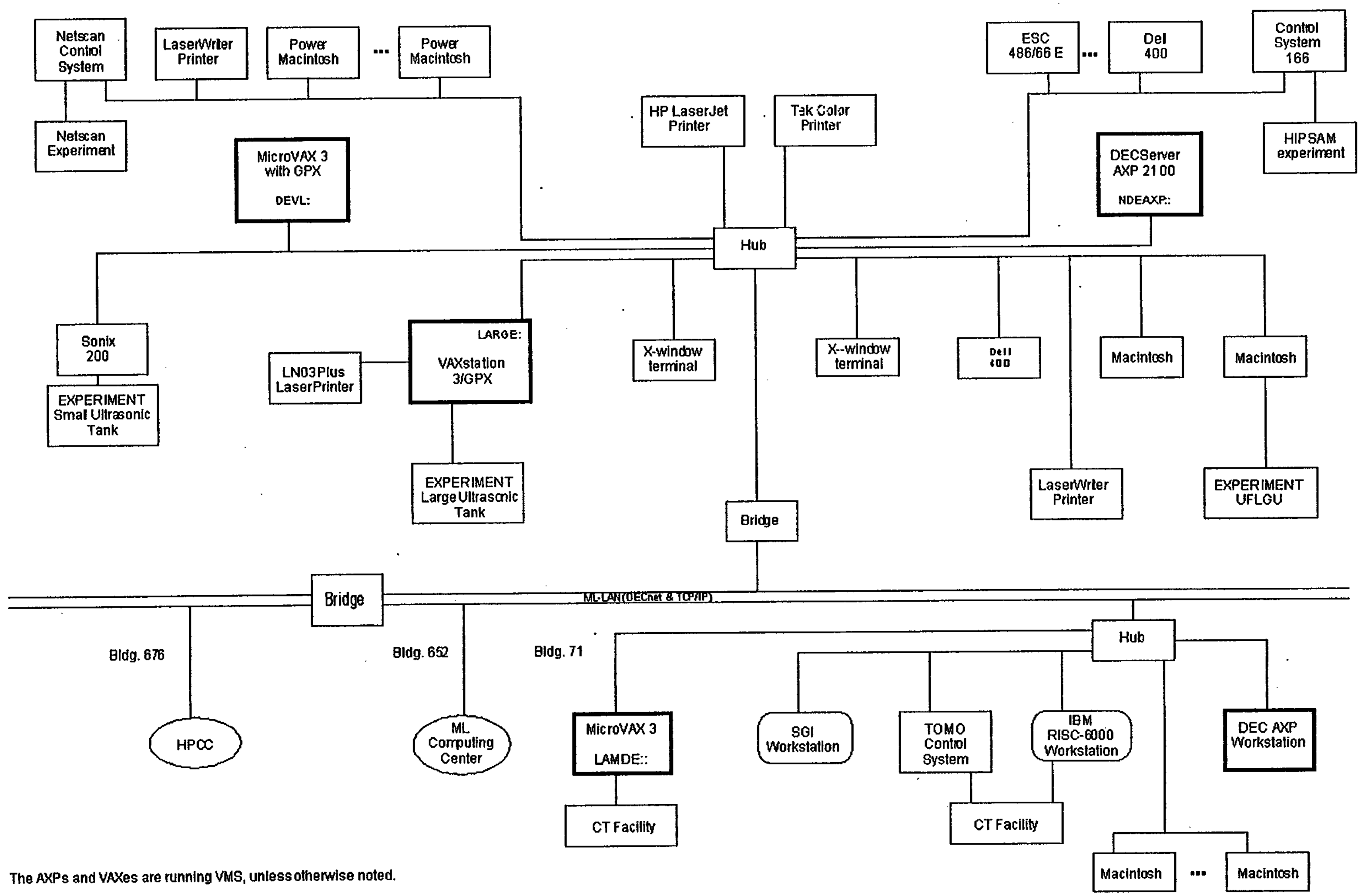

FIGURE 5.11-1
MLLP Computing Resources

Table 5.11-1. Node NDEAXP, AXP 2100 Computer System Components

Central Processing Unit (CPU)

- AXP 2100 Series
- 128-MByte main memory

Disk Drives (5)

- One RZ28 (2.1 GBytes) used as the system disk drive
- One RZ28 (2.1 GMBytes) used as the main users' disk drive
- One RZ28 (2.1 GBytes) used as the library disk drive
- One RRD43 (650 MBytes) CD-ROM drive
- One RX26 (2 MBytes) floppy disk

Magnetic Tape Drives (2)

- One TLZ07 (2 Gbyte) DAT cartridge tape drive

Display Unit – 17-Inch, Color Graphics

- Serves as the boot console terminal & X-window terminal
- 1024 by 864 pixels resolution
- 256 simultaneously displayable colors, user-selectable from a palette of 16.7 million

Serial Ports (2) – Asynchronous

Printers

- Network access to a DECLaser Writer 3500 laser printer – 600 DPI

Software

- DEC Ada for OpenVMS Alpha
- DEC Fortran for OpenVMS Alpha
- DEC C for OpenVMS Alpha
- DECmigrate for OpenVMS AXP
- DECprint Supervisor (DCPS) for OpenVMS
- DECset
  - Code Management System
  - DECtest Manager
  - Environment Manager
  - Language-Sensitive Editor
  - Module-Management System
  - Performance and Coverage Analyzer
  - Source Code Analyzer
- DECWindows Motif for OpenVMS
- Exodus for Macintosh
- IMSL Fortran Numerical Libraries
- Interleaf
- NAS Base Server 200/OpenVMS AXP
  - DECnet/OSI for OpenVMS Alpha
  - Digital TCP/IP Services for OpenVMS AXP
  - Pathworks for OpenVMS
  - Pathworks for OpenVMS (Macintosh)
  - Pathworks for DOS & Windows (LAN Mgr)
- Netscape Navigator
- OpenVMS Alpha
- PV-Wave
- Tektronix XpressWare
- VMSCluster

Table 5.11-2. Node LARGE, MicroVAX 3500 Computer System Components

Central Processing Unit (CPU)

3000-Series
32-MByte main memory

Disk Drives (5)

One RA81 (456 MBytes) used as the master VAXcluster system disk drive
One RA81 (456 MBytes) used as the main users' disk drive
One RA81 (456 MBytes) used as the library disk drive
One RA81 (456 MBytes) used as the Appleshare disk drive
One RD53 (71 Mbytes) not in use
One 600-MByte removable cartridge disk drive (eraseable optical)
Used for off line storge

Magnetic Tape Drives (2)

One 95-MByte cartridge unit
One 2-GByte QIC cartridge

Display Unit – 19-Inch, Color Graphics

Serves as the boot console terminal & X-window terminal
1024 by 864 pixels resolution
256 simultaneously displayable colors, user-selectable from a palette of 16.7 million

Serial Ports (4) – Asynchronous

Printers

Network access to a DECLaser Writer 3500 laser printer – 600 DPI

Software

DEC Ada for VAX
DECnet VAX
DECwindows Motif for OpenVMS
DECwindows Tools Package for Motif (VUIT, Graphical Interface Tools, Linkworks)
OpenVMS Vax 5.5-2
Pathworks
VAX C
VAX Fortran
VMSCluster
VMS/Ultrix Connection
CA-DISSPLA

Table 5.11-3. Node LARGE, MicroVAX 3500 Computer System Components

Central Processing Unit (CPU)
3000-Series
16-MByte main memory
Disk Drives (4)
One RA81 (456 MBytes) used as the system disk drive
One RA81 (456 MBytes) used as the data collection disk drive
One RA81 (456 MBytes) used as a backup disk drive
One RD53 (71 Mbytes) not in use
Magnetic Tape Drives (2)
One 95-MByte cartridge unit
Display Unit – 19-Inch, Color Graphics
Serves as the boot console terminal & graphics output unit
1024 by 864 pixels resolution
256 simultaneously displayable colors, user-selectable from a palette of 16.7 million
Serial Ports (4) – Asynchronous
Printers (1)
LN03 laser printer – 300 DPI
Software
DECnet – VAX
DEC Test Manager
LSE
OpenVMS VAX 4.7a
UIS
VAX DEC/CMS
VAX Fortran
VAX PCA
VWS
VWS/Sight

Table 5.11-4. SONIX Enhanced FlexSCAN-C Computer System Components

Central Processing Unit (CPU)
Intel Pentium-Pro 200
64-MByte main memory
Disk Drives
One 2.0 GByte disk used as the system drive
One 2.0 Gbyte disk used as a data collection drive
One 1.0 Gbyte JAZZ removeable disk used as a backup drive
3½ Floppy
24x CD-ROM
Display Unit – 17-Inch, Color Graphics
Serves as the boot console terminal & graphics output unit
1024 by 768 pixels resolution
256 simultaneously displayable colors, user-selectable from a palette of 16.7 million
Printers
Network access to all ML printers
Software
Windows 95 / DOS Operating System
FlexSCAN-C Version 4.71a

Table 5.11-5. HIPSAM – High-Precision Scanning Acoustic Microscopy Computer System Components

Central Processing Unit (CPU)
Intel Pentium-II 166 MHz – 64-MByte main memory
Intel 386 25 MHz – Display Processor
Disk Drives
One 4.0 GByte disk used as the system drive
One 1.2 Gbyte disk used as a data collection drive
3½ Floppy
12x CD-ROM
Magnetic Tape Drives
One DAT 4 GByte cartridge unit
Display Units
17-Inch, Color Graphics Serves as the boot console terminal
21-Inch, Color Graphics Serves as graphics output unit
1024 by 768 pixels resolution
256 simultaneously displayable colors, user-selectable from a palette of 16.7 million
Printers
Network access to all ML printers
Software
Windows 95 / DOS Operating System
HIPSAM Collection & Control

This page intentionally left blank.

Section 6
References

Netravali, A.N., R.B. Henstenburg, S.L. Phoenix and D. Schwartz, "Interfacial Shear Strength Studies Using the Single Filament Composite Test," *J. Material Science*, 26, p. 6631 (1991).

Drzal, L.T., "Composite Characterization," 15th National SAMPE Technical Conference, p. 190 (1983).

Quate, C.F, A. Atalar and H.K. Wickramasinghe, "Acoustic Microscopy with Mechanical Scanning," *Proc. IEEE,* 67, 1092 (1979).

Kushibiki, J., and N. Chubachi, "Material Characterization by Line Focus Beam Acoustic Microscope," *IEEE. Trans.*, SU-32, p. 189, (1985).

Kulik, A., G. Gremaud and S. Sathish, "Direct Measurement of the SAW Velocity and Attenuation Using Continuous Wave Reflection Scanning Acoustic Microscope," in *Acoustical Imaging*, Vol.18, pp. 227-235, Ed. H. Lee and G. Wade, Plenum Press, New York (1991).

Nagy, P.B., M. Blodgett, and M. Golis, "Weep Hole Inspection by Circumferential Creeping Waves," *NDT & E International,* 27(3), pp. 131-142 (1994).

This page intentionally left blank.

Section 7
Publications

Journal Articles – Published

Benson D., P. Karpur, D.A. Stubbs, T.E. Matikas, "Evaluation of Damage Evolution and Material Behavior in SIGMA/Ti-6242 Composite Using Nondestructive Methods," Sixth ASTM Symposium on Composites: Fatigue and Fracture, (ASTM, Denver, Colorado, 1995), ASTM STP.

Benson D., P. Karpur, D.A. Stubbs, T.E. Matikas, "Characterization of Damage Progression and Its Correlation to Residual Strength in a SIGMA/Ti-6242 Composite Using Nondestructive Methods," P.F. Joseph, G.P. Carman and S.L. Donaldson, Eds., *Durability and Damage Tolerance of Composites*, MD Vol. 69-1, pp. 285-292 (1995).

Berens, A.P., "NDE Reliability of the ECII Series E Eddy Current Inspection System," UDR-TR-94-45, University of Dayton Research Institute, OH (May 1995).

Frantziskonis G.N., P. Karpur, T.E. Matikas, S. Krishnamurthy, P.D. Jero, "Fiber Matrix Interface – Information from Experiments via Simulation," *Composite Structures*, Vol. 29, pp. 231-247 (1994).

Hu S., P. Karpur, T.E. Matikas, L. Shaw, N.J. Pagano, "Free Edge Effect on Residual Stresses and Debond of a Composite Fiber/Matrix Interface," *Mechanics of Composite Materials and Structures*, Vol. 2, pp. 215-225 (1995).

Karpur P., D.M. Benson, T.E. Matikas, T. Kundu, P.D. Nicolaou, "An Approach to Determine the Experimental Transmitter-Receiver Geometry for the reception of Leaky Lamb Waves," *Materials Evaluation*, Vol. 53(12), pp. 1348-1352 (1995).

Karpur P., T.E. Matikas, M.P. Blodgett, J.R. Jira, D. Blatt, "Nondestructive Crack Size and Interfacial Degradation Evaluation in Metal Matrix Composites Using Ultrasonic Microscopy," *Special Applications and Advanced Techniques for Crack Size Determination*, J.J. Ruschau, J.K. Donald, Eds., (ASTM, Philadelphia, 1995), ASTM STP 1251, pp:130-146.

Karpur P., T.E. Matikas, S. Krishnamurthy, "Ultrasonic Characterization of the Fiber-Matrix Interphase/Interface for Mechanics of Continuous Fiber Reinforced Metal Matrix and Ceramic Matrix Composites," *Journal of Composites Engineering*, Vol. 5(6), pp. 697-711 (1995).

Kent, R., M.J. Ruddell, "In-Situ Sensor Guided Process Characterization of Advanced Composite Materials," *JOM, The Technical Journal of The Minerals, Metals, and Materials Society* (Sept. 1996).

Kent R.M., P. Karpur, T.E. Matikas, P.D. Jero, "Ultrasonic Analysis of Interfacial Debond in Ceramic Matrix Composites" in *Nondestructive Characterization of Materials VI*, R.E. Green, K.J. Kozaczek, C.O. Ruud, Eds., (Plenum Press, New York, Oahu, Hawaii, 1994), pp. 707-713.

Krishnamurthy S., T.E. Matikas, P. Karpur, D.B. Miracle, "Ultrasonic Evaluation of the Processing of Fiber-Reinforced Metal Matrix Composites," *Composites Science and Technology*, Vol. 54(2), pp. 161-168 (1995).

Krishnamurthy S., T.E. Matikas, P. Karpur, D.B. Miracle, "Role of Matrix Microstructure in the Ultrasonic Characterization of Fiber Reinforced Metal Matrix Composites," *Acta Met.* (1995).

Kundu T., K. Maslov, P. Karpur, T.E. Matidkas, P.D. Nicolau, "A Lamb Wave Scanning Approach for Mapping of Defects in [0/90] Titanium Matrix Composites," *Ultrasonics*, Vol. 34, pp: 43-49 (1996).

MacLellan P.T., D.A. Stubbs, P. Karpur, "In Situ Ultrasonic Surface Wave Assessment of Mechanical Fatigue Damage Accumulation in Metal Matrix Composites," *Composites Engineering*, Vol. 5 (12), pp. 1413-1422 (1995).

Matikas T.E., P. Karpur, R.E. Dutton, "Damage Assessment of Fiber/Matrix Interface in Ceramic Matrix Composites Using Elastic Stress Waves," *High-Temperature Ceramic-Matrix Composites I: Design, Durability, and Performance,* A.G. Evans, R. Naslain, Eds., (American Ceramic Society, Westerville, Ohio, 1995), Ceramic Transactions, Vol. 57, pp. 477-482.

Matikas T.E., P. Karpur, R.E. Dutton, R. Kim, "Influence of the Interface and Fiber Spacing on the Fracture Behavior of Glass Matrix Composites," *Materials Evaluation*, Vol. 53(9), pp. 1045-1051 (1995).

Matikas T.E., P. Karpur, S. Krishnamurthy, R.E. Dutton, "A Nondestructive Approach to Characterize the Interfacial Defects Induced During Processing of MMCs and CMCs with the Consolidation Parameters," *Applied Composite Materials* (1995).

Matikas T.E., P. Karpur, S. Shamasundar, "Measurement of the Dynamic Elastic Moduli of Porous Titanium Aluminide Compacts," *Journal of Material Science* (1995).

Matikas T.E., M. Rousseau, P. Gatignol, "Analytical Modeling of Acoustic Beam Nonspecular Reflection from Liquid-Solid Plane Interfaces," *Acta Acoustica.*

Shaw L.L., T.E. Matikas, P. Karpur, S. Hu, D.B. Miracle, "Fracture Strength and Damage Progression of the Fiber/Matrix Interfaces in Titanium-Based MMCs with Different Interfacial Layers," *Composites Part B: Engineering* (1996).

Waterbury M.C., P. Karpur, T.E. Matikas, S. Krishnamurthy, D.B. Miracle, "In Situ Observation of the Single Fiber Fragmentation Process in Metal Matrix Composites by Ultrasonic Imaging," *Journal of Composites Science and Technology*, Vol. 52(2), pp. 261-266 (1994).

Conference Articles – Published

Benson D.M., P. Karpur, T.E. Matikas, T. Kundu, "Experimental Generation of Lamb Wave Dispersion Using Fourier Analysis of Leaky Modes," D.O. Thompson, D.E. Chimenti, Eds., 21st Annual Review of Progress in Quantitative Nondestructive Evaluation, Vol. 14A, pp. 187-194, Plenum Press (1995).

Frantziskonis G.N., T.E. Matikas, P. Karpur, S. Krishnamurthy, "Lattice Analysis Approach to Assess Fiber-Matrix Interface Behavior Under Various Experimental Configurations," S.N. Atluri, G. Yagawa, T.A. Cruse, Eds., *International Conference on Computational Engineering Science*, Vol. 2, pp. 2563-2567, Springer Verlag, Berlin, Mauna Lani, Hawaii (1995).

Frantziskonis G.N., T.E. Matikas, P. Karpur, S. Krishnamurthy, "Simulation of Fiber-Matrix Interface Behavior under Various Experimental Configurations," *Proceedings of the International Conference on Composites Engineering (ICCE/1),* pp. 147-148, New Orleans (1994).

Hu S., P. Karpur, T.E. Matikas, "A Preliminary Investigation of Fiber/Matrix Interphase Oxidation in Metal Matrix Composites Using Acoustic Microscope," D.O. Thompson, D.E. Chimenti, Eds., *21st Annual Review of Progress in Quantitative Nondestructive Evaluation*, Vol. 14B, pp. 1263-1270, Plenum Press (1995).

Hu S., D. Gundel, T.E. Matikas, P. Karpur, "Quantitative Ultrasonic Characterization of Metal Matrix Composites Fiber/Matrix Interfacial Failure," *Review of Progress in Quantitative Nondestructive Evaluation*, Vol. 15, D.O. Thompson and D.E. Chimenti, Eds., Plenum, Seattle, Washington (1995).

Karpur P., T.E. Matikas, "Shear-Wave Back Reflectivity and Acoustic Microscopy Techniques for the Characterization of Damage in Titanium Matrix Composites," *Proceedings of the ASNT Spring Conference*, pp. 179-181, Las Vegas, Nevada (1995).

Karpur P., T.E. Matikas, "Theoretical Modeling and Experimental Characterization of Fiber-Matrix Interface in Advanced Composites," D.O. Thompson, D.E. Chimenti, Eds., 21st Annual Review of Progress in Quantitative Nondestructive Evaluation, vol. 14B, pp. 1449-1456, Plenum Press (1995).

Karpur P., T.E. Matikas, M.P. Blodgett, "Acoustic Microscopy as a Tool for Fiber-Matrix Interface Evaluation," *Proceedings of the International Conference on Composites Engineering (ICCE/1)*, pp. 253-254, New Orleans (1994).

Karpur P., T.E. Matikas, S. Krishnamurthy, D.B. Miracle, "Recent Developments in Ultrasonic Methods for Metal Matrix Composites Research," A. Poursartip, K. Street, Eds., *The Tenth International Conference on Composite Materials (ICCM-10)*, Vol. 5, pp. V-479 to V-486, Woodhead Publishing Ltd., Whistler, British Columbia, Canada (1995).

Karpur, P., T.E. Matikas, S. Shamasundar, R.L. Crane, "Ultrasonic Verification of the Densification and Measurement of Elastic Properties of Porous Metallurgical Compacts," I. Rokhlin and T. Kishi, Eds., The First US-Japan Symposium on Advances in NDT, June 24-28, 1996, Kahuku, Hawaii, pp. 453-455.

Kent, R.M., P. Karpur, T.E. Matikas, and M.J. Ruddell, "A Quantitative Approach for the In Situ Analysis and Characterization of Interfacial Consolidation in Metal Matrix and Ceramic Matrix Composites," *Proceedings of the International Conference on Composites Engineering (ICCE/1)*, New Orleans, LA (1994).

Kent, R.M. and M.J. Ruddell, "Laser Based Ultrasonics for Fiber Characterization and Intelligent Processing of Composite Materials," *Review of Progress in Quantitative Nondestructive Evaluation*, Vol. 14, D.O. Thompson and D.E. Chimenti, Eds., Plenum, Snowmass Village, CO (1994).

Kent, R.M. and M.J. Ruddell, "An In Situ Sensor for Process Control of Fiber Reinforced Composites," presented at the Conference on Nondestructive Evaluation for Process Control of Composites, St. Louis, MO (October 1994).

Kent, R.M. and M.J. Ruddell, "In Situ Characterization of Fiber and Fiber-Matrix Interfaces in Ceramic Matrix Composites," presented at the Materials Research Society Symposium on Ceramic Matrix Composites, Boston, MA (November 1994), invited.

MacLellan P.T., D.A. Stubbs, P. Karpur, "Evaluation of Mechanical Fatigue Damage Accumulation in Metal Matrix Composites Using Ultrasonic Surface Waves," D.O. Thompson, D.E. Chimenti, Eds., Review of Progress in QNDE, D.O. Thompson, D.E. Chimenti, Eds., *21st Annual Review of Progress in Quantitative Nondestructive Evaluation*, Vol. 14B, pp. 1319-1326, Plenum Press (1995).

Kundu T., P. Karpur, T.E. Matikas, P. Nicolaou, "Lamb Wave Mode Sensitivity to Detect Various Material Defects in Multilayered Composite Plates," *Review of Progress in Quantitative Nondestructive Evaluation*, Vol. 15, D.O. Thompson, D.E. Chimenti, Eds., Plenum, Seattle, Washington (1995).

MacLellan P.T., D.A. Stubbs, P. Karpur, "Monitoring Fatigue Damage in Metal Matrix Composites, In Situ, Using Ultrasonic Surface Waves," *Society for Experimental Mechanics*, pp. 920-928 (SEM, 1994), invited.

Martin R.W., M.J. Ruddell, J.A. Fox, P. Karpur, T.E. Matikas, "Acoustic Microscopy of Advanced Aerospace Materials," *Review of Progress in Quantitative Nondestructive Evaluation*, Vol. 15, D.O. Thompson, D.E. Chimenti, Eds., Plenum, Seattle, Washington (1995).

Matikas T.E., P. Karpur, R. Dutton, R. Kim, N.J. Pagano, "Assessment of Cracking Behavior of Glass Matrix Composites by Ultrasound," *Proceedings of the ASNT Spring Conference*, pp. 238-240, Las Vegas, Nevada (1995).

Matikas T.E., P. Karpur, S. Krishnamurthy, "Study of Elastic Behavior of Fiber-Matrix Interface Using Stress Wave Mechanics Analysis," *Proceedings of the International Conference on Composites Engineering (ICCE/1)*, pp. 331-332, New Orleans (1994).

Matikas T.E., P. Karpur, N.J. Pagano, S. Hu, L. Shaw, "In-situ Ultrasonic Characterization of Failure Strength of Fiber-Matrix Interface in Metal Matrix Composites Reinforced by SCS Series Fibers," D.O. Thompson, D.E. Chimenti, Eds., *21st Annual Review of Progress in Quantitative Nondestructive Evaluation*, Vol. 14B, pp. 1327-1332, Plenum Press (1995).

Pagano N.J., R.E. Dutton, R.Y. Kim, P. Karpur, T.E. Matikas, C. Gustafson, "Influence of The Fiber-Matrix Interface on the Micro-Cracking in Unidirectional Glass Matrix Composites," *Proceedings of the International Conference on Composites Engineering (ICCE/1)*, pp. 387-388, New Orleans (1994).

Rokhlin, I., T. Kishi, Eds., *The First US-Japan Symposium on Advances in NDT*, June 24-28, Kahuku, Hawaii, pp. 453-455, ASNT, Kahuku, Oahu, Hawaii (1996).

Shaw L.L., T.E. Matikas, P. Karpur, S. Hu, D.B. Miracle, "A Novel Method of In-Situ assessment of Fracture and Deformation of the Fiber/Matrix Interface in Metal-Matrix Composites," *Proceedings of the International Conference on Composites Engineering (ICCE/1)*, pp. 479-480, New Orleans (1994).

<u>Conference Articles – Submitted</u>

Martin, R.W., S. Sathish, T.E. Matikas, "Development of a Scan System for Rayleigh Wave Velocity Mapping," Vol. 18, *Review of Progress in Quantitative Nondestructive Evaluation*, Salt Lake City, UT (1998).

Sathish, S., R.W. Martin, T.E. Matikas, "Rayleigh Wave Velocity Mapping Using Scanning Acoustic Microscope," Vol. 18, *Review of Progress in Quantitative Nondestructive Evaluation*, Salt Lake City, UT (1998).

Mann, L.L., R.W. Martin, S. Sathish, T.E. Matikas, "Local Elastic Property Mapping via Automation of V(z) Curve Measurements in Short-Pulse Excited Acoustic Microscope," Vol. 18, *Review of Progress in Quantitative Nondestructive Evaluation*, Salt Lake City, UT (1998).

<u>Reports – Unpublished</u>

Frock, B., "MAUS III Ultrasonic Scans of Simulated Defects in a Honeycomb-Core Composite," UDR-TM-96-18, July 1996.

Frock, B., "MAUS III Resonance Scans of Impact Damage in Woven Graphite-Fiber-Reinforced Composite Samples," UDR-TM-96-21, July 1996.

Frock, B., "MAUS III Ultrasonic Scans of Impact Damage in a Multi-Directional Graphite-Epoxy Composite," UDR-TM-96-20, July 1996.

Hart, D., R.W. Martin, "Analysis of Multilayer Chip Capacitors (Lot Code 9721 Failure Analysis)," Report Number WL/MLS 96-59, Wright Laboratory, WPAFB, Ohio, June 1996.

Appendix A
Compendium of Publications

This page intentionally left blank.

An Approach to Determine the Experimental Transmitter–Receiver Geometry for the Reception of Leaky Lamb Waves

by Prasanna Karpur,* Dianne M. Benson,* Theodore E. Matikas,* Tribikram Kundu,† and Perikles D. Nicolaou‡

Abstract

Often, either the swept frequency technique or a combination of swept frequency and geometric analysis is used to produce the experimental Lamb wave dispersion data. This paper describes an approach for constructing dispersion curves in solid plates using Fourier analysis of received leaky Lamb wave signals. The Lamb waves are produced by pulsed ultrasound generated using two broad band transducers positioned in a pitch-catch orientation. The relative distances among the plate and the two transducers are set to specific values as per geometric calculations based on beam diffraction. The transducer defocus is used in conjunction with geometric calculation to determine the phase velocity of the Lamb wave mode being monitored. Subsequent to appropriate positioning of the transducers, the plate wave signals are Fourier transformed to obtain a magnitude versus frequency spectrum. Peaks in the spectrum indicate the presence of a Lamb wave root. The feasibility of this method, tested by successfully constructing dispersion curves for a steel plate, is compared with the "null zone" monitoring method of generation of the dispersion curves. The geometric positioning method is further applied to a metal matrix composite sample wherein the sensitivity of various experimentally generated Lamb wave modes is assessed to detect many types of preprogrammed defects in different layers of the composite plate.

Keywords: *composite materials, defects, Lamb waves, nondestructive evaluation, stainless steel, steel, ultrasonic testing.*

Introduction

Leaky Lamb waves are generated by ultrasonic waves that are obliquely incident on an immersed plate at frequencies that excite plate wave modes. The generation of the leaky Lamb waves leads to distortion of the reflected beam in the specular reflection region. A phase cancellation occurs when the leaky Lamb wave and the geometrically (specularly) reflected beam interfere, generating a null zone. The null zone is monitored in a swept frequency mode to generate dispersion curves in the traditional method. The sensitivity of the leaky Lamb waves to variations in elastic properties, thickness, and boundary conditions provides valuable information about the material. Theoretical studies by Kundu and Blodgett (1993), Yang (1994), and Yang and Kundu (1994a and 1994b) have shown that different Lamb wave modes produce different levels of excitation in various layers in a multilayered solid plate.

The conventional tone burst swept frequency technique is commonly used to experimentally generate Lamb wave roots. Previous efforts of using leaky waves to inspect defects in composite and metal plates include the works of Bar-Cohen and Chimenti (1985, 1986), Chimenti and Bar-Cohen (1986), Chimenti and Fiedler (1987), Chimenti and Martin (1991), Chimenti and Nayfeh (1985), Ditri and Rajana (in press), Ditri and Rose (1994), Mal and Bar-Cohen (1988), Martin and Chimenti (1987), Nagy et al. (1986), Nayfeh (1986), Pearson and Murri (1986), Rajana et al. (in press), and Rose et al. (1986), among others. In this technique, two broad band transducers are positioned in the pitch-catch orientation. The transmitter is excited by a signal function generator, which produces continuous wave forms (tone burst) and varies the signal frequency continuously between two limits (frequency sweeping). An oscilloscope screen displays the reflected signal amplitude (vertical axis) versus the frequency (horizontal axis). If a Lamb wave mode is generated for a particular angle, energy leaks through the fluid-solid interface in the form of leaky Lamb waves (Kundu and Maxfield, 1993). Destructive interference of the leaky Lamb waves with the back-surface reflection produces a null zone that is discernible as a dip (local minimum) in the amplitude-frequency plot of the reflected signal as shown in Figure 1. The corresponding phase velocity can be obtained using

$$C_{ph} = C_w / \sin \Theta \qquad (1)$$

where C_{ph} = phase velocity, C_w = longitudinal wave speed in water (1,490 m/s [4,890 ft/s]), and Θ = angle of incidence.

The null zone position changes in presence of an internal defect. Hence, when a defect is encountered, the receiver voltage amplitude is altered and the image of the defect is generated. The major problem with this arrangement is that the null zone position is very sensitive to the plate thickness. Therefore, a few percent change in the plate thickness alters the receiver voltage amplitude significantly. To avoid this problem one needs to filter the *L*-scan generated

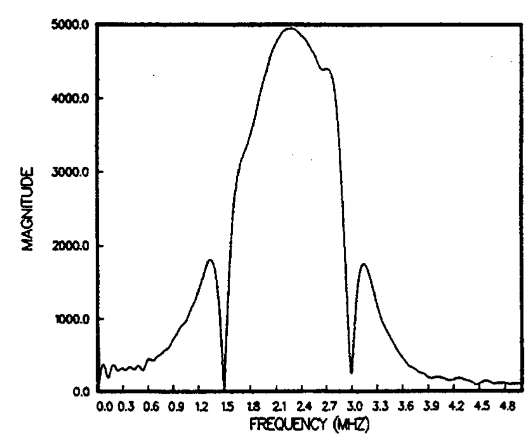

Figure 1 — Spectral nulls produced in the swept frequency "null zone monitoring" method.

* Research Institute, University of Dayton, 300 College Park Ave., Dayton, OH 45469-0127.

† Department of Civil Engineering and Engineering Mechanics, University of Arizona, Tucson, AZ 85721.

‡ Systran Corporation, 4126 Linden Ave., Dayton, OH 45432.

data through a special filter, called MFq filter (Chimenti and Martin, 1991). This signal processing helps to minimize the effect of the plate thickness variation on the null zone, but retains the sensitivity to the defects of interest. An additional problem in the null monitoring technique is that the technique is very sensitive to the relative position among the plate, the transmitter, and the receiver. However, this problem can be avoided/reduced by placing the receiver beyond the null zone as well as the specularly reflected zone of the ultrasonic beam.

This paper provides expressions to numerically calculate the positions of the transmitter and the receiver relative to the plate. Thus only propagating leaky Lamb waves are received by the receiver (similar approach with a single transducer has been reported in the literature by Nagy et al., 1986). Also, dispersion curves are experimentally generated here for a stainless steel plate and compared with the analytical curves as well as curves obtained by traditional "null monitoring" method. Further, the method is used to assess the sensitivity and selectivity of different modes to detect various preprogrammed defects in different layers of a metal matrix composite sample.

PULSE ECHO TECHNIQUE OF LEAKY LAMB WAVE GENERATION

In this technique, Lamb waves are produced by pulsed ultrasound generated using two broad band transducers positioned in a pitch-catch orientation as shown in Figure 2. The relative distances among the plate and the two transducers are set to specific values as per geometric calculations based on beam diffraction (Figure 3).

The near field distance, i.e., the distance from the transducer where the axial pressure fluctuations cease and begin to monotonically reduce, is defined by

$$N = (D^2 - \lambda^2)/4\lambda \tag{2}$$

where λ is the ultrasonic wavelength in water given by $\lambda = c/f$, c is the longitudinal velocity of sound in water (1,490 m/s [4,890 ft/s]), f is the frequency of the transducer, and D is the diameter of the transducer.

Further, half angle of the transducer is given by $\gamma = \sin^{-1}(1.2\lambda/D)$. These equations were first used to calculate the wavelength, near-field distance, and half-angle of the transducers used in this study as shown in Table 1.

Table 1 Transducer specifications (1 mm = 0.04 in)

Frequency (MHz)	Wavelength (mm)	Near-field Distance (mm)	Half-angle (degrees)
2.25	0.658	61.214	3.56
3.5	0.424	214.122	1.53

Once the values in Table 1 are calculated, the "range of validity" for positioning the receivers can be calculated using geometric considerations (Figure 3). Since the objective here is to avoid the geometric reflection completely and receive only the leaky Lamb waves, it is essential to calculate the separation distance, W, between the transmitter and the receiver given the angle of incidence, Θ, and the nearfield, N, of the transducers ($W = 2N \sin \Theta$). Initially, the plate being evaluated needs to be positioned such that the plate is at a distance of N (measured along the axis of the obliquely positioned transmitter) from the transmitter-receiver pair. In this position, the receiver will be aligned to receive only the specular reflection from the surface. The transmitter-receiver pair will now have to be moved ("defocused") towards the plate by a specific distance, Z, such that the receiver is avoiding the specularly reflected beam which is diffracting with a half angle of γ. Thus, from geometrical considerations, the defocus distance is given by

$$Z = N^*\{\cos E - [\sin \Theta/\tan (\Theta + \gamma)]\} \tag{3}$$

The defocus, Z, will now position the receiver such that it is just beyond the specular reflection region, thus avoiding the null zone completely. Hence, in this defocus configuration, W will be the minimum required distance between the transmitter and the receiver to receive only the leaky Lamb waves (Figure 4). Any position of the receiver beyond W will be suitable (Figure 5); however, increasing the distance of separation between the transmitter and the receiver will result in increased attenuation due to leakage. Thus, the positions of the transmitter, receiver, and the test sample as described in this paragraph will enable the positioning of the receiver as close to the transmitter as possible without entering the "geometric reflection zone." This will avoid the ambiguities that will occur if the receiver is improperly positioned so that the edge of the receiver is slightly encroaching on the "geometric reflection zone" (Figure 6).

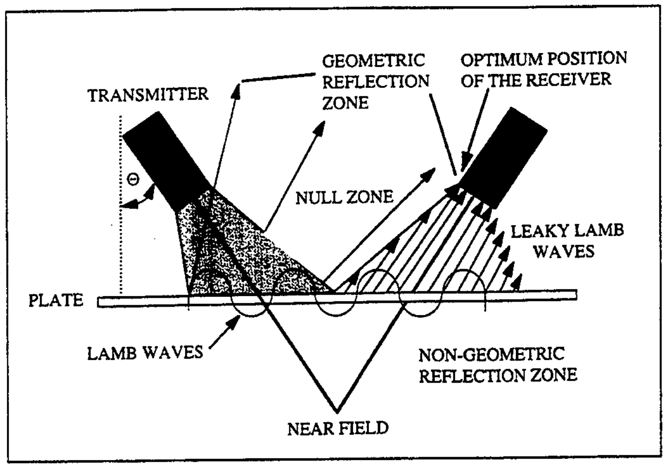

Figure 2 — Schematic of the optimum geometry for the Fourier analysis technique.

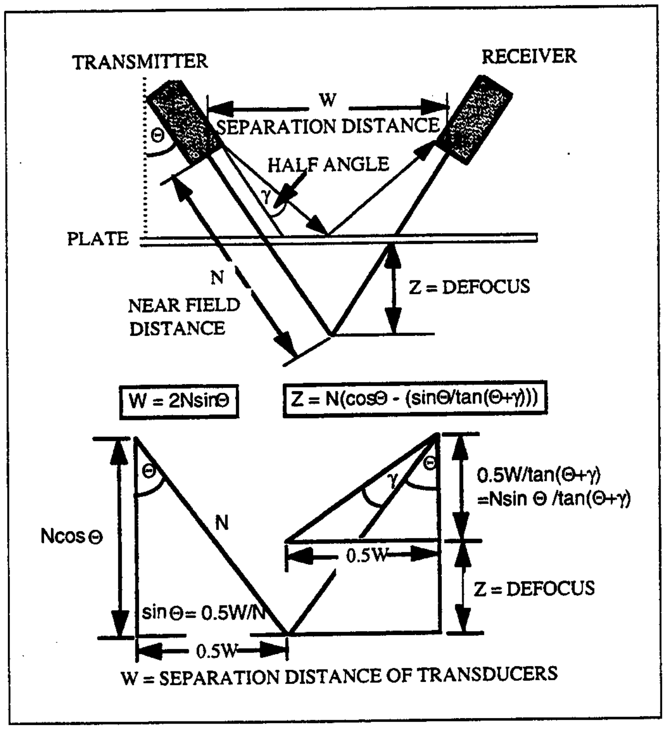

Figure 3 — Geometric considerations based on beam diffraction and nearfield calculations.

EXPERIMENTAL GENERATION OF LAMB WAVES

Conventional Swept Frequency Technique

Theoretical dispersion curves produced by Kundu and Maxfield (1993) was used (Figure 7) as the basis for these experiments. Experimental dispersion curves were constructed for a 1.6 mm (0.063

in.) thick stainless steel plate using the conventional method. One set of broad band transducers was used to generate the curves. The transducers used for the experiments were 19 mm (0.75 in.) diameter transducers of 3.5 MHz center frequency. The frequency sweeping was carried out using programmable wave form synthesizer in the interval from 1 to 5 MHz. The incident angle of the waves was changed from 10 to 22 degrees at an interval of one degree. The experimental data were plotted against theoretical data (Figure 7).

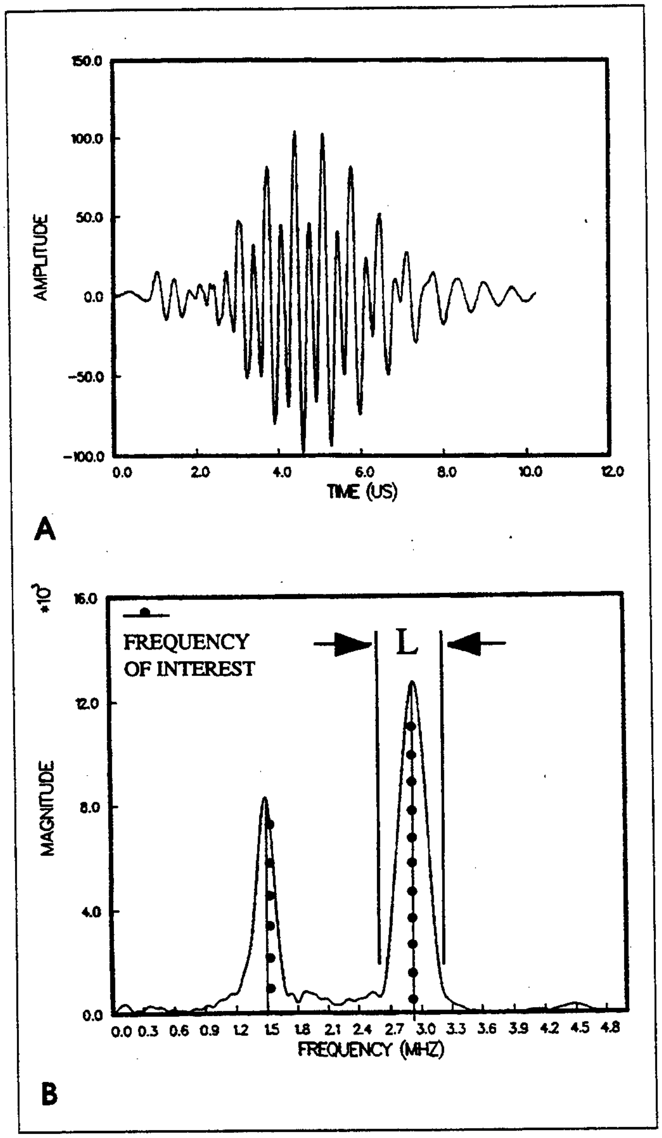

Figure 4 — (a) Received signal when the transducers are properly positioned as per the calculations shown in Figure 3. (b) Fourier analysis of the reflected (leaky) signal in the optimum position.

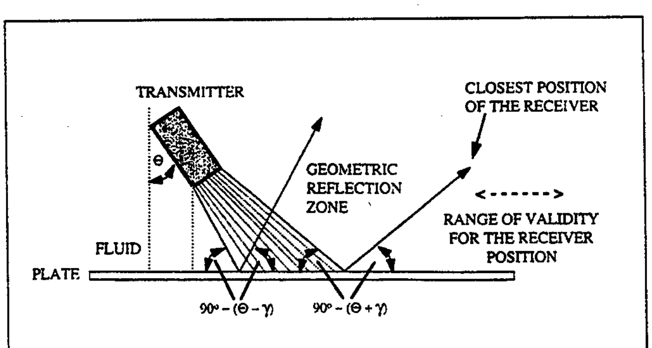

Figure 5 — Valid range of the position of the receiver for the pulse-echo Fourier technique.

Pulse Echo Fourier Analysis Technique

Two pairs (one pair of 3.5 MHz, 19 mm [0.75 in.] diameter, and the other pair of 2.25 MHz, 12.7 mm [0.5 in.] diameter) of broad band transducers were used to generate the dispersion curves for the 1.6 mm (0.063 in.) stainless steel plate. The transducers were suitably positioned and defocused as described earlier to produce a characteristic leaky Lamb wave signal similar to the one shown in Figure 4a. The plate wave signals in the nonspecular region are subsequently Fourier transformed to obtain a magnitude versus frequency spectrum (Figure 4b). In contrast to the conventional tone burst method wherein spectral nulls are produced (Figure 1), leaky Lamb wave signals are monitored here in the nonspecular region wherein frequency peaks are produced(Figure 4b). Peaks present in the spectrum indicate the presence of a Lamb wave. The phase velocity of the Lamb wave mode is calculated using geometric considerations (Figure 3). The information obtained from the transformations and calculations was then used to construct dispersion curves (Figure 7).

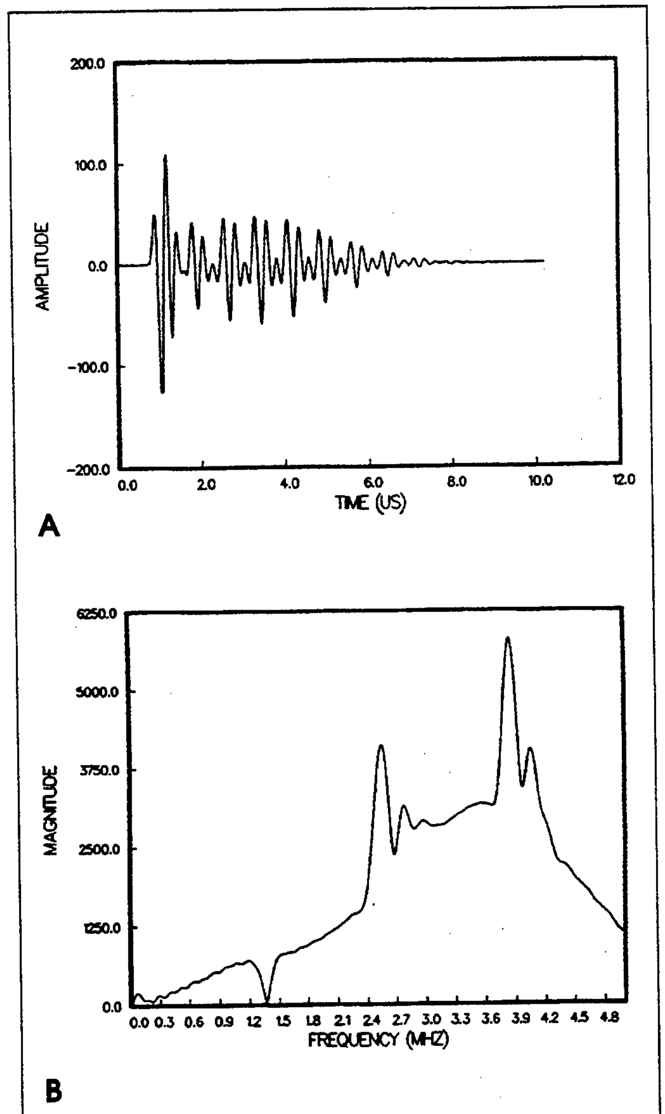

Figure 6 — (a) Received signals when the transducers are in an undesirable location bounded by both the geometric and non-geometric reflection zones. (b) Fourier analysis of the reflected (combination of specular and leaky signal shown in (a).

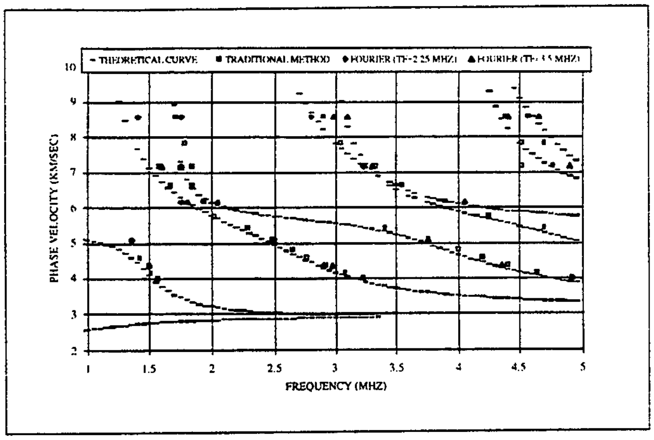

Figure 7 — Theoretical dispersion curves superimposed by experimental data generated by the two methods (frequency and pulsed Fourier techniques).

Metal Matrix Composite with Preprogrammed Defects

The sample used for this study was made (Kundu et al., 1995 and in press) with 5 layers of SCS-6 fibers in (0, 90, 0, 90, 0) lay-up configuration. The matrix material was Ti-6A1-4V. The composite was made by the foil-fiber-foil technique. The first and the fifth layers of fibers were undamaged. A part of the second layer of fibers (90 degrees) were coated with boron nitride to impede the formation of good bonding between the fibers and the matrix as schematically shown in Figure 8a. The fibers in the third layer (0 degrees) were intentionally broken as shown in the photograph in Figure 8b. The fourth layer (90 degrees) had two areas of missing fibers as shown in the photograph in Figure 8c.

The geometric positioning of the transducers was done as per the approach discussed earlier in the paper to avoid both the null zone and the specular reflection region. Frequency magnitude spectrum was used to determine the various modes propagating at each incidence (and reception) angle. Selected modes were monitored while scanning the sample and Lamb wave scans were produced as shown in Figures 9a–c.

RESULTS AND DISCUSSION

The dispersion curves generated using the conventional swept frequency and pulse-echo Fourier analysis techniques are shown in Figure 7. These experimental curves agree quite well with the theoretical dispersion curves generated by Kundu (1995 and in press). Any Lamb wave roots below 1 MHz were undetectable due to the limitations of the experimental equipment.

The pulse-echo Fourier analysis technique requires no frequency sweeping; therefore, additional equipment such as programmable waveform synthesizers, gated amplifiers, and boxcar averagers are not required, unlike the conventional method. In addition, slight changes in the vertical position of the transducers in the Fourier analysis technique does not affect the position of the peak as long as the transducer angle and experimental geometry are properly calculated. On the other hand, the minima in the reflected spectra of the null zone monitoring method are sensitive to the relative positions of the transducers and reflecting surface. Assuming a constant incident angle, slight changes in the vertical position of the transducers can cause the minima to shift on the frequency axis.

Figures 9a–c indicate selective sensitivity of different Lamb wave modes to defects in various layers. Figure 9a shows the lack of interface bonding in the second layer. The mode used for this scan was generated using 1.556 MHz at 18 degrees angle of incidence. Figure 9b shows a mode of 2.620 MHz frequency at 16 degrees angle of incidence which is sensitive to the fiber breaks in the third layer of fibers. Another mode of frequency 2.310 MHz, incident at 18 degrees angle shows sensitivity to a host of features in the plate in addition to the two areas of missing fibers in the fourth layer of the composite. Additional information on this selective detection of this composite specimen can be found in literature (Kundu et al., 1995 and in press).

SUMMARY AND CONCLUSIONS

A method for constructing dispersion curves in solid plates using Fourier analysis of received leaky Lamb wave signals was developed and tested. In addition, Lamb wave dispersion curves were experimentally constructed using a conventional tone burst frequency swept technique. The experimental curves agreed quite well with the theoretical dispersion curves generated by Kundu and Maxfield (1993). A new method for constructing dispersion curves in solid plates using Fourier analysis of received leaky Lamb wave signals has been successfully verified by constructing a dispersion curve for a stainless steel plate. An advantage of this technique is its simplicity. No special type of transducer is required. In addition, the arrangement of the experimental components is based on simple geometric calculations and beam diffraction. The data repeatability and accuracy makes this method easy to standardize for practical applications such as the identification and classification of defects and material properties.

The application of the geometric positioning of the transducer-receiver pair has been demonstrated for the evaluation

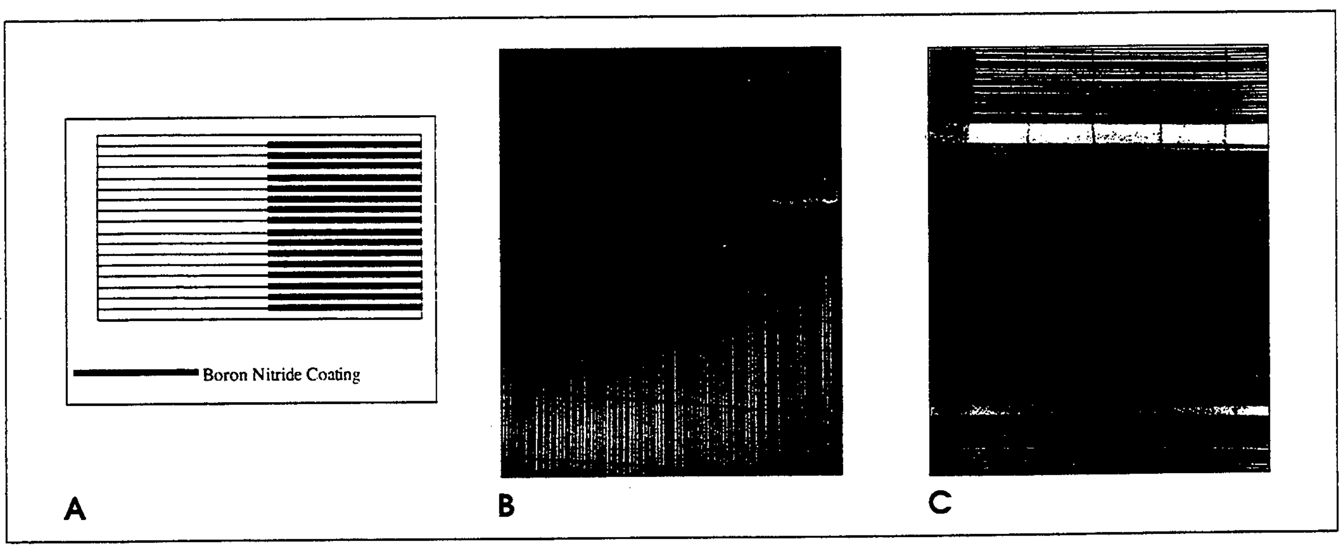

Figure 8 — (a) Schematic of the boron nitride coating of the fiber mat to induced lack of bonding at the fiber-matrix interface; (b) photograph of the fiber mat from the third layer showing the broken fibers, the distance between the neighboring cross waves is 5 mm (0.2 in.); (c) photograph of the fiber mat from the second layer showing the two areas of missing fibers.

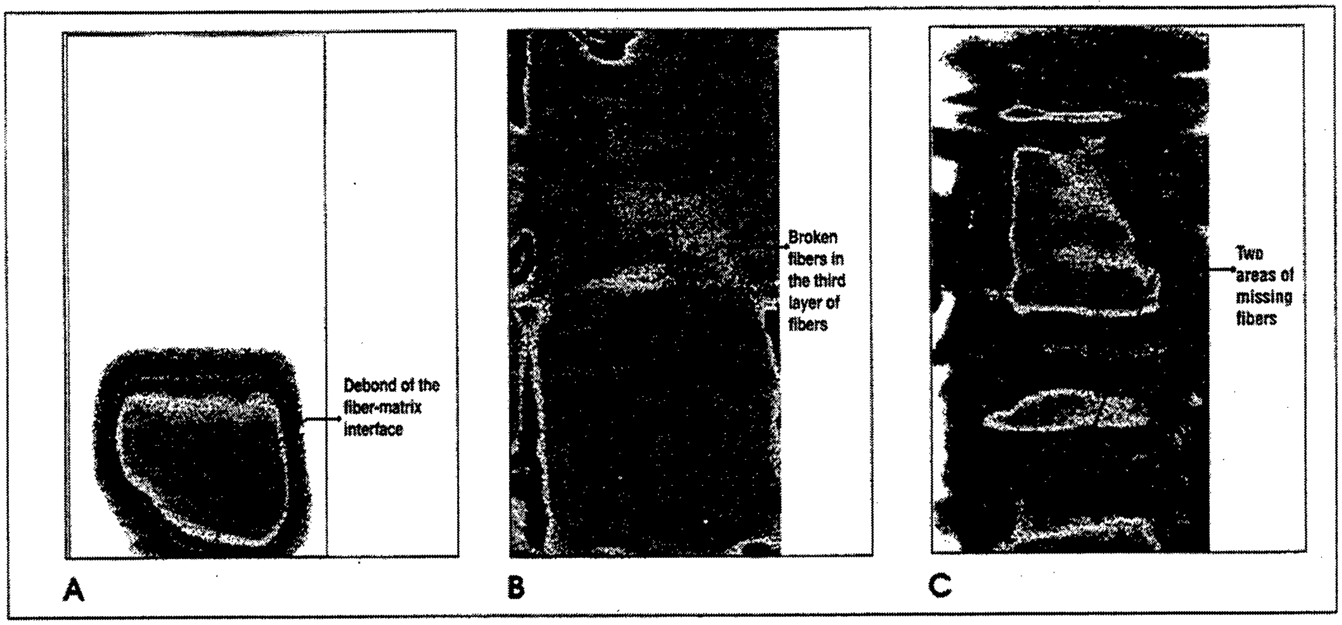

Figure 9 — (a) Lack of interface bonding in the second layer. The mode used for this scan was generated using 1.556 MHz at 18 degrees angle of incidence; (b) Lamb wave scan shows a mode of 2.62 MHz frequency at 16 degrees angle of incidence which is sensitive to the fiber breaks in the third layer of fibers; (c) a mode of frequency 2.31 MHz, incident at an 18 degree angle, shows sensitivity to a host of features in the plate in addition to the two areas of missing fibers in the second layer of the composite.

of selective sensitivity of Lamb wave modes to defects in various layers of a metal matrix composite.

Acknowledgments

This work was supported by and performed on-site in the Materials Directorate, Wright Laboratory, Wright-Patterson Air Force Base, Ohio 45433. Contract No. F33615-94-C-5213. Partial support (Dianne Benson) provided by AFOSR Grant No. F49620-93-1-0461 (Program Manager: Walter F. Jones).

References

Bar-Cohen, Y., and D.E. Chimenti, "NDE of Defects in Composites Using Leaky Lamb Waves," in *Proceedings of the 15th Symposium on Nondestructive Evaluation,* 1985, pp 202–208. Southwest Research Institute, San Antonio, TX.

Bar-Cohen, Y., and D.E. Chimenti, "Nondestructive Evaluation of Composites by Leaky Lamb Waves," *Review of Progress in Quantitative Nondestructive Evaluation, Vol. 5,* 1986, pp 1199–1206, ed. by D.O. Thompson and D.E. Chimenti. Plenum Press, New York, NY.

Chimenti, D.E., and Y. Bar-Cohen, "Signal Analysis of Leaky Lamb Wave Spectra for NDE of Composites," *Proceedings of 1985 IEEE Ultrasonic Symposium,* 1986, p 1028–1031, ed. by B.R. McAvoy. IEEE, New York, NY.

Chimenti, D.E., and C.J. Fiedler, "Leaky Plate Waves for NDE of Composites," in *Ceramic Engineering and Science Proceedings,* Vol. 8, 1987, pp 538–546. 11th Annual Conference on Composites and Advanced Ceramic Materials, Cocoa Beach, Florida, 18–23 Jan. 1987. American Ceramic Society, Westerville, OH.

Chimenti, D.E., and R.W. Martin, "Nondestructive Evaluation of Composite Laminates by Leaky Lamb Waves," *Ultrasonics,* Vol. 29, 1991, pp 13–21.

Chimenti, D.E., and A.H. Nayfeh, "Leaky Lamb Waves in Fibrous Composite Laminates," *Journal of Applied Physics,* Vol. 58, 1985, pp 4531–4538.

Ditri, J.J., and J.L. Rose, "Excitation of Guided Waves in Generally Anisotropic Layers Using Finite Sources," *ASME Journal of Applied Mechanics,* Vol. 61, No. 2, 1994, pp 330—338.

Kundu T., P. Karpur, T.E. Matikas, and P.D. Nicolaou, "Lamb Wave Scanning to Detect Material Defects in Multilayered Composite Plates," accepted for publication in *Ultrasonics,* Butterworth Publishers, United Kingdom.

Kundu T., P. Karpur., T.E. Matikas, and D. Nicolaou, "Lamb Wave Mode Sensitivity to Detect Various Material Defects in Multilayered Composite Plates," to be presented at the 22nd Annual Review of Progress in Quantitative Nondestructive Evaluation, Seattle, Washington, Jul. 30–Aug. 4, 1995.

Kundu, T., and M. Blodgett, "Detection of Material Defects in Layered Solids Using Lamb Waves," *Review of Progress in Quantitative Nondestructive Evaluation,* Vol. 13, 1993, p.1343–1350, ed. by D.O. Thompson and D.E. Chimenti. Plenum Press, New York, NY.

Kundu, T., and B. Maxfield, "A New Technique for Measuring Raleigh and Lamb Wave Speeds," *Journal of the Acoustical Society of America,* Vol. 93, Jun. 1993, pp 3066–3073.

Mal, A.R., and Y. Bar-Cohen, "Ultrasonic Characterization of Composite Laminates," *Wave Propagation in Structural Composites,* AMD Vol. 90, 1988, pp 1–16, ed. by A.R. Mal and T.C.T. Ting. ASME, New York, NY.

Martin, R.W., and D.E. Chimenti, "Signal Processing of Leaky Lamb Wave Data for Defect Imaging in Composite Laminates," *Review of Progress in Quantitative Nondestructive Evaluation, Vol. 7,* 1987, pp 815–824, ed. by D.O. Thompson and D.E. Chimenti. Plenum Press, New York, NY.

Nagy, P.B., W.R. Rose, and L. Adler, "A Single Transducer Broadband Technique for Leaky Lamb Wave Detection," *Review of Progress in Quantitative Nondestructive Evaluation,* Vol. 5, 1986, pp 483–490, ed. by D.O. Thompson and D.E. Chimenti. Plenum Press, New York, NY.

Nayfeh, A.U., "Acoustic Wave Reflection from Water-Laminated Composite Interfaces," *Review of Progress in Quantitative Nondestructive Evaluation,* Vol. 5, 1986, pp 1119–1128, ed. by D.O. Thompson and D.E. Chimenti. Plenum Press, New York, NY.

Pearson, L.H., and W.J. Murri, "Measurement of Ultrasonic Wavespeeds in Off-Axis Directions of Composite Materials," *Review of Progress in Quantitative Nondestructive Evaluation,* Vol. 5, 1986, pp 1093–1101, ed. by D.O. Thompson and D.E. Chimenti. Plenum Press, New York, NY.

Rajana, K.M., and J.J. Ditri, "Analysis of the Wedge Method of Generating Guided Waves," *Review of Progress in Quantitative Nondestructive Evaluation,* Vol. 14, pp 163–170, ed. by D.O. Thompson and D.E. Chimenti. Plenum Press, New York, NY.

Rajana, K.M., D. Hongergolt, J.J. Ditri, and J.L. Rose, "Analysis of the Wedge Method of Generating Guided Waves: An Experimental Approach," *Review of Progress in Quantitative Nondestructive Evaluation,* Vol. 14, pp 171–180, ed. by D.O. Thompson and D.E. Chimenti. Plenum Press, New York, NY.

Rose, W.R., S.I. Rokhlin, and L. Adler, "Evaluation of Anisotropic Properties of Graphite-Epoxy Composites Using Lamb Waves," *Review of Progress in Quantitative Nondestructive Evaluation,* Vol. 5, 1986, pp 1111–1117, ed. by D.O. Thompson and D.E. Chimenti. Plenum Press, New York, NY.

Yang, W., "Elastic Wave Propagation in Multilayered Anisotropic Plates and Its Potential Application in Non Destructive Testings," PhD Dissertation, 1994, Department of Civil Engineering and Engineering Mechanics, University of Arizona, Tucson, AZ.

Yang, W., and T. Kundu, "Efficient Use of Lamb Waves to Characterize Multilayered Anisotropic Plates," paper presented at ASME Winter Annual Meeting, Chicago, IL, Nov. 1994.

Yang, W., and T. Kundu, "Lamb Wave Propagation in Multilayered Anisotropic Solids and Its Applications Towards Imaging Material Defects," Proceedings of the 21st International Symposium on Acoustical Imaging, Laguna Beach, CA, 1994.

This page intentionally left blank.

ASSESSMENT OF SINGLE FIBER FRAGMENTATION USING SCANNING ACOUSTIC MICROSCOPY

Shamachary Sathish

Research Institute, University of Dayton

300 College Park, Dayton OH 45469 - 0127

Madhu S. Madhukar

Department of Mechanical and Engineering and Engineering Sciences

University of Tennessee, Knoxville, TN 37996 - 2030

John H. Cantrell and William T. Yost

NASA Langley Research Center

Mail Stop #231, Hampton, VA 23681-2199

This page intentionally left blank.

ABSTRACT

Scanning acoustic microscopy (SAM) is used to obtain the critical fragmentation length of a 7μm diameter carbon fiber embedded in an optically transparent epoxy matrix and subjected to a standard fiber fragmentation test. The SAM-assessed critical fragmentation length of (356 ± 59.5) μm compares favorably with the value (341 ± 52.3) μm obtained independently from commonly used photoelastic techniques. Additionally, the SAM images allow an assessment of regions of fiber-matrix debond, including the measurement of an average debond of (61.0 ± 11.8) μm along the fiber from the fragment ends, that cannot be obtained with photoelastic methods. The application of SAM to the assessment of optically opaque composite materials is pointed out.

This page intentionally left blank.

I. INTRODUCTION

High performance fibers are commonly used as reinforcements in polymers, metals and ceramics to produce high strength, high modulus, low density composite materials. The mechanical properties of the composite materials have been found to depend not only on the composite constituents but also on the properties of the interface/interphase region between the fiber and the matrix [1,2,3]. It is also known that the interface/interphase region in large measure determines the load transfer characteristics from the matrix to the fiber, the transfer of load from the broken fibers to the surviving fibers, and greatly affects the overall mechanical properties of the composite [1,2,3]. It is thus important to understand and measure the properties of the interface/interphase region in order to help tailor or "engineer" the performance of the composite materials. One of the parameters that is often used to quantify the properties of the fiber matrix interface is the interfacial shear strength (IFSS).

Several direct and indirect measurement techniques have been developed in the last three decades to determine the IFFS. The interlaminar shear strength, the transverse shear strength, and the flexural strength of full-scale composites have been found to have an indirect relation to the interfacial shear strength. Some of the well-established techniques for the direct measurement of IFSS are fiber pull out [4], shear debond [4,5], microindentation [6], and fiber fragmentation [7] tests. These tests provide quantitative measurements of IFFS that are dependent on the sample geometry and the model of the stress field around the fiber. The single fiber fragmentation test is generally believed to have stress transfer characteristics that are similar to that of full-scale composites. This attribute, together with the simplicity of the technique, have contributed to the increasing popularity of the single-fiber fragmentation test for assessing IFSS.

In the fiber fragmentation test a single fiber embedded in a matrix in the shape of a dog-bone is axially loaded in tension. As the tensile load is increased the fiber fractures when the axial stress transferred to the fiber by the interfacial shear exceeds the fracture strength s_f of the fiber. A further increase in the axial stress on the specimen results in successive fragmentation until the fragmented fiber lengths become so short that the shear stress transfer along their lengths can no longer build up sufficiently large tensile stresses to cause further fiber breaks. The final fragmentation length is called the critical length L_c. If the matrix is assumed to be perfectly plastic then the average interfacial shear strength τ can be obtained from the simple balance of force

$$\tau = \frac{\;}{2L_c} \tag{1}$$

where d is the diameter of the fiber.

The determination of the critical length L_c in fragmentation tests are usually obtained using photoelastic techniques[1] to identify the positions of the fiber cracks. Photoelastic techniques, however, must be used in optically transparent materials and are subject to measurement uncertainties in determining the critical length of fibers having fibriluar structures [8,9]. In a recent effort to overcome these limitations, an acoustic emission-based technique[10] has been proposed to assess critical fiber lengths. This technique utilizes the acoustic waves generated by the breaking fibers by placing transducers at various locations on the sample surface to detect the waves. The transducer arrangement is used in a triangulation procedure to determine the position of the break from the arrival times of the crack-generated acoustic signal and knowledge of the velocity of sound in the matrix. Acoustic emission techniques have been applied to a variety of composites. For those composites having optically transparent matrices good correlation has been obtained with photoelastic measurements[10]. However, a major

difficulty with the acoustic emission technique is the development of a suitable signal amplitude threshold criterion to isolate acoustic emission signals due to fiber breakage from signals due to other sources. Another difficulty is that the thickness of composite specimens are often comparable to the wavelength of sound in the material at acoustic emission frequencies. This can result in the generation of plate mode vibrations that travel with velocities that are complex combinations of longitudinal and shear waves in the matrix. Such a situation complicates the determination of critical length from the wave arrival times.

In another effort to observe the fiber fragmentation in optically non transparent materials shear back reflected ultrasonic waves technique[11] has been used. This technique has been used to assess the fragmentation of large diameter 142 μm SCS-6 fibers in a titanium matrix. Although fiber fragmentation was observed having a reasonable correlation with an acoustic emission-based assessment of the fiber break points, an unequivocal determination of the fragmentation length (of the order of microns) was obscured by the low resolution of the acoustic images (of the order of hundreds of microns)[12]. Moreover, as the fragments become smaller the image interpretation, as well as a clear identification of the breaks, become more difficult due to the presence of several fragments within the diameter of the acoustic beam.

In order to overcome the limitations associated with both acoustic emission-based techniques and low resolution ultrasonic scanning methods, we have developed a methodology using the scanning acoustic microscopy (SAM) to directly image the fiber, assess the fiber fragmentation, and accurately determine the critical fragmentation length in composites.

II. EXPERIMENTAL PROCEDURE

A. Sample preparation

Composite test samples having a single 7 μm diameter carbon fiber centered along the axis of a dog-bone shaped, optically transparent matrix were prepared in a manner described elsewhere[13]. Two samples (Sample A and Sample B) having a gauge length of 30mm, a width of 4mm, and a thickness of 2mm were prepared for study. Optically transparent epoxy matrix material was chosen so that photoelastic measurements of fiber fragmentation could be directly compared to those obtained from SAM.

Sample thickness and surface topography are generally not critical concerns for photoelastic observations. However, for scanning acoustic microscopy contrast due to wave scattering from rough surfaces can result in "noisy" images and large distances between the sample surface and the imaged object within the sample could restrict image depth, if the acoustic attenuation in the matrix is sufficiently large. To avoid such problems both samples were carefully lapped and polished in a special jig designed for dogbone shaped specimens to decrease both surface topography and sample thickness. A 9 μm diamond paste was used for the final polishing. Following the photoelastic measurements of sample A, one of the sides of the sample was lapped and polished to a thickness of approximately 200 μm between the surface of the matrix and the embedded carbon fiber. Sample B was symmetrically polished on both sides in order to keep the carbon fiber centered in the sample. The final thickness of sample B was approximately 400 μm, leaving an approximately 200 μm distance between the carbon fiber and either sample surface.

B. Fiber fragmentation test

Sample A was placed in the grips of a load frame equipped with a load cell for direct measurement of the applied load. Fiber fragmentation resulting from an increasing load was observed using the photoelastic experimental set-up. The sample was then unloaded and the SAM images of the fiber fragmentation were obtained. An ELSAM scanning acoustic microscope with a 200 MHz lens was used to obtain the acoustic images. At this frequency the surface resolution of the microscope is better than 8 μm. A drop of distilled water was used between the sample and the lens to couple the acoustic waves to the sample. The distance between the lens and the sample was reduced to focus the acoustic waves at the interface between the fiber and the matrix. Acoustic images covering a 1μm x 1μm area of the sample were acquired.

Sample B was used to obtain SAM images, while the sample is under load, of fiber fragmentation resulting from the applied load. The grips of the load frame used in photoelastic measurements were modified to accommodate the thinner sample. The load frame was then attached to the specimen stage of the SAM and adjusted such that the acoustic lens was focused on the fiber. Since the scan length of the acoustic lens (1 mm) was smaller than the gauge length of the fiber, it was necessary to obtain overlapping acoustic images along the gauge length to form a composite image field encompassing the whole fiber. Such a composite image field was obtained for each incremental increase in load.

C. Fiber fragmentation micrographs

a. Photoelastic images

Typical photoelastic images of the fiber fragmentation in Sample A are shown in Fig.1. Fiber breaks are observed from optical birefringence effects resulting from anisotropic stresses produced as the sample is loaded. A bright spot away from the fiber,

resulting from a trapped air bubble or pore formed during the consolidation of the composite, also appears in the image near the break number six. The bubble was used as a reference point in comparing the photoelastic and SAM images. The initial fiber break in this sample was detected at a load of approximately 40 MPa.. Several subsequent breaks were observed from which an average critical fragmentation length is calculated using the average measurements of seven fragments (eight breaks).

b. SAM images

Fig. 2a and Fig. 2b show SAM images of the fiber fragmentation from the same general region of sample A as that of the photoelastic image in Fig.1. Since the area covered in Fig 1. could not be imaged in SAM in a single scan, two images are presented. Contrary to the requirements of photoelastic imaging, it is not necessary in SAM to load the sample to detect fiber breaks. This is because the image contrast mechanism in SAM is quite different from that of photoelastic imaging. SAM contrast depends on the variation in the acoustic impedance along the fiber length. When the acoustic lens is positioned over the fiber break, the acoustic waves propagating through the matrix encounter a void resulting from fiber separation at the fiber break. The change in the acoustic impedance is relatively large and the phase of the incident wave undergoes a 180° phase shift upon reflection. In addition, if the fiber and matrix are debonded in a region on either side of the fiber separation region, a similarly large change in the acoustic impedance would be encountered by the incident acoustic wave with a correspondingly large phase shift upon reflection. This is especially true, if the sample loading produces fiber-matrix sliding that results in a decorrelation of initially matching fiber and matrix geometries. Hence, the crack region (defined here as the region of fiber break and separation plus a possible debonded region on either side of the region of fiber separation) appears very bright in the SAM image.

When the acoustic lens scans a region where the fiber is present and intact with the matrix, the acoustic waves propagating through the matrix encounter relatively smaller changes in the acoustic impedance and phase. Much of the acoustic energy is thus transmitted through the interface and a relatively smaller amount is reflected back to the lens. This makes the intact fiber-matrix region appear much darker than the break region in the SAM image. The pore or the trapped air bubble, used as a marker, produces a large change in acoustic impedance and phase similar to that of the fiber break region and thus appears as a bright spot in the SAM image.

A one-to-one correspondence in the locations of the fiber cracks and the matrix bubble is found from the photoelastic image of Fig.1 and the SAM images of Fig.2a and Fig. 2b. We note that the width of the fiber crack region appears smaller in the photoelastic image than in the SAM image. A likely explanation is the appearance of a fiber-matrix debond region on either side of the region of fiber separation. Such a region would appear in the SAM image but not in the photoelastic image for reasons related to the acoustic impedance as stated above. A slight difference in contrast is observed in SAM images of Crack 5 region in Fig. 2a and Fig. 2b. This is possibly due to a small tilt in the specimen or slight inclination of the fiber to the front surface introduced during specimen polishing.

c. Edge diffraction effects

An important feature in the SAM image is the appearance of multiple bright spots in the region of the fiber cracks. These bright spots result from the diffraction of the acoustic waves in the region of the fiber cracks and may be nominally explained in terms of edge diffraction effects.

Consider a typical edge diffraction pattern generated by a sound wave of unit intensity normally incident along the positive z direction onto a planar, sound absorbing object with a well defined edge[14]. We assume that the object occupies the $z = 0$ plane for all $x \bullet > 0$. We define the diffraction parameter $X = (k/\pi z)^{1/2}x$. The sound amplitude detected at some positive distance z beyond the planar object rises monotonically from a zero value for positive z and large negative X. At $X = 0$ (the edge of the object) the relative intensity is approximately 1/4. At large, positive values of X the relative intensity oscillates as $\{1 - 2^{1/2}(\pi X)^{-1}\cos[(\pi/2)X^2 + \pi/4]\}$. Thus, the maximum amplitude occurs at a distance of approximately $X = (3\lambda z/4)^{1/2}$ from the edge of the object. Thereafter, the amplitude oscillates with decreasing amplitude as the distance from the edge increases.

With the above model in mind we now assume that the fiber and matrix are intact up to an edge of the crack region. The acoustic wave reflected at such an edge changes phase by 180° in passing from the region where the fiber and matrix are intact to a region where the fibers are either separated or debonded from the matrix. The waves subsequently received by the transducer from these regions may be viewed as that of two waves, 180° out of phase, each contributing to the net edge diffraction pattern from the broken fiber end. If we assume that the two waves have roughly equal amplitudes, then we would expect that the superposed diffraction patterns would result in an absolute amplitude minimum (square root of intensity) at the edge of the crack region and relative absolute amplitude maxima on either side of this minimum.

However, the reflected acoustic wave amplitudes are not equal, since the acoustic impedances of the crack region and the intact fiber region are not equal. This results in a slight shift (which we neglect in the present experiments) of the position of the diffraction absolute amplitude minimum into the bonded fiber region and reduces the

amplitude of the diffraction oscillations in that region. A typical diffraction pattern obtained from a broken fiber is illustrated in the amplitude line scan of Fig.3, which shows the amplitude of the received acoustic signal as a function position along the axis of the fiber. The larger amplitude diffraction oscillations are evident in the crack region. The two amplitude minima in the line scan correspond in reasonable approximation to the edges of the fiber crack region. In the SAM image of Fig.2 these amplitude minima correspond to the dark areas between the maxima (bright spots) in the crack region and the bonded fiber region (appearing as a continuous bright line).

In addition to the crack regions there also appear in Fig.2 a series of single bright spots between fiber breaks four and five. Intensity nulls at corresponding positions in the photoelastic image are also evident. Since these single bright spots in the SAM image resemble the diffraction pattern of smaller fiber break regions, their appearance could lead to some confusion in assessing the critical fiber length. In order to determine the origin of these diffraction patterns we mounted sample B on the SAM stage with an attached load frame and followed the process of fiber fragmentation during the entire loading process from the virgin state to fiber breakage. SAM images of sample B obtained with loads less than 15 MPa showed a uniform fiber matrix interface without any features. As the load was increased to roughly 15 MPa features similar to the breaks (bright spots of roughly 20μm in length) appeared at several locations simultaneously in the SAM images. Previous photoelastic measurements indicate that the first fiber break occurs at a load of 40 MPa and that only one break occurs at a given load level. A load of 15 MPa is much too low to produce a single fiber break and is impossible to produce multiple breaks. We thus conclude that the features observed in the SAM images are not due to fiber breaks, but most likely result from fiber/matrix debonding.

The edges of the debonded regions interrupting the bonded segment between the crack regions generate edge diffraction patterns similar to that of the crack regions. However, these relatively shorter debond regions generally produce fewer diffraction maxima (individual bright spots) in the SAM image than do the crack regions. Assuming that the edges of the debond region correspond to acoustic intensity minima, we obtain from Fig.2 that the lengths of the fiber debond regions are of the order of 15 - 20 μm.

III. RESULTS AND CONCLUSION

Table I shows a comparison between the photoelastic measurements of fiber fragment lengths in sample A and the corresponding measurements using SAM. The lengths of Seven fiber fragments were measured from eight breaks in the gauge portion of the sample. Column one gives the fiber fragment designation and column two in the table lists the fragmentation length measurements obtained from the photoelastic images. The fragment lengths were estimated from measurements of the distance between the middle of two successive fiber cracks (breaks plus separations) defining the ends of the fiber fragment (see Fig.1). Measurements from the middle of the cracks are used because at the low magnifications used in the photoelastic images the middle of the cracks are easier to ascertain than the "fuzzy" ends of the fiber fragments. The average fiber segment length calculated from the photoelastic measurements is (341 ± 52.3) μm.

The cracks at the fragment ends are not readily apparent in the SAM images because of the possibility of fiber-matrix debond along the fiber from the fragment ends. However, an estimate of the fiber fragment lengths can be obtained by measuring the distance between the middle of two successive diffraction patterns associated with the crack regions. If the fiber debond regions associated with the breaks are symmetrical about the fiber cracks, then the SAM measurements of individual fiber fragment lengths

would be expected to give values identical to that of the photoelastic measurements. Differences between the photoelasic and SAM measurements of individual fiber fragments can be attributed largely to asymmetry in the debond regions. The difference between the average fragment lengths obtained from the photoelastic and SAM measurements is expected to decrease as the number of successive fiber fragments included in the average is increased.

Column three of Table I lists the SAM measurements of the fragment lengths. The photoelastic and SAM values for individual fragment lengths generally agree to within 9%. The average fragment length determined from the SAM measurements is (356 ± 59.5) μm. This value is approximately 4 percent larger than that determined by the photoelastic measurements. However, the difference between the photoelastic and SAM measurements in all cases is considerably less than the variation (~15%) in the measured lengths of the fragments themselves. In this context the agreement between the photoelastic and SAM measurements is seen to be quite acceptable.

Column four of Table I provides an SAM assessment of the length of fiber between crack regions in the fiber fragments. These lengths are obtained from measurements of the minima in the diffraction patterns associated with the edges of the crack regions. They are thus measurements of fragment length minus the length of debond along the fiber from the fragment ends. The average distance between crack regions is calculated to be (295 ± 53.0) μm as indicated in column four of the table. The total length of fiber/matrix debond along the fiber from the ends of a given fragment is calculated by substracting the entry in column four of Table I for that fragment from the corresponding entry in column three. The average total debond length from the ends of the fragments is calculated from these data to be (61.0 ± 11.8) μm.

Finally, the overall agreement between the photoelastic and SAM assessments of critical fiber fragmentation lengths establishes SAM as a quantitative tool for assessing the results of fiber fragmentation tests. The capability of SAM to render such measurements in opaque materials and the ability to observe and quantify the occurrence of fiber-matrix debonds make scanning acoustic microscopy an attractive alternative for the assessment of interfacial shear stress in composite materials.

ACKNOWLEDGEMENTS

One of the authors (S.S.) acknowledges the financial support for the research by a NASA grant to the University of Tennessee and High Speed Research Program, NASA Langley Research Center. He also acknowledges the financial support by NDE Branch, AFRL, Materials and Manufacturing Directorate, Wright-Patterson Air Force Base, Ohio, through contract F33615-94-C-5213.

This page intentionally left blank.

REFERENCES

1. L. T. Drzal, M. J. Rich, and P. F. Lloyd J. Adhes., **16**, 1, (1982).
2. P. Herrera, W. L. Wu, M. S. Madhukar and L. T. Drzal, " Contemporary methods for the Measurement of fiber-matrix interfacial shear strength" 46 Annual conference, composite institute, The Society of the Plastics industry, Inc (1991).
3. M. Narkis, E. J. H. Chen, and R. B. Pipes, Poly. Compos., **9**, 245 (1988).
4. L. J. Broutman "Measurement of the fiber-polymer matrix interfacial strength" in Interfaces in Composites STP 452, American Society for Testing and Materials, Philadelphia 1969) p 27 - 41.
5. H. M. Hawthorne and E. Teghtsoonian, J. Adhesion **6**, 85 (1974).
6. J. F. Mandel, J. H. Chen and F. J. McGarry, Intl. J. Adhesion and Adhesives, **1**, 40(1980).
7. A. Kelly and W. R. Tyson, J. Mech. Phys. Solids. **13**, 329 (1965).
8. A. N. Netravali, Z.-F. Li W. Sachse and H. F. Wu, J. Materl. Sci. **26**, 6631 (1991).
9. L. T. Drzal, 15th National SAMPE Tech. Conf., 1983, p. 190.
10. A. N. Netravali, L. T. T. Topoleski, W. Sachse and S. L. Phoenix Compos. Sci. Tech. **35**, 13 (1989).
11. P. Karpur, T. Matikas and S. Krishnamurthy., "Matrix-fiber interface characterization in metal matrix composites using ultrasonic imaging of fiber fragmentation" in American Society for Composites, Pennsylvania State University, University Park, PA, 1992, pp 420.
12. M. C. Waterbury, P. Karpur, T. E. Matikas, S. Krishnamurthy and D. B. Miracle., Compos. Sci. Techn. **52**, 261 (1994).
13. M. S. Madhukar, R. P. Kosuri and K. J. Bowles., "Reduction of curing induced fiber stresses by curing cycle optimization in polymer matrix composites" in Proc. ICCM-10, Vol.III, pp 157, Ed. A. Poursartip and K. Street, The Tenth International

Conference on Composite Materials Society, Vancouver, Canada and Woodhead Publishing Ltd, Cambridge, England, (1995).

14. Allan D. Pierce, *Acoustics: An Introduction to Its Physical Principles and Applications* (Acoustical Society of America, Woodbury, 1989).

Table I. Comparison of photoelastic and SAM measurements of fiber fragmentation lengths of seven fragments. SAM measurements of distance between fiber crack regions.

Fragment Designation	Fragment Length (Photoelastic meas.) (μm)	Fragment Length (SAM meas.) (μm)	Distance Between Crack Regions (SAM) (μm)
L7	372	409	356
L6	308	294	245
L5	315	331	274
L4	392	409	327
L3	408	417	344
L2	328	360	303
L1	261	270	213
Average Value	(341 ± 52.3)	(356 ± 59.5)	(295 ± 53.0)

FIGURE CAPTIONS

Figure 1.	Photo-Elastic image of fiber fragmentation (Sample A)
Figure 2a. and Figure 2b.	Scanning Acoustic Microscopic images of fiber fragmentation in Sample A (region same as shown in Figure 1)
Figure 3.	Amplitude line scan of the acoustic diffraction pattern from a broken fiber end in the single fiber composite

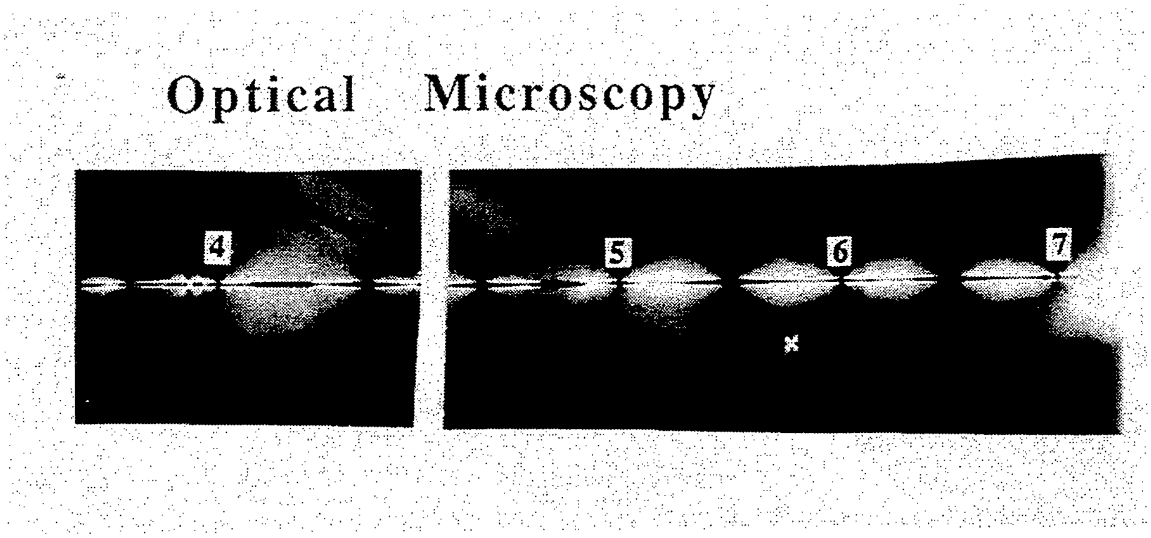

Figure 1.

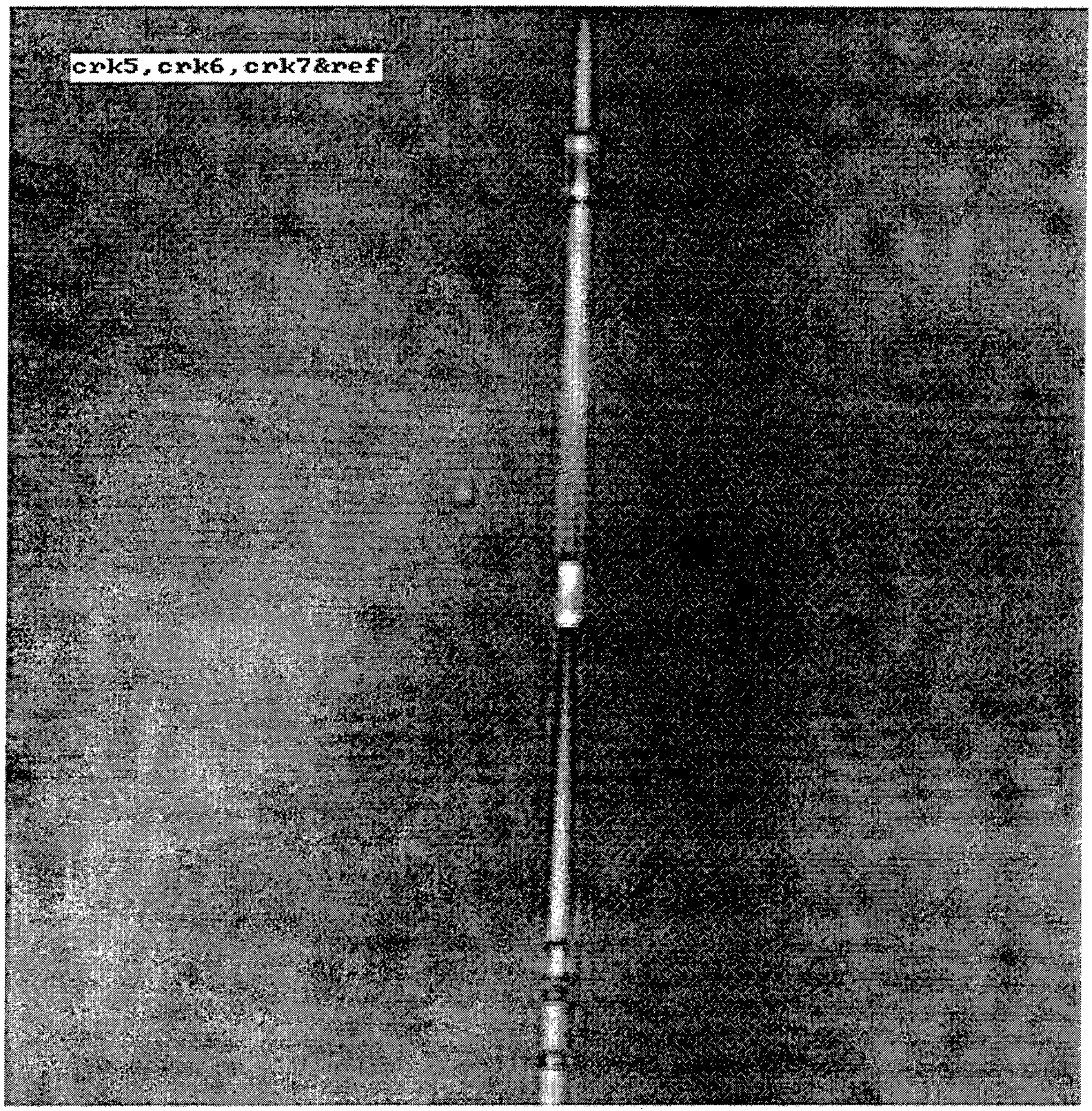

Figure 2a.

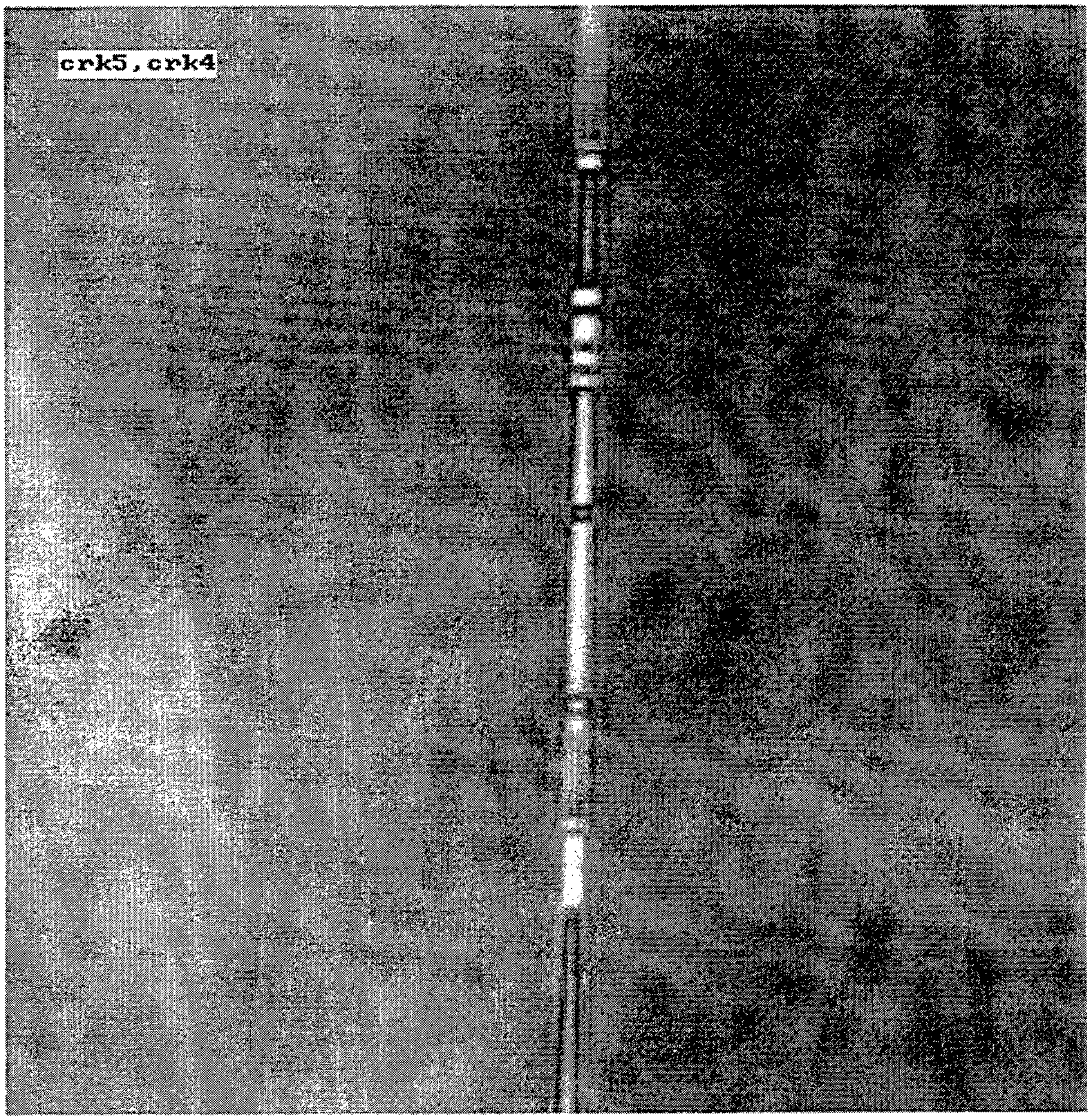

Figure 2b.

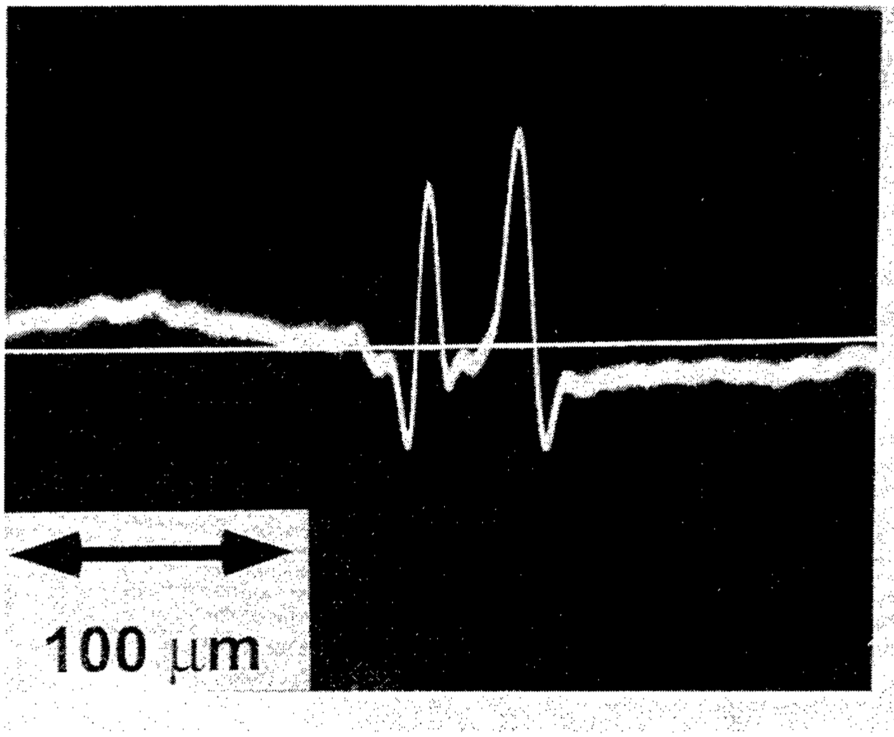

Figure 3.

DEVELOPMENT OF A SCAN SYSTEM FOR RAYLEIGH WAVE VELOCITY MAPPING

Richard W. Martin, Shamachary Sathish and Theodore E. Matikas
University of Dayton Research Institute
300 College Park Drive
Dayton Ohio 45469-0127

INTRODUCTION

A velocity map contains more quantitative information than an amplitude image because Rayleigh wave velocity is related to the elastic constants of the material.

A high-precision scanning acoustic microscope system has been developed by the University of Dayton Research Institute with the capability to generate Rayleigh wave velocity map images of aerospace materials. The velocity map is presented in a C-scan format in order to visualize the velocity distribution in a material or around a defect. Rayleigh wave velocity is measured using a time-of-flight (TOF) technique. This system utilizes impulse excitation in order to separate the direct reflected signal and the Rayleigh wave signal in the time domain. Time differences between these signals at two defocus depths are used to calculate Rayleigh wave velocity in real-time and display a 2D x/y velocity map image during the scan. Velocity measurement accuracy is demonstrated to be better than 1%. Software techniques that were developed to improve time measurement accuracy will be quantitatively compared with the velocity in standard materials. Both measurement accuracy and standard deviation of experimental data are used as the basis of comparison for each investigated technique. Techniques discussed include improved peak detection, signal averaging requirements, digitization rate, and software gate placement. C-scan images of Rayleigh wave velocity maps of several materials will be presented. [1][2]

THEORY

The time-of-flight (TOF) technique of measuring Rayleigh wave velocity on the surface of a specimen is an alternative to the more often used V(z) curve technique. The TOF technique is much faster and therefore a better choice when a hundred thousand velocity measurements are being collected in a raster scanning mode. This technique collects TOF measurements at only two different defocus locations of the transducer.

In order to utilize the TOF technique a very short impulse excitation must be provided to the transducer so that the direct reflection from the surface and the signal from the Rayleigh wave may be separated in time.

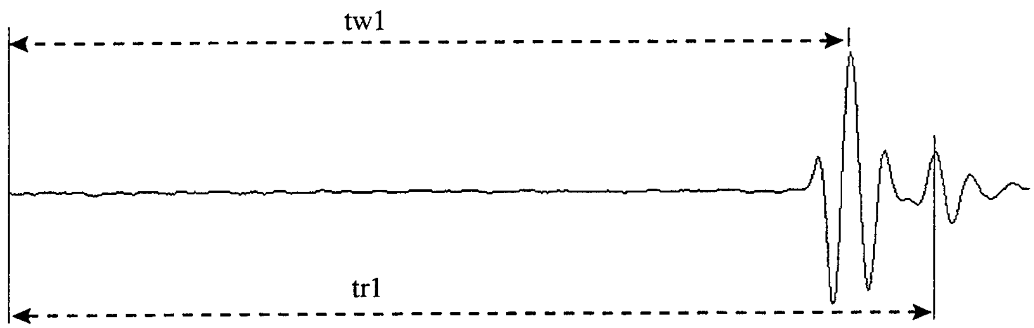

(a) Z1 Defocus 0.4mm

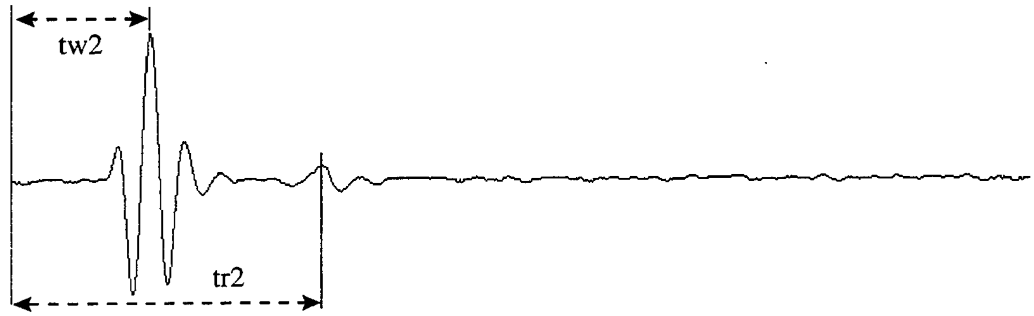

(b) Z2 Defocus 1.0 mm

Figure 1. Time domain waveforms collected at (a) Z1 with transducer defocused 0.4mm and (b) Z2 with transducer defocused 1.0 mm. Each waveform is 2 microseconds in length.

The first defocus location is named Z1. The transducer must be defocused to a point where the direct reflection and the Rayleigh wave separate in the time domain. In most materials this is usually a defocus of 0.4mm to 0.6 mm. A peak detection algorithm is utilized to measure the TOF to the location in time of the direct reflection (tw1) and the Rayleigh wave (tr1). An oscilloscope plot of the waveform at location Z1 is shown in Figure 1(a).

The second defocus position is named Z2 and its location is more arbitrary, but generally a greater defocus distance improves velocity measurement accuracy. In most cases Z2 should be an additional defocus distance of 0.4mm to 0.6mm from the initial defocus position Z1. This results in Z2 having a total defocus distance of 0.8mm to 1.2mm. A peak detection algorithm measures the TOF to the location in time of the direct reflection (tw2) and the Rayleigh wave (tr2). An oscilloscope plot of the waveform at location Z2 is shown in Figure 1(b).

The Rayleigh wave velocity (Vr) is calculated using the equation:

$$Vr = 2\,(Z2 - Z1) \,/\, \left((tw1 - tw2)^2 - (tr1 - tr2)^2 \right)^{1/2} \qquad (1)$$

where the units of Z1 and Z2 are in meters and the time measurements are in units of seconds.

LIMITATIONS OF RAYLEIGH WAVE TOF VELOCITY MEASUREMENT

The accuracy limitations of the velocity measurement were examined by inputting into the Rayleigh velocity equation (1) typical values of tw1, tr1, tw2, tr2, Z1 and Z2 from the experimental data. These values yielded a Rayleigh velocity of 3033 m/sec from timing measurements determined on a specimen of polished E6 glass. Then the various time measurements were in-

creased and/or decreased by an amount equal to the time measurement errors inherent to our digitizer. Since the digitizing rate is 2 Gsps (0.5 ns time interval between samples) the four timing measurements were altered by all combinations of +/- 0.5 ns. Although the complete table of all possible combinations for 0.5 ns errors for each timing measurement is not listed here, there are significant velocity changes caused by these very small differences in timing. Errors ranged from +/- 2 m/sec to +/- 15 m/sec (+/- 1/2 % error). Since our goal is to measure Rayleigh velocity to better than 1% accuracy, errors of a few nanoseconds would be unacceptable. This characteristic is why enhanced peak detection and extensive averaging is required to reduce TOF errors.

EFFECTS OF DATA COLLECTION PARAMETERS ON RAYLEIGH WAVE VELOCITY DATA SCATTER

The effects of several data collection parameters upon velocity accuracy and repeatability were determined by collecting 100 measurements each at a single location on a specimen of polished E6 glass. These parameters are: (1) different Z1 defocus depths, (2) Z-axis scan step size (Z2 - Z1), (3) effects of averaging A-scans, (4) effects of repeating, sorting and averaging velocity measurements, and (5) effects of enhanced peak detection. For each test a single parameter was varied while all other parameters were kept at our "standard conditions". The standard conditions for all tests were:

1. 50 MHz transducer, 0.2" fl. And 0.25" diameter.
2. Each A-scan is 4096 points in length and digitized at a rate of 2 Gsps (0.5 ns sample interval).
3. Each A-scan averaged 25 times.
4. Starting (Z1) defocus depth is 0.6 mm.
5. Ending (Z2) defocus depth is 1.2 mm (Z-axis step size of 0.6 mm).
6. Enhanced peak detection, shifted gate and data sorting algorithms enabled.

The basis for judging repeatability is the value of the 1 standard deviation error of each 100 measurements. The 1 standard deviation value is shown on the following plots as error bars. The basis for judging the velocity accuracy is the Rayleigh wave velocity of 3026 +/- 4 m/sec as measured by Sathish et al. [3] on the same specimen of E6 glass by using the V(z) curve technique. The value of 3026 m/sec is shown as a dashed line on each of the plots in Figure 2..

Variations of the data collection parameters are presented in Figure 2 and yield the following conclusions: Figure 2(a) indicates that the best repeatability (lowest standard deviation) is achieved with the least initial defocusing possible (0.4 mm). With the least defocus possible signal amplitudes are higher and therefore the peak is more accurately detected. The initial Z1 defocus depth had no real effect on accuracy since all average velocities were within 7 m/sec of each other. Figure 2(b) indicates that the greatest possible Z-axis step size (Z2-Z1) of 0.6mm results in the best accuracy and repeatability. The reason is that the resulting longer tr2 time reduces the percentage of error in the measurement. However increasing the step size beyond 0.6 mm resulted in errors due to insufficient signal amplitude. Figure 2(c) shows clearly that averaging A-scans in order to reduce noise improves both accuracy and repeatability. Figure 2(d) indicates that repeating the Z-axis scan at each point several times and then sorting and averaging velocities improves accuracy and repeatability significantly only up to 4 repetitions. Sorting and averaging will be discussed later. Figure 2(e) clearly shows the benefits of using an enhanced peak detection algorithm for both improved accuracy and repeatability.

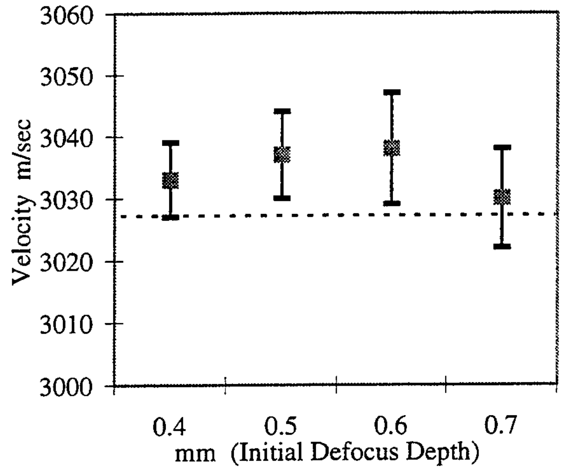

(a) Effect of Z1 initial defocus depths

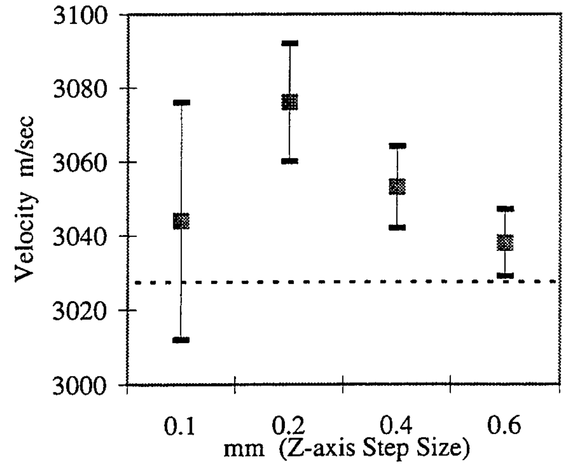

(b) Effect of Z-axis Step Size (Z2-Z1)

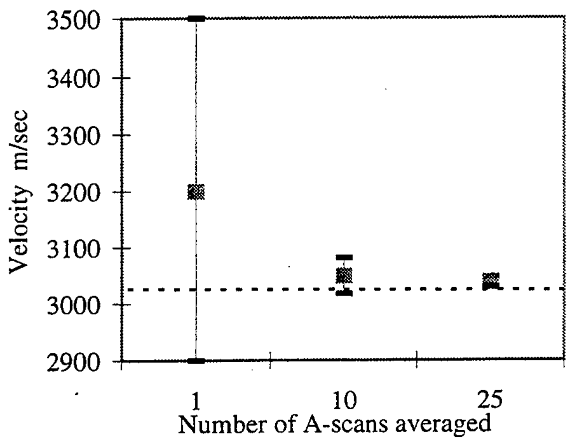

(c) Effect of Averaging A-scans

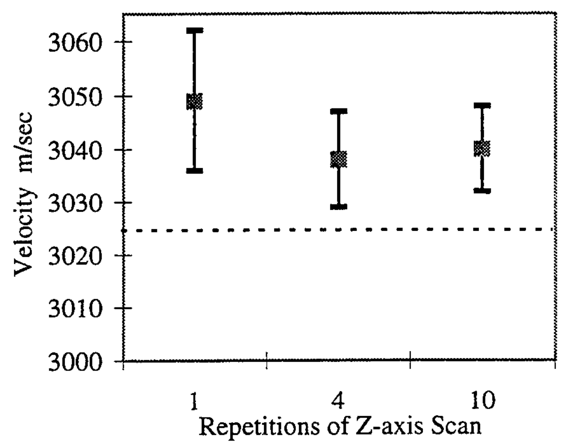

(d) Effect of Repeating & Sorting Scans

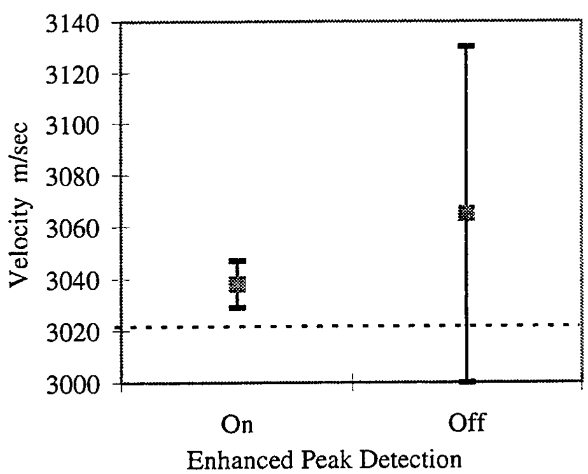

(e) Effect of using Enhanced Peak Detection

Figure 2. Effects of data collection parameters on scatter of Rayleigh wave velocity data. Each data point represents the result of 100 velocity measurements at the same location.

DATA SORTING ALGORITHM

Experimentation with our system indicates that occasional computed velocity errors are consistently values that are extremely high (> 100 m/sec errors). These errors are due to noise, peak detection and system triggering. Therefore, each Z-axis scan is repeated 4 times and the 4 velocities sorted in ascending order. The 3 lowest values are averaged to arrive at the final velocity. The highest velocity is always omitted. This is especially important on scans of titanium or other noisy or highly attenuative material.

ENHANCED PEAK DETECTION ALGORITHM

Because velocity errors are introduced by very small timing differences in the TOF measurements, an enhanced peak detection algorithm was developed. The old algorithm detected only the first occurrence of the highest (or lowest) peak value within a defined software gate. This method was insufficient because the Rayleigh wave peak is usually flat. That is, the peak consists of several successive data points of the same value. Also, noise levels of +/- 1 data bit on the peak cause the peak's shape to become distorted. The 8-bit resolution of the digitizer combined with low Rayleigh wave amplitudes and low frequencies (compared to the digitizing rate) cause these problems.

The new algorithm finds the first occurrence of the highest (or lowest) amplitude on a peak, and then it searches ahead up to 9 data sample points to find the last occurrence of the same value. The position in time of these two locations are then averaged to estimate the location in time of the actual peak. This method overcomes the problems associated with flat-topped peaks and distorted peaks as shown in Figure 3.

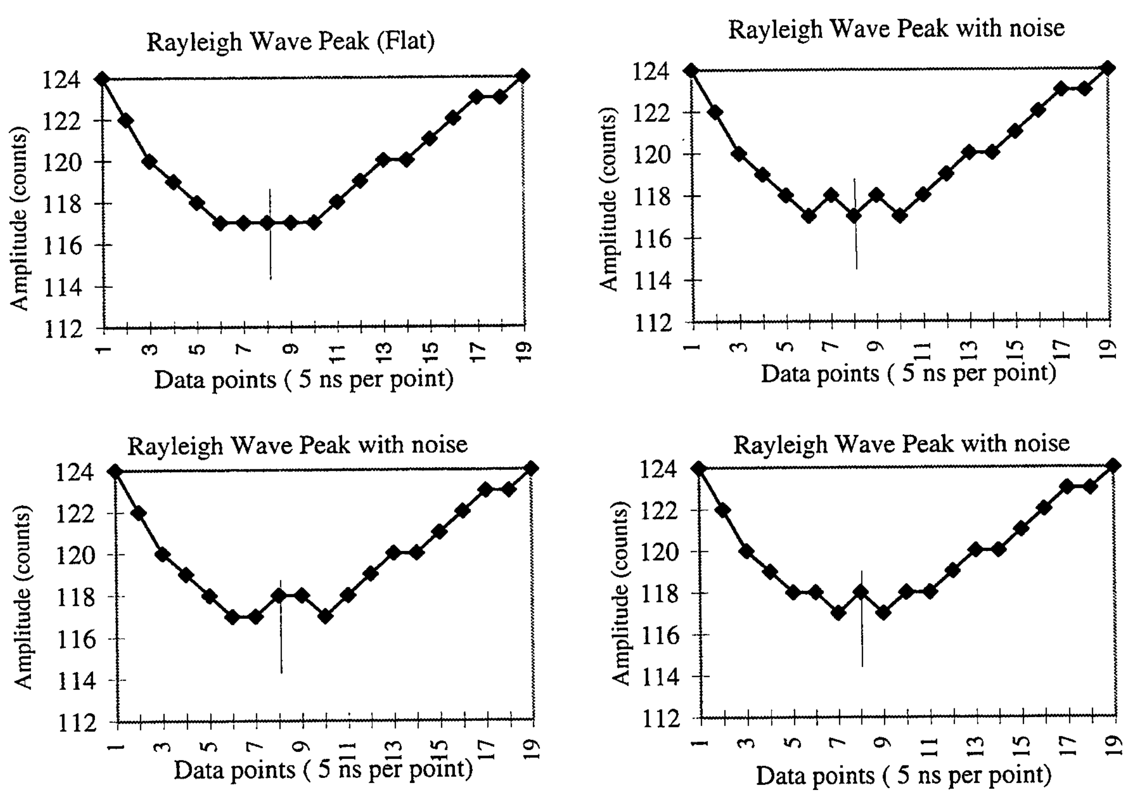

Figure 3. Enhanced peak detection finds the same peak location in time in all 4 examples. The vertical line indicates the peak location on these data plots of a negative-going peak.

RAYLEIGH WAVE VELOCITY MAPS

Each of the following images of Rayleigh wave velocity maps and Rayleigh wave amplitude images are of the same 9 mm X 9 mm area on a specimen of Ti-6Al-4V material. This particular specimen has very large colonies of grains with many of them about 2mm in length. All data was collected at 50 MHz at the "standard conditions" previously mentioned. Each image is a 256 X 256 data point C-scan using a spatial step size of 35 microns. The amplitude C-scan is 8-bit data while the velocity maps are 16-bit velocity data in units of m/sec stored in a C-scan format. This data was collected using the High Precision Scanning Acoustic Microscope (HIPSAM) system developed at the Air Force AFRL/MLLP branch laboratories at WPAFB, Ohio.

The first image, presented in Figure 4, is a Rayleigh wave peak-to-peak amplitude C-scan and not a velocity map. This image represents a standard acoustic microscopy image of the colonies in this specimen. Many large colonies and their boundaries can be seen and large areas have nearly the same Rayleigh wave amplitude. The transducer was defocused 0.6 mm and a software gate placed on the Rayleigh wave portion of the waveform in order to collect this image. This image should be used to compare with the following Rayleigh wave velocity map images. The grey scale in this image represents amplitude with black indicating the highest amplitude levels and white the lowest amplitudes.

The next 3 Rayleigh wave velocity map images are presented to illustrate several improvements to the to the data collection system. Figure 5 is a Rayleigh wave velocity map of the same area shown in the previous figure. In the grey scale image white represents high velocities and black lower velocities. This velocity scan was collected without using the "shifted gate option which we developed. The image is covered with undesirable black and white speckles. The titanium material has high attenuation and is acoustically noisy. Therefore the Rayleigh wave is of low amplitude at the Z2 defocus location and in high noise. The direct reflection echo on the surface also has a longer ring at the Z2 defocus and some of its waves enter the Rayleigh wave's software gate. These factors cause errors in locating the true Rayleigh wave peak location and cause noise in the image. This situation did not occur on the E6 glass specimen. The problem was solved by having the software shift the starting location of the software gate away from the direct reflection at location Z2 by an amount equal to ¼ of the time value of (tr2 - tw2) - (tr1 - tw1).

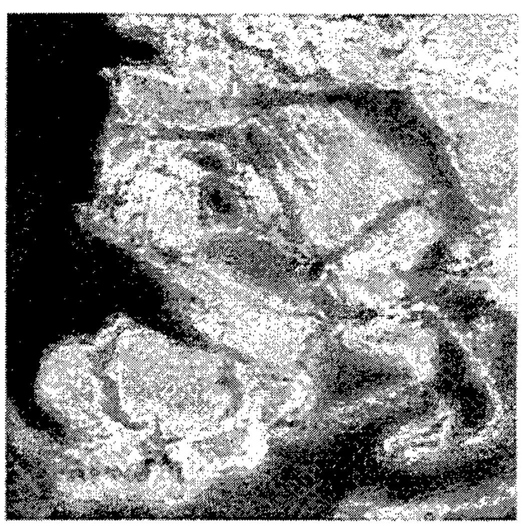

Figure 4. Rayleigh wave peak amplitude C-scan of a 9mm X 9mm area on a Ti-6Al-4V plate. Black indicates the highest amplitudes and white the lowest amplitudes.

Figure 6 is a Rayleigh wave velocity map image that employed the "shifted gate feature and eliminated the speckles. However this image did not employ the data sorting algorithm which was previously described. Therefore system timing errors caused the Rayleigh velocity data to be inconsistent across and near the boundaries of colonies.

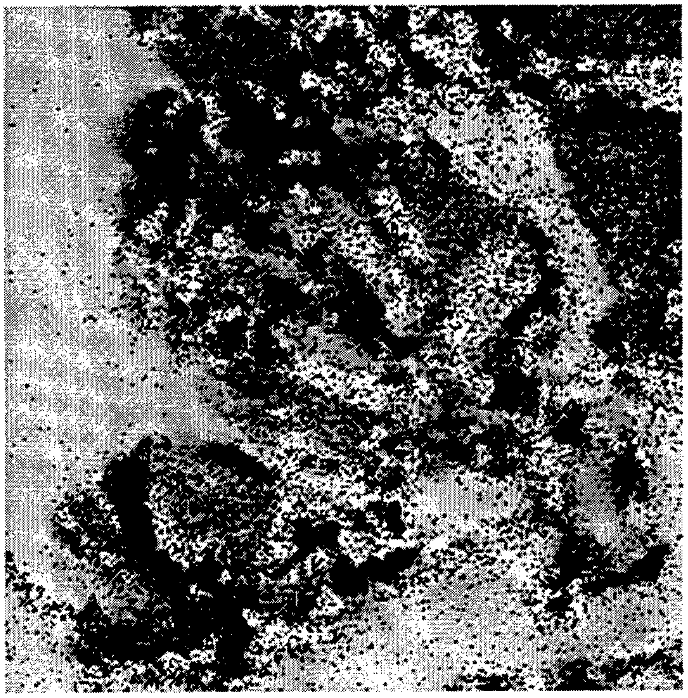

Figure 5. Rayleigh wave velocity map generated without the "shifted gate" feature.

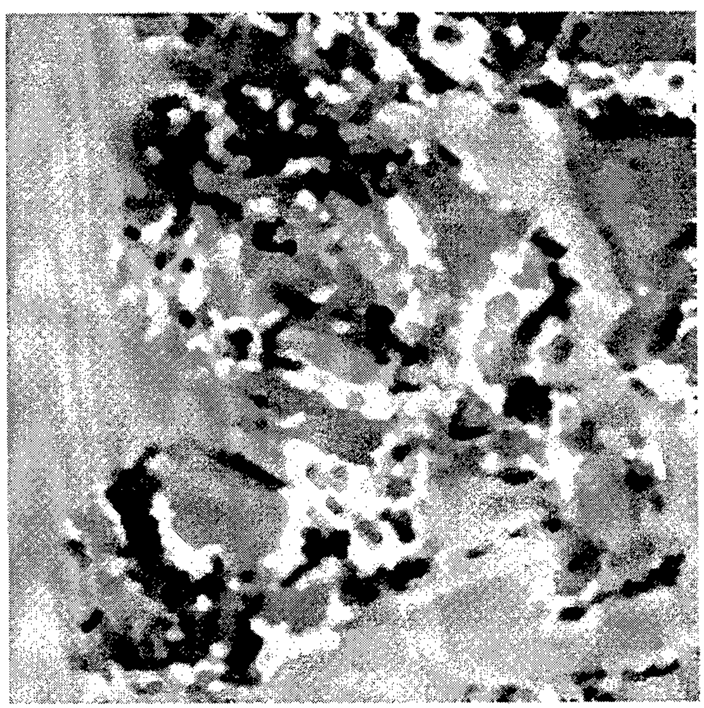

Figure 6. Rayleigh wave velocity map using the "shifted gate feature but not using the data sorting algorithm. The velocity of grain colonies are not clearly defined in many cases.

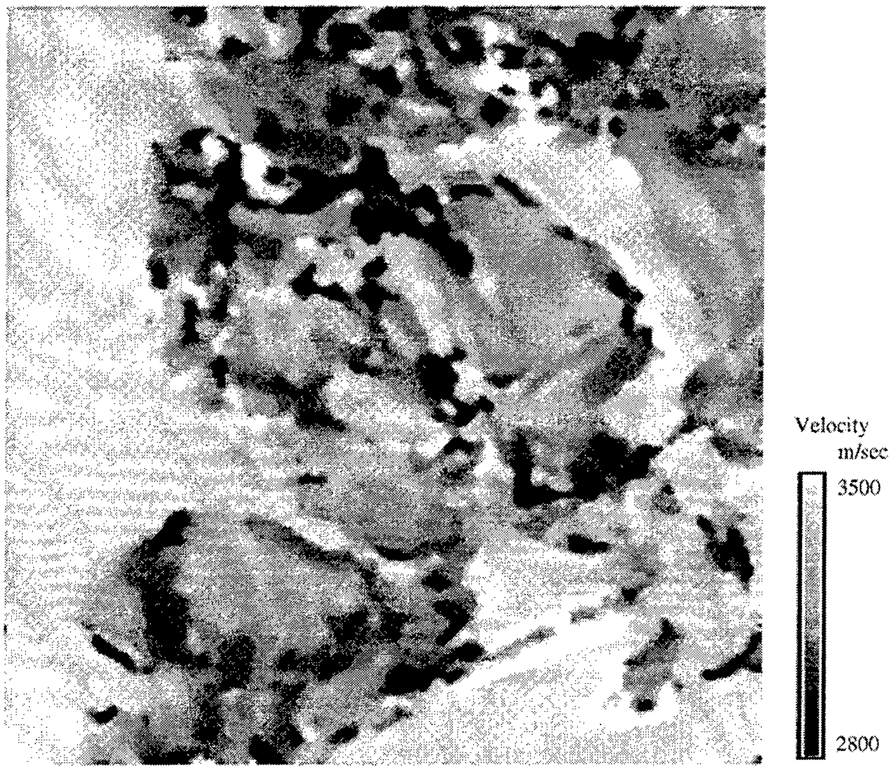

Figure 7. Final Rayleigh wave velocity map of colonies of grains in titanium. Rayleigh velocities of each colony of grains are defined. Velocities are indicated by the grey scale.

Figure 7 is a Rayleigh wave velocity map which utilized all the features of the acoustic microscope's Rayleigh wave velocity TOF data collection system. Rayleigh velocities are consistent across colonies. Velocities differ between colonies because of the orientation of the grains of each colony. The velocities are in error only near the colony boundaries where the acoustic beam overlaps multiple colonies. The Rayleigh wave velocity is related to the elastic constants of the material.

CONCLUSIONS

Rayleigh wave velocity mapping has been shown to be a valuable tool in indicating the orientation of colonies of grains in titanium. Velocity has been measured to better than 1% accuracy. A velocity map contains more quantitative information than an amplitude image because Rayleigh wave velocity is related to the elastic constants of the material.

ACKNOWLEDGEMENTS

This work was sponsored and performed on-site at the NDE Branch of the AFRL Materials and Manufacturing Directorate at Wright-Patterson Air Force Base, Ohio.

REFERENCES

1. R. S. Gilmore, R. A. Hewes, L. J. Thomas and J. D. Young, " Broadband Acoustic Microscopy: Scanned Images with Amplitude and Velocity Information, *Acoustical Imaging*, ed. H. Shimizu, N. Chubachi and J. Kushibiki, Vol. 17, 1988
2. A. M. Sinton, A. D. Briggs and Y. Tikahara, "Time resolved acoustic microscopy of polymer coatings",*Acoustical Imaging*, *op. cit.* ,Vol. 17, 1988
3. Sathish et al., *Journal of Acoustic Society Of America*, Vol. 98, 1995, p. 2854

MAUS III -- ULTRASONIC RESONANCE OPERATING CHARACTERISTICS

SUMMARY

Survey data were acquired to determine some of the basic characteristics of the MAUS III ultrasonic resonance system. The term "survey data" is used here to mean that data collection experiments were not statistically designed to test specific hypotheses. Rather, the data will be used to form hypotheses which can be tested at a later date with data from designed experiments. The major findings of this survey effort are:

(1) systematic errors in the output values (amplitude and phase) remain after the null voltages are removed from the peak-detected signal values,

(2) measured *amplitude and phase output versus gain setting response curves* for constant inputs are nonlinear,

(3) under certain operating conditions the measured outputs (amplitude and phase) decrease as the gain settings are increased, and

(4) considerable scatter exists in the phase output values at higher gain settings, i.e., the standard deviation of the scatter appears to increase with increasing gain settings. It does, however, appear to be possible to minimize the scatter by careful selection of the operating frequency.

BASICS

According to the developers (McDonnell Douglas) of the MAUS III system, ultrasonic resonance measurements are measurements of the mechanical impedance of the transducer as it is loaded by the structure with which it is in contact. The electronics of the MAUS III measure the mechanical impedance of the transducer while a relatively low-frequency continuous acoustic wave is being transmitted into the structure. The amplitude and phase components of the mechanical impedance are provided to the user as the system outputs.

TUNING AND NULLING

McDonnell Douglas recommends that a tuning and nulling procedure be followed prior to scanning in the resonance mode. The basics of the tuning and nulling procedure are outlined in the following paragraphs.

Tuning is performed to guide the user in the selection of the appropriate operating frequency. During tuning, the MAUS electronics generate the amplitude versus frequency response curve of the transducer for its particular loading condition, and determine the frequency for which the amplitude is at a minimum. This is accomplished by sweeping the frequency through a range of values and measuring the amplitude as a function of frequency during the sweep. The minimum of the response curve is the "tune" frequency. **The displayed amplitude-versus-frequency-response curve is inverted so that the "tune" frequency appears as a maximum in the curve (Fig. 1).**

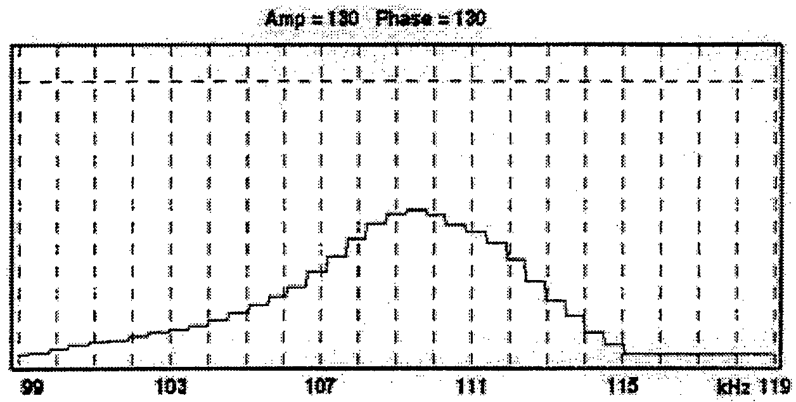

FIGURE 1
Typical amplitude versus frequency curve for ultrasonic resonance technique

Nulling is performed to establish reference amplitude and phase levels for data collection and storage. When the system is nulled, the MAUS measures the voltage at a single, specified operating frequency (the tuning frequency unless the operator specifies otherwise). This voltage is referred to as the null-offset voltage.

SCANNING OPERATION

During the scanning operation the amplitude value which is displayed and stored by the MAUS results from the following four-step process:

(1) first, the signal is peak detected (sampled and held) at the operating frequency (often the tune and null frequency);

(2) second, the null-offset voltage (from the nulling operation) is subtracted from the peak-detected signal value which results from the application of step 1;

(3) third, the selected gain is applied to the residual signal which results from the application of step 2; and finally

(4) the data value is converted to an 8-bit count (0 to 255) and the **DATA OFFSET** value (64, 128, or 192) is added to the data value.

It is the result of step four that is displayed to the user and which is stored and used for image generation during C-scanning. The phase value is generated in an analogous manner.

The **DATA OFFSET** value should not be confused with the null-voltage offset. The **DATA OFFSET** is user selected as Low (64 counts), Medium (128 counts) and High (192 counts) and is intended to improve the image display by preventing saturation where possible.

DATA COLLECTION -- GENERAL

All data were collected from a marked region of a 29.21 cm (11.5 in.) long by 7 cm (2.75 in.) wide by 12.7 cm thick (0.5 in.) quasi-isotropic graphite-epoxy composite sample. The marked region was sprayed with water – which served as the couplant – and a 110 kHz transducer was placed on the water-wetted area. Tuning, nulling and operation (data collection) were accomplished with the transducer mounted onto the sample in the manner shown in figure 2.

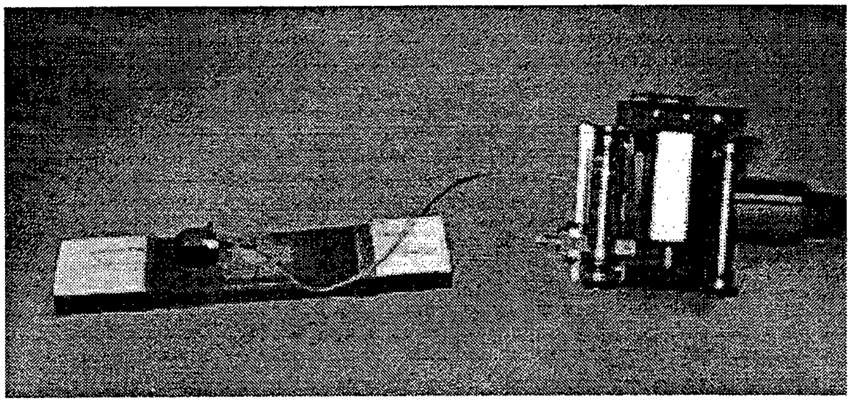

FIGURE 2
Sample and transducer configuration for all data collection

DATA COLLECTION AND RESULTS – MEASURED AMPLITUDE VS AMPLITUDE SETTING

Data offset survey. For this study the output amplitude value was collected as a function of the amplitude setting at each of the three different data offset values – low, middle and high. The system was nulled and operated at the "tune" frequency, 109,500 Hz. The frequency, Probe Drive %, Amplitude and Phase settings used during tuning, nulling and data collection are shown in table 1. A plot of the data are shown in figure 3.

Table 1 – MAUS System Parameter Values for Measured Amplitude VS Amplitude Settings, Three Levels of Data Offset

Tune Settings	Null Settings	Operating Settings
Freq at 109,500	Freq = 109,500	Freq = 109,500
Probe (%) = 50	Probe (%) = 50	Probe (%) = 50
Amp = 30	Amp = 30	Amp = Varied
Phase = 20	Phase = 20	Phase = 20

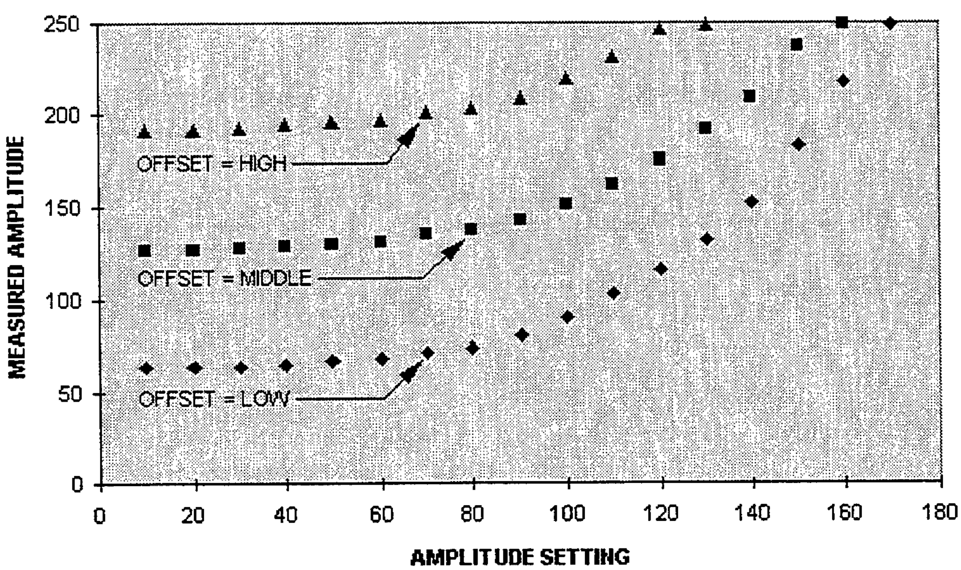

FIGURE 3
Measured Amplitude VS Amplitude Setting
for Three Values of Data Offset

Probe drive study #1 – tune, null and operating frequencies = 109,500 Hz. The amplitude value was collected as a function of amplitude setting at each of three different levels of Probe Drive % -- 50, 47 and 45. Tuning and nulling was conducted at a Probe Drive % value of 50. All parameters for tuning and nulling were the same. Parameter settings for nulling (same as tuning) and data collection are shown in table 2. Plots of the results are shown in figure 4. Plots of the *resonance amplitude VS frequency curves* for specific locations on each of the curves in figure 4 are shown in figures 5, 6 and 7.

Table 2 – MAUS System Parameter Values for Probe Drive Study #1; Tune, Null and Operating Frequencies = 109,500 Hz.

FIRST DATA SET		
Tune Settings	**Null Settings**	**Operating Settings**
Freq = 109,500	Freq = 109,500	Freq = 109,500
Probe (%) = 50	Probe (%) = 50	**Probe (%) = 50**
Amp = 30	Amp = 30	Amp = Varied
Phase = 20	Phase = 20	Phase = 20
SECOND DATA SET		
Tune Settings	**Null Settings**	**Operating Settings**
Freq = 109,500	Freq = 109,500	Freq = 109,500
Probe (%) = 50	Probe (%) = 50	**Probe (%) = 47**
Amp = 30	Amp = 30	Amp = Varied
Phase = 20	Phase = 20	Phase = 20
THIRD DATA SET		
Tune Settings	**Null Settings**	**Operating Settings**
Freq = 109,500	Freq = 109,500	Freq = 109,500
Probe (%) = 50	Probe (%) = 50	**Probe (%) = 45**
Amp = Varied	Amp = 30	Amp = Varied
Phase = 20	Phase = 20	Phase = 20

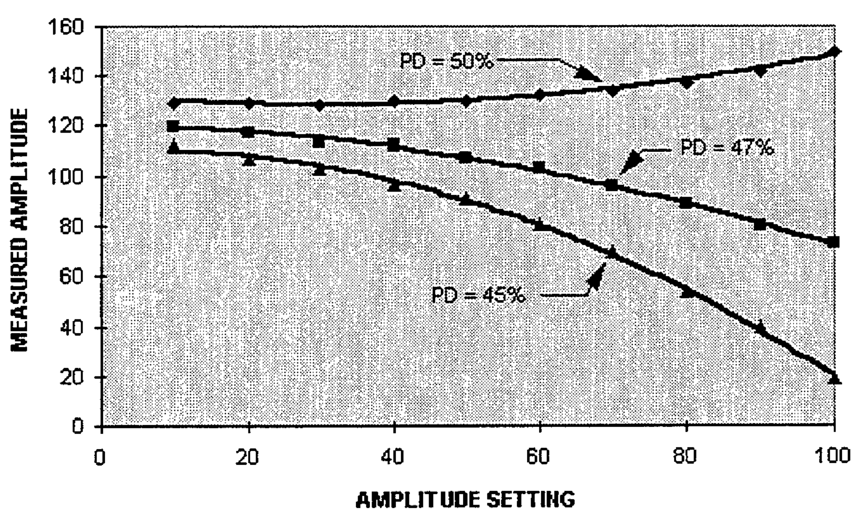

FIGURE 4
Measured amplitude VS amplitude setting for three values of Probe Drive %. The tune, null and operating frequencies were all the same.

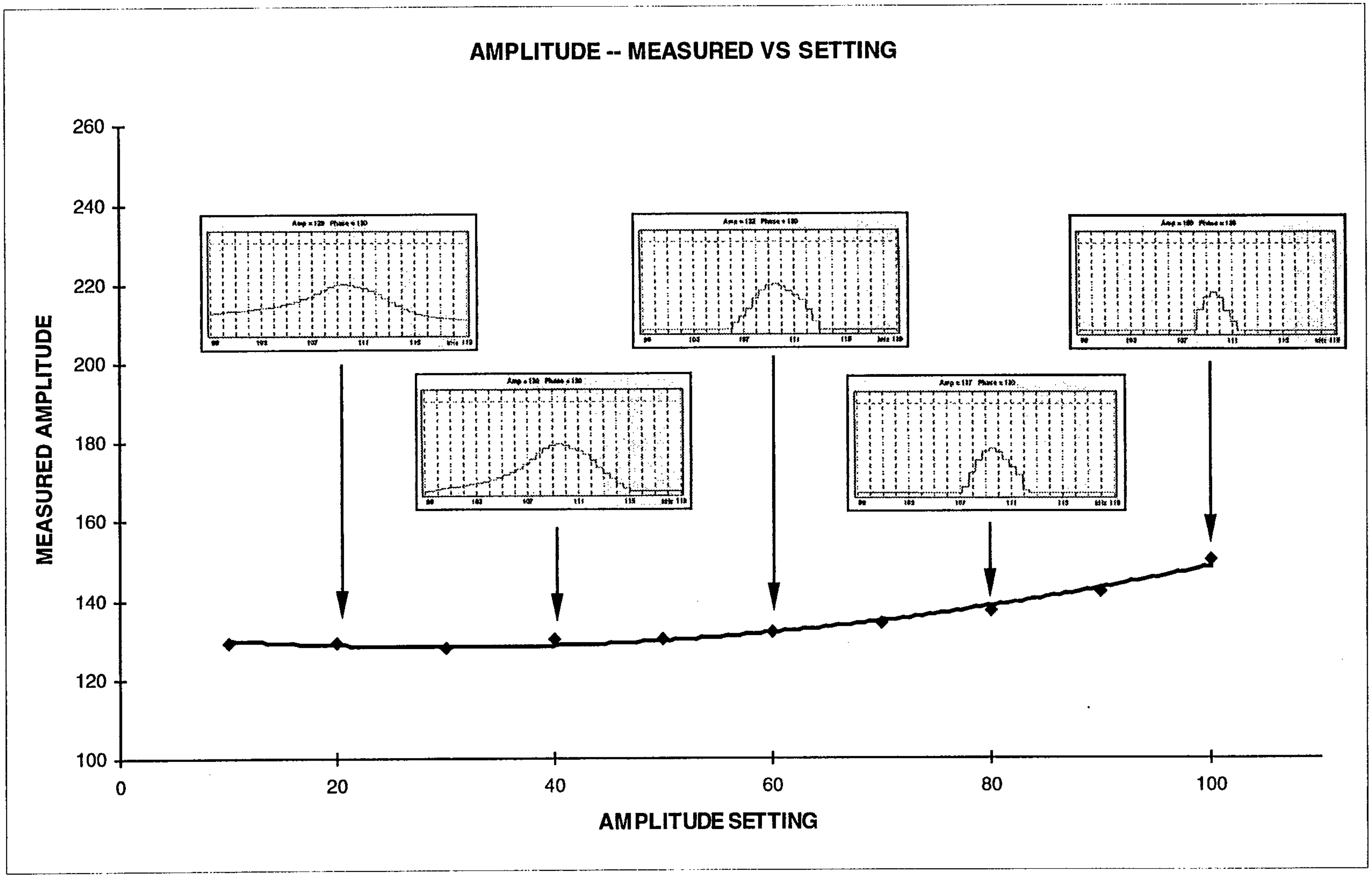

FIGURE 5
Resonance amplitude VS frequency curves for specific locations of the Probe Drive % = 50 curve from figure 4

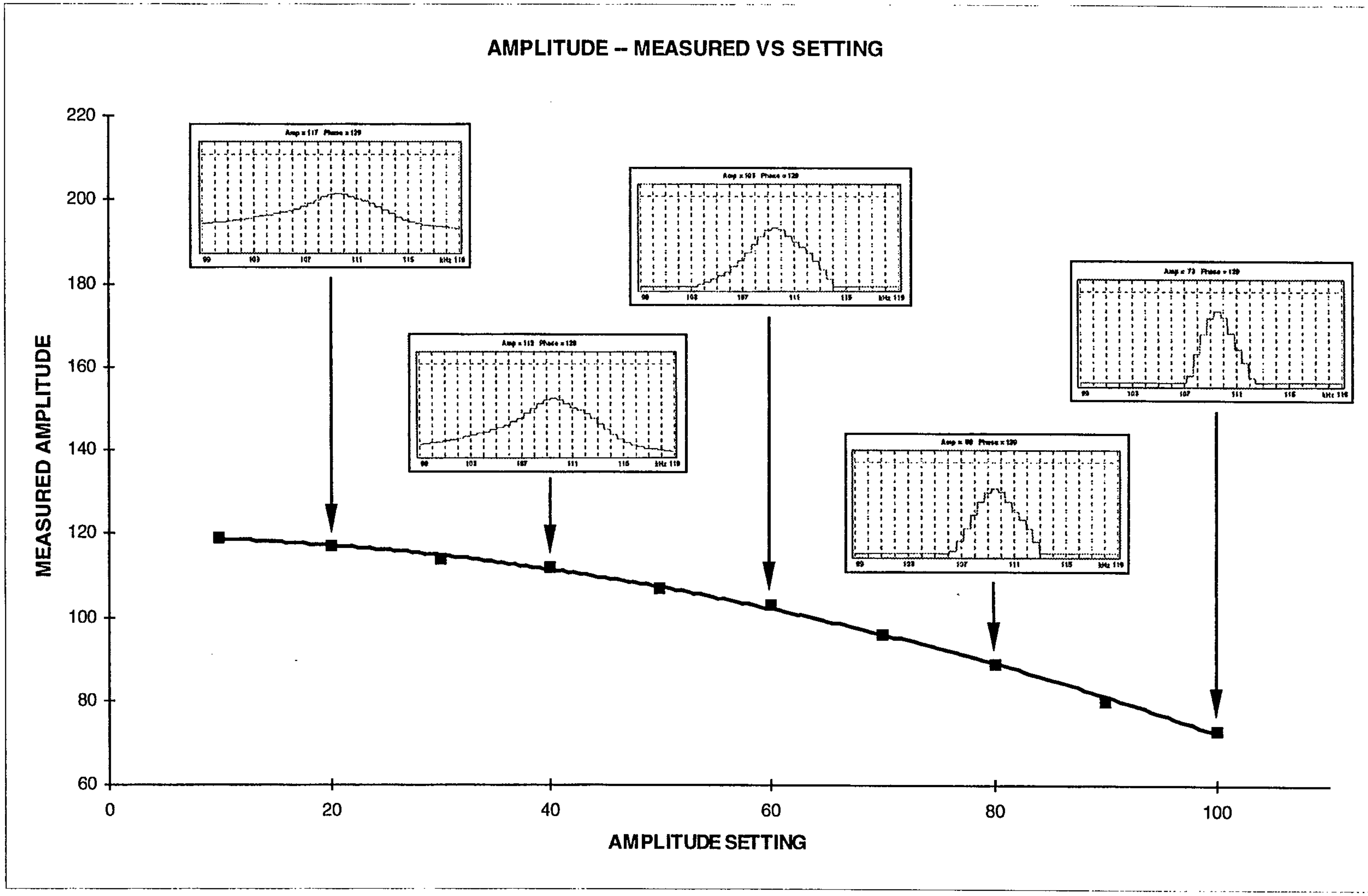

FIGURE 6

Resonance amplitude VS frequency curves for specific locations on the Probe Drive % = 47 curve from figure 4

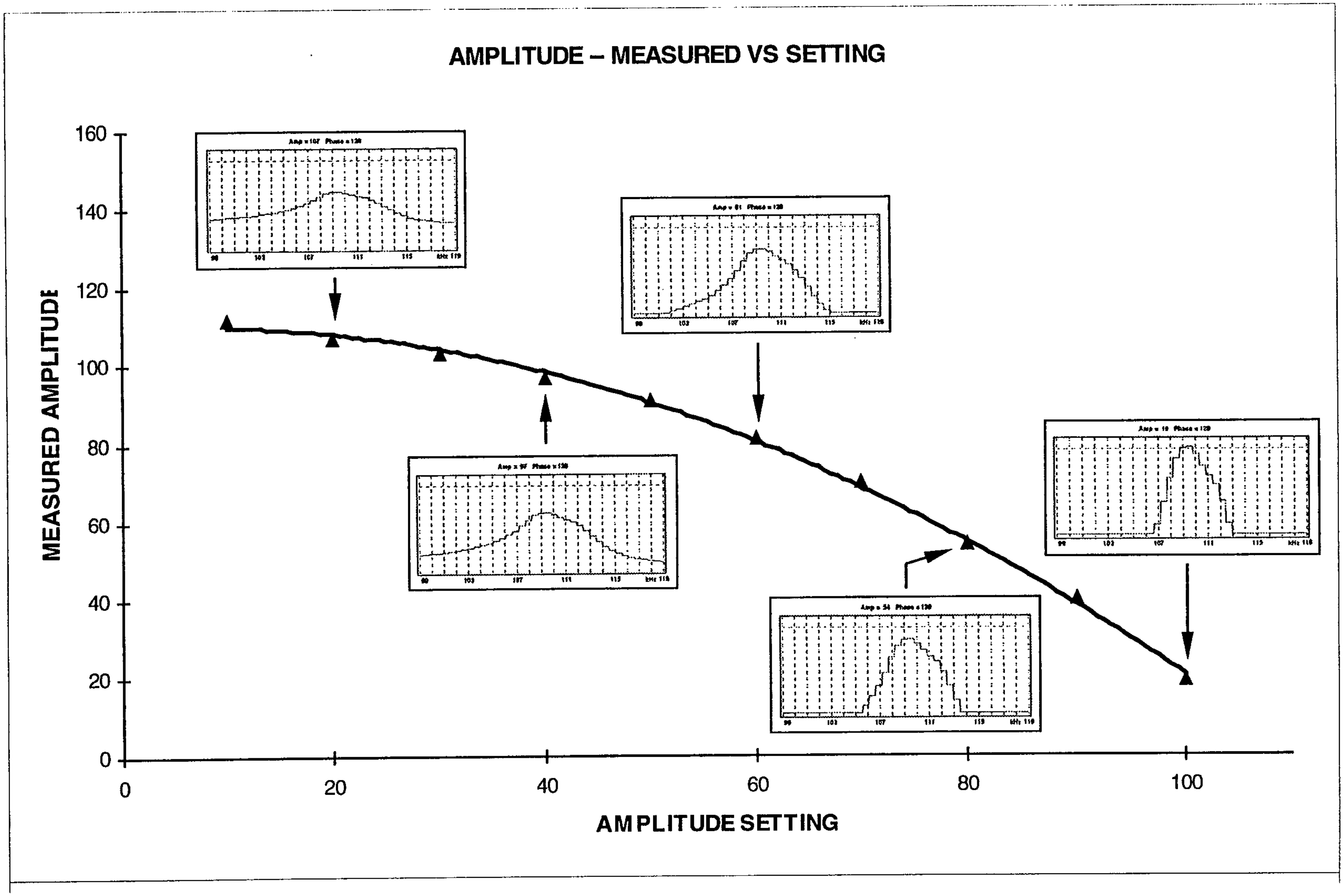

FIGURE 7
Resonance amplitude VS frequency curves for specific locations on the Probe Drive % = 45 curve from figure 4

Probe drive study 2 – null and operate at a frequency below the tune frequency. The amplitude value was collected as a function of amplitude setting at each of three different levels of Probe Drive % -- 50, 47 and 45. Tuning and nulling was conducted at a Probe Drive % value of 50. All parameters for tuning and nulling were the same. Parameter settings for nulling (same as tuning) and data collection are shown in table 3. Plots of the results are shown in figure 8.

Table 3 – MAUS System Parameter Values for Probe Drive Study #2; Null and Operate at a Frequency Below the Tune Frequency

FIRST DATA SET		
Tune Settings	**Null Settings**	**Operating Settings**
Freq = 110,000	Freq = 107,000	Freq = 107,000
Probe (%) = 50	Probe (%) = 50	**Probe (%) = 50**
Amp = 30	Amp = 30	Amp = Varied
Phase = 20	Phase = 20	Phase = 20
SECOND DATA SET		
Tune Settings	**Null Settings**	**Operating Settings**
Freq = 110,000	Freq = 107,000	Freq = 107,000
Probe (%) = 50	Probe (%) = 50	**Probe (%) = 47**
Amp = 30	Amp = 30	Amp = Varied
Phase = 20	Phase = 20	Phase = 20
THIRD DATA SET		
Tune Settings	**Null Settings**	**Operating Settings**
Freq = 110,000	Freq = 107,000	Freq = 107,000
Probe (%) = 50	Probe (%) = 50	**Probe (%) = 45**
Amp = 30	Amp = 30	Amp = Varied
Phase = 20	Phase = 20	Phase = 20

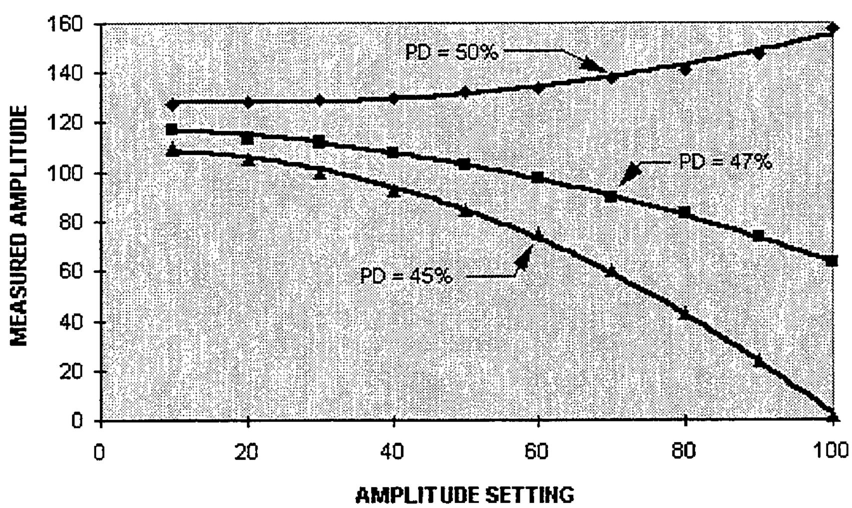

FIGURE 8

Measured amplitude VS amplitude setting for three values of Probe Drive % . The null and operating frequencies were below the tune frequency.

<u>Effect of nulling at one frequency and operating at a different frequency</u>. Two sets of data were collected for this portion of the survey study. For one data set the system was nulled at 109,500 Hz and data were collected at 106,500 Hz. For the second data set the system was nulled at 106,500 Hz and data were collected at 109,500 Hz. The tune frequency was 109,500 Hz in both cases. Parameter settings for nulling (same as tuning) and data collection are shown in table 4. Plots of the results are shown in figure 9.

Table 4 – MAUS System Parameter Values for Studying the Effects of Nulling and Operating at Different Frequencies.

FIRST DATA SET		
Tune Settings	**Null Settings**	**Operating Settings**
Freq = 109,500	**Freq = 109,500**	**Freq = 106,500**
Probe (%) = 50	Probe (%) = 50	Probe (%) = 50
Amp = 30	Amp = 30	Amp = Varied
Phase = 20	Phase = 20	Phase = 20
SECOND DATA SET		
Tune Settings	**Null Settings**	**Operating Settings**
Freq = 109,500	**Freq = 106,500**	**Freq = 109,500**
Probe (%) = 50	Probe (%) = 50	Probe (%) = 50
Amp = 30	Amp = 30	Amp = Varied
Phase = 20	Phase = 20	Phase = 20

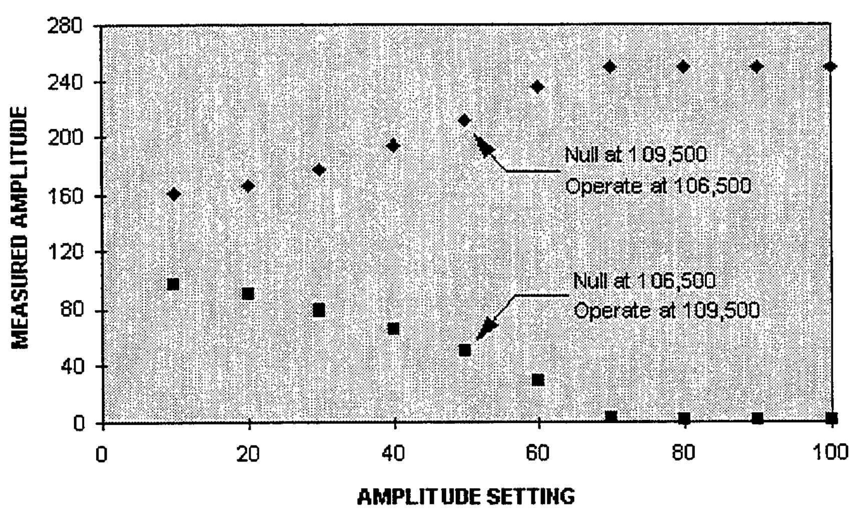

FIGURE 9
Effects of nulling and operating at different frequencies

DATA COLLECTION AND RESULTS – MEASURED PHASE VS PHASE SETTING

Data offset survey. For this study the output phase value was collected as a function of the phase setting at each of the three different data offset values – low, middle and high. The system was nulled and operated at the "tune" frequency, 109,500 Hz. The frequency, Probe Drive %, Amplitude and Phase settings used during tuning, nulling and data collection are shown in table 5. A plot of the data are shown in figure 10.

Table 5 – MAUS System Parameter Values for Studying Measured Phase VS Phase Settings at Three Levels of Data Offset

Tune Settings	Null Settings	Operating Settings
Freq = 109,500 Probe (%) = 50 Amp = 30 Phase = 10	Freq = 109,500 Probe (%) = 50 Amp = 30 Phase = 10	Freq = 109,500 Probe (%) = 50 Amp = 30 Phase = Varied

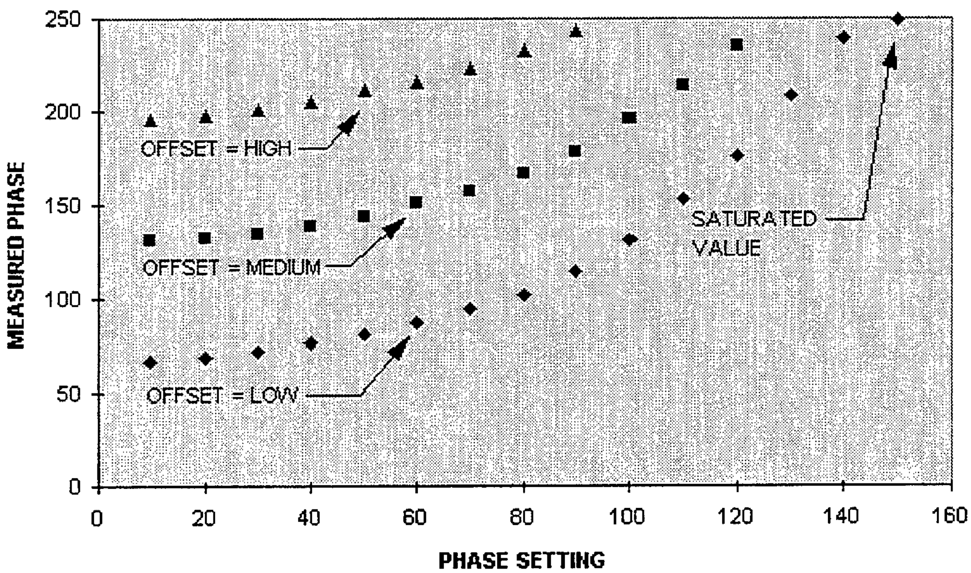

FIGURE 10
Measured Phase VS Phase Setting for Three Values of Data Offset

Effect of nulling at one frequency and operating at a different frequency. Two sets of data were collected for this portion of the survey study. For one data set the system was nulled at 109,500 Hz and data were collected at 106,500 Hz. For the second data set the system was nulled at 106,500 Hz and data were collected at 109,500 Hz. The tune frequency was 109,500 Hz in both cases. Parameter settings for nulling (same as tuning) and data collection are shown in table 6. Plots of the results are shown in figure 11.

Table 6 – MAUS System Parameter Values for Studying the Effects of Nulling and Operating at Different Frequencies.

FIRST DATA SET		
Tune Settings	**Null Settings**	**Operating Settings**
Freq = 109,500	Freq = 109,500	Freq = 106,500
Probe (%) = 50	Probe (%) = 50	Probe (%) = 50
Amp = 30	Amp = 30	Amp = 30
Phase = 10	Phase = 10	Phase = Varied
SECOND DATA SET		
Tune Settings	**Null Settings**	**Operating Settings**
Freq = 109,500	Freq = 106,500	Freq = 109,500
Probe (%) = 50	Probe (%) = 50	Probe (%) = 50
Amp = 30	Amp = 30	Amp = 30
Phase = 10	Phase = 10	Phase = Varied

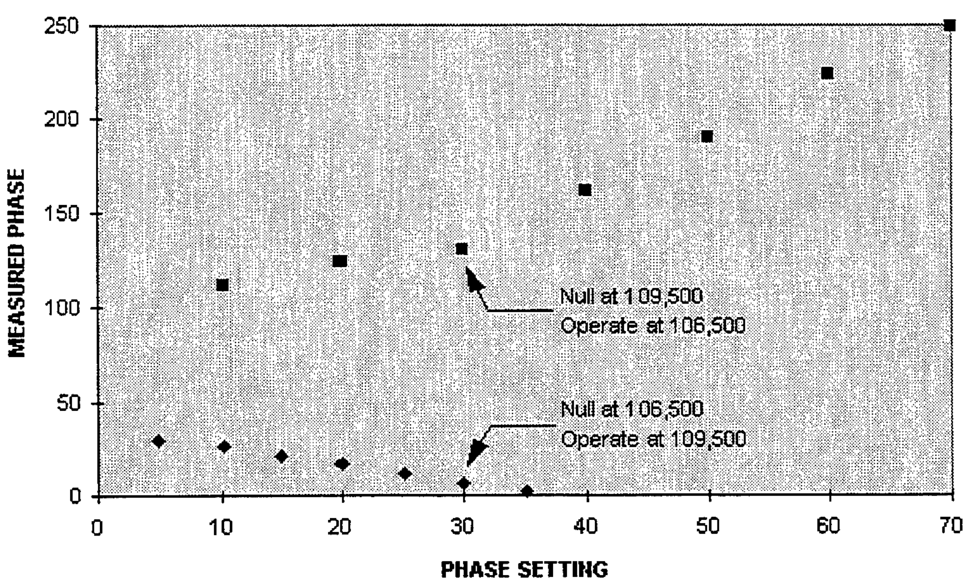

FIGURE 11
Effects of nulling and operating at different frequencies

Effect of nulling at different phase settings. Two sets of data were collected. For one data set the system was nulled with a phase setting value of 10; for the other data set, the system was nulled with a phase setting value of 80. The frequency used for tunning, nulling and operating was 109,500 Hz. Parameter settings are shown in table 7; the results are plotted in figure 12.

Table 7 – MAUS System Parameters for Studying the Effects of Nulling at Two Different Values of Phase Setting

FIRST DATA SET		
Tune Settings	**Null Settings**	**Operating Settings**
Freq = 109,500	Freq = 106,500	Freq = 106,500
Probe (%) = 50	Probe (%) = 50	Probe (%) = 50
Amp = 30	Amp = 30	Amp = 30
Phase = 10	**Phase = 20**	Phase = Varied
SECOND DATA SET		
Tune Settings	**Null Settings**	**Operating Settings**
Freq = 109,500	Freq = 106,500	Freq = 106,500
Probe (%) = 50	Probe (%) = 50	Probe (%) = 50
Amp = 30	Amp = 30	Amp = 30
Phase = 10	**Phase = 80**	Phase = Varied

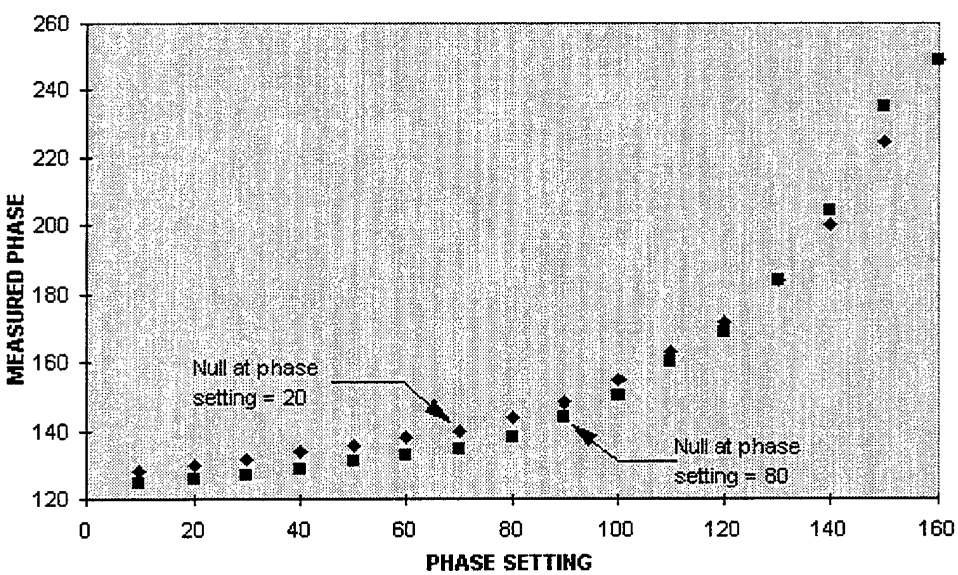

FIGURE 12
Effects of nulling at two different values of phase setting

DATA COLLECTION AND RESULTS – SCATTER IN PHASE DATA

Data offset effects. Three data sets were collected – one for each of the three data offset conditions (Low, Middle and High). Image data were generated for this study to allow statistics to be collected on a large number of points (1369 for a 37 X 37 pixel image). Image-data generation was accomplished by adjusting the instrument controls to the desired settings, and then moving the front wheels of the MAUS III while the probe remained in stationary contact with the sample. The image data were analyzed (using NIH Image) to determine the minimum, maximum, mean, mode, standard deviation and range of data values for each of the phase setting and data-offset conditions.

The tuning, nulling and operating frequencies used during this portion of the study were 109,500 Hz for each of the three data sets collected. The frequency, Probe Drive %, Amplitude and Phase settings used during tuning, nulling and data collection are shown in table 8. The high, low and mean values which were obtained for each phase setting within all data-offset conditions (Low, Middle and High) are plotted in figure 13.

Table 8 – MAUS System Parameter Values for Estimating Phase Data Scatter as a Function of Phase Setting at Three Levels of Data Offset

Tune Settings	Null Settings	Operating Settings
Freq = 109,500	Freq = 109,500	Freq = 109,500
Probe (%) = 50	Probe (%) = 50	Probe (%) = 50
Amp = 30	Amp = 30	Amp = 30
Phase = 10	Phase = 10	Phase = Varied

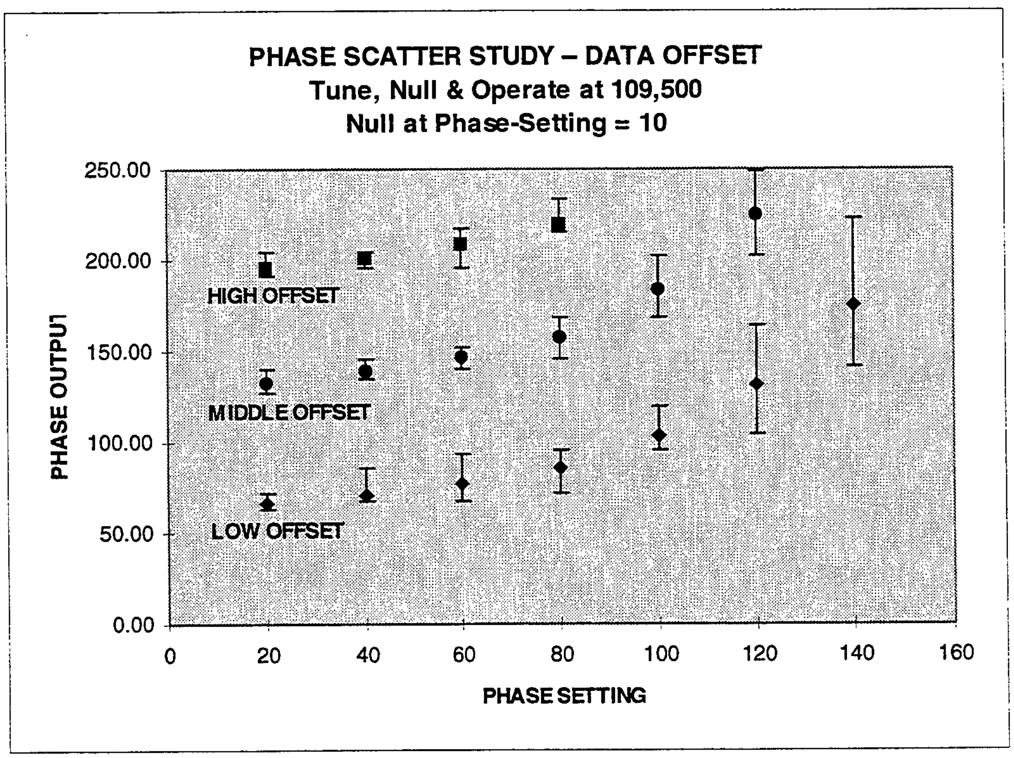

FIGURE 13
Measured phase VS phase setting for all three data offsets

Effect of nulling and operating at a frequency below the tune frequency. For this effort the tune frequency was 109,500 Hz whereas the nulling and operating frequencies were 106,500 Hz. Two sets of image data were collected and analyzed for this study. For the first set of data, the system was nulled with a phase setting of 10; for the second set of data, the system was nulled with a phase setting of 20. In each case, the Low value for data offset was used. The tuning, nulling and operating parameters are shown in table 9 for each of the two data sets. NIH Image was used to analyze the image data. The results are plotted in figures 14 and 15.

Table 9 – MAUS System Parameter Values for Studying the Effects of Nulling and Operating at a Frequency Below the Tune Frequency on Phase Data Scatter

FIRST DATA SET – NULL AT PHASE = 10		
Tune Settings	**Null Settings**	**Operating Settings**
Freq = 109,500 Probe (%) = 50 Amp = 30 Phase = 10	Freq = 106,500 Probe (%) = 50 Amp = 30 Phase = 10	Freq = 106,500 Probe (%) = 50 Amp = 30 Phase = Varied
SECOND DATA SET – NULL AT PHASE = 20		
Tune Settings	**Null Settings**	**Operating Settings**
Freq = 109,500 Probe (%) = 50 Amp = 30 Phase = 10	Freq = 106,500 Probe (%) = 50 Amp = 30 Phase = 20	Freq = 106,500 Probe (%) = 50 Amp = 30 Phase = Varied

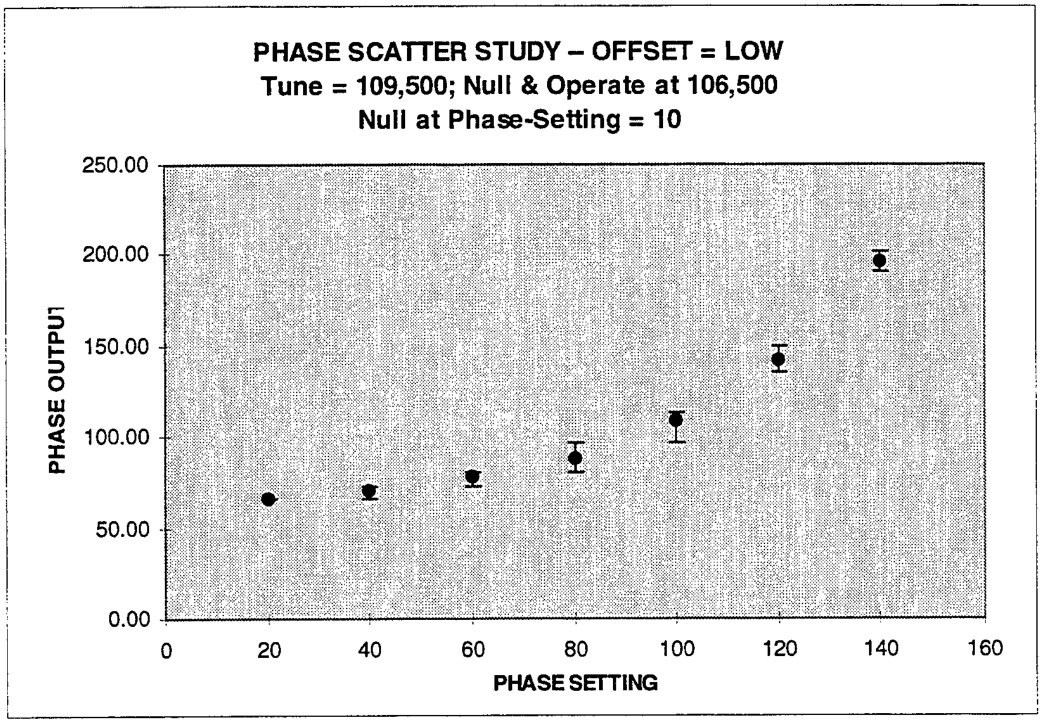

FIGURE 14
Phase output VS phase setting for nulling
at Phase Setting = 10, other conditions as shown

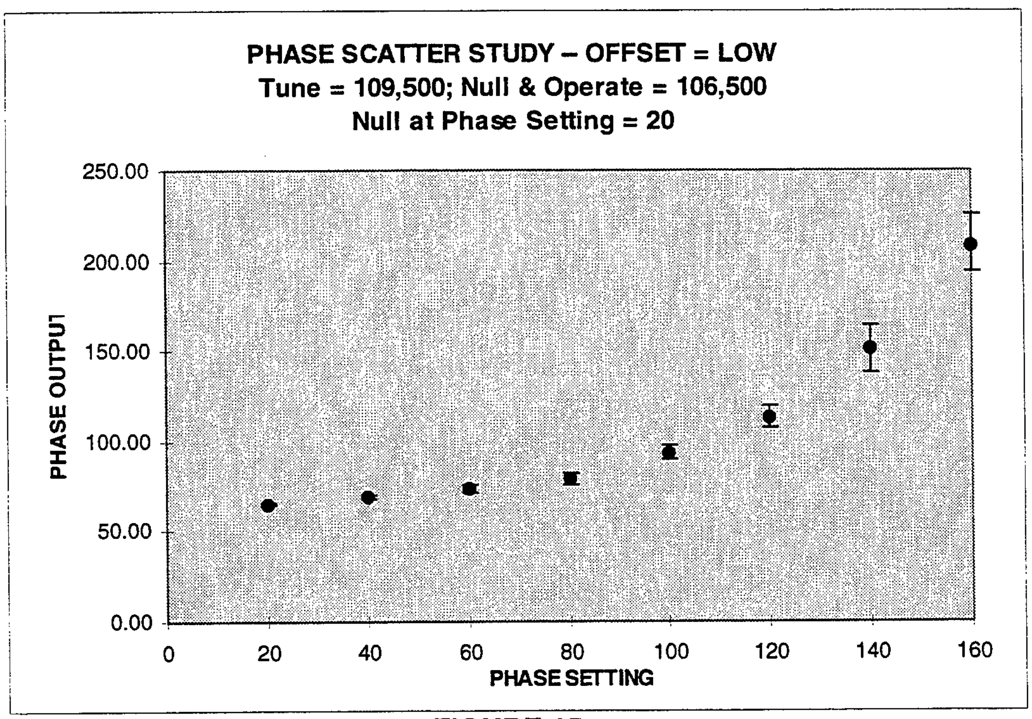

FIGURE 15
Phase output VS phase setting for nulling
at phase setting = 20, other conditions as shown

This page intentionally left blank.

MAUS III ULTRASONIC SCANS OF IMPACT DAMAGE IN A MULTI-DIRECTIONAL GRAPHITE-EPOXY COMPOSITE

Brian Frock

July 8 and 9, 1996

SAMPLE

An impact-damaged, multi-directional, graphite-epoxy composite sample was nondestructively scanned in an attempt to image the lateral extent of damage. The sample dimensions were 7 inches long, 4-5/8 inches wide, and 3/16 inch thick. The number of plies and the lay-up pattern are not known. The impact energy was written on the sample as 5.1 foot pounds. The sample is shown in Figure 1 in the holder used during scanning; the MAUS III scanner is also shown in that figure.

NONDESTRUCTIVE SCANNING TECHNIQUE

The Mobile Automated Scanner III (MAUS III) system developed by the McDonnell Douglas Corporation was used to scan the samples and to generate the C-scan images. An ultrasonic resonance technique and an ultrasonic pulse-echo technique were used to interrogate the sample.

Ultrasonic resonance data were collected at 110 KHz and 160 KHz from both the impacted (front) surface of the sample and from the back surface of the sample. Since the sample was relatively narrow and the impact energy was relatively low, only one transducer was used (at each frequency) to scan the sample.

Ultrasonic pulse-echo data were collected at 5 MHz from both major surfaces of the sample. Only one transducer was used for the pulse-echo data collection.

The setup parameters for the resonance scans are provided in Tables 1 and 2 of the Appendix. The setup parameters for the pulse-echo scans are provided in Tables 3 through 6 of the Appendix.

RESULTS -- RESONANCE

Ultrasonic resonance amplitude images are shown in Figure 2 for both frequencies, and for both the front-surface and back-surface scans. The corresponding ultrasonic resonance phase images are shown in Figure 3. The back-surface images were flipped vertically (both amplitude and phase) to provide better visual comparisons with the front-surface images. Horizontal and vertical dimensional measurements are also provided.

RESULTS -- PULSE-ECHO

Pulse-echo amplitude and depth images from scans of the front and back-surfaces of the sample are shown in Figure 4. Additional pulse-echo depth images from the same scans are shown in Figures 5. As was the case for the resonance images, the back-surface images were flipped vertically to provide better visual comparisons with the front-surface images. Horizontal and vertical dimensional measurements are overlaid on the images.

DISCUSSION

Comparison of the images in Figures 2 and 3 with the images in Figures 4 and 5 reveals that the resonance technique, when applied with the transducer in contact with the impact-damaged surface, provides smaller estimates of the impact-damage dimensions than does the pulse-echo technique. The reason for this difference in dimensional estimates between the two techniques is not known. The resonance technique also does not provide any layer-by-layer delamination-damage depth information, whereas some layer-by-layer delamination-damage depth information is provided by the pulse-echo technique (depth C-scan images only).

ACKNOWLEDGMENTS

The MAUS III system used for this effort is the property of the MLLP Branch of the WL/Materials Directorate. Mr. Charles Buynak is the Air Force lead engineer for development and transition of the MAUS III technology. Dr. Robert Crane is the Air Force WUD leader for the MLLP Branch and is the Contract Monitor for the UDRI NDE effort which is on site in the MLLP Branch. Mr. Jeffrey Fox, UDRI, developed the image-file-transfer procedure which enabled the printing of the MAUS III images in color.

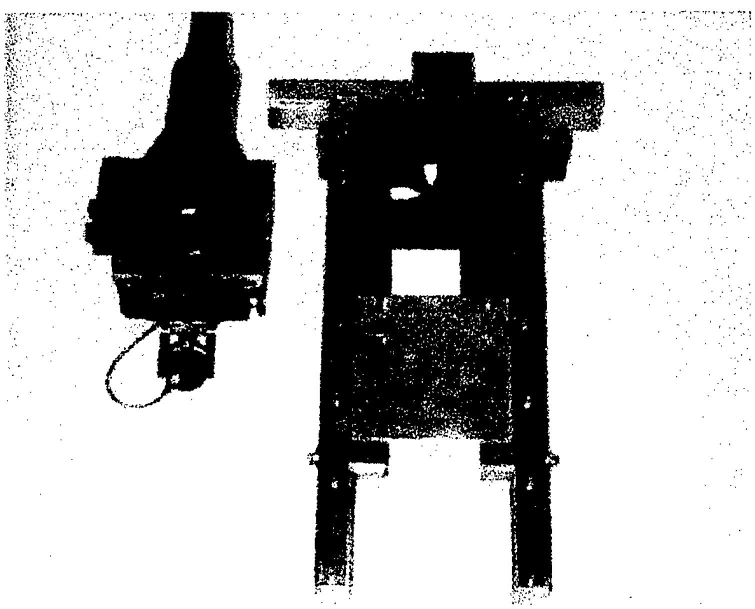

FIGURE 1
The Impact-Damaged Sample Together with its Holder and the MAUS III Scanner -- Yellow Arrows Indicate the Location of the Impact

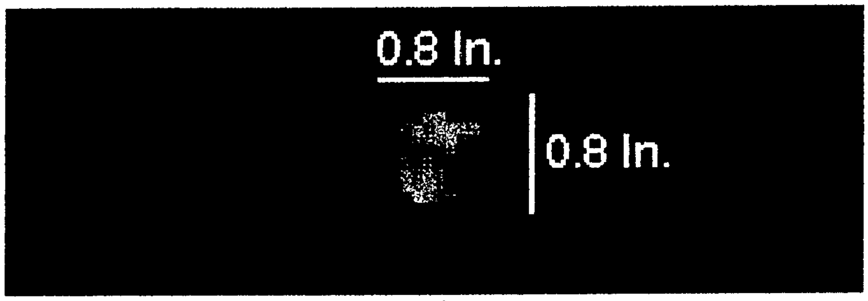

(a)

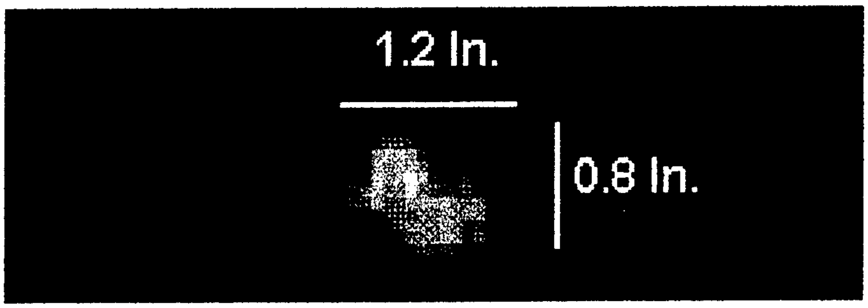

(b)

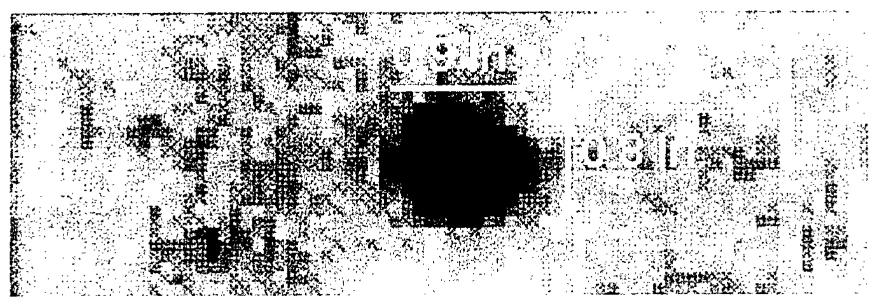

(c)

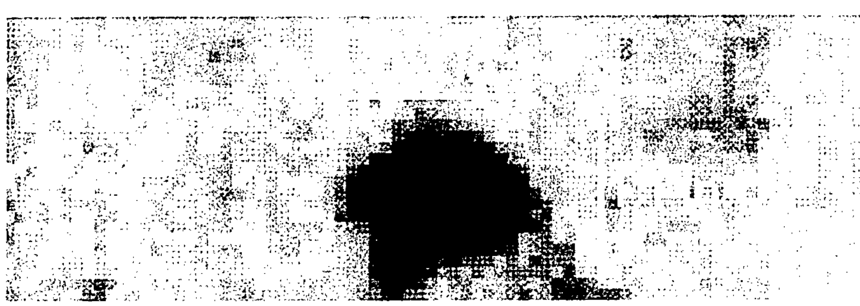

(d)

FIGURE 2
Resonance Amplitude Images of Impact Site -- (a) Front Surface, 110 KHz, (b) Back Surface, 110 KHz, (c) Front Surface, 160 KHz, and (d) Back Surface, 160 KHz

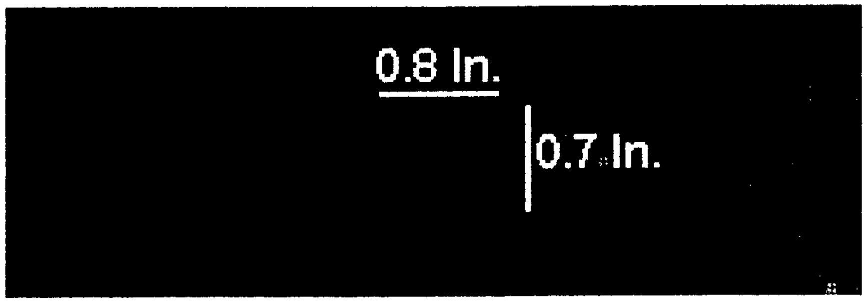

(a)

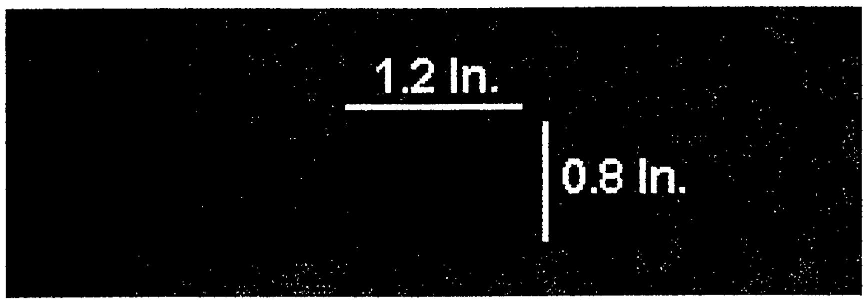

(b)

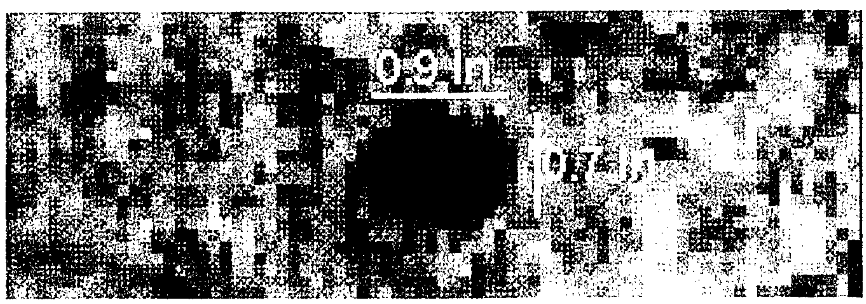
(c)


(d)

FIGURE 3
Resonance Phase Images of Impact Site -- (a) Front Surface, 110 KHz, (b) Back Surface, 110 KHz, (c) Front Surface, 160 KHz, and (d) Back Surface, 160 KHz

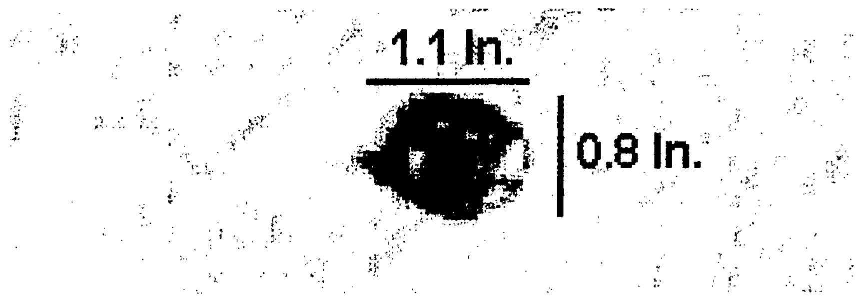

(a)

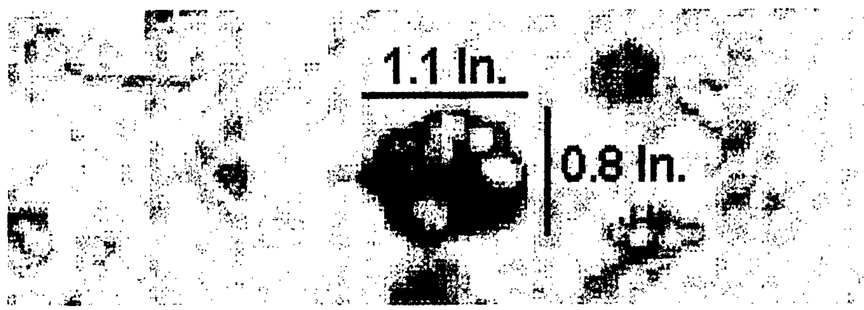

(b)

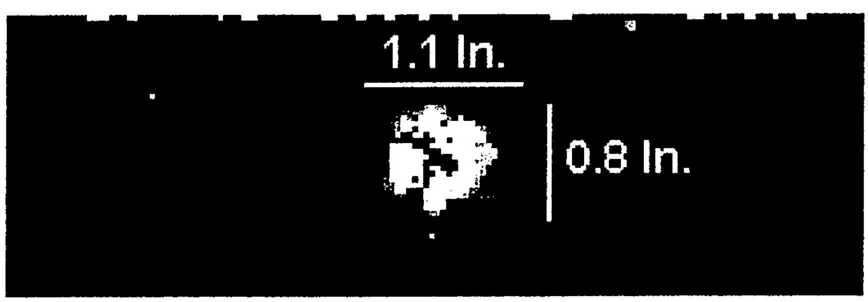

(c)

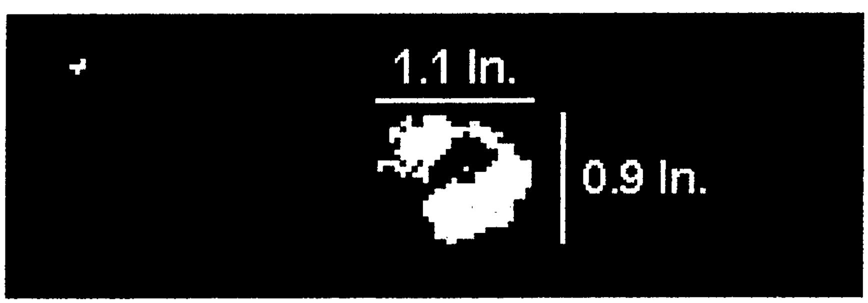

(d)

FIGURE 4
Pulse-Echo Images of Impact Site -- (a) Front Surface, Amplitude, (b) Back Surface, Amplitude, (c) Front Surface, Depth, and (d) Back Surface, Depth

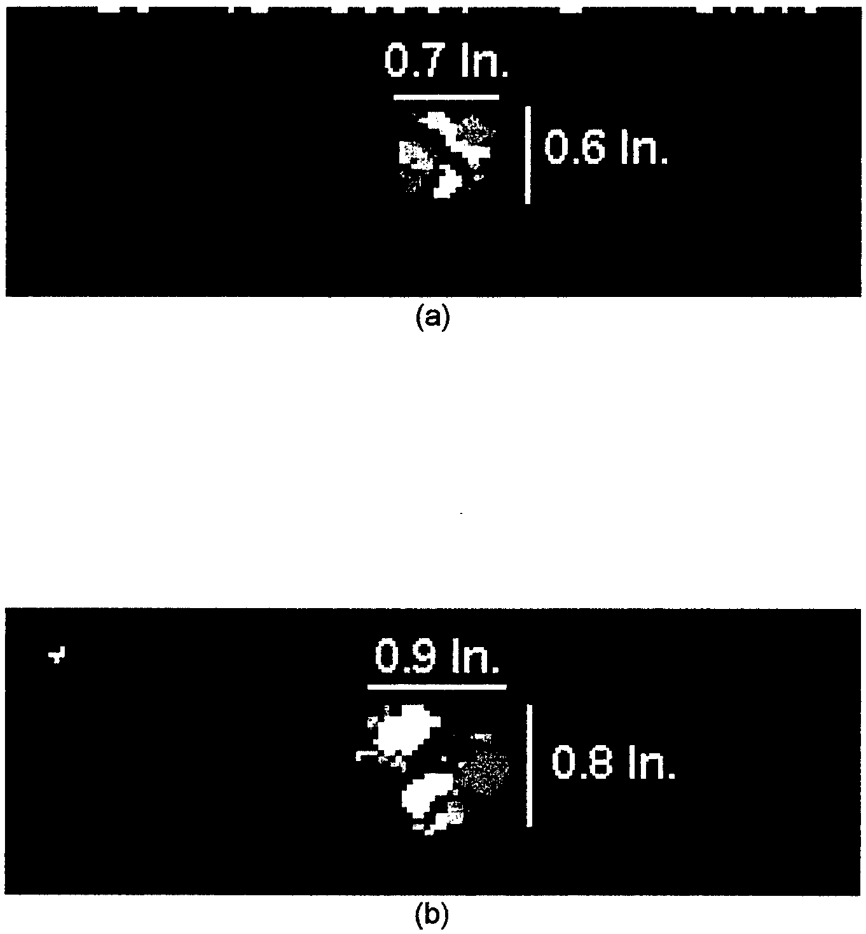

FIGURE 5
Pulse-Echo Depth Images Showing Near-Surface Damage -- (a) Interrogation from the Front Surface and (b) Interrogation from the Back Surface

APPENDIX
INSTRUMENT SETTINGS FOR DATA COLLECTION

ULTRASONIC RESONANCE TECHNIQUE

Table 1 -- Scanner Setup for Resonance Technique

PARAMETER	SETTING
Sensor 4 Type	Off
Sensor 3 Type	Off
Sensor 2 Type	Off
Sensor 1 Type	Resonance
Scan Width (Inches)	4
Flaw Resolution (Inches)	0.08
Scanning Mode	Bi-Directional

Table 2 -- Transducer and Imaging Setup for Resonance Technique

PARAMETERS	SETTINGS	
	110 KHZ	160 KHZ
Frequency (Hz)	106000	138000
Amplitude	5	25
Phase	10	50
Data Offset	Middle	Low

ULTRASONIC PULSE-ECHO TECHNIQUE

Table 3 -- Scanner Setup for Pulse-Echo Technique

PARAMETER	SETTING
Sensor 4 Type	Off
Sensor 3 Type	Off
Sensor 2 Type	Off
Sensor 1 Type	Pulse Echo
Scan Width (Inches)	4
Flaw Resolution (Inches)	0.04
Scanning Mode	Bi-Directional

Table 4 -- General Setup for Pulse-Echo Technique

PARAMETERS	SETTINGS	
	ENERGY LEVEL	DAMPING LEVEL
Sensor 4	Medium	Medium
Sensor 3	Medium	Medium
Sensor 2	Highest	Highest
Sensor 1	Highest	Highest
CGA Trigger	Part Surface	
Pulsers	Enabled	

Table 5 -- Setup for Pulse-Echo Depth Data Collection

PARAMETER	SETTING
Filter (MHz)	4
Maximum Depth (Inches)	0.30
Start Depth Measurement at	Part Surface
Material Velocity (uSec/in)	8.47
Gate Start (uSec)	16.0
Gate Width (uSec)	8.00
Front Surface Gate Width (uSec)	0.25
Threshold (%)	30
Sensor Gain (#1 only)	115
CGA Gain	Off

Table 6 -- Setup for Pulse-Echo Amplitude Data Collection

PARAMETERS	SETTINGS
Frequency (MHz)	5
Gate Trigger	Part Surface
Gate Start (uSec)	0.50
Gate Width (uSec)	10.0
Sensor Gain (#1 only)	30
CGA Gain	Off

UDR-TR-95-45

NDE RELIABILITY OF THE ECII SERIES E EDDY CURRENT INSPECTION SYSTEM

May 1995

Prepared for:

Materials Directorate
Wright Laboratory
Wright -Patterson Air Force Base, OH 45433-6503

Prepared by:

Alan P. Berens

STRUCTURAL INTEGRITY DIVISION
300 College Park
Dayton, OH 45469-0120

This page intentionally left blank.

Foreword

This is the final report of a task assigned under Air Force Contract F33615-94C-5213. Dr. Thomas Moran, WL/MLLP, is the Air Force contract monitor and the technical monitor for this task was Mr. Matthew Robbins, ASC/SMEE. The report presents the results of an analyses of NDE reliability data collected by GE Aircraft Engines during the capability demonstration of the ECII Series E eddy current inspection system. The analyses were performed by Dr. Alan P. Berens of the University of Dayton Research Institute during April, 1995.

This page intentionally left blank.

Section 1

Introduction

Under the ENSIP approach to ensuring the structural integrity of turbine engines, emphasis is centered on the size of flaws that might be present at the start of each period of operational usage. Accordingly, the capability of the inspection systems that are used in production and maintenance must be quantified in terms of the maximum flaw sizes that might be missed at an inspection. Because the inspection process is stochastic in nature for the small flaws of primary interest, capability must be characterized in terms of the probability of detecting cracks of a given size, POD(a). The POD(a) function is estimated from capability demonstration experiments using specimens and materials judged to be representative of the actual application. For the automated eddy current systems, NDE capability is defined as the best estimate of the crack length which corresponds to a probability of detection of 0.90.

To evaluate the capability of the ECII Series E eddy current inspection system, General Electric Aircraft Engines conducted a large number of demonstration experiments using different materials, specimen configurations, and signal processing methods. The original analyses of the resulting data, Reference 1, did not account for violations of the statistical assumptions in the analysis approach specified by the Air Force. The study of this report was undertaken to evaluate the validity of these assumptions and, when necessary, to re-analyze data.

This report is organized as follows. Section 2 presents a description of the methods used to test the assumptions and a summary of the results of these tests. Section 3 presents the results of the POD analyses. Since most of the data sets were re-analyzed, this report primarily comprises the results of these analyses which are presented in the appendices. The appendices of this report correlate exactly with those of the original data report, Reference 1.

This page intentionally left blank.

Section 2

Evaluation of Assumptions

The ECII Eddy Current Inspection System makes decisions on the basis of the magnitude of a signal response, â, that results from the presence of a flaw in the structure being inspected. This response is correlated with flaw size but, since many factors other than size influence the magnitude of the response, a distribution of â values is obtained from the population of different flaws of the same size. When a decision threshold, a_{dec}, is set, flaws whose response is greater than a_{dec} at an inspection will be detected while those that are smaller will be missed. Thus, the probability of detection for cracks of a given size is the probability that the signal response exceeds a_{dec}. Note that repeat inspections of the same crack will also produce different response values due to sources of variability such as calibration set up, transducer variability, and noise. These sources of variation can (and should) be included in an overall POD(a) function evaluation.

This general framework forms the basis of the POD(a) characterization methodology that the Air Force has adopted for characterizing the inspection reliability of automated inspection systems, Reference 2. In particular, for automated eddy current inspection systems, there is usually a range of crack sizes over which the log-log relation between crack size, a, and signal response, â, is linear with the scatter of â values about the linear relation being normally distributed with uniform variance. Given these assumptions, the POD(a) function will have the same form as a cumulative lognormal distribution function. In particular, if

$$\ln \hat{a} = \beta_0 + \beta_1 \ln a + \epsilon$$

and ϵ (the residual) is normally distributed with a mean of zero and common standard deviation, $\sigma(\epsilon)$, for all a, then

$$\text{POD(a)} = \Phi[(\ln a - \mu)/\sigma]$$

where Φ is the cumulative lognormal distribution function and

$$\mu = (\ln a_{dec} - \beta_0) / \beta_1,$$

$$\sigma = \sigma(\epsilon) / \beta_1.$$

To implement this analysis, a computer code (AHAT) was programmed which calculates the maximum likelihood estimates of β_0, β_1, and $\sigma(\epsilon)$ allowing for censored â values at signal threshold and signal saturation values. The maximum likelihood estimates of these parameters

are labeled B0, B1, and SIGMA in the output from the program.

In the ENSIP application, inspection capability of automated systems is characterized by the best estimate of the crack size, a90, which has a 90 percent probability of detection, POD(a90) = 0.90. (This is often referred to as the a90/50 crack size, where the 50 refers to the level of confidence in the estimate of the 90 percent detectable crack size.) a90 is calculated for any decision threshold as:

$$a90 = \exp(\mu + 1.282\ \sigma)$$

Therefore, the characterization of the system is directly dependent on the estimates of μ and σ which in turn are dependent on the validity of the assumptions.

For many sets of specimens and inspections, the basic assumptions are reasonable for automated eddy current inspections. However, it is very common to have a nonlinear (concave down) $\hat{a}$ versus a relation or to have greater scatter at the smaller crack size ranges of greatest interest. In these circumstances, it is often possible to restrict the analysis to a range of crack sizes for which the assumptions are more reasonable. At present, restricting the analysis to a range of smaller crack sizes is the only approach that can be used with the current AHAT analysis program to provide an estimate of the a90 value in the crack size ranges of interest.

The validity of the three assumptions for each of the ECII, Series E demonstration experiments was tested using the entire data set as originally recorded. In all but two of the data sets, either the assumption of ln $\hat{a}$ versus ln a linearity or the assumption of constant standard deviation (homogeneity) of the residuals was violated. For each data set, a reduced range of crack sizes to be included in the POD(a) analysis was determined and the assumptions were retested for the smaller data sets. The criteria for selection of the reduced crack size ranges were subjective. The objective was to find as large a data set as possible for which the three assumptions could not be rejected at a significance level of 0.10. In general, the assumptions required by the POD analysis were reasonable for the data sets that were finally selected. Tables 1 and 2 summarize the results of the tests of the validity of the assumptions for the POD results presented in the Appendices. Table 1 is for the conventional POD data sets while Table 2 is for the imaging POD data sets.

The tests of assumptions that were applied are built into the statistical analysis package, MINITAB, Release 10 for Windows. Linearity was tested by a regression analysis of the non-censored ln $\hat{a}$ versus ln a data. MINITAB performs two tests of linearity, Reference 3. First,

Table 1 Assumption Validation List for Conventional POD Data

Material	Specimen	Probe	Orient.	Linear	Eq.Var.	Normal
Ti 6-4	Holes	Diff.	Across	0.08*	<0.01*	Y
	Flats	Side	With	Y	Y	0.08*
	Flats	Diff.	Across	Y	Y	Y
	Flats	Diff.	With	Y	Y	0.05*
Ti 17β	Holes	Diff.	Across	Y(1)	Y(1)	Y(1)
	Flats	Side	With	Y	Y	Y
	Flats	Diff.	Across	Y	Y	Y
	Flats	Diff.	With	Y	Y	Y
DA718	Holes	Diff.	Across	Y	Y	Y
	Scallops	Diff.	Across	Y	Y	Y
	Flats	Side	With	Y	Y	Y
	Flats	Diff.	Across	Y	0.07*	Y
	Flats	Diff.	With	Y	Y	0.05*
PR718	Flats	Side	With	0.05*	Y	0.02*
RENE 95	Holes	Diff.	Across	Y	Y	Y
	Flats	Diff.	Across	Y	Y	Y
	Flats	Diff.	Across	Y	0.07*	Y
RENE88DT	Holes	Diff.	Across	0.07*	Y	Y
	Flats	Side	With	N(2)	Y	Y
	Flats	Diff.	Across	N(2)	Y	Y
	Flats	Diff.	With	N(2)	Y	Y
WASPALOY	Holes	Diff.	Across	0.09(3)	Y(3)	Y(3)
CH22	Holes	Diff.	Across	Y	Y	<0.01*

* - Level of significance for rejecting hypothesis
(1) - Without outlier (high â) at 5 mils
(2) - Concave up
(3) - Without outlier (high â) at 3 mils

Table 2 Assumption Validation List for Imaging POD Data

Material	Coil	Model	Linear	Equal Variance	Normal
Ti 6-4	0.060	Small	Y	Y	Y
	0.060	Large	Y	Y	0.05*
	0.025	Small	Y	0.05*	Y
	0.025	Large	Y	Y	Y
Ti 17β	0.040	Large	0.04*	Y	Y
DA718	0.025	Large	Y	0.04*	Y
	0.040	Large	Y	Y	Y
RENE 95	0.025	Small	Y	<0.01*	0.05*
RENE88DT	0.025	Small	Y	Y	Y
	0.040	Small	Y	Y	0.07*
	0.040	Large	Y	Y	Y
	0.060	Small	Y	Y	Y
	0.060	Large	Y	Y	0.05*

*   - Level of significance for rejecting hypothesis

the data are divided into two sets to see if the regression fit is significantly improved by fitting the two halves separately as compared to a single fit. Second, the regression fit using only data from a central region are evaluated for significance against the total data set. If the hypothesis of linearity was not rejected at the 0.10 level of significance, the linearity assumption can be treated as valid. In all but two of the data sets, using all of the cracks resulted in rejecting the validity of the linearity assumption. When this assumption was violated, tests of the other assumptions were not performed. When the range of crack sizes in the analysis was restricted, linearity was accepted for 27 out of the 35 data sets. In three of the cases in which linearity was rejected at level of significance less than 0.01 (level of confidence greater than 0.99), the curvature was due to high â values for some small cracks rather than the typical pattern of low â values at larger crack sizes. The level of significance for rejecting linearity in the other five data sets ranged from 0.04 to 0.09. Linearity was judged to be reasonable for the restricted ranges of crack sizes used in the POD analyses.

Equality of variance of the residuals from the regression analyses was tested using MINITAB's Bartlett's test for homogeneity of variance. The residuals were partitioned into two or three groups based on crack size and the equality of variances for the groups was tested. Again, failure to reject equality of variance at the 0.10 level of significance was taken as sufficient evidence for accepting the validity of the assumption. The equal variance assumption was accepted for 29 out the 35 reduced data sets. In two cases, homogeneity of variance was rejected at the 99 percent level of confidence (0.01 level of significance). In the conventional Ti 6-4 bolt hole data, the scatter appears to be continuously increasing with crack size. However, when the POD(a) analysis was performed using all cracks less than 25 mils, all cracks less than 20 mils, and all cracks less than 15 mils, equivalent a90 values (within 0.3 mil) were obtained over the entire range of a_{dec} values. That is, the a90 values were not sensitive to the changing variances of residuals. The equality of variances was also rejected for the imaging RENE 95 bolt hole set but the specimen set was not further reduced since the number of â values greater than the signal threshold was already reduced to 18 when all cracks less than 20 mils were included in the analysis. In the other four data sets, homogeneity of variance was rejected at levels of significance between 0.04 and 0.07.

The assumption of normality of the residuals was tested by the MINITAB modification to the Shapiro-Wilk test, References 4. This powerful (in the statistical sense) test is based on

the correlation coefficient of the normal probability plot of the residuals. Since very high correlations would be consistent with normality, rejection of the normal distribution is obtained from correlation coefficients below critical values for the sample size. The normality hypothesis could not be rejected at the 0.10 level of significance in 26 of the 35 data sets and was rejected at the 0.01 significance level in one of the data sets. Since any adjustment to the data for non-normality would depend on the distributions observed in a given data set and since the estimates of β_0 and β_1 are insensitive to the normality assumption, the residuals from all of the data sets were treated as though they were normally distributed.

In the conventional Ti 17β and Waspaloy data sets, very high $\hat{a}$ readings for small crack lengths were not included in the evaluation of the validity of the assumptions. These particular cracks have produced very high $\hat{a}$ values in every test that has been performed using these specimens and it was concluded that these cracks are miscategorized with respect to size. The outliers were included in the POD(a) analyses, however, as they produced slightly more conservative a90 values.

Section 3

POD Results

The list of all of the data sets that were made available for the analyses of this study and comments on the test matrix are presented in Appendix A. Complete POD results were re-calculated for all available data sets. The results for the eight materials used in the conventional POD data evaluations are contained in Appendices B through I. The five materials of the bolt hole imaging POD data results are contained in Appendices J through N. These appendices coincide exactly with those of Reference 1.

The POD results for each data set comprise three figures and a table:

a) the a90 versus a_{dec} plot for the recommended set of cracks to be included in the POD(a) analysis for the set.

b) a comparison of the a90 values obtained from the recommended crack set with those obtained using all of the cracks (as in Reference 1). There is only one a90 versus a_{dec} plot for the two data sets for which all cracks were used in the analysis.

c) a plot of all â versus a data showing the fits over the restricted range of crack sizes and over the entire set of cracks;

d) the summary table obtained from the AHAT computer run for the data set.

No POD(a) plots are presented because the specific decision thresholds of interest were not known.

The a90 versus a_{dec} plot is considered pivotal in the characterization of inspection capability since different decision thresholds can be employed for different applications. The a_{dec} value for a desired a90 value can be read from the plot but can also be calculated from the B0, B1, and SIGMA values reported in the AHAT output table. The relation between the parameters is as follows. From the cumulative lognormal distribution

$$a90 = \exp(\mu + 1.282 \cdot \sigma).$$

Using the best estimates of μ and σ from the AHAT analysis

$$\ln a90 = (\ln a_{dec} - B0)/B1 + 1.282 \cdot SIGMA$$

$$\ln a_{dec} = B1 \cdot \ln a90 + B0 - 1.282 \cdot B1 \cdot SIGMA$$

or

$$a_{dec} = \exp(B1 \cdot \ln a90 + B0 - 1.282 \cdot B1 \cdot SIGMA)$$

This page intentionally left blank.

Section 3

References

1. "Probability of Detection for the ECII Series E Eddy Current Inspection System," Document No. OC129-ALL-(ECII E) POD, Ge Aircraft Engines, Cincinnati, OH, May, 1994.

2. MIL-STD-1823, Draft Military Standard, "Non-Destructive Evaluation System Reliability Assessment."

3. Burn, D.A. and Ryan, T.A., Jr., "A Diagnostic Test for Lack of Fit in Regression Models," American Statistical Association, 1983 Proceedings of the Statistical Computing Section, pp. 286-290, 1983.

4. Filliben, J.J., "The Probability Plot Correlation Coefficient Test for Normality," Technometrics, Volume 17, p.111, 1975.

This page intentionally left blank.

APPENDIX A
POD DEMONSTRATION TESTS

The types of demonstration tests for each material for which data were made available are as follows:

<u>CONVENTIONAL POD DATA</u>

TITANIUM 6-4	HOLES: DIFFERENTIAL PROBE – ACROSS THE CRACKS FLATS: SIDE MOUNT PROBE – WITH THE CRACKS FLATS: DIFFERENTIAL PROBE – ACROSS THE CRACKS FLATS: DIFFERENTIAL PROBE – WITH THE CRACKS
TITANIUM 17β	HOLES: DIFFERENTIAL PROBE – ACROSS THE CRACKS FLATS: SIDE MOUNT PROBE – WITH THE CRACKS FLATS: DIFFERENTIAL PROBE – ACROSS THE CRACKS FLATS: DIFFERENTIAL PROBE – WITH THE CRACKS
DA718	HOLES: DIFFERENTIAL PROBE – ACROSS THE CRACKS SCALLOPS: DIFFERENTIAL PROBE – ACROSS THE CRACKS FLATS: SIDE MOUNT PROBE – WITH THE CRACKS FLATS: DIFFERENTIAL PROBE – ACROSS THE CRACKS FLATS: DIFFERENTIAL PROBE – WITH THE CRACKS
PR718	FLATS: SIDE MOUNT PROBE – WITH THE CRACKS
RENE 95	HOLES: DIFFERENTIAL PROBE – ACROSS THE CRACKS FLATS: DIFFERENTIAL PROBE – ACROSS THE CRACKS FLATS: DIFFERENTIAL PROBE – WITH THE CRACKS
RENE 88 DT	HOLES: DIFFERENTIAL PROBE – ACROSS THE CRACKS FLATS: SIDE MOUNT PROBE – WITH THE CRACKS FLATS: DIFFERENTIAL PROBE – ACROSS THE CRACKS FLATS: DIFFERENTIAL PROBE – WITH THE CRACKS
WASPALOY	HOLES: DIFFERENTIAL PROBE – ACROSS THE CRACKS
CH 22	HOLES: DIFFERENTIAL PROBE – ACROSS THE CRACKS

<u>IMAGING POD DATA</u>

TITANIUM 6-4	.060 COIL – SMALL MODEL .060 COIL – LARGE MODEL .025 COIL – SMALL MODEL .025 COIL – LARGE MODEL (No data available)
TITANIUM 17β	.040 COIL – LARGE MODEL
DA718	.025 COIL – LARGE MODEL .040 COIL – LARGE MODEL
RENE 95	.025 COIL – SMALL MODEL
RENE 88 DT	.025 COIL – SMALL MODEL .040 COIL – SMALL MODEL .040 COIL – LARGE MODEL .060 COIL – SMALL MODEL .060 COIL – LARGE MODEL

Not all of the data called for in the original test matrix were available for the analyses of this study. The discrepancies are as follows:

a) The original test matrix called for multiple runs for five of the material, specimen configurations. The multiple runs were both repeat inspections with no changes to quantify repeatability and repeat inspections with a different probe of the same type. No data were available for any of these multiple runs. None of the POD characterizations include the source of variability due to different probes. In previous evaluations of other eddy current systems, the effects of multiple probes have been included. Including multiple probes of the same type can shift the POD(a) function up or down, but always increased SIGMA, making the POD(a) function at least somewhat flatter. In Reference 1, â versus a plots are presented for only the repeat runs of conventional Ti 6-4 bolt hole specimens and no POD analyses were presented which combine the results from the two probes in a single analysis. The variability due to repeat runs with the same probe is generally negligible.

b) In the imaging POD data tests, only three of the bolt hole specimens from each of the material types were used in the demonstration experiments. Because the analyses of these data had to be restricted to a range of short cracks, the number of cracks available for the POD characterizations fell below the recommended minimum. The distributions of crack sizes in the specimens that were included in the demonstration experiments were about equivalent to the distribution of crack sizes in the two or three specimens that were not included.

c) The data set for the imaging, Ti 6-4, .025 coil, large cracks model was not available for this study. The data file that was intended for this data set was a mislabeled set that was identical to that of the Ti 6-4, .025, small cracks model.

The In-Situ Sensor-Guided Process Characterization of Advanced Composite Materials

Renee M. Kent and Mark J. Ruddell

This article describes the multifunctional use of fibers as reinforcements and acoustic waveguides for sensing the fiber-matrix interfacial conditions during processing. It is shown that monitoring the ultrasonic signal response through a reinforcing fiber in a composite material yields on-line information that is related to the densification of the composite in the vicinity of the interface. Leakage of ultrasound from the fiber to the matrix is shown to be a function of the density of the matrix at the interface. It is also shown that these data can then be used to feed back to the process for optimization and control.

INTRODUCTION

It is well known that the fiber/matrix interface plays a dominant role in the mechanical behavior of composite materials.[1,2] Engineering and control of the interface is paramount to producing the properties for a desired mechanical performance of the final composite structure. This is particularly critical for advanced composites (e.g., metal-matrix composites and ceramic-matrix composites), which are currently being investigated for structural applications in aerospace and other structures. However, to date, there is little empirical information related to the evolution of the time-related characteristics of the interface. In particular, the manufacture of advanced metal-matrix composites (MMCs) and ceramic-matrix composites (CMCs) is largely established by experiential determination of an optimized process in which little quantitative foundation to on-line measurement of interfacial properties for control and feedback to the process is included.

The properties and characteristics of the interface continually change during the manufacturing process of the composite material until the interfacial characteristics are produced that will ultimately result in the desired mechanical behavior for structural performance. However, presently there is no way to determine a priori (or as the material is being processed) the nature of the interface; instead, a specific pressure/temperature profile, usually empirically determined, is applied to a particular material class system. It is generally assumed that the empirically determined temperature profile will produce the desired characteristics. However, this approach does not allow the process to be updated on-line in response to uncontrolled processing variables.

In this work, a technique for in-situ interfacial characterization and determination is described and demonstrated for in-process analysis and mechanical behavior studies of composites. The methodology described is based on an optical analysis of a guided ultrasonic signal response, but with appropriate technology, the fundamental parameters used in this study can be effectively applied to other conventional and nonconventional detection systems.

The approach for analyzing the process cycle of composite materials on-line utilizes the multifunctional use of fibers as reinforcement and sensors. The fact that typical reinforcing fibers can be effectively used as ultrasonic wave guides implies a mechanism at transfer for ultrasonic information along the length of the fiber-matrix interface. Ultimately, this information can be fed back to the processing line to update the process for optimization and manufacturing affordability.

ULTRASONIC WAVE GUIDES

It has been shown in independent research that small-diameter, structural-reinforcing fibers such as those being investigated for reinforcing structural aerospace components can be used as ultrasonic wave guides.[3-5] In this case, the fiber is unconstrained along its axial-radial boundaries, and an ultrasonic wave applied to the end of the fiber propagates at a characteristic velocity determined by the elastic properties of the fiber material.[6]

In the most general case, ultrasonic wave propagation in a right circular cylinder (rod) exhibits velocity dispersion. However, in the low-diameter, high-frequency limit (i.e., when the wavelength of the ultrasound is much larger than the transverse dimension of the rod), the propagation velocity approaches the bar velocity of the rod, and the velocity of propagation is directly related to the elastic modulus of the rod.

The point germane to the present discussion is that the reinforcing fibers themselves act as ultrasonic wave guides. The fiber, insonified with an ultrasonic wave, provides a channel for the exchange of ultrasonic information transfer. When the fiber is constrained at its axial-radial boundaries, the ultrasonic wave no longer propagates unimpeded; instead, some of the ultrasonic energy leaks from the fiber across the fiber/matrix interface. The rate and nature of the leakage is related to the stiffness, density, and thickness of the interfacial region.[7-9]

An ultrasonic pulse may be physically represented as a small-magnitude, periodic

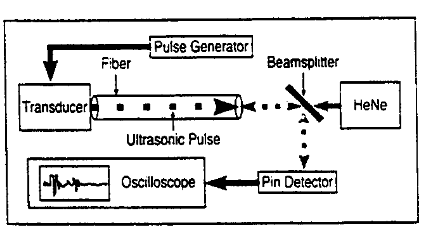

Figure 1. The optical configuration for the detection of ultrasound.

mechanical elastic disturbance within the host medium. Therefore, leakage of the ultrasonic energy across the fiber-matrix interface is a direct indication of the stress-wave transfer from the fiber to the matrix within the elastic regime, which determines the mechanical characteristics of the composite material. Direct monitoring of the ultrasonic signal response is an indication of the mechanical integrity of the interface along the length of the fiber.

In this work, we have demonstrated the in-situ measurement of interfacial characteristics of selected CMCs for application to understand and control the process. Where appropriate, an optical interferometric detection system (Figure 1) was employed for local interrogation of the composite materials. The interferometric cavity is contained within the end of the fiber and the plate beamsplitter. A HeNe laser beam is focused on the fiber end (focal spot size 40 μm). The light scattered from the rough surface of the fiber mutually interferes to form a speckle distribution whose amplitude and phase is characteristic of the fiber. The coherent speckle (sample beam) interferes with the incoming light reflected from the beamsplitter (reference beam) to form interference fringes characteristic of the phase relationship between the reference and sample beams.

As the ultrasonic wave propagates along the fiber, it undergoes periodic displacements that result in periodic fluctuation in the optical path length of the interferometric cavity. This causes a corresponding shift in the interferometric fringes that are detected at a photo detector and used to map the response of the fiber to ultrasonic-wave propagation of specific modes.

In each case, as the characteristics of the fiber-matrix change (due to the formation of residual stresses, consolidation at the interface, etc.), alteration in either the transit time of the zero-order extensional mode and/or the frequency content is observed. These changes may be correlated to the properties of the interface.[10]

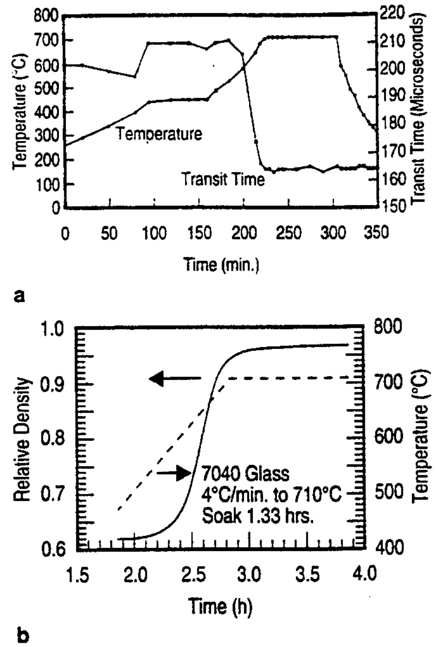

Figure 2. (a) Ultrasonic transit time through reinforcing fiber as related to process cycle and (b) relative density vs. time for a glass compact as related to process cycle.

RESULTS AND DISCUSSION

Figure 2 shows the velocity measured through the reinforcing-fiber-wave guide as a function of time into the process cycle. For convenience, the thermal cycle is plotted on the same graph. From these data alone, it is clearly evident that the velocity data track the process cycle. During the burnout phase of the process, there is a slight increase in the ultrasonic velocity through the fiber. As the polymeric binder is burned out of the matrix precursor, the fiber is constrained by the porous glass frit. At the hold temperature (450°C), the data indicate a marked decrease in velocity, which levels off after approximately the first 10–15 minutes of the 450°C hold. At this point, holding the temperature constant no longer produces an effect on the interfacial conditions. During the consolidation phase of the process, there is a precipitous increase in the fiber-wave guide velocity immediately prior to the 710°C hold. It is at this stage where the most significant changes in the interfacial characteristics take place. Once the 710°C hold is reached, no discernible variations in the velocity are observed. This is indicative of an equilibrium-type state being reached within the composite material (i.e., the interfacial properties remain constant).

EXPERIMENTAL DESIGN AND PROCEDURES

A monolayer composite was placed for consolidation in a 1.3 m long tube furnace (Figure A). A single layer of Sigma chemical vapor deposition (CVD)-SiC based (TiB_2-coated) fibers was placed in a 7040 glass frit, bound in a polymeric binder. One of the reinforcing fibers extended approximately 10 cm on either end from the furnace (Figure A). This fiber was the ultrasonic wave guide used for on-line analysis. A 0.5 MHz piezoelectric element was epoxied to one end of the wave-guide fiber. In this case, the epoxy was used as the acoustic coupling medium to ensure effective acoustic transfer from the transducer to the fiber. A matching piezoelectric element was similarly epoxied to the other end of the fiber for detection of the ultrasonic signal response. The raw ultrasonic signal responses were collected and stored at periodic time intervals throughout the burnout cycle, matrix-consolidation (sintering) cycle, and the cool-down cycle. The data were analyzed for velocity and frequency content, respectively, and plotted as a function of time and temperature to demonstrate the relationship of the reported data to consolidation.

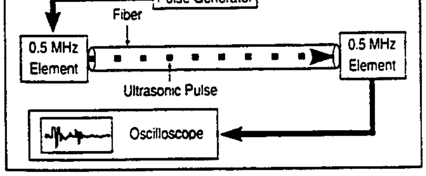

Figure A. An experimental configuration using fiber as a sensor.

The process cycle (Figure B), which had been previously determined on an experiential basis as appropriate for the SiC/glass composite, consists of three major steps. These are:

- Binder burn out. Thermal ramp-up occurs at a rate of 4°C/min. from ambient temperature to 450°C. The temperature is held for 80 min. During this phase of the process, the polymeric binder within the 7040 glass is burned out, leaving the fiber in its state of minimum constraint during the process.
- Sintering. Thermal ramp-up from 450°C to 710°C occurs at a rate of 4°C/min. The temperature is then held at 710°C for 90 min. During this phase, flowing argon is introduced to the furnace to minimize any oxidative effects that may occur at high temperatures. During this phase, sintering occurs to produce the dense glass matrix.
- Cool down. The temperature is brought down to ambient at a rate of 5°C/min. During cool down, residual stresses are created at the fiber/matrix interface due to the mismatch of the coefficients of thermal expansion between the fiber and the matrix.

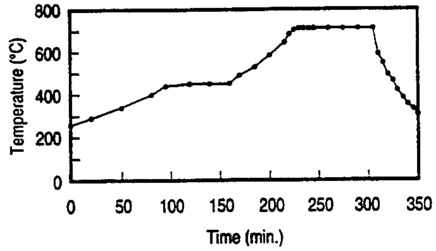

Figure B. The experiential-based process cycle for sigma/glass.

The resulting Sigma/glass composite contains inherent residual stresses due to the coefficient-of-thermal-expansion mismatch between the matrix and the fiber. The softening of the material and resulting relief of residual stresses at the fiber/matrix interface was then directly interrogated by monitoring the frequency content of the ultrasonic signal response propagating through a reinforcing fiber as the formed composite was reheated to 500°C at a rate of 4°C/min. During the reheat cycle, ultrasonic data through the fiber were taken at periodic time intervals. The ultrasonic response was analyzed in the Fourier domain. The first axisymmetric longitudinal mode was software gated for Fourier analysis. The bandwidth of the resulting signal was measured and normalized to the acoustic impedance of the fiber. The measured bandwidth was plotted as a function of reheat temperature.

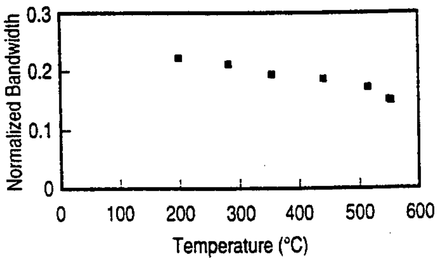

Figure 3. The bandwidth of ultrasonic signal response showing residual stress relief.

For comparison, Figure 2b is a plot of the relative density as a function of time from dilatometric measurements of a glass compact using the same process cycle. Note that the relative density exhibits similar behavior to that described (i.e., it increases rapidly from 600°C to 700°C but remains constant after the 710°C hold is reached).

It is clear that the velocity data alone yield little, if any, evidence of the residual stress state that is formed during cool down in the composite. However, the frequency content of the ultrasonic signal is altered as the residual stress state (and constraint on the reinforcing fiber) changes. In Figure 3, the bandwidth (full width at half maximum) of the Fourier transform of the ultrasonic pulse through the fiber is plotted as a function of the reheating temperature. Figure 3 shows a linear relationship between the bandwidth of the detected signal response and the relief of residual stress, which occurs at the fiber-matrix interface due to reheating the composite. At the hold temperature, the slope of the bandwidth curve increases dramatically, indicative of the softening of the matrix. These data are consistent with those previously reported for the relationship between changes in residual stress and ultrasonic signal responses.[11] It should, however, be noted that the technique employed does not provide a measure of the residual stress but an indication of changes in the stress state.

CONCLUSIONS

The preliminary data presented in this work indicate that the use of in-situ sensors that monitor the progression of a composite-process cycle can be used to characterize and optimize the process. In particular, it appears that the sensor data can provide a direct indication of the pertinent characteristics of the interface during the process itself. Therefore, the process can be optimized on-line for improved interfacial properties and performance. Although the data presented in this work are specific to glass-matrix composite materials, the sensor technology presented can also be applied to CMCs, polymer-matrix composites, and MMCs.

ACKNOWLEDGEMENTS

The authors gratefully acknowledge the assistance of Roland Dutton of the National Institute of Standards and Technology (colocated Wright Laboratory/Materials Development Branch, Materials Directorate, Wright-Patterson Air Force Base) and John Schuck of the University of Dayton for their participation in the processing of the materials, and Gregg Jessen of Wright State University for the data acquisition. This work was supported by Wright Laboratory/ Nondestructive Evaluation Branch, Wright-Patterson Air Force Base under contract number F33615-94-C-5213.

References

1. T.W. Coyle, E.R. Fuller, and P. Swanson, "Fracture Mechanics Characterization of Crack/Fiber Interactions in Ceramic Matrix Composites," *Cer. Eng. Sci. Proc.*, 8 (7-8) (1987).
2. D.B. Marshall, B.N. Cox, and A.G. Evans, "The Mechanics of Matrix Cracking in Brittle-Matrix Fiber Composites," *Acta. Metall.*, 33 (11) (1985).
3. J.J. Smith et al., "Laser Generation of Ultrasound in High-Modulus Fibers," *Polymer Communications*, 28 (1987).
4. P.R. Stibich, D.A. Stubbs, and R.M. Kent, "Load-displacement and Ultrasonic Methods for Determining the Elastic Modulus of SiC Fibers," *J. Exp. Mech.*, in press.
5. P.B. Nagy and R.M. Kent, "Ultrasonic Assessment of Poisson's Ration in Thin Rods," *J. Acoust. Soc. Am.*, 98 (5) (1995).
6. D. Bancroft, "The Velocity of Longitudinal Waves in Cylindrical Bars," *Phys. Rev.*, 59 (April 1941).
7. E. Drescher-Krasicka, J.A. Simmons, and H.N.G. Wadley, "Guided Interface Waves," *Rev. Prog. Quantitative NDE*, 6B, ed. D.O. Thompson and D.E. Chimenti (New York: Plenum Press, 1987).
8. J.A. Simmons, E. Drescher-Krasicka, and H.N.G. Wadley, "Leaky Symmetric Modes in Infinite Clad Rods," *J. Acoust. Soc. Am.*, 92 (1992).
9. E. Drescher-Krasicka, J.A. Simmons, and H.N.G. Wadley, "Fast Leaky Modes on Cylindrical Metal-Ceramic Interfaces," *Rev. Prog. Quantitative NDE*. 9A, ed. D.O. Thompson and D.E. Chimenti (New York: Plenum Press, 1990).
10. P.B. Nagy, "Leaky Guided Wave Propagation Along Imperfectly Bonded Fibers in Composite Materials," *J. of Non Destructive Eval.*, 13 (3) (September 1994).
11. R.M. Kent and M.J. Ruddell, "An In Situ Sensor for Process Monitoring and Control of Composites" (Paper presented at the 41st Sagamore Conference on Intelligent Processing of Materials, Plymouth, MA, 1994).

ABOUT THE AUTHORS

Renee M. Kent earned her Ph.D. in materials science in 1992. She is currently a research scientist for the National Institute of Standards and Technology at the Materials Directorate, Wright-Patterson Air Force Base.

Mark J. Ruddell earned his technician's diploma in electronic technology from the Ohio Institute of Technology in 1976. He is currently a nondestructive evaluation technologist in the Structural Integrity Division of the University of Dayton Research Center.

For more information, contact R.M. Kent, Materials Directorate, Wright-Patterson Air Force Base, Ohio 45433-7817; (513) 255-9794; fax (513) 255-9804.

This page intentionally left blank.

ULTRASONIC EVALUATION OF FIBER-MATRIX INTERFACIAL DEGRADATION OF TITANIUM MATRIX COMPOSITES DUE TO TEMPERATURE AND MECHANICAL LOADING

Mark P. Blodgett
Wright Laboratory, Materials Directorate
WL/MLLP, Wright-Patterson AFB, OH 45433-7817

Theodore E. Matikas
National Research Council Associate
WL/MLLP, Wright-Patterson AFB, OH 45433-7817

Prasanna Karpur
Research Institute, University of Dayton
Dayton, OH 45469-0127

Jay R. Jira
Wright Laboratory, Materials Directorate
WL/MLLN, Wright-Patterson AFB, OH 45433-7817

Drew Blatt
Wright Laboratory, Materials Directorate
WL/MLLN, Wright-Patterson AFB, OH 45433-7817

INTRODUCTION

The study of elevated temperature interfacial degradation in environmentally-exposed titanium matrix composites (TMC) is essential for the life prediction of this important class of intermediate temperature materials. Ultrasonic evaluation of the interface, using scanning ultrasonic microscopy, is well suited for the evaluation of the interfacial degradation process [1-3]. The ultrasonic microscopy can be effectively used to delineate the impact of stress, temperature, and duration of exposure of the fiber-matrix interface in titanium matrix composite materials [1, 2]. In this study, test coupons have been subjected to cyclical mechanical loading with either isothermal exposure to temperature, or superimposed cyclical thermal loading (in-phase or out-of-phase with mechanical loading). Ultrasonic microscopy (50 MHz) has been used, which clearly demonstrates the capability to monitor the matrix cracking as well as the growth and accumulation of interfacial degradation. The progress of the interfacial degradation process for composite specimens with different stress concentration geometries has been studied. The results of this study provide an understanding of the failure mechanisms because of the interrupted fatigue crack growth tests. Metallographic analyses have been conducted to validate the ultrasonic evaluations.

BACKGROUND INFORMATION

Scanning Acoustic Microscopy (SAM), schematically shown in Figure 1, was developed by Quate, *et al.* [4] for the nondestructive evaluation of electronic components. Since that time, SAM has been found to be extremely useful for materials research [1-3, 5-9]. The versatility of SAM for materials

research applications is due to the ability of ultrasound to penetrate optically-opaque materials to map the surface and subsurface elastic properties [10, 11]. The primary contrast mechanism in a SAM is the existence of Rayleigh waves when suitably defocused [1, 5, 12].

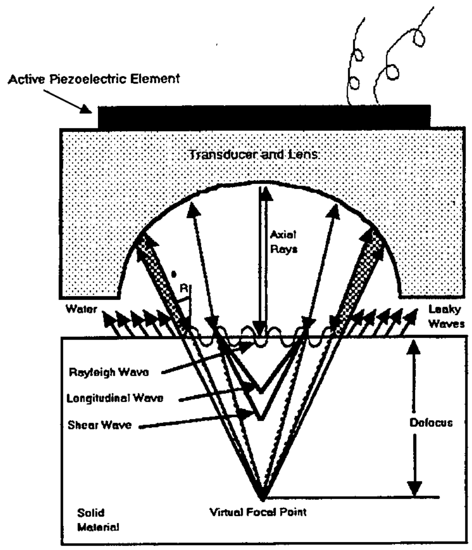

Figure 1. Schematic of a Scanning Acoustic Microscope showing the production of various modes of ultrasonic waves.

EXPERIMENTAL APPROACH

The primary objectives of this investigation were: to apply the principles of scanning ultrasonic microscopy to study the fiber-matrix interface after fatigue loading at elevated temperatures; to monitor the damage initiation, accumulation, and growth due to temperature and/or fatigue loading; and to understand the failure mechanisms in TMC using interrupted fatigue tests. Although shear waves are equally useful for the evaluation of fiber-matrix interface [13-16], this paper will outline the application of SAM technique for the interfacial evaluation.

A scanning acoustic microscope of 50 MHz frequency was used [1] to probe TMC samples for the characteristics of their fiber-matrix interface conditions, with broadband excitation. As seen from the transducer schematic, oblique rays near the perimeter of the transducer lens give rise to ultrasonic surface acoustic waves (SAW) in the samples which radiate energy back to the transducer for detection. In the TMC samples examined for this study, the penetration depth of the surface wave is approximately 0.066 mm. In addition to the surface waves, a specularly-reflected component of energy is generated from the direct ultrasonic beam, and also weakly scattered energy from shear waves. In order to separate (in time) the SAW from the specular reflection, the transducer was defocused by approximately 0.75 mm. The defocusing of the SAM provides an excellent, high-contrast image for the analysis of elastic property information [1, 5].

RESULTS AND DISCUSSION

To image the first layer of fibers and the associated interfacial conditions, the SAM transducer was scanned and the reflected SAW signal amplitude data was software-gated [17]. An example of data from one of the preliminary scans is illustrated in Figure 2, which shows the first layer fiber-matrix interface of a four-ply undirectional TMC sample. This sample was isothermally fatigue [18] loaded ($R = 0.1$, 182 Kilocycles, 650°C) for approximately 50 hours, after which the sample failed. Figure 2 clearly

shows the capability of the SAM technique to locate surface-breaking cracks and to determine the extent of fiber-matrix interfacial oxidation damage in this material.

Preliminary results shown in Figure 2 illustrate some interesting details regarding the interfacial damage accumulation process in TMC. Surrounding the stress concentration notch (hole), the indications of surface-breaking cracks and interfacial damage are clearly seen. The damage is dictated by the composite lay-up, as well as the thermal and mechanical environment, as predicted by the shear-lag model [2, 3, 19]. Also, the stresses cross over from tensile to compressive (near 8 and 10 o'clock positions of the hole) and are obvious from the figure wherein the reduced interfacial damage occurs at the locations of least stress intensity. An additional indication from Figure 2 is that compressive residual stresses (9 o'clock position of the hole) are less conducive to interfacial oxidation process than tensile stresses, but more conducive than no stresses of either type.

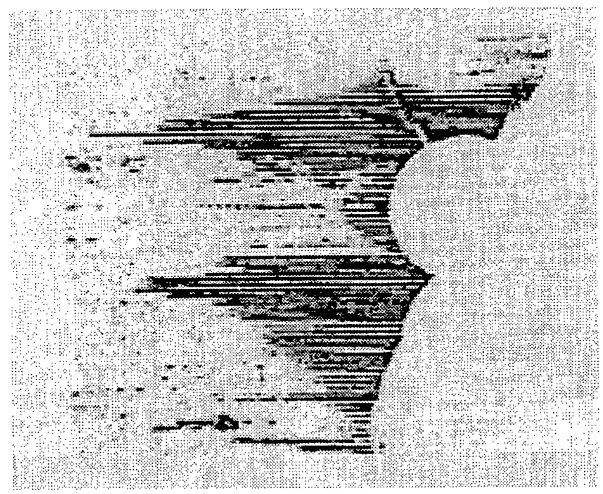

Figure 2. SAM image of TiMetal/SCS-6 after undergoing isothermal fatigue for 182 Kcycles, 650°C.

In order to further understand the damage accumulation process in TMC materials due to the combination of heat and fatigue loading, an interrupted fatigue crack growth experiment was conducted with SAM imaging at each interruption. A four-ply, bi-directional $[0/90]_S$ TMC consisting of a TiMetal matrix (Ti-15Mo-3Nb-3Al-0.2Si) and SCS-6 reinforcing fibers was used for the experiment. A series of three images is shown in Figure 3 (a, b and c) resulting from SAM scanning prior to thermomechanical testing, after an initial increment of thermomechanical testing, and after a final increment of testing, respectively. In all cases, the scan parameters were identical. Figure 3a shows no damage before fatigue loading. Figure 3b shows the results of 154 Kcycles fatigue loading during 43 hours at 650°C. In this image, similar features to those of Figure 2 are seen. Differences between the image of Figure 2 and Figure 3b are primarily due to composite lay-up, *i.e.*, unidirectional versus bi-directional.

In Figure 3c, the results of an additional 97 Kcycles fatigue loading and 27 hours at 650°C are shown. The shape of the damage at the crack tip and wake suggests that it is not only stress and temperature which dictate the level of interfacial degradation, but a third factor related to the duration of exposure to the damage-inflicting environment that the interface incurs. This suggestion also seems to hold based on the shape of interfacial degradation at the crack wakes, where the distinctive 'parabolic' growth pattern is observed. Fiber bridging [2, 3, 19] and oxygen pumping due to mechanical fatigue loading at the crack tips and at the wakes is thought to be a key factor which produces this interesting damage growth phenomenon.

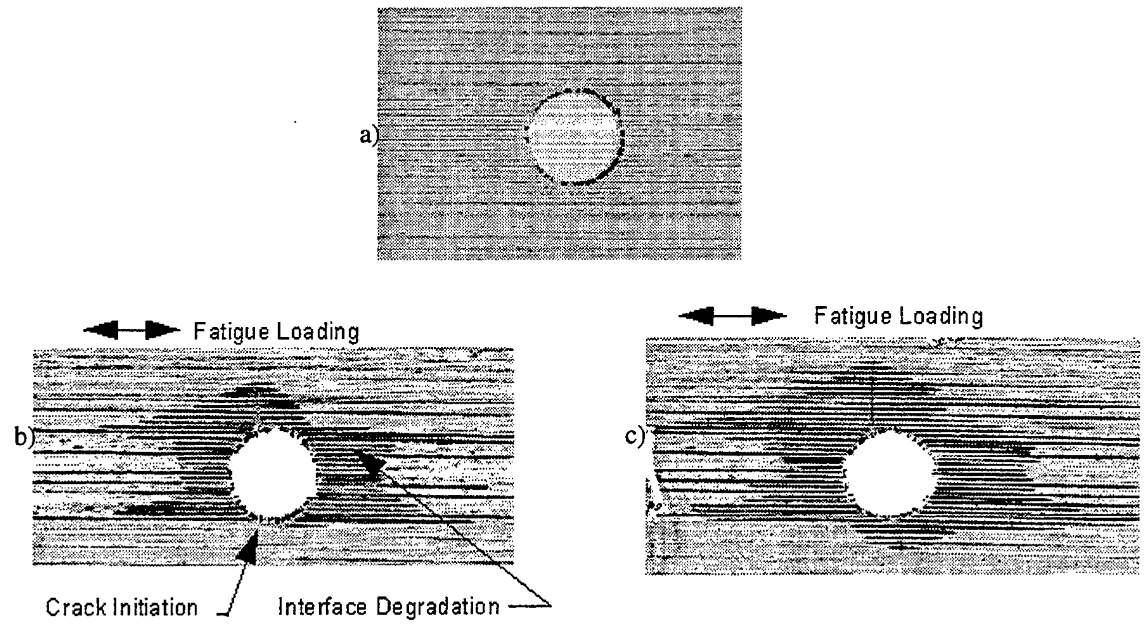

Figure 3. a) SAM image of a bi-directional $[0/90]_s$ TiMetal/SCS-6 TMC with circular notch configuration prior to mechanical testing; b) SAM image following 154 Kcycles isothermal fatigue at 650°C for 43 hours; c) SAM image following an additional 97 Kcycles of fatigue at 650°C for 27 hours.

The metallographic result from chemical etching of the matrix material is shown in Figure 4, which indicates in the region of the cracks, the interfacial degradation process occurs in a more diffuse manner than initially believed, and grows to a level where it finally becomes saturated, which is thought to result in complete loss of the interface load transfer capability. The indications in Figure 4 show that the interface degradation process is gradual and takes time, as seen where the 'older' (above) of the two cracks is visually distinguishable in contrast to the 'new' (below) crack.

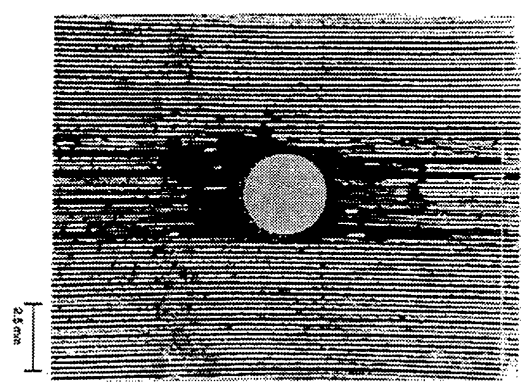

Figure 4. Metallographic result of sample from Fig. 3 showing visible evidence of interfacial degradation.

In another study, a TMC sample (TiMetal/SCS-6) with a different notch configuration was analyzed with the SAM approach. This sample (4-ply, unidirectional) was thermomechanically fatigue tested (R = 0.1, 150°C-538°C, 36 days) with out-of-phase heating and loading. The result of SAM is shown in Figure 5. This image holds a variety of interesting features which illustrate the effect of the combination of stress, temperature, and duration of exposure on the fiber-matrix interfacial properties in TMC.

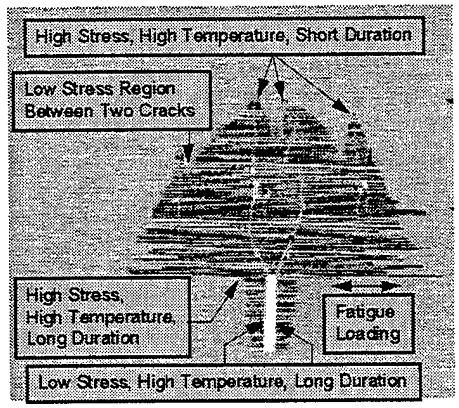

Figure 5. SAM image of TiMetal/SCS-6 TMC with slotted notch configuration following thermomechanical fatigue for 36 days.

In Figures 5 and 6, the most severe damage is seen at the notch root, where the stresses are the highest; therefore, the combined affects of high stresses, high temperatures and long duration accrue the most. Also emanating from the notch root are surface-breaking cracks that act as extreme stress concentrators at the crack tip with stresses falling off towards the wake. These cracks have clearly grown to a substantial length. At the crack tip regions, again, the characteristic degradation growth pattern is observed, resulting primarily from affects of high stress and temperature. In the region of the notch away from the root, it is interesting to note the shape of damage taking place where the affects from stress are the least significant, resulting in effectively flat growth. Finally, in this image (Fig. 5), there was observed a region between two cracks where the degradation pattern changed significantly due to the relief of stress between adjacent cracks, resulting in a region where the growth rate effectively decreases in comparison to those regions without adjacent cracks in the load path. Metallographic analysis was also performed on this specimen, as shown in Figure 6, which provided a close correlation to the NDE result. It is thought that the interfacial damage in this sample had reached maturity as the duration of exposure was very long and the crack growth rate was slow, resulting with all interfacially-degraded regions having fully-visible damage.

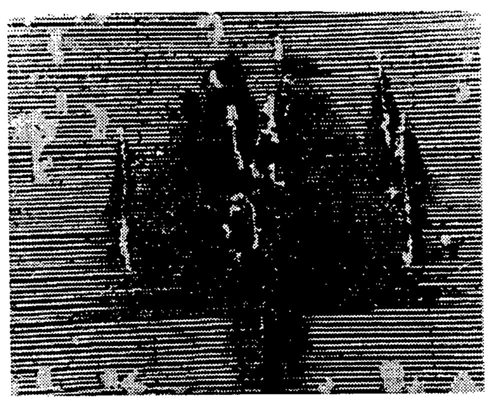

Figure 6. Metallographic result of sample from Fig. 5.

CONCLUSIONS

This investigation has shown that ultrasonic NDE facilitates interrupted tests during fatigue experiments by ensuring that the sample is available for further tests of interest. Additionally, it has been shown that ultrasonic NDE is effective in characterizing the fiber-matrix interface in TMCs and provides a useful tool to help the materials developers to: 1) evaluate the interface for degradation and debonding during temperature and mechanical fatigue tests; 2) obtain an accurate measurement of the fiber degradation length

produced due to material behavior experiments; and 3) monitor crack initiation and growth. The results seen in this study conclusively demonstrate the usefulness of the SAM to evaluate TMC materials subjected to the combined effects of stress, temperature, and extended duration of exposure to severe environment.

REFERENCES

1. P. Karpur, T.E. Matikas, M.P. Blodgett, J.R. Jira and D. Blatt, "Nondestructive Crack Size and Interfacial Degradation Evaluation in Metal Matrix Composites Using High Frequency Ultrasonic Microscopy", *Symposium on Special Applications and Advanced Techniques for Crack Size Determination*, in print, Atlanta, Georgia, USA (1993).
2. D. Blatt, P. Karpur, D.A. Stubbs and T.E. Matikas, "Observations of Interfacial Damage in the Fiber Bridged Zone of a Titanium Matrix Composite", *Scripta Metallurgica et Materialia*, Vol. 29 (1993) pp. 851-856.
3. D. Blatt, "Fatigue Crack Growth of Metal Matrix Composites Under Thermomechanical Loading," Ph.D. (under preparation), Purdue University (1993).
4. C.F. Quate, A. Atalar and H.K. Wickramasinghe, "Acoustic Microscopy with Mechanical Scanning – A Review", *Proceedings of the IEEE*, Vol. 67 (1979) pp. 1092-1114.
5. H.L. Bertoni, "Rayleigh Waves in Scanning Acoustic Microscopy", *Rayleigh-Wave Theory and Application*, Vol. 2, The Royal Institution, London (1985) pp. 274-290.
6. C.W. Lawrence, G.A.D. Briggs, C.B. Scruby and J.R.R. Davies, "Acoustic Microscopy of Ceramic-Fibre Composites; Part I: Glass-Matrix Composites", *Journal of Materials Science*, Vol. 28 (1993) pp. 2635-3644.
7. C.W. Lawrence, G.A.D. Briggs and C.B. Scruby, "Acoustic Microscopy of Ceramic-Fibre Composites; Part II: Glass-Ceramic-Matrix Composites", *Journal of Materials Science*, Vol. 28 (1993) pp. 3645-3652.
8. C.W. Lawrence, G.A.D. Briggs and C.B. Scruby, "Acoustic Microscopy of Ceramic-Fibre Composites; Part III: Metal-Matrix Composites", *Journal of Materials Science*, Vol. 28 (1993) pp. 3653-3660.
9. K.K. Liang, G.S. Kino and B.T. Khuri-Yakub, "Material Characterization by the Inversion of V(z)", *IEEE Transactions on Sonics and Ultrasonics*, SU-32 (1985) pp. 213-224.
10. G.A.D. Briggs, *An Introduction to Scanning Acoustic Microscopy*, Oxford University Press – Royal Microscopical Society, Oxford (1985).
11. G.A.D. Briggs, *Acoustic Microscopy*, Oxford University Press, Oxford (1992).
12. C.F. Quate, "Acoustic Microscopy", *Physics Today*, Vol. 38 (1985) pp. 34-42.
13. T.E. Matikas and P. Karpur, "Ultrasonic Reflectivity Technique for the Characterization of Fiber-Matrix Interface in Metal Matrix Composites", *Journal of Applied Physics*, Vol. 74 (1993) pp. 228-236.
14. P. Karpur, T.E. Matikas and S. Krishnamurthy, "A Novel Parameter to Characterize the Fiber-Matrix Interphase/Interface for Mechanics of Continuous Fiber Reinforced Metal Matrix and Ceramic Matrix Composites", *Journal of Composites Science and Technology*, submitted (1993).
15. P. Karpur, T.E. Matikas and S. Krishnamurthy, "Matrix-Fiber Interface Characterization in Metal Matrix Composites Using Ultrasonic Imaging of Fiber Fragmentation", *Seventh Technical Conference on Composite Materials, Mechanics and Processing*, Vol. 1, Pennsylvania State University, University Park, PA (1992) pp. 420-427.
16. P. Karpur, T.E. Matikas, S. Krishnamurthy and N. Ashbaugh, "Ultrasound for Fiber Fragmentation Size Determination to Characterize Load Transfer Behavior of Matrix-Fiber Interface in Metal Matrix Composites", *Review of Progress in Quantitative NDE*, Vol. 12B, eds. D.O. Thompson, D.E. Chimenti (1992) pp. 1507-1513.
17. C.F. Buynak, T.J. Moran and R.W. Martin, "Delamination and Crack Imaging in Graphite-Epoxy Composites", *Materials Evaluation*, Vol. 47 (1989) pp. 438-447.
18. J.R. Jira and J.M. Larsen, "Fatigue of Unidirectional SCS-6/Ti-24Al-11Nb Composite Containing a Circular Hole (Part II)", companion paper submitted to *Metallurgical Transactions A*, Carnegie Mellon University, Pittsburgh, PA 15213 (*Metall. Trans.*) (1993).
19. D.B. Marshall, B.N. Cox and A.G. Evans, "The Mechanics of Matrix Cracking in Brittle-Matrix Fiber Composites", *Acta Metallurgica*, Vol. 33 (1985) pp. 2013-2021.

ULTRASONIC IMAGING OF CORRODED ALUMINUM SHEET

OBJECTIVE

This work effort was conducted to determine some of the capabilities of the SMALL-tank ultrasonic system relative to quantifying the depth and lateral extent of corrosion on a thin aluminum sheet. The work was undertaken to provide information regarding these capabilities to the NDE group in MLSA.

RESULTS -- OPTIMAL IMAGES

An optical image of a section of the corroded surface is shown in Figure 1. This image was obtained by using an optical scanner which scanned the actual aluminum part. The wide, dark lines in Figure 1 are from a marking pencil. An optimized, 256-grey-level, ultrasonic C-scan image of the same corroded section of the aluminum sheet is shown in Figure 2. Darker shades in the ultrasonic image represent more material loss whereas lighter shades represent less material loss. A grey-level calibration scale is provided to allow the reader to estimate the percent thickness loss from the ultrasonic image. The image in Figure 3 (same image as in Figure 2) shows percent loss of thickness due to the corrosion in six discrete shades of grey. The ultrasonic C-scan images shown in Figures 2 and 3 were generated from B-scans after applying signal-processing techniques (deconvolution and filtering) to the individual A-scans; this signal-processing optimized the depth and lateral resolution for the transducer used during data acquisition.

Figure 1 -- Optical image of corroded aluminum sheet

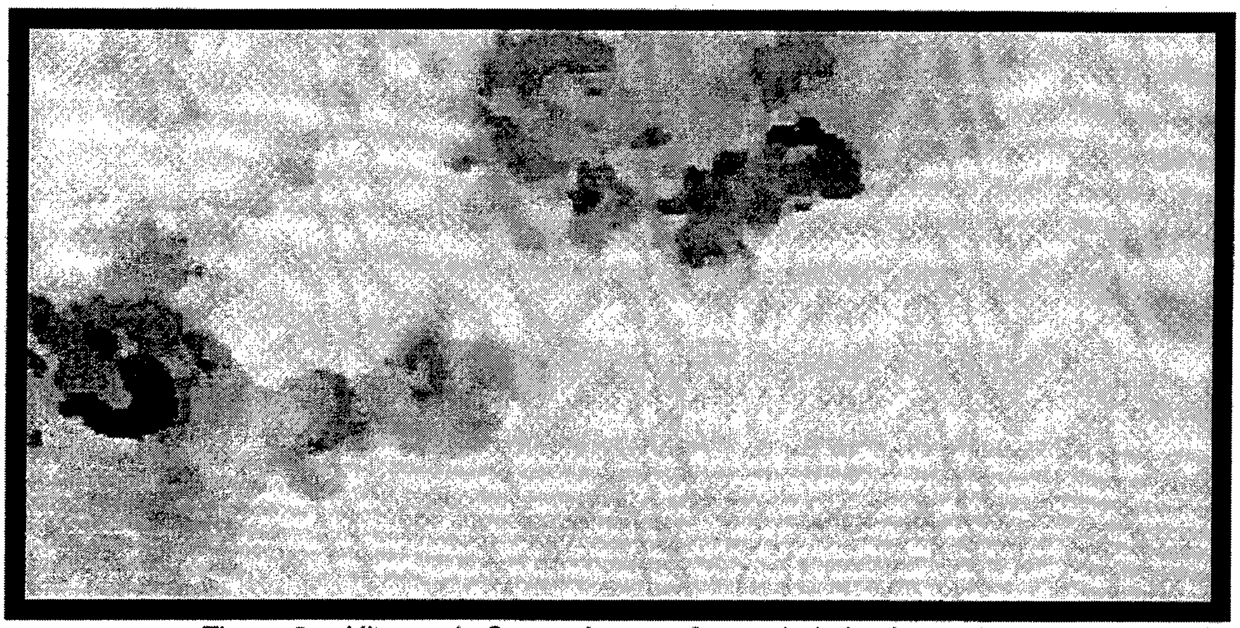

Figure 2 -- Ultrasonic C-scan image of corroded aluminum sheet

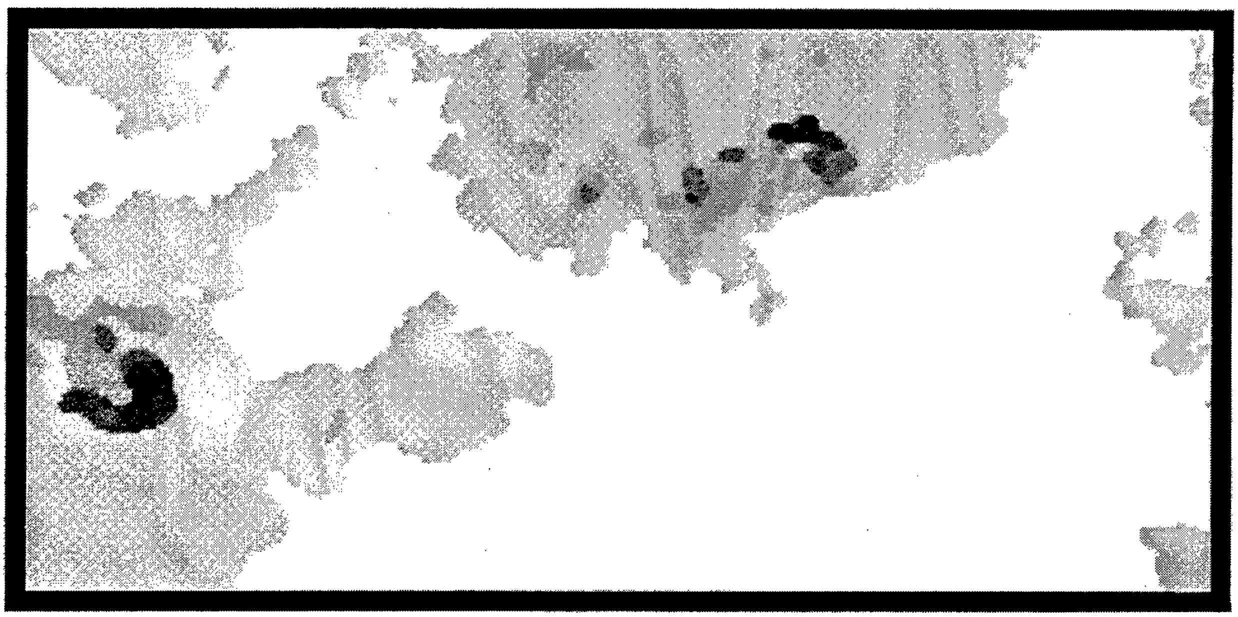

Figure 3 -- C-scan image from Figure 2 representing thickness loss in six discrete shades of grey: (1) > 0 to 10%, (b) > 10% to 20%, (c) > 20% to 30%, (d) > 30% to 40%, (e) > 40% to 50%, and > 50%.

ULTRASONIC-DATA ACQUISITION

Data were acquired from a 7.4 cm X 3.5 cm (2.9 in X 1.4 in) section of a 0.10 cm (0.04 in) thick aluminum sheet via immersion ultrasonic scanning. The noncorroded side of the aluminum sheet was used as the ultrasonic entry-surface and the corroded surface as the ultrasonic back surface; this simulated "hidden" corrosion. Three-dimensional RF B-scan data were digitized and stored prior to any image generation. This allowed signal-processing techniques to be applied to the data prior to image generation. The "align all A-scans" functions was used during data collection because of the slight curvature of the aluminum. This made visual interpretation of the RF B-scans easier. The transducer and data-collection parameters are listed in Table 1.

TABLE 1 -- Data Acquisition Parameters

PARAMETER	VALUE OR LOCATION
Transducer	
Center Frequency	25 MHz
Element Diameter	6.3 mm (0.25 in)
Focal Length in Water	51 mm (2 in)
Focal-Spot Size in Water	0.47 mm (0.019 in)
Location of Focal Spot	Front Surface of Sample
Scan Parameters	
Number of B-Scans	139
Distance Between B-Scans	0.25 mm (0.01 in)
No. of A-Scans per B-Scan	290
Distance Between A-Scans	0.25 mm (0.01 in)
Digitizing Parameters	
Digitizing Rate	200 MegaSamples/Sec
Time per Point	5 nSec
No. of Points per A-Scan	512

SIGNAL PROCESSING

Cutting the B-Scans. Each of the A-scans in the original data sets was 512 points long. This was longer than necessary to include the back surface echo from aluminum sheets with no curvature, but was necessary to ensure collection of back-surface echoes from the curved sheet. However, since the software algorithm, BTOC, which converts the B-scans to C-scans stores data in an 8-bit format, the depth resolution in time-of-flight (TOF) C-scans would decrease from a theoretical (but unachieved) maximum of 0.04 mm (0.0015 in) to 0.08 mm (0.003 in). After alignment of the A-scans by the collection algorithm it was evident that the length of the A-scans could be cut to less than 256 points (Figure 4). Therefore, the algorithm EXTRACT_3D_VOLUME was applied to the three-dimensional data sets to decrease the length of each A-scan to 256 points. This preserved the theoretical maximum depth resolution.

Deconvolving the A-Scans. Deconvolution is a signal-processing technique that is used to remove the system response from a signal. When applied to ultrasonic signals, the effect is to widen the bandwidth (shorten the pulse length) of the ultrasonic transducer being used. This pulse-length shortening improves the depth and near-entry-surface resolution. Deconvolvution can also improve lateral resolution by decreasing the focal spot size due to the amplification of the higher frequencies which are present in the ultrasonic pulse. For these reasons (primarily for improvement in near-entry-surface depth resolution), all A-scans in the three-dimensional B-scans were deconvolved using the algorithm, AXWIENER_POST-FILTER. The value of the noise constant used for the deconvolution process was 1. The deconvolved A-scans were bandpass filtered to remove very low frequencies (below 3 MHz) and very high frequencies (above 36 MHz).

Figure 5 shows an example of the entry-surface echo from the aluminum sheet before and after deconvolution. Also shown in the figure are the frequency spectra (magnitude only) of an entry-surface echo for the before and after deconvolution cases. In this case, the relatively large value (1.0) of the pseudo noise constant did result in a decrease in the ring time, but did not broaden the band width significantly.

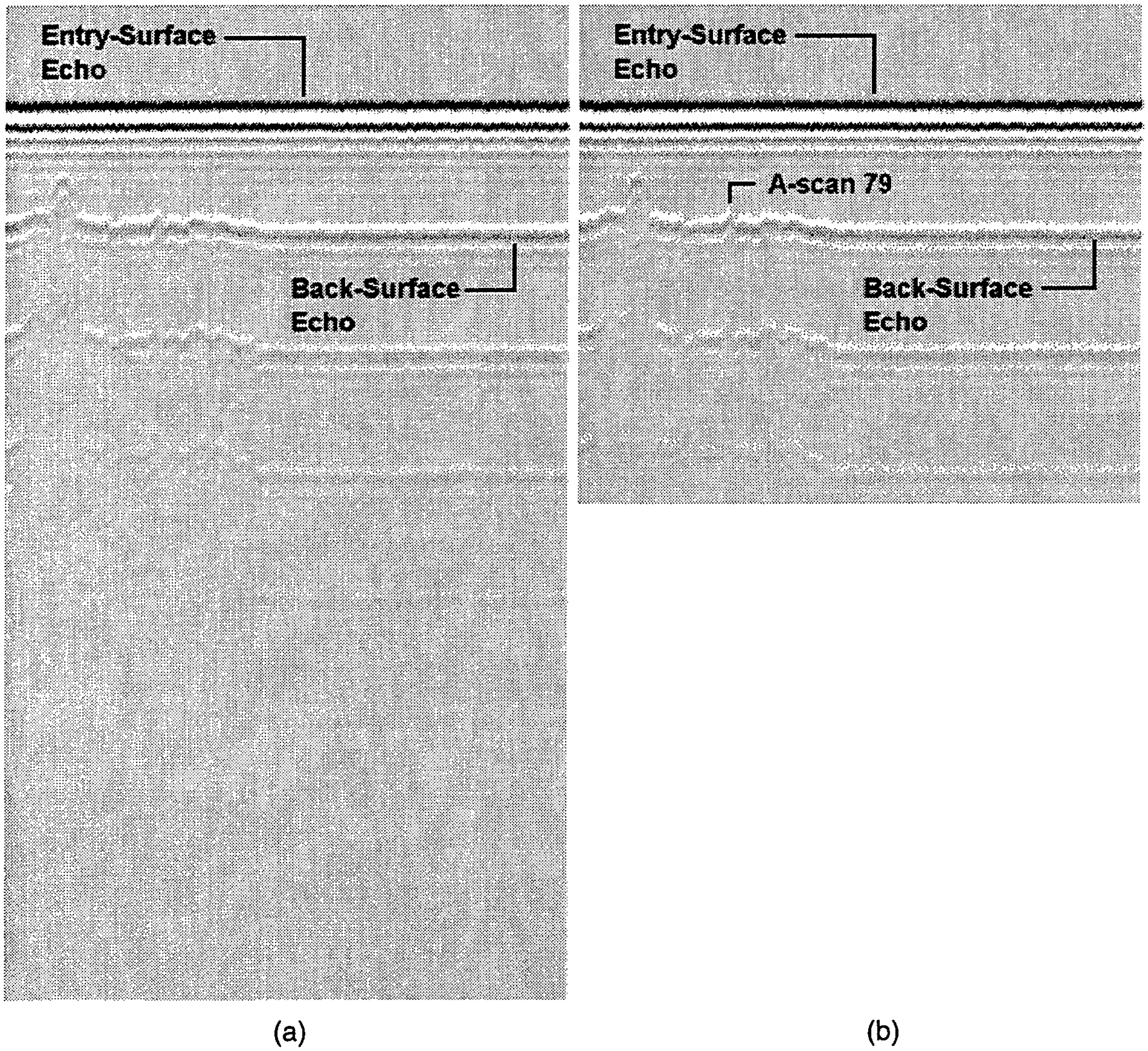

Figure 4 -- B-scan number 89: (a) original, and (b) after eliminating last 256 points from each A-scan.

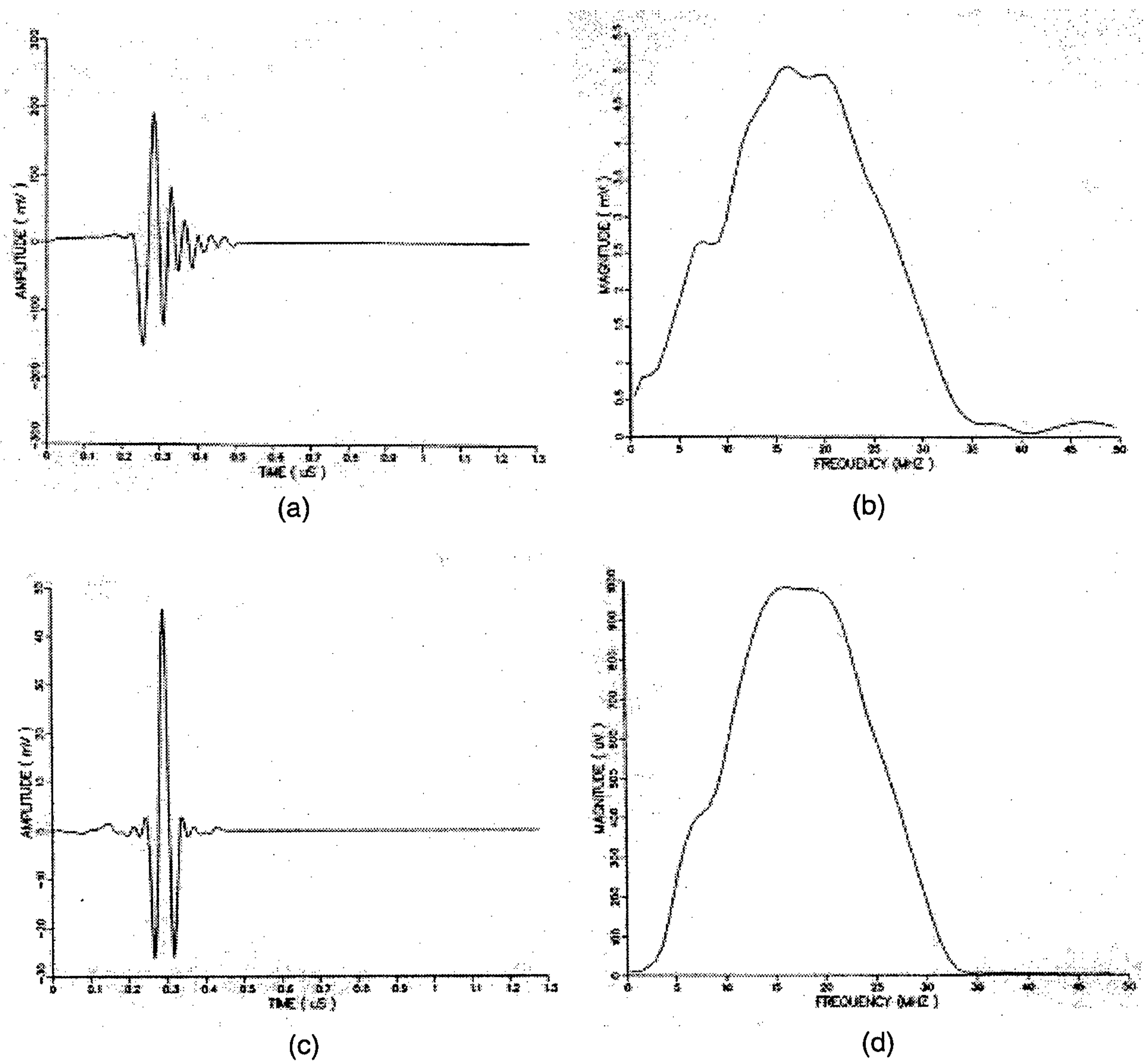

Figure 5 -- Entry-surface echoes and their Fourier magnitude spectra: (a) Entry-surface echo before signal processing; (b) Fourier magnitude spectra of "a"; (c) entry-surface echo after deconvolution; and (d) Fourier magnitude spectra of "c".

C-SCAN IMAGE GENERATION

The computer algorithm BTOC was used to generate C-scans from the cut but not deconvolved three-dimensional B-scans as well as from the cut, deconvolved and bandpass filtered three-dimensional B-scans. C-scans were made from time-of-flight data (TOF to the back-surface echo) and from the amplitude of the back-surface echo.

<u>C-Scans from B-Scans which Were Not Deconvolved</u>. The entry-surface echo of the ultrasonic transducer continued ringing for a time period which was sufficient for ultrasound to travel more than half-wave through the aluminum sheet (Figure 6). It was, therefore, highly probable that the echo returning from regions of deep corrosion would

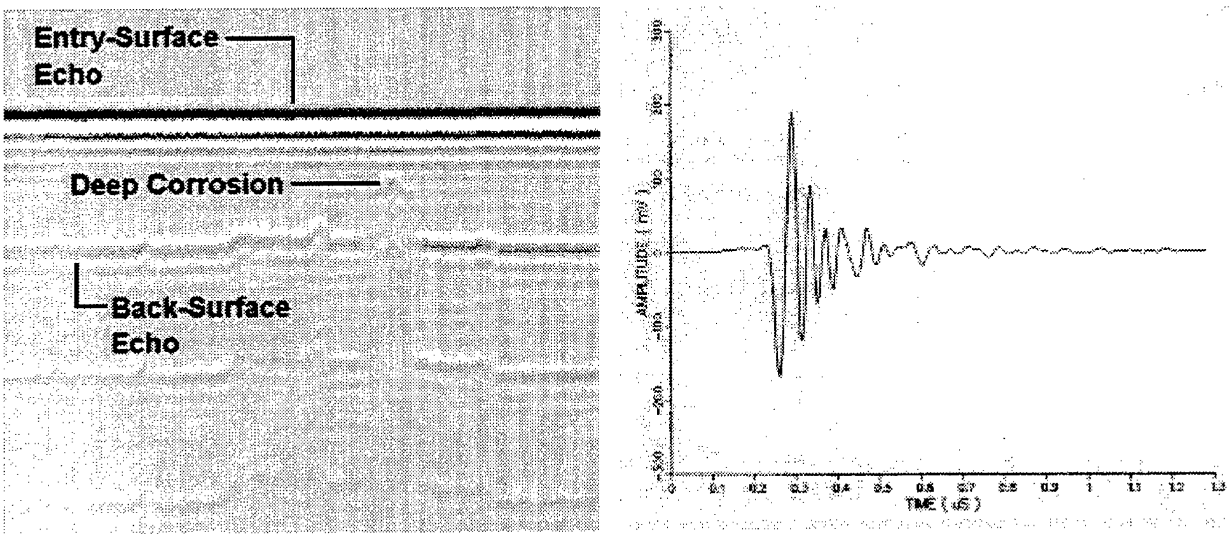

(a) (b)

Figure 6 -- Deep corrosion: (a) B-scan image after eliminating last 256 points in each A-scan, but before deconvolution; and (b) A-scan from "deep corrosion" area of "a".

be overlapped by part of the entry-surface echo. Mapping the deepest regions of corrosion required setting the start of the gate in the part of the entry-surface echo. This might, however, give rise to false indications of corrosion depth in some cases. Thus, three different sets of C-scans were generated from these nondeconvolved B-scans by varying the width of the gate. The gate width was varied by changing the starting time of the gate -- relative to a reference which was slaved to a threshold level of the entry-surface echo -- while holding the ending time of the gate constant. For the two wider gates, the trailing cycles of the entry-surface echoes extended into the starts of the gates (Figure 7).

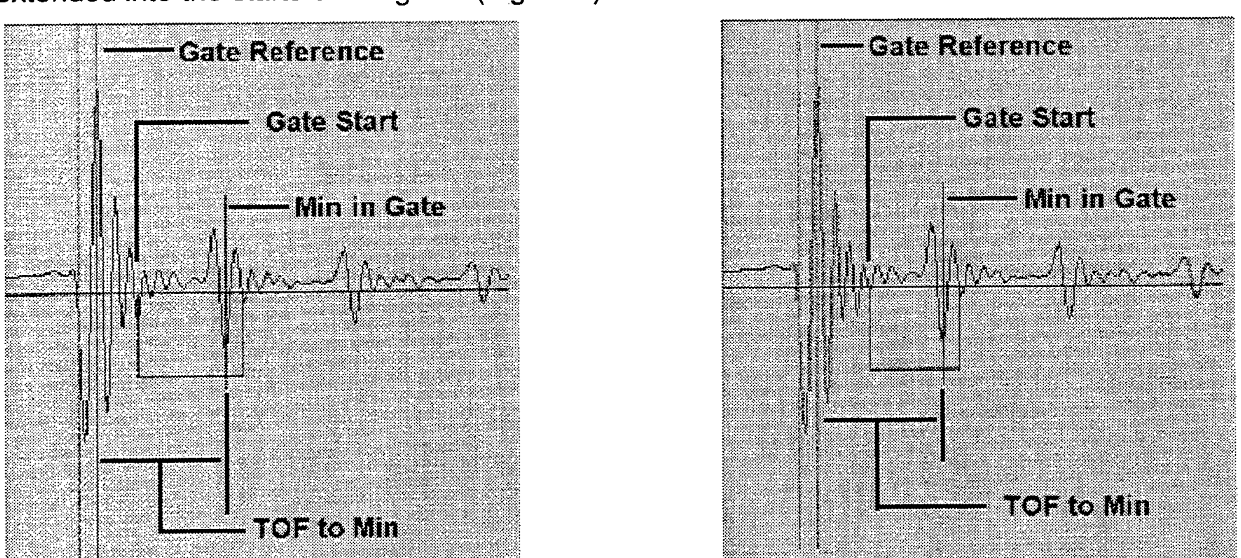

(a) (b)

Figure 7 -- Two gate settings for generating C-scan data: (a) gate start at 100 nS from reference (255 nS wide), and (b) gate start at 130 nS from reference (225 nS wide).

C-Scans from Deconvolved B-Scans. Since the deconvolution process significantly shortened the entry-surface echo, the entry-surface echo did not overlap echoes from the back surface even in regions for which the corrosion was very deep (Figure 8). Thus, a single wide gate was used to generate the C-scans from the B-scans, and only one set of C-scans was generated for each of the two deconvolved three-dimensional B-scans.

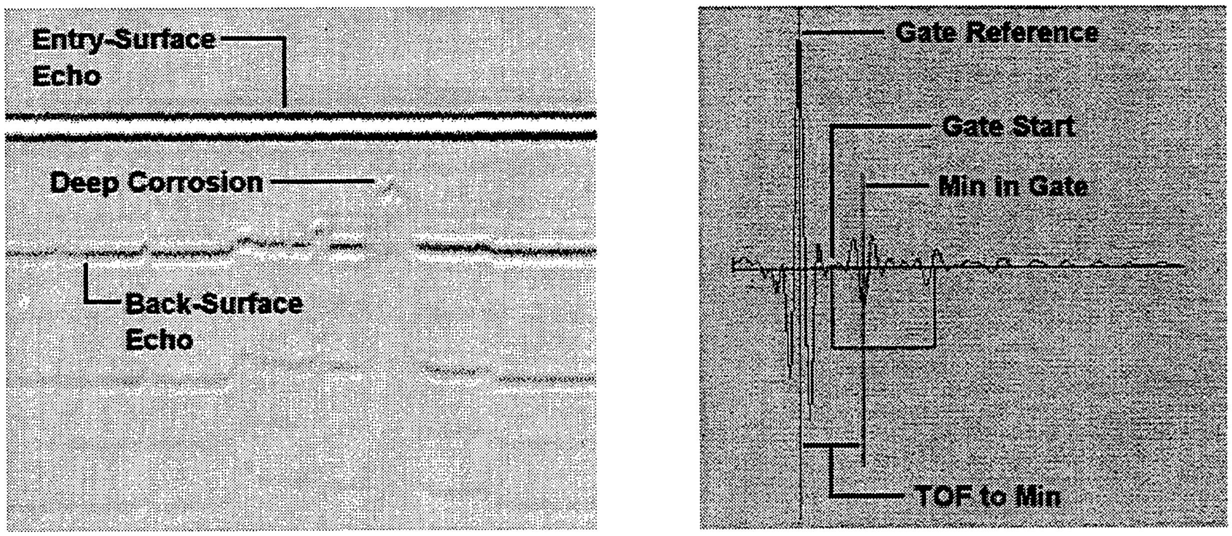

(a) (b)

Figure 8 -- Results of deconvolving the A-scans: (a) deconvolution of the image in Figure 6a; and (b) deconvolution of the A-scan in Figure 6b.

C-SCAN IMAGE RESULTS

C-Scans from B-Scans which Were Not Deconvolved. Time-of-flight C-scan images generated from the nondeconvolved B-scans are shown in Figure 9. The most important feature to note is the correlation between gate-start-time and number of dark speckles in the image. As the time between the reference and the start of the gate was decreased, the number of speckles increased.

The time-of-flight C-scans were generated from the time-of-flight from a reference location in the entry-surface echo to the maximum absolute value of the negative half-cycles in the gate. This maximum absolute value of the negative half cycles should occur in an echo from the back surface of the sheet or from a corrosion pit. However, in some cases enough energy was scattered away from the transducer that the maximum absolute value of the negative half cycles occured in the ring-down portion of the entry-surface echo which was within the gate. This is illustrated in the A-scans (number 79 from the image in Figure 4b) of Figure 10. Setting the start of the gate closer to the peak of the entry-surface echo increased the probability that one of the negative half cycles in the entry-surface echo would be the maximum negative half cycle within the gate.

C-Scans from Deconvolved B-Scans. The time-of-flight C-scan images in Figures 2 and e were generated from deconvolved B-scans. These C-scan images have almost no dark speckles. Figure 11 shows the deconvolved B-scan and A-scan which correspond with the B-scan (Figure 4b) and A-scan (number 79) shown in Figure 10.

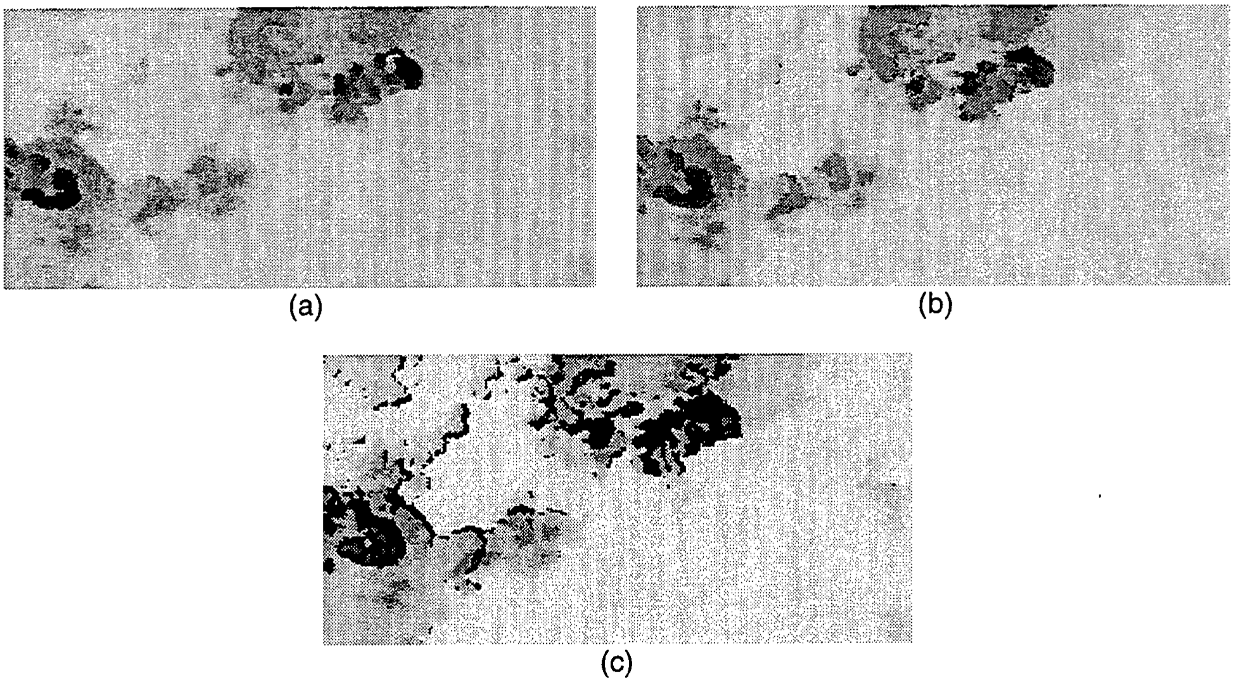

Figure 9 -- Time-of-Flight C-Scans acquired with three different gate start times: (a) 170 nS from reference; (b) 130 nS from reference; and (c) 100 nS from reference.

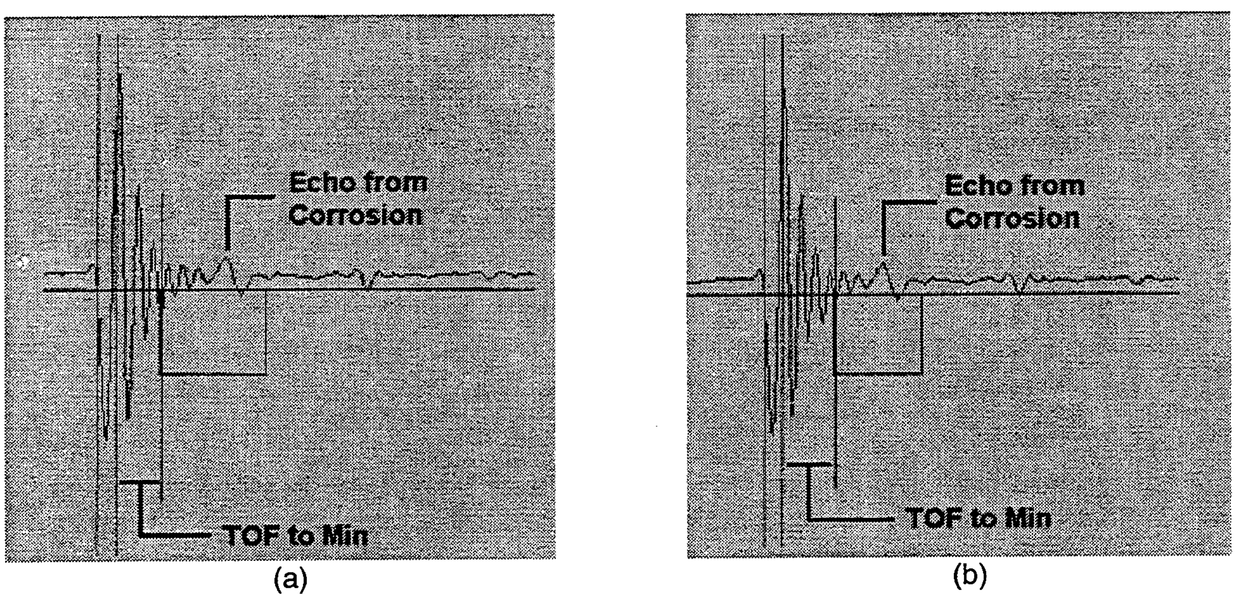

Figure 10 -- Source of Some False Indications of Thin Material: (a) gate start time = 100 nS from reference; and (b) gate start time = 130 ns from reference.

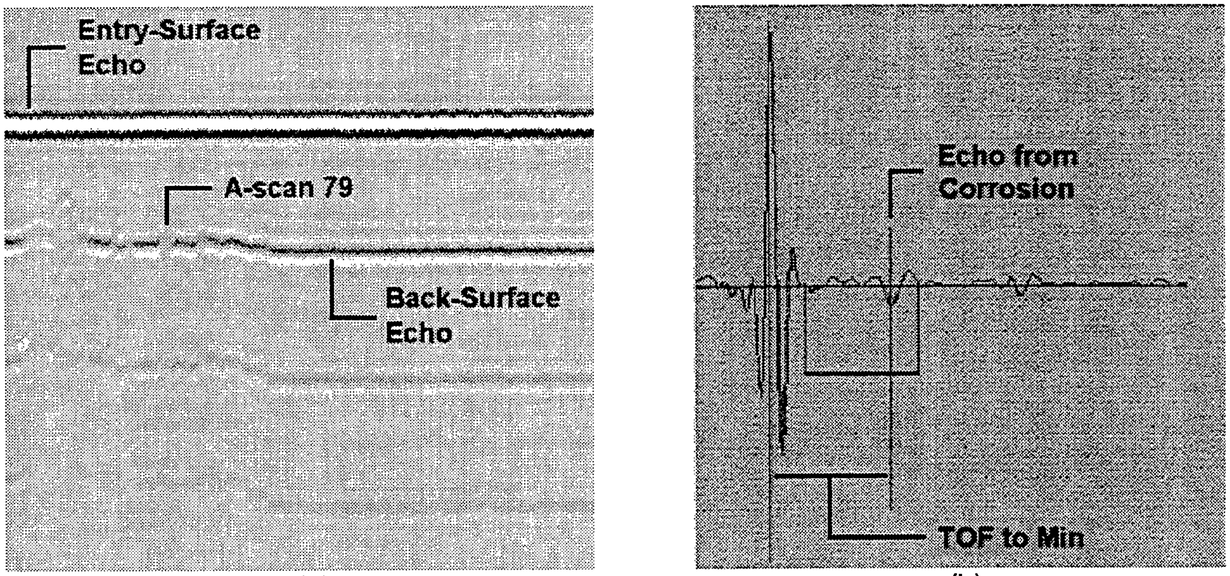

(a) (b)

Figure 11 -- Results of Deconvolving the B-scan in Figure 4b: (a) deconvolved B-scan; and (b) A-scan 79 (with TOF gate) from “a”.

This page intentionally left blank.

UDR-TR-97-118

ULTRASONIC LAMB WAVE CHARACTERIZATION OF ADHESIVE JOINTS*

Final Report

Submitted to:

Mr. Tobey M. Cordell
Branch Chief
NDE Branch - WL/MLLP
Materials Directorate, Wright Laboratory
Wright-Patterson Air Force Base. OH

Prepared by:

Prasanna Karpur
Research Institute
University of Dayton
300 College Park Avenue
Dayton, OH 45469-0120

Phone: (937) 229-4481
FAX: (937) 229-3712
e-mail: karpurp@udri.udayton.edu

* This work was supported by the NDE Branch - WL/MLLP. Materials Directorate, Wright Laboratory, Wright Patterson Air Force Base, Ohio. Contract No. F33615-94-C-5213.

This page intentionally left blank.

Table of Contents

List of Figures

List of Tables

Executive Summary

This study outlines a Lamb wave-based methodology of assessing adhesively bonded structures. A novel approach of Lamb wave mode selection based on the displacement distribution profile has been used wherein the in-plane displacement distribution across the thickness of the sample has been used as a measure of mode sensitivity to interfacial conditions.

Steps necessary for the theoretical modeling of Lamb wave propagation in the structure and the calculation of the displacement, stress, and energy distributions have been shown. Further, two adhesively bonded samples have been used to demonstrate the feasibility of the methodology. One of the samples is an Al-epoxy-Al structure while the other is a Cu-epoxy-Al structure. Geometrical dimensions of these sample were measured and the values were used in the theoretical model to generate the dispersion curves as well as the displacement profiles (in-plane displacement).

The results obtained in this study very clearly demonstrate the robustness, sensitivity, and hence the feasibility of the approach. It has been shown that by proper mode selection based on the distribution profile, interfacial features from individual interfaces can be imaged. Any deviations from image to image obtained by different modes of Lamb waves can be easily described by the changes in the corresponding displacement distributions at the interfaces.

While this work has shown the feasibility of Lamb wave mode selection based on displacement distribution, further studies are necessary to understand the effect of the distribution patterns of normal displacement, stresses, and energy. Also, experimental Lamb wave imaging of several (statistically significant) samples followed by destructive corroborative analyses are necessary for the implementation of this technique with any degree of confidence.

Ultrasonic Lamb Wave Characterization of Adhesive Joints

1.0 Introduction

Use of adhesive joints in structures has become common practice in industries such as aerospace, automotive, civil infrastructure, etc. While the use of adhesive joints is increasing, the science of adhesive joint characterization during both production and use are inadequate at best for a reliable and confident use of these structures. Therefore, it is not uncommon to see redundant load bearing design when adhesive joints are used in critical applications. However, there are instances where such redundant design is impractical thereby necessitating a reliable method of nondestructive characterization of adhesive joints to assess the quality of the joints when made as well as to monitor the deterioration of properties during use.

There are various issues of concern during the manufacturing of adhesive joints. However, all the issues are primarily those of 'quality' of the bonded structure. The word 'quality' of a bonded structure is used to encompass porosity measure, voids, disbonds, bondline thickness, degree of curing, bond strength, and the life forecast of the structure. Thus, it is difficult to easily quantify the quality of an adhesive joint. However, both destructive and nondestructive techniques exist to individually quantify some aspects of quality such as porosity, debonding (with void), and bondline thickness. One of the most elusive yet critical problem is that of 'kissing bond' wherein good contact exists among the adherend and the adhesive, however with no acceptable levels of adhesion. To date, the

kissing bond is impossible to be detected reliably by any of the methods including conventional ultrasound and thermal waves.

Deterioration of adhesively bonded structure due to aging poses a different type of challenges for detection and quantification. Even if it can be assumed (although it is obviously not entirely true) that the bonded structure in service is devoid of any manufacturing defects and anomalies, the adhesive-adherand structure continues to lose its load bearing ability due to progressive property loss of the interface. Such loss of property might be due to damage (loading induced cracking, impact damage, etc.) induced in service or due to chemical changes occurring due to exposure to moisture, heat, chemicals, etc. In any case, such loss of functional properties of the structure is usually gradual. Nondestructive methods of tracking such property loss have been reported in the literature.

One of the most challenging problems to date has been the detection of kissing bonds wherein the adherend-adhesive interface exhibits good physical contact while lacking adhesion, either completely or partially. Such a manufacturing defect/anomaly will substantially compromise the load bearing capability of the adhesive joint by initiating adhesive failure (compared to cohesive failure wherein the failure occurs within the thickness of the adhesive layer instead of a failure at the interface). Attempts to develop methods of detection of kissing bonds have been unsuccessful to date because of lack of reliability. Development of a methodology to characterize kissing bonds and other adhesive joint defects/anomalies requires a knowledge of the developmental work to date, understanding of the manufacturing process, and mechanism of bonding. Therefore, next three sections will deal with these issues.

2.0 Adhesive Joints – Manufacturing Process

There are various types of adhesive joints such as metal-to-metal, metal-to-composite, composite-to-composite, metal-to-rubber, etc. The first two types namely, metal-to-metal and metal-to-composite, are of interest for this report. Further, the adhesive used can be thermosetting or thermoplastic. Most of the structural adhesive joints are based on thermosetting epoxy adhesives.

The various steps involved in the manufacturing of adhesive joints are preparation of adherends and adhesive, application of adhesive, assembly, curing, and finishing. Of these steps, preparation of the adherends and the curing process are the most two critical steps for the overall finished quality of the adhesively bonded joints.

Preparation of the adherends, a critical step for the overall quality of the finished joint, includes cleaning of the surfaces, washing to remove any cleaning residue and contaminants, treating the surface/s to be joined using chemical agents, rinsing to remove all traces of chemicals used to prepare the surface, and finally drying of the plates as a prelude for the adhesion. The initial cleaning of the plates will usually involve some mechanical process such as ultrasonic cleaning and/or sand blasting along with the application of solvents to remove any grease, oils from hand prints, etc. Particles resulting from sand blasting and other mechanical operations as well as traces of solvents used are removed by thoroughly washing the plates in deionized or distilled water. Chemical etching or anodizing is performed on the plates usually using a combination of chromic acid, sulfuric acid, and/or

phosphoric acid. The adherends are again thoroughly washed using distilled water to remove all traces of acids and other chemicals. At this stage, a coat of primer may be applied to promote bonding. Depending on the type of primer that may be applied, the adherends might be subjected to a curing cycle. Depending on whether a film type adhesive is used or a paste/liquid type adhesive is used, the application of the adhesive layer will be accomplished by placing the film and smoothing the wrinkles or by spraying or rolling process. The adherend-adhesive pairs are placed/stacked as required and cured.

The curing process is another important step which determines the overall quality of the finished product. There are several important factors during curing process which can adversely affect the quality if proper care is not exercised. The combination of degassing, curing temperature, time, and pressure determine the elastic properties of the cured epoxy, bonding at the interface, porosity, voids, uniformity of thickness of the adhesive layer, etc. If the preparation of the adherends as described in the previous paragraph is not accomplished as necessary, it has been shown that the quality of the adhesive joint will suffer even though proper processing conditions are utilized. Similarly, well prepared adherends can yield poor quality adhesive joints if improper processing conditions exist during manufacturing.

3.0 Mechanisms of Adhesion

Many theories have been proposed to describe the bonding mechanism in adhesive joints although no one mechanism has been conclusively shown to be true. Most of the theories can be grouped under four broad categories: (1) surface roughness and the resulting mechanical locking, (2) electrical bonding forces due to electrostatic locking, (3) atomic bonding forces due to adsorptive mechanisms such as covalent bonds, Van der Waals bond, etc., and (4) bonding due to molecular diffusion. While no one mechanism might solely contribute to adhesion, one or more mechanisms might play dominant roles in providing the adhesive forces necessary for the load bearing requirements of these joints.

Surface asperity – roughness and the resulting locking mechanism explains the need for surface preparation by sand blasting or similar other method. It is postulated that when the adherend surface is rough, the adhesive can flow into the ridges and depressions of the surface thereby bringing about the locking mechanism after curing. While this hypothesis appears to be a logical source of adhesive forces, the model fails to describe fully the force necessary to break the bonded structure. Electrical bonding theory postulates that the adhesive forces result from the electrostatic force between the electrically charged layers of the adherend-adhesive pair. The theory fails to adequately describe the total adhesive forces that exist in an adhesive joint. Atomic bonding forces due to adsorption appear to be widely accepted theory of adhesive bonding wherein several bonding mechanisms such as Vander Waals bonding, hydrogen bonding, ionic bonding, covalent bonding, etc., result in the bonding forces. Diffusion bonding process is a result of molecular diffusion at the interface. When the adherend and adhesives have loosely bonded molecules at the interface, the molecules can diffuse into each other thereby bringing about the bonding forces.

4.0 Work to Date by Other Researchers

Although almost all the existing NDE techniques have been studied for several decades to characterize adhesive joints, no one nondestructive method has been found to be completely successful for the application. For example, techniques such as thermal wave, are very effective in finding debonds (with physical separation), radiography is useful for finding voids and lack of adhesives, ultrasound is effective for the detection of porosity, lack of bonding and separation, etc. Techniques such as X-ray radiography, neutron radiography, eddy current, holography, acoustic emission, ultrasound, etc., have been used in the past for the characterization of adhesive joints. Since this report pertains to ultrasonic characterization of adhesive joints, this section will be dedicated to outlining past research reported in literature pertaining to acoustics and ultrasound.

Some of the early acoustic (or mechanical vibratory) method of assessment were based on inducing resonant vibration [1-3] in the structure to monitor the integrity of the adhesive joint as well as to determine the degree of curing. The logic behind the technique was that as the adhesive joint curing progressed (or progressively deteriorated during use), the elastic/mechanical properties of the structure undergo changes which are reflected in the modes of resonance of the structure as a whole. However, it is obvious from the approach that there is a sensitivity threshold under which the accumulated property changes are not detectable. Another method of characterization was the mechanical impedance method wherein localized mechanical impedance was measured [4]. The technique resulted in commercially available bond testing instrumentation. However, the technique was somewhat unreliable because the total impedance measured at a point was dependent not only on the

impedance of the structure but also on the impedance of the local support holding the sample. Mechanical tap testing has been used for a long time to test the localized structural 'tone' when stuck with a hammer-like transducer. The technique is a modification of the resonance method in that only the localized vibration is measured by tap testing. However, the technique is not very reliable and precise.

4.1 Ultrasonic Methods of Adhesive Joint Characterization

Ultrasonic techniques for the evaluation of adhesive joints can be broadly grouped into three categories: normal incidence reflection and transmission techniques, oblique incidence reflection and transmission techniques, and guided wave techniques. Each technique can be implemented in either time domain or frequency domain through Fourier transformations and signal processing approaches.

4.1.1 Normal incidence reflection and transmission techniques

These techniques involve the measurement of the reflection and/or transmission coefficients as indicators of adhesive joint quality. The transducers are set up normal to the sample and pulse-echo and/or through transmitted amplitudes are measured to calculate the respective coefficients [5-8]. When a 'perfect' bond exists at the interface, experimentally measured coefficients are expected to match the theoretically predicted coefficients based on elastic properties and densities of the materials mating at the interface. Any substantial deviations are attributed to the presence of debonds, voids, porosity, improper curing, etc.

However, the major drawback of this approach is the fact that compressional waves are insensitive to 'kissing bonds' wherein physical contact exists between the mating materials, with minimal or no bonding. Also, when implemented in the time domain, experimentally measured coefficients are due to many frequencies of ultrasound existing at the same time. Implementation in the frequency domain has been reported [6, 9-11] as an attempt to improve the accuracy as well as to apply feature based classification techniques [12] for the characterization of adhesive bonds.

4.1.2 Oblique incident reflection and transmission techniques

These techniques were introduced [13, 14] to overcome the limitation of the normal incidence technique which was found to be insensitive to the interfacial bonding conditions. Since oblique incidence applies shear stresses to the interface, the technique is believed to be sensitive to the boundary conditions (interfacial conditions). Researchers have shown [13, 14] that the reflection coefficients measured from the mode converted longitudinal waves and mode converted shear waves incident at the interface are very sensitive to the curing and interfacial bonding conditions. While the technique has been demonstrated to be effective in bond integrity assessment, implementation of the technique is not essentially easy since the sample will have to be scanned at various angles of incidence. Additionally, since the reflection coefficient of oblique ultrasonic waves is also dependent on the frequency of the ultrasound, implementation of the technique requires implementation either in the frequency domain or through tone burst operation.

4.1.3 Guided waves for interface characterization

Guided waves are generated by oblique incidence although the goal here is not to measure the reflection and/or transmission coefficients. Guided waves can be any one of several modalities: surface wave, interface waves - Stoneley waves, Lamb waves, etc. Surface waves have been used [2, 15, 16] to characterize the adhesive joints in applications wherein a smaller plate is applied as a patch on a larger area substrate or plate. This facilitates the launching of surface or Rayleigh type wave in the substrate which can be made to propagate into the adhesive joint. The technique has been recently utilized to inspect composite patches applied to aircraft structure to repair fatigue cracking [15]. This technique can also launch interfacial or Stoneley waves in the joint. Stoneley waves are shear type waves traveling along the interface between two solid layers and therefore are sensitive to the boundary condition at the interface. The Lamb wave or plate wave method of adhesive joint characterization has been studied extensively and will be discussed in the next chapter as a prelude to reporting the contributions of the present project.

5.0 Adhesive Joint Characterization Using Lamb and Guided Waves – Literature

Lamb waves or plate waves are generated by an obliquely incident transducer transmitting ultrasonic waves to interrogate layered structures such as adhesive joints, composites, etc. The plate waves travel along the layered structure in many modes of propagation. Each mode generated in the structure is dependent on the combination of wavelength to thickness ratio and the interfacial conditions. The experimental setup usually consists of two transducers arranged in a pitch-catch arrangement as shown in Figure 1.

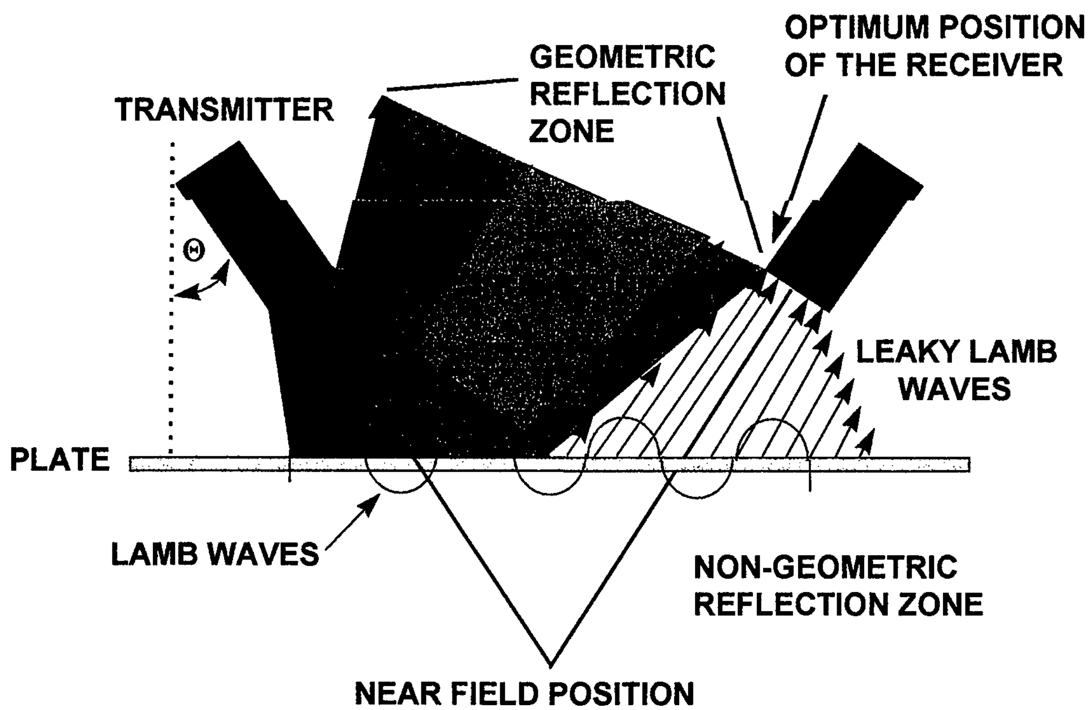

Figure 1 – Transmitter-receiver-sample geometry for a pitch-catch arrangement for Lamb wave evaluation of layered structure.

The null zone shown in Figure 1 has been traditionally used by many researchers to monitor the existence of Lamb waves in the layered structure [17]. Another method of implementation would be positioning the receiver in the leaky region as shown in Figure 1. In either implementation, the Lamb wave generation and propagation are sensitive to the overall layered structure geometry as well as the boundary conditions at the interface among the adherends and the adhesive layers. Therefore, many researchers have reported successful implementation as discussed in the next few paragraphs.

Several researchers have studied the use of Lamb waves for the characterization of adhesive joints. The results of these research efforts have been documented by Nagy, Rokhlin, Mal, Rose, Pilarski, and others in many journal and conference publications. Nagy and Adler [18] outlined nondestructive evaluation of adhesive joints by guided waves. They proposed interface waves traveling into the adhesive layer as well as the interfaces as an alternative approach to adhesive joint characterization. Rokhlin et al., [19, 20] have applied the use of Lamb waves through measurement of phase delay and transmission losses. They proposed the mode selection and optimization on an adherend outside the adhesive joint to optimize the modes in the adhesive joint itself. Mal et al, and Xu et al. [21, 22] studied the correlation between the dispersion of Lamb waves and the interfacial properties of Lamb waves. They reported that the correlation was 'quite strong' and was identifiable in at least the laboratory specimen. They further outlined an inversion scheme based on an iterative least-squares procedure to determine the cohesive properties of the adhesive bonds from the Lamb wave dispersion data.

Rose et al. and Pilarski et al. have conducted several studies involving various ultrasonic techniques to assess adhesive joints. They have reported [23-25] their research wherein the Lamb wave modes were propagated through the adhesive structure. They applied feature extraction and mapping techniques to extract information from Lamb wave amplitude, velocity, and frequency and correlated these features to the bond quality. Rose et al. [26, 27] further proposed an approach to guided wave mode selection for inspection of laminated plates wherein they discussed concepts of mode selection based on field distributions of each mode as a function of thickness of the plates. They discussed possibilities of using energy distribution, stress distribution, and normal as well as in-plane displacement distributions for the evaluation.

6.0 Lamb Wave Mode Selection Based on Field Distribution in Adhesive Joints – Present Work

The Air Force has an immediate need to monitor adhesive joints in weapon systems. Development of NDE methods for characterizing the stiffness and 'quality' of adhesive joints is critical to maintainability for aging systems applications. However there are significant technological challenges for the development of the specialized NDE methods because of the need for extreme sensitivity to subtle changes in localized properties of adhesives and the adhesive joints. For example, the ability to detect 'poor' adhesion of adhesive bonds cannot be achieved without a method of assessing small changes in bond interfacial behavior as well as changes in adhesive mechanical properties.

6.1 Background Information

Many researchers have used Lamb waves in the past for the evaluation of adhesive joints. However, little work has been done to date regarding the selection of Lamb waves based on the stress profile and/or displacement profile of various Lamb Wave modes for maximum sensitivity to the interfacial conditions. It is logical that when Lamb waves are selected for the inspection, it will be critical to select a mode which has an amplitude profile suitable for the intended evaluation. For example, in Figure 2a, the amplitude distribution is maximum near the two adhesive layer interfaces (metal-to-epoxy), and therefore such a mode will be suitable for the evaluation process. However, the mode in Figure 2b will be unsuitable for the inspection because of its amplitude distribution which has minima near the adhesive

interfaces. The amplitude distributions shown here are only schematic of just two of the possible distributions which can vary (even for a given mode of Lamb wave) as a function of the individual plate/layer thicknesses, elastic properties, and the wavelength of ultrasound used. Therefore, it is critical to select the mode of Lamb wave as well as the frequency of operation for effective adhesive joint assessment. Such a selection is possible only with a thorough Lamb wave dispersion and modal analysis. *Thus, even though this study has utilized Lamb Waves for the adhesive joint evaluation similar to many previous researchers, the mode selection based on amplitude profile* [26, 27] *of the Lamb wave modes is a novel approach being used in this work.*

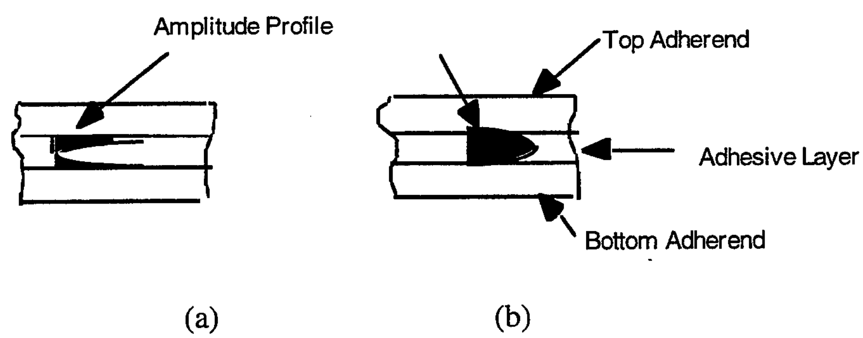

Figure 2 – (a)Displacement profile of a suitable lamb wave mode.
(b) Displacement profile of an unsuitable lamb wave mode.

6.2 Modeling of Lamb Waves for Mode Selection Using Field Distribution as a Criterion

Rose et al. and Pilarski et al. [26, 27] have provided the steps necessary for modeling with welded as well as smooth boundary conditions for cases using either Lamb waves or surface waves (surface waves, interfacial waves, and Lamb waves will exist when one of the

adherends is a semi infinite plate compared to the wavelength as in the case of a thin composite patch on an underlying thick aluminum plate). However, in the present study, since only metal-to-metal samples are considered with similar plate thicknesses and with a geometry of two adherends with one layer of adhesive in-between, the modeling to be presented herein will be specific for this geometry and has been extracted from Pilarski et al. and Rose et al. [26, 27] and modified for 3 layered case. A more generalized analysis can be found in literature [26, 27].

Consider three flat layers of homogeneous, isotropic, ideally elastic or viscoelastic media which represent the adhesively bonded structure of the geometry discussed above. The two dimensional, plane strain state equations are

$$\nabla^2\varphi = \frac{1}{c_L^2}\varphi_{,tt}, \quad \nabla^2\psi = \frac{1}{c_T^2}\psi_{,tt}, \quad \nabla^2 = \partial_{,xx} + \partial_{,zz} \tag{1}$$

with scalar potentials as shown below:

$$\varphi(x,z,t) = \varphi^*(z)\exp[ik(x+ct)] \tag{2}$$

$$\psi(x,z,t) = \psi^*(z)\exp[ik(x+ct)] \tag{3}$$

The longitudinal wave velocity is c_L and shear wave velocity is c_T for the harmonic wave propagating in negative 'x' direction. The wave number, k is given by,

$$k = \frac{\omega}{c} - i\alpha \tag{4}$$

wherein ω is the angular frequency, α is the attenuation, and c is the phase velocity.

The solution for (1) for the m^{th} layer will be,

$$\varphi_m = [A_m\cosh(ksz) + B_m\sinh(ksz)]\exp[ik(x+ct)] \tag{5}$$

$$\psi_m = [C_m\cosh(kqz) + D_m\sinh(kqz)]\exp[ik(x+ct)] \tag{6}$$

$$\text{with } s = \left[1 - \left(\frac{c}{c_L}\right)\right]^{\frac{1}{2}},\ q = \left[1 - \left(\frac{c}{c_T}\right)\right]^{\frac{1}{2}} \qquad (7).$$

Therefore, the displacements u and w as well as the stresses σ_{zz}, σ_{xz}, and σ_{xx} are given by,

$$u = (\varphi_{,x} - \psi_{,z}),\ w = \varphi_{,z} + \psi_{,x},$$

$$\sigma_{xx} = G\left[\left(\frac{c_L}{c_T}\right) - 2\right]\psi_{,zz} + G\left(\frac{c_L}{c_T}\right)^2 \varphi_{,xx} - 2G\psi_{,xz}, \qquad (8)$$

$$\sigma_{,xz} = 2G\varphi_{,xz} + G\,\psi_{,xx} - G\,\psi_{,zz}, \text{ and}$$

$$\sigma_{zz} = G\left[\left(\frac{c_L}{c_T}\right) - 2\right]\varphi_{,xx} + G\left(\frac{c_L}{c_T}\right)^2 \varphi_{,zz} + 2G\psi_{,xz}, \text{ wherein } G = \text{shear modulus.}$$

By using the boundary conditions of continuity of displacement and stresses at the interfaces, a system of homogeneous linear equations can be written for the three layer example being discussed here:

$$\sum_{j=1}^{12} a_{ij} A_j = 0 \qquad (i = 1,\ldots,12) \qquad (9)$$

Therefore, the characteristic equation is obtained by,

$$\mathrm{D} \equiv \det(a_{ij}) = 0 \qquad (10)$$

which is a determinant of the order 12 for the three layered case. The characteristic equations provide the dispersive curves when the required material elastic, physical, and geometrical properties are used. The cross-sectional distributions of displacements, stresses and energy can be obtained by solving the system of linear homogeneous equations (Eqn. 9) for Aj for the point of interest on the dispersion curves. Pilarski et al [27] have found that Aj and the related displacement and stress distributions are either real or purely imaginary (purely imaginary implies a 90° phase shift).

Mode selection based on field distribution has been proposed [27] for fields of normal displacement, in-plane displacement, stresses - σ_{xx}, σ_{zz}, and σ_{xz}, as well as the energy. However, the analysis presented herein will be based only on in-plane displacement due to the constraints imposed by the available time and resources. Further details of using other types of distributions (energy, stress, etc.) can be obtained from literature [27]. Further, a detailed review of NDE of adhesive joints is available in literature [28] and has been utilized in this as well as the preceding sections.

7.0 Results and Discussion

Two types of samples have been used during the program. One each of traditional aluminum-to-aluminum and copper-to-aluminum joints (which were readily available) were used for the experiments.

7.1 Sample Geometry, Properties and Dispersion Curves

TABLE 1
Geometrical dimensions and material properties for the aluminum-epoxy-aluminum sample used for the experiments.

Layer No.	Material	Longitudinal Velocity (m/s)	Shear Velocity (m/s)	Density (kg/m^3)	Thickness (mm)
1	Aluminum	6348	3133	2700	1.6764
2	Epoxy	2610	1100	1170	0.1092
3	Aluminum	6348	3133	2700	1.5621

Table 1 shows the geometry and properties of the aluminum-epoxy-aluminum joint used in the experiments. Since the plate thicknesses are not identical, the structure is asymmetric in nature. Figure 3 shows the dispersion curves for this adhesive joint structure. Since the total thickness of the structure is known, X-axis has been shown in MHz instead of the usual mmMHz scale. For simplicity, the structure is assumed to be nonattenuative. There are 12 modes of Lamb waves propagating in the structure in the frequency range up to 3.5 MHz.

Table 2 shows the geometry and properties of the copper-epoxy-aluminum joint used in the experiments. Since the plate thicknesses and materials are not identical, the structure is asymmetric in nature. Figure 4 shows the dispersion curves for this adhesive joint structure. Since the thickness of the structure is known, the X-axis has been shown in MHz instead of the usual mmMHz scale. For the sake of simplicity, the structure is assumed to be nonattenuative. There are over 14 modes of Lamb waves propagating in the structure in the frequency range up to 5 MHz.

TABLE 2
Geometrical dimensions and material properties for the copper-epoxy-aluminum sample used for the experiments.

Layer No.	Material	Longitudinal Velocity (m/s)	Shear Velocity (m/s)	Density (kg/m^3)	Thickness (mm)
1	Copper	4857	2361	8537	1.7780
2	Epoxy	2610	1100	1170	0.0762
3	Aluminum	6348	3133	2700	0.5080

Figures 3 and 4 show dispersion curves for Lamb waves in these joints described in Tables 1 and 2. Each curve is for a specific mode of Lamb wave. The mode shape (in-plane displacement amplitudes, in specific) are variable from mode-to-mode as well as from frequency to frequency for a given mode. Therefore, it is imperative that a mode at a specific frequency should be selected such that the amplitude of displacement provides maximum sensitivity at the two metal-to-adhesive interfaces in the joint.

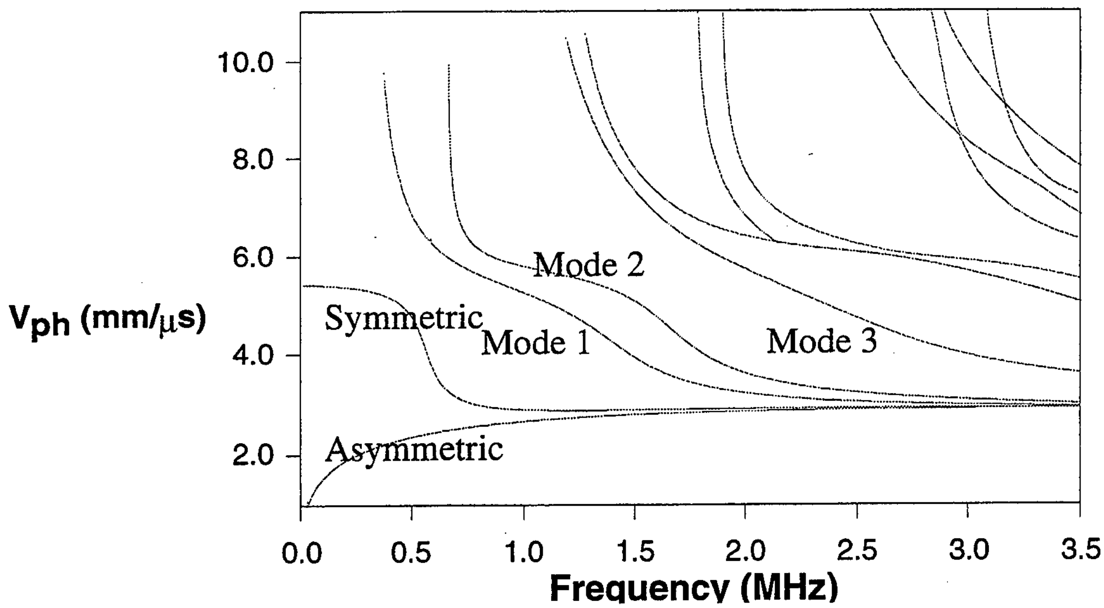

Figure 3 – Lamb wave dispersion curves for the al-epoxy-al adhesive joint sample.

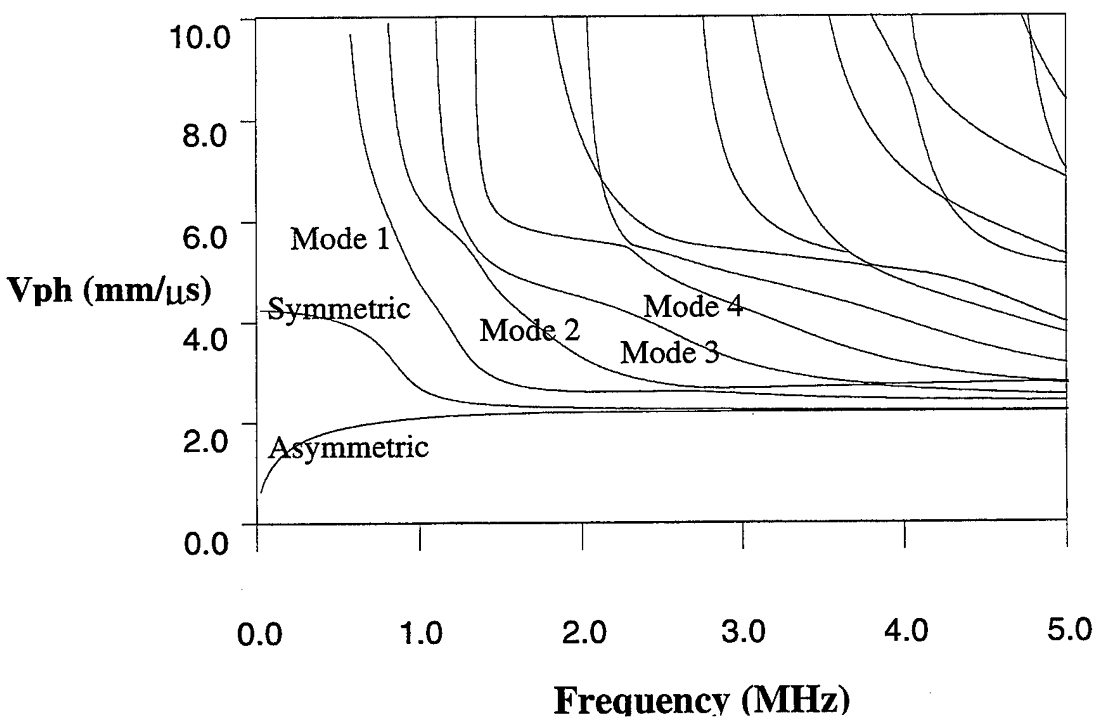

Figure 4 – Lamb wave dispersion curves for the cu-epoxy-al adhesive joint sample.

7.2 Experimental Results – Ultrasonic Images

The first set of images in Figures 5 through 9 are from the Al-epoxy-Al sample. The sample was scanned with various modes generated by varying either the frequency, angle, or both. The modes were selected based on the in-plane displacement distribution at the two interfaces. Since the interfacial conditions are of interest, the modes selected for the analysis had large amplitudes of in-plane displacement at one or both the interfaces.

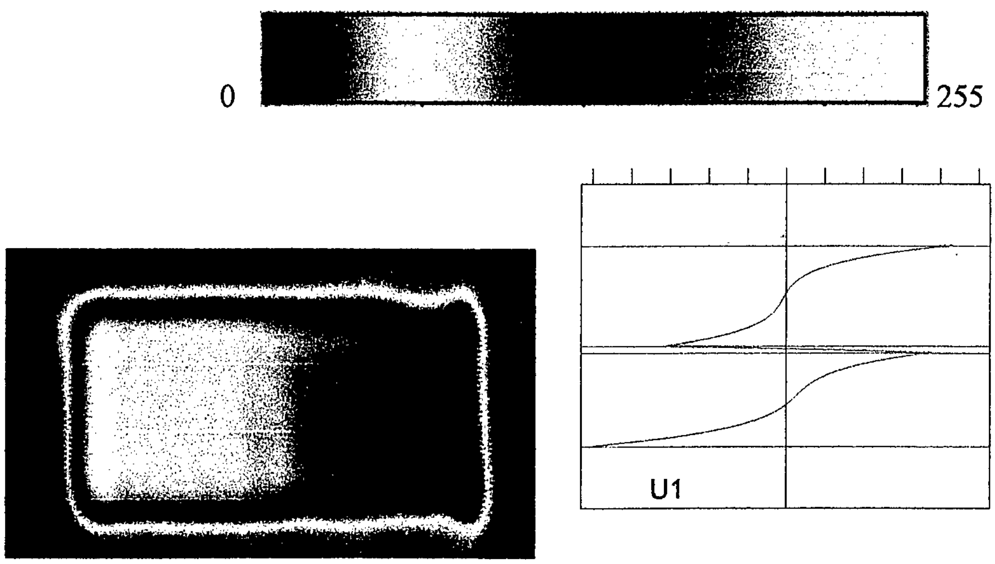

(a) (b)

Figure 5 – (a) Ultrasonic Lamb wave image of Al-epoxy-Al adhesive joint using asymmetric mode at 0.9872 MHz (V_{ph} of 2.645 mm/μs).
(b) In-plane displacement amplitude distribution for the mode along the thickness of the sample.

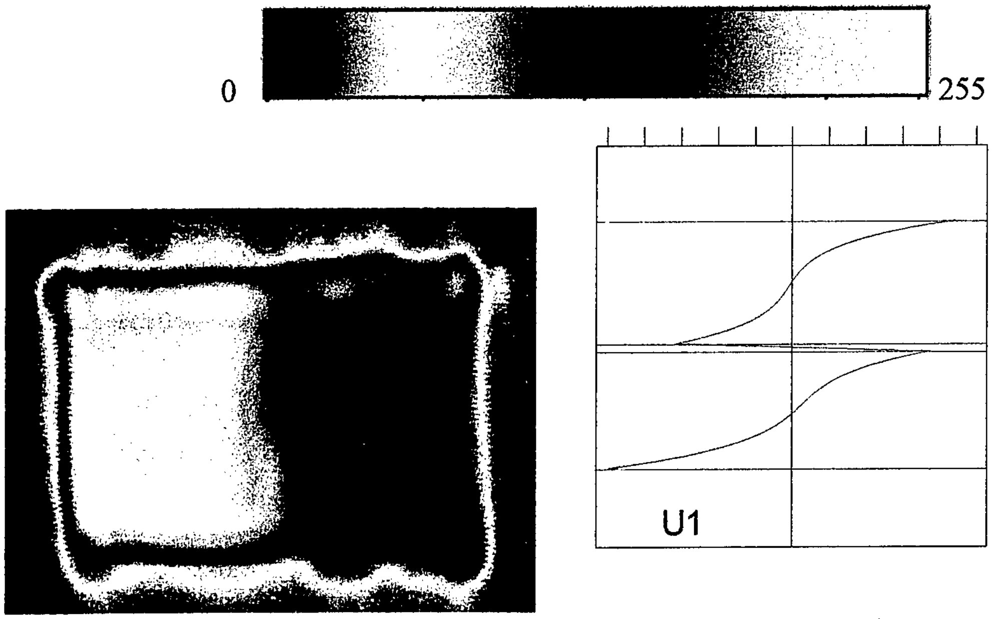

(a) (b)

Figure 6 – (a) Ultrasonic Lamb wave image of Al-epoxy-Al adhesive joint using asymmetric mode at 0.8773 MHz (V_{ph} of 2.598 mm/μs).
(b) In-plane displacement amplitude distribution for the mode along the thickness of the sample.

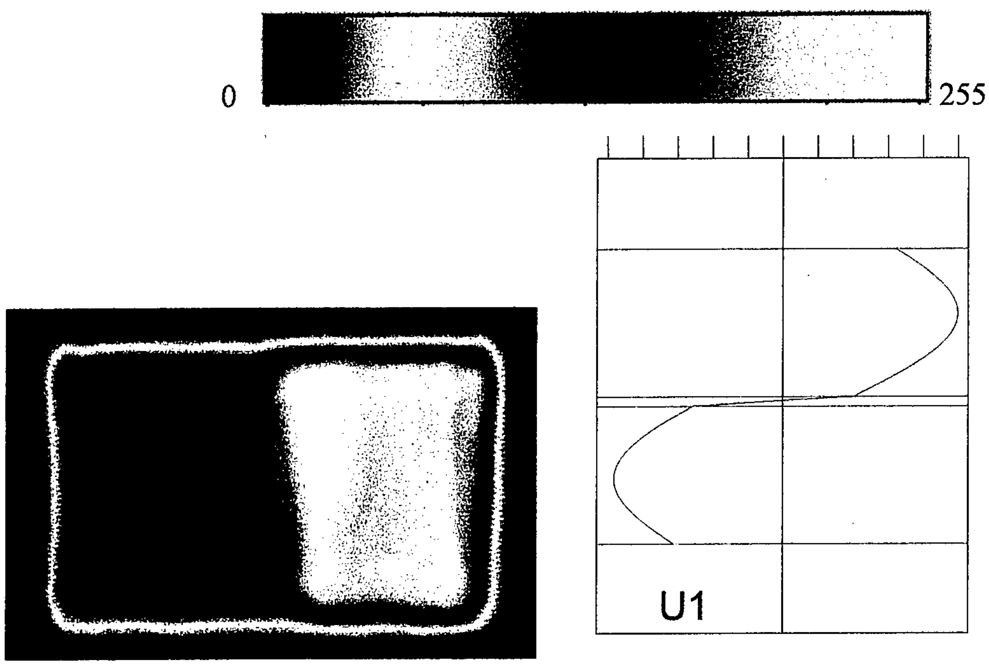

(a) (b)

Figure 7 – (a) Ultrasonic Lamb wave image of Al-epoxy-Al adhesive joint using Mode 1 at 1.001 MHz (V_{ph} of 5.255 mm/μs).
(b) In-plane displacement amplitude distribution for the mode along the thickness of the sample.

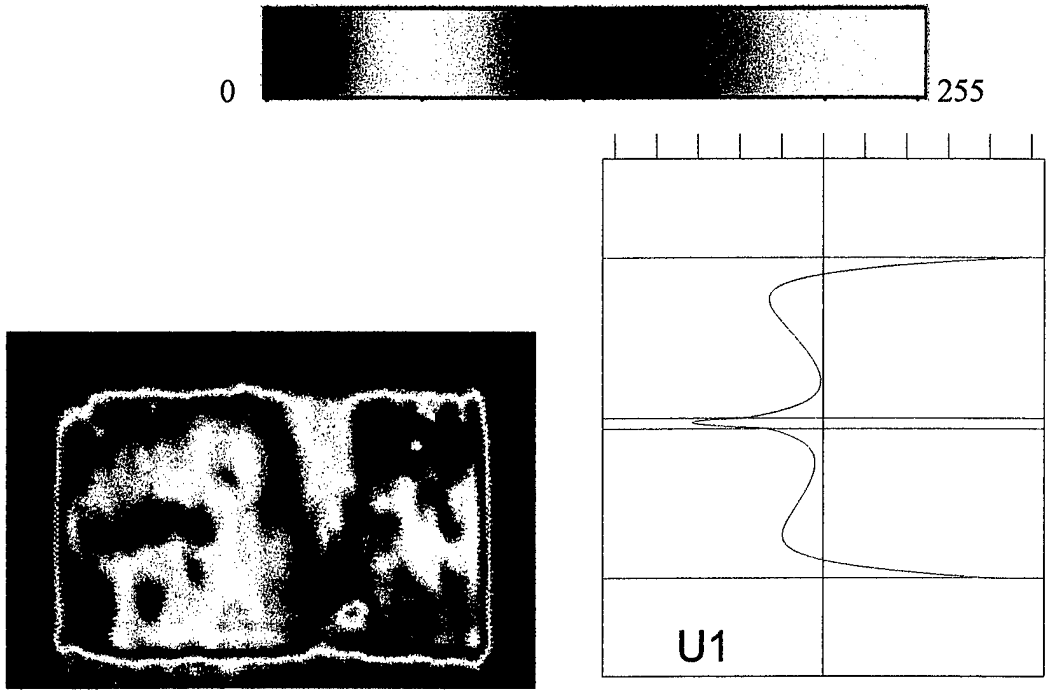

(a) (b)

Figure 8 – (a) Ultrasonic Lamb wave image of Al-epoxy-Al adhesive joint using symmetric mode at 2.836 MHz (V_{ph} of 2.915 mm/μs).
(b) In-plane displacement amplitude distribution for the mode along the thickness of the sample.

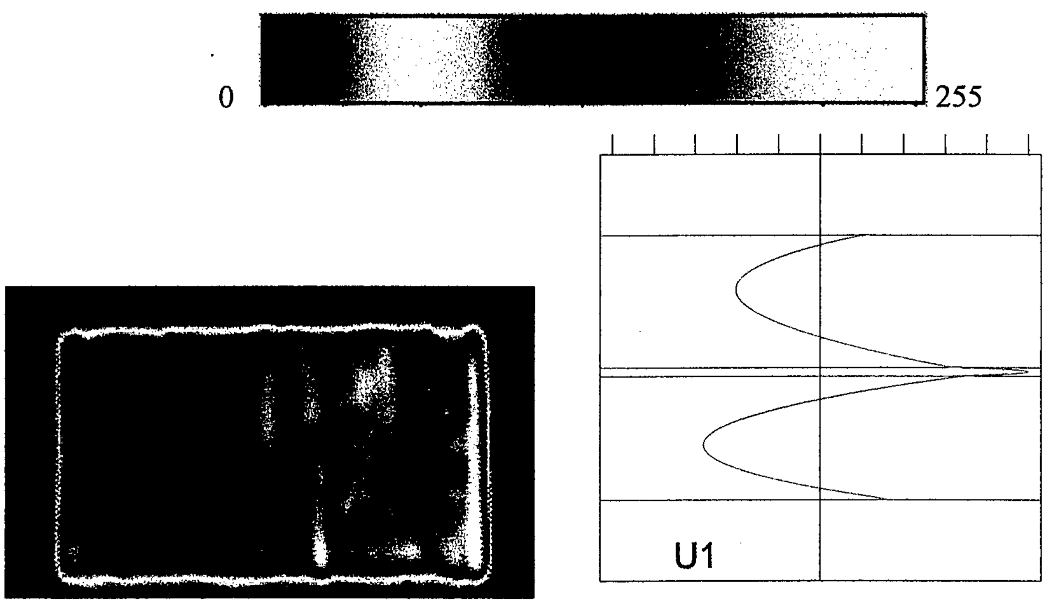

(a) (b)

Figure 9 – (a) Ultrasonic Lamb wave image of Al-epoxy-Al adhesive joint using Mode 2 at 2.002 MHz (V_{ph} of 3.608 mm/μs).
(b) In-plane displacement amplitude distribution for the mode along the thickness of the sample.

The second set of images in Figures 10 through 14 are from the Cu-epoxy-Al sample. The sample was scanned with various modes generated by varying either the frequency, angle, or both. The modes were selected based on the in-plane displacement distribution at the two interfaces. Since the interfacial conditions are of interest, the modes selected for the analysis had large amplitudes of in-plane displacement at one or both the interfaces.

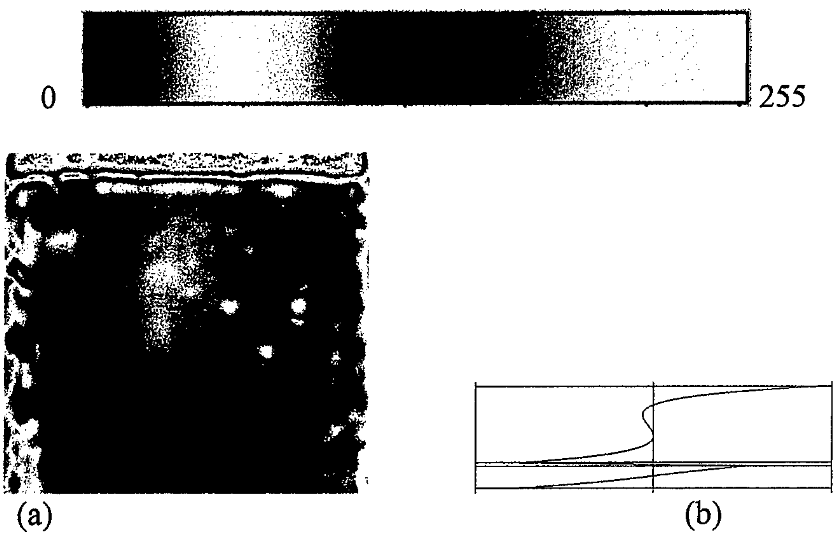

Figure 10 – (a) Ultrasonic Lamb wave image of Cu-epoxy-Al adhesive joint using asymmetric mode at 1.074 MHz (V_{ph} of 2.104 mm/μs).
(b) In-plane displacement amplitude distribution for the mode along the thickness of the sample.

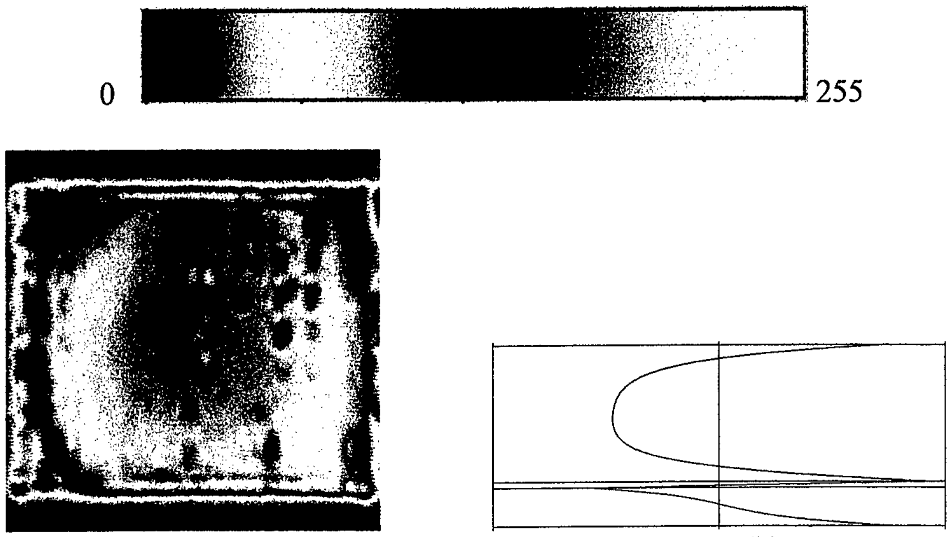

(a) (b)

Figure 11 – (a) Ultrasonic Lamb wave image of Cu-epoxy-Al adhesive joint using symmetric mode at 1.855 MHz (V_{ph} of 2.295 mm/μs).
(b) In-plane displacement amplitude distribution for the mode along the thickness of the sample.

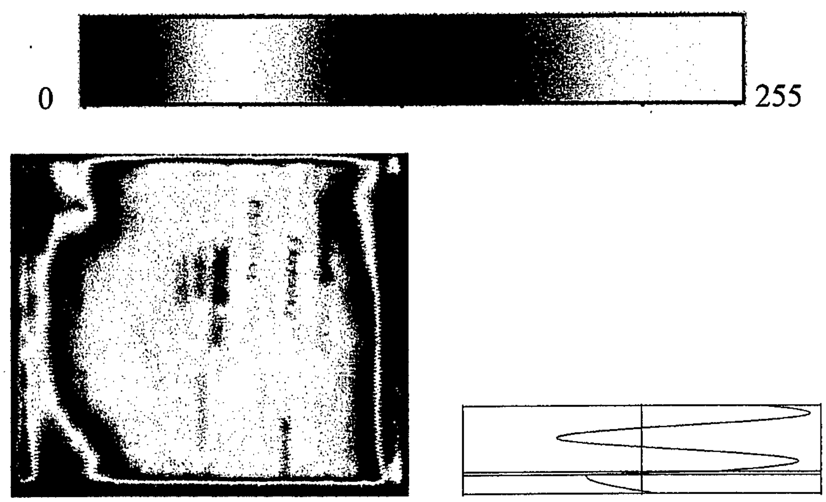

(a) (b)

Figure 12 – (a) Ultrasonic Lamb wave image of Cu-epoxy-Al adhesive joint using Mode 3 at 2.316 MHz (V_{ph} of 4.139 mm/μs).
(b) In-plane displacement amplitude distribution for the mode along the thickness of the sample.

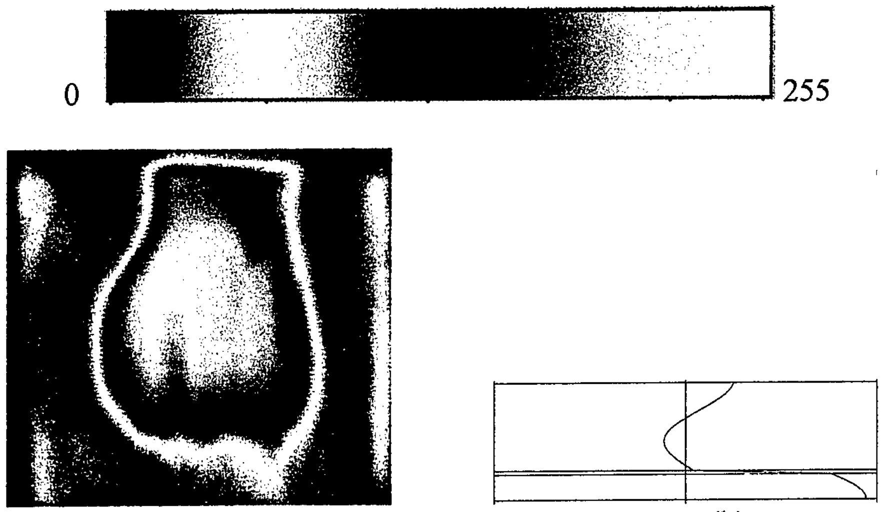

(a) (b)

Figure 13 – (a) Ultrasonic Lamb wave image of Cu-epoxy-Al adhesive joint using Mode 2 at 1.023 MHz (V_{ph} of 6.377 mm/μs).
(b) In-plane displacement amplitude distribution for the mode along the thickness of the sample.

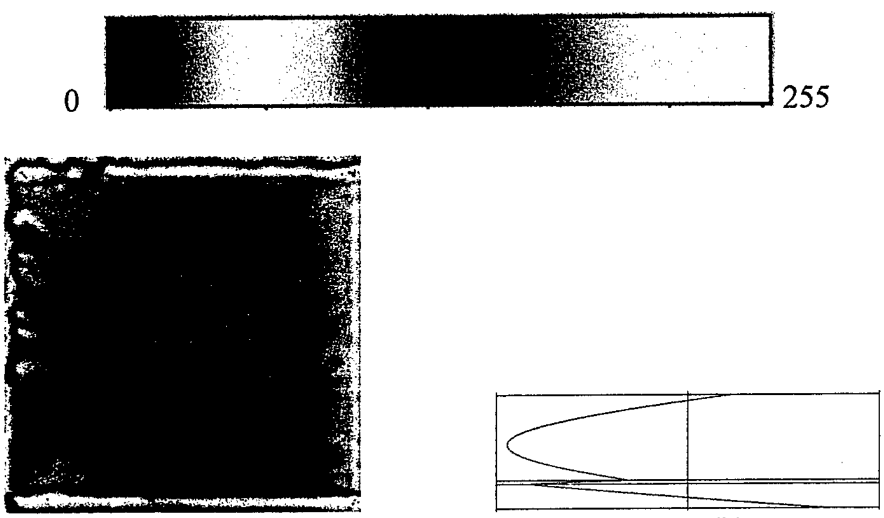

(a) (b)

Figure 14 – (a) Ultrasonic Lamb wave image of Cu-epoxy-Al adhesive joint using symmetric mode at 0.8803 MHz (V_{ph} of 3.063 mm/μs).
(b) In-plane displacement amplitude distribution for the mode along the thickness of the sample.

7.3 Discussion

Figures 5 and 6 show the image of the bonded joint wherein 'asymmetric' fundamental mode was utilized with slightly different phase velocities and frequencies, however with similar displacement distribution patterns (it has to be pointed out here however that the distribution pattern for a given mode will change when the deviations in phase velocities and frequencies are substantial). The resulting images are remarkably similar indicating consistency and robustness and show a clear difference between the two halves of the sample (the lines along the edges of the sample are artifacts produced when one of the transducers gets too close to the edge while the other is still within the boundaries of the sample). Figure 7 shows the same sample, however using Mode 1 (see Figure 3 for mode labeling) which has substantially different in-plane displacement distribution pattern with a 'reversed' amplitude distribution at the interfaces. The image clearly reflects this pattern while still showing a difference between the two halves of the sample. A change in image manifestation without the corresponding displacement distribution can be easily misconstrued as a lack of robustness and consistency due to 'extreme' sensitivity of Lamb waves (a comment often seen in literature) when in reality the modes are imaging exactly what the displacement distribution is 'seeing' within the sample. Figure 8 shows a similar manifestation of the bondline which can be easily interpreted as lack of consistency. The ultrasonic image in Figure 8 shows no difference between the two halves of the sample (while showing, due to higher frequency of interrogation, some trapped voids in the epoxy region). However, one glance at the distribution pattern in Figure 8b shows that the amplitudes at both the interfaces are similar in sign but with small deviations in magnitude. Because of the higher frequency of interrogation, the voids (perhaps due to trapped air bubbles) are resolvable and are visible in the image.

Figures 10 through 12 are obtained from the Cu-epoxy-Al sample using asymmetric, symmetric, and Mode 3 Lamb waves respectively. As can be seen from the corresponding in-plane displacement distribution pattern, the amplitudes at the interfaces are non-zero. However, the amplitudes for images in Figure 11 and 12 are inverse of that in Figure 10. The frequency of interrogation is progressively higher from Figure 10 to Figure 12. Therefore, the image in Figure 10 is similar, but inverted from those in Figures 11 and 12 while the definition of bubbles/voids are progressively getting better because of better resolution at higher frequency. In fact, in Figure 12, the bubbles can be very clearly seen as lines whose length is defined by the separation distance between the transmitter and the receiver. Since the amplitudes at both the interfaces are nonzero, the images obviously will map the features and anomalies at both the interfaces. However, when a mode is selected with zero or near zero amplitude at one of the interfaces as in Figure 13, the features at only one of the interfaces can be mapped. In Figure 13, the in-plane displacement at the Cu-epoxy interface is near zero for Mode 2. Therefore, the image of the bondline is predominantly from the second interface alone (epoxy-Al interface). Therefore, the images of the bubbles are somewhat suppressed while the 'bottle shaped' feature from the second interface is enhanced. In Figure 14, asymmetric mode is selected at 0.879 MHz with a mode shape as shown in Figure 14b (this in-plane displacement shape is much different when compared to the shape for the same mode in Figure 11 which is at 1.855 MHz). The mode shape in Figure 14b is nonzero at both the interfaces, however with the same 'polarity' instead of opposite 'polarity; as in Figures 10 through 12. The resulting image shown in Figure 14a therefore has features from both the interfaces, but manifesting differently than the well contrasted images (changes in displacement magnitude at the interfaces) in Figures 10 through 12. Thus, the sequence of

images in Figures 10 through 14 very clearly demonstrates the reason for changes in ultrasonic Lamb wave images from mode-to-mode as well as for the same mode from one point on the dispersion curve to the other. It is obvious from these results that the changes in images DO NOT indicate the lack of robustness or stability due to excessive sensitivity of Lamb waves. On the contrary, the sensitivity of the technique is high, robust, and consistent from mode-to-mode when the changes are viewed in light of the mode shapes (distribution patterns).

8.0 Summary and Conclusions

This section will summarize the work done under this program and will draw some conclusions while providing some recommendations based on the results obtained from the theoretical as well as experimental aspects of this program.

8.1 Summary

In summary, the problem of inspection of adhesive joints is challenging and difficult. There are several models which attempt to describe the mechanism of adhesion which is critical to develop any successful approach to bondline integrity assessment. Many researchers have studied the problem and have applied various nondestructive techniques to evaluate the integrity of adhesive joints. Many techniques have shown a great deal of success to .evaluate cohesive forces/properties of the adhesive joint. However, the success of evaluating adhesive forces/properties have been limited at best. Ultrasonic approaches for the NDE of adhesive joints has been one of the most studied methodologies. Normal incidence pulse-echo and through transmission techniques have been studied with limited success. Spectral analysis and feature extraction techniques have been explored. Oblique incidence reflection coefficient techniques have been applied with some degree of success. Lamb wave techniques to date have shown successes, however while suggesting 'excessive sensitivity' to be used successfully to evaluate the interface bonding. The work presented in this report has attempted to evaluate the possibilities of using Lamb waves to assess the adhesively bonded joints with Lamb modes selected because of their 'Mode Shapes'.

The adhesively bonded structure has been modeled as three flat layers of homogeneous, isotropic, ideally elastic or viscoelastic media. Therefore, the general solution to the two dimensional wave equations can be obtained. By using the welded boundary conditions, a set of 12 homogeneous linear equations can be obtained for the three layered case which will provide the dispersion curves as well as the displacement, stress, and power distributions for each mode across the thickness of the adhesively bonded structure. Such mode shapes can now be used as the basis for the selection of various modes for an optimized and robust assessment of the structure. For example, if the interfacial conditions are of utmost importance, then modes with maximum amplitudes of displacement at the interface can be selected. However, if cracking in the top and/or bottom plates is of interest, modes with large amplitudes at the surface will have to be selected.

Two adhesively bonded samples have been used in this study, one Al-epoxy-Al sample and another Cu-epoxy-Al sample. The samples were imaged with various Lamb wave modes to assess the feasibility of interfacial condition assessment. Some of the modes had large sensitivity at both the interfaces while others were selected with zero or close to zero amplitude at one of the interfaces. Yet other modes were selected to have reversed distribution pattern at the interfaces. The results show a high degree of robustness, reliability, and sensitivity from image to image.

8.2 Conclusions

Adhesively bonded structures pose a challenge to nondestructive assessment of their integrity. However, Lamb waves have been found to be well suited for the application especially when mode selection is based on the mode shape (for example, the shape distribution of in-plane displacement). In this study, only in-plane displacement amplitude distributions were considered for the analysis. Based on this distribution, deviations in ultrasonic images can be easily understood which would have been otherwise described as instability due to excessive sensitivity of Lamb waves to property changes. The scope, duration, and available resources of this project precluded further studies based on other distributions such as out-of-plane displacement, stress, and energies. It is recommended to conduct a study with these distributions, especially with a 'resultant' combination of in-plane and out-of-plane distributions. Further, since lack of resources precluded these tests, destructive tests of the samples for the corroboration of the ultrasonic results are necessary.

9.0 References

[1] R. D. Adams, P. Cawley, "Mechanics of the Coin-Tap Method of Non-Destructive Testing", *Journal of Sound and Vibration*, **122**, 299-316 (1988).

[2] D. O. Thompson, R. B. Thompson, G. A. Alers, "Nondestructive Measurement of Adhesive Bond Strength in Honeycomb Panels", *Materials Evaluation*, 81-85 (1974).

[3] F. J. Meyer, G. B. Chapman, "Nondestructive Testing of Bonded FRP Assemblies in the Auto Industry", *Adhesives Age*, 21-25 (1980).

[4] C. C. H. Guyott, P. Cawley, R. D. Adams, "The Non-Destructive Testing of Adhesively Bonded Structure: A Review", *Journal of Adhesion*, **20**, 129-159 (1986).

[5] E. Segal, J. L. Rose, "Nondestructive Testing Techniques for Adhesive Bond Joints", *Research Techniques m NDT*, **IV**, 275-316 (1980).

[6] J. L. Rose, P. A. Meyer, "Ultrasonic Procedure for Predicting Adhesive Bond Strength", *Materials Evaluation*, 109-114 (1973).

[7] P. A. Meyer, J. L. Rose, "Ultrasonic Determination of Bond Strength Due to Surface Preparation Variations in Aluminum to Aluminum Adhesive Bond System", *Journal of Adhesion*, **8**, 145-153 (1976).

[8] T. Chernobefskaya, S. Kovnovich, E. Harnik, "The Testing of Adhesive-Bonded Joints by a Very High Resolution Ultrasonic Probe", *Journal of Physics D: Applied Physics*, **12**, (1979).

[9] J. W. Raisch, J. L. Rose, "Computer Controlled Ultrasonic Adhesive Bond Evaluation", *Materials Evaluation*, 55-64 (1979).

[10] J. L. Rose, G. H. Thomas, "The Fisher Linear Discriminant Function for Adhesive Bond Strength Prediction", *British Journal of Nondestructive Testing*, **21**, 135-139 (1979).

[11] G. A. Alers, R. K. Elsley, Measurement of Metal to Adhesive Bond Quality Using Digital Signal Analysis, *IEEE Ultrasonics Symposium* (IEEE, 1977), vol. No. 77CH1264- ISU.

[12] R. S. Williams, P. E. Zwicke, "Assessment of Adhesive Properties Using Pattern Recognition Analysis of Ultrasonic NDE Data", *Materials Evaluation*, **40**, 312-317 (1982).

[13] A. Pilarski, J. L. Rose, "A Transverse Wave Ultrasonic Oblique Incidence Technique for Interfacial Weakness Detection in Adhesive Bonds", *Journal of Applied Physics*, **63**, (1988).

[14] S. I. Rokhlin, D. Marom, "Study of Adhesive Bonds Using Low Frequency Obliquely Incident Ultrasonic Waves", *Journal of the Acoustical Society of America*, **80**, 585-590 (1986).

[15] C. M. Scala, P. A. Doyle, "Ultrasonic Leaky Interface Waves for Composite-Metal Adhesive Bond Characterization", *Journal of Nondestructive Evaluation*, **14**, 49-59 (1995).

[16] P. W. Staecker, W. C. Wang, "Propagation of Elastic Waves Bound to a Fluid Layer Between Two Solids", *Journal of the Acoustical Society of America*, **53**, 65-74 (1973).

[17] D. E. Chimenti, Y. Bar-Cohen, "Signal Analysis of Leaky Lamb Wave Spectra for NDE of Composites", *Proceedings of IEEE Ultrasonics Symposium*, 1028-1031 (1985).

[18] P. B. Nagy, L. Adler, "Nondestructive Evaluation of Adhesive Joints by Guided Waves", *Journal of Applied Physics*, **66**, 4658-4663 (1989).

[19] S. I. Rokhlin, B. Li, A. I. Lavrentyer, "Ultrasonic Evaluation of Interfacial Properties in Adhesive Joints. Assessment of Environmental Degradation", *Ultrasonics Symposium*, (1992).

[20] S. I. Rokhlin, "Lamb Wave Interaction with Lap-shear Adhesive Joints: Theory and Experiment", *Journal of Acoustical Society of America*, (1989).

[21] A. K. Mal, P.-C. Xu, Y. Bar-Cohen, "Leaky Lamb Waves for the Ultrasonic Nondestructive Evaluation of Adhesive Bonds", *Journal of Engineering Materials and Technology*, **112**, 255-259 (1990).

[22] P.-C. Xu, A. K. Mal, Y. Bar-Cohen, "Inversion of Leaky Lamb Wave Data to Determine Cohesive Properties of Bonds", *International Journal of Engineering Science*, **28**, 331-346 (1990).

[23] J. L. Rose, J. J. Ditri, D. Gallela, T. Grant, Adhesive Bond Inspection Utilizing Ultrasonic Lamb Waves, *Proceedings of 15th Annual Meeting of the Adhesion Society* (Hilton Head, SC, 1992), pp. 181-183.

[24] J. L. Rose, J. J. Ditri, "Pulse-Echo and Through Transmission Lamb Waves Techniques for Adhesive Bond Inspection", *British Journal of Nondestructive Testing*, **34**, 591-594 (1992).

[25] J. L. Rose, K. Rajana, A. Pilarski, "Ultrasonic Guided Waves for NDE of Adhesively Bonded Joints in Aging Aircraft", *The Adhesion Society*, 272-275 (1994).

[26] J. L. Rose, A. Pilarski, J. J. Ditri, "An Approach to Guided Wave Mode Selection for Inspection of Laminated Plate", *Journal of Reinforced Plastics and Composites*, **12**, 536-544 (1993).

[27] A. Pilarski, J. L. Rose, "Lamb Wave Mode Selection Concepts for Interfacial Weakness Analysis", *Journal of Nondestructive Evaluation*, **11**, 237-249 (1992).

[28] G. M. Light, H. Kwun, NTIAC Report, Nondestructive Evaluation of Adhesive Bond Quality (1989).